Alma Mater Studiorum - Università di Bologna

DOTTORATO DI RICERCA IN

SCIENZE DELLA TERRA, DELLA VITA E DELL'AMBIENTE

Ciclo 34

Settore Concorsuale: 04/A3 - GEOLOGIA APPLICATA, GEOGRAFIA FISICA E GEOMORFOLOGIA

Settore Scientifico Disciplinare: GEO/05 - GEOLOGIA APPLICATA

NUMERICAL SIMULATION OF RAPID FLOW-LIKE LANDSLIDES AND SOME RELATED PHENOMENA BASED ON IMPROVED DEPTH-AVERAGED MODELS

Presentata da: Wei Shen

Coordinatore Dottorato

Maria Giovanna Belcastro

Supervisore

Matteo Berti

Co-supervisore

Alessandro Gargini

Esame finale anno 2022

Acknowledgements

These three years of PhD study passed almost like a dream to me when I look back to the things happened. Together with my colleagues, friends and family members, we got though a lot of memorable moments. To be honest, because of the language barrier and cultural differences, it was quite difficult for me to get used to the environment here in the first few months when I arrived in this beautiful country. Nevertheless, I was lucky because most people I met here were nice and supportive. Without their generous help and encouragement, I will not be able to overcome the difficulties that easy. Here, I would like to thank all the people who supported me, encouraged me and shared this unforgettable journey with me.

First of all, I would like to thank my colleagues at Unibo. Thanks to my PhD supervisor Prof. Matteo Berti for his patient guide in the last three years. He is a very easy-going 'boss' and an inspiring leader, and he was always ready to help when I had questions in research and life. Without his generous support I will never be able to complete this PhD thesis. My sincere thanks also give to my kind and thoughtful teammates Dr. Benedict Bayer, Dr. Silvia Franceschini, Dr. Gabriela Squarzoni, Zhitian Qiao, Shuangshuang Wu and Prof. Alessandro Simoni. I will always remember their precious friendships. In addition, thanks to all the other lovely colleagues in our department.

Secondly, I would like to thank my collaborators. I would like to give my sincere thanks to my supervisors at Chang'an University, Prof. Tonglu Li and Prof. Ping Li, and all their team members who supported me. Thanks to Prof. Qiuhua Liang, Dr. Xilin Xia and their teammates in

Loughborough University. Thanks to Prof. Dongpo Wang and his team at Chengdu University of Technology. They helped me a lot in my research work in these three years.

Last but not the least, I must express my endless thanks to my beloved wife Miao, my parents, my sister and all my other family members. Without their love and support, life would be too bitter and meaningless.

Thanks to all of you!

To my wife.

Abstract

Rapid flow-like landslide is a flow-type mass movement which commonly has a large speed and a long run-out distance. The high mobility of this kind of landslide increases the risk to the infrastructures and people's security on the run-out path. Numerous catastrophic flow-like landslides have occurred in the last few decades claiming thousands of life tolls. Although notable progresses have been made in terms of the development of early-warning systems and numerical modeling technologies in the recent two decades, the threat caused by flow-like landslide is still very intensive because of complex factors such as the rapid urbanization process and the increasing extreme climate events. Therefore, it is still an urgent task for the scientists and engineers to develop effective measures to address the challenges caused by rapid flow-like landslide.

Numerical simulation is an efficient tool for the run-out analysis of rapid flow-like landslide. In this thesis, I address three topics related to the modeling of flow-like landslide which were not sufficiently investigated in the previous studies. Three improved depth-averaged models are used to simulate the selected typical flow-like landslides and related phenomena. In the first topic, a two-layer depth-averaged model is proposed to simulate the frontal plowing phenomenon in some rapid flow-like landslides. The propagation process of a loess landslide in Shaanxi Province, China and its interaction with the terrace material is analyzed. The second topic is related to the influence of the slope gradient and gully channel on the run-out behavior (especially the entrainment and deposition characteristics) of rockslide-debris flow. The run-out process of the Verghereto rockslide-debris flow in Italy is analyzed by using an improved depth-averaged model. The third

topic is related to the numerical assessment of the impeding effect of check dam on debris flow. Another improved depth-averaged model, which takes both entrainment and the impeding effect of check dam into account, is proposed and adopted to analyze the interaction of debris flow and check dams in a debris flow gully in Sichuan province, China. The model is then used to assess the efficiency of the actual check dams in this debris flow gully.

The main purpose of this thesis is to investigate the capacity of the improved depth-averaged models on the simulation of rapid flow-like landslides and the related phenomena (frontal plowing, entrainment, and interaction between debris flow and check dam). The simulation results of the case studies in this thesis show that these improved models perform well in simulating the rapid flow-like landslides and the phenomena mentioned above, which demonstrates the potential application ability of these models for the risk assessment of rapid flow-like landslides.

Content

1. INTRODUCTION **1**

1.1 State of the art 1

1.1.1 Rapid flow-like landslides and related phenomena 1

1.1.2 Modeling methods for rapid flow-like landslides 10

1.1.3 Brief summary of the state-of-the-art 22

1.2 Motivation and outline of the thesis 24

1.3 Reference 27

2. PAPER 1 ..... **36**

A two-layer numerical model for simulating the frontal plowing phenomenon of flow-like landslides 36

3. PAPER 2 ..... **49**

The influence of slope gradient and gully channel on the run-out behavior of rockslide-debris flow: an analysis on the Verghereto landslide in Italy 49

4. PAPER 3 ..... **82**

The effect of check dams on the dynamic and bed entrainment processes of debris flows 82

5. PAPER 4 ..... **100**

Numerical assessment of the impeding effect of check dams in the Hongchun debris flow gully, Sichuan Province, China 100

6. CONCLUSIONS **114**

Appendix A: Co-author declaration 119

Appendix B: Derivation of the depth-averaged model 121

1. INTRODUCTION

1.1State of the art

1.1.1 Rapid flow-like landslides and related phenomena

Definition of rapid flow-like landslides

According to the type of movement, landslides can be classified into six groups (fall, topple, slide, spread, flow and complex movement) in the original Varnes classification (Varnes 1978) or five groups (fall, topple, slide, spread, and flow) in the updated Varnes classification (Cruden and Varnes 1996). More recently Hungr et al. (2014) reviewed the classification of flow-like landslides. In the existing classifications, flow-type landslides include a wide range of mass movements. As shown in Table 1.1, the main difference between the Varnes and Hungr classifications on the definition of flow is that only two types of materials (rock and soil) are identified in the Hungr classification, while in the original classification three materials (rock debris and earth) are presented. The Hungr classification agrees with the standard geotechnical terminology, so we adopt this classification for the definition of the flow-like landslide in this thesis.

The speeds of flow-like landslides vary significantly depending on the material properties of the landslides. The rapid flow-like movements like debris flows and debris avalanches can reach a speed of tens meters per second, while the slow movements like earthflows only have a peak velocity of a few meters per hour (Berti et al. 2019). A method for the description of landslide velocity was proposed by the Working Party of the International Geotechnical Societies (WP/WLI 1995). According to the suggestion of WP/WLI, a landslide can be defined as

extremely rapid (>5 m/s), very rapid (5 m/s - 3 m/min), rapid (3 m/min - 1.8 m/h), moderate (1.8 m/h - 13 m/month), slow (13 m/month - 1.6 m/year), very slow (1.6 m/year - 1.6 mm/year), and extremely slow (<1.6 mm/year). However, the rapid landslide in the present context refers to the landslide reaches at least meters per second which basically belongs to the extremely rapid class in the WP/WLI velocity scale. Therefore, the rapid flow-like landslide here can be defined as the flow-like movement classified by the Hungr classification which reaches a velocity of at least meters per second. Debris flow, rock avalanche, debris avalanche, flowslide, and mud flow are typical rapid flow-like landslides (as illustrated in Table 1.1), and they are the objects of study in this thesis. Some typical catastrophic rapid flow-like landslides are illustrated in Fig.1.1, 1.2 and 1.3.

Table 1.1 Classification of flow-like landslides

Hungr classification		**Original Varnes classification**		
Rock	Soil	Rock	Debris	Earth
Rock/ice avalanche*	Sand/silt/debris dry flow Sand/silt/debris flowslide* Sensitive clay flowslide* Debris flow* Mud flow* Debris flood Debris avalanche* Earthflow Peat flow	Rock creep	Talus flow Debris flow Debris avalanche Solifluction Soil creep	Dry sand flow Wet sand flow Quick clay flow Earth flow Rapid earth flow Loess flow
*Flows reach extremely rapid velocities (> 5 m/s)				

Catastrophic events caused by rapid flow-like landslides

In comparison with slow landslides, rapid flow-like landslides are commonly more dangerous because of the high-speed and long run-out characteristics of these movements. Catastrophic events caused by rapid flow-like landsides occurred frequently in mountainous regions, especially in the developing countries with high population

density and poor urban planning. In Table 1.2, we list several most notorious rapid flow-like landslides occurred around the world. Some of these events occurred in the downtown areas resulting in thousands of deaths. For instance, the huge debris flow triggered by a local extreme rainfall destroyed almost half of the downtown area of the Zhouqu County (shown in Fig. 1.1), which is the most catastrophic debris flow event occurred in China in this century up to now (Hu et al. 2012, Tang et al. 2011, Wang 2013). More seriously, intense storms may trigger a group of debris flows in the same region at almost the same time, resulting in more damages. A typical example is the debris flow events occurred in Venezuela on December 15–16, 1999, in which nearly 30,000 people were killed and 126,000 homes were damaged (García-Martínez and López 2005, Pérez 2001). Moreover, sometimes rapid flow-like landslides may generate a disaster chain such as landslide-surge wave-dam break flood, forming a series of events that endanger a broader region (Fan et al. 2020). A typical landslide dam formed by a rock avalanche is illustrated in Fig. 1.3. These catastrophic events remind us the importance of developing reliable technologies for the identification, early-warning, and risk assessment of the potential rapid flow-like landslides.

Table 1.2 Several catastrophic rapid flow-like landslide occurred worldwide

Landslide	Time	Country	Volume (10^6 m^3)	Run-out (km)	Fatality	Reference
Leyte rockslide-debris flow	17 Feb. 2006	Philippines	20	4.1	1119	Catane et al. (2007)
Caucasus glacier-debris flow	20 Sep. 2002	Russia	130	19	125	Evans et al. (2009)
Zhouqu debris flow	8 Aug. 2010	China	2.2	2.1	1765	Tang et al. (2011)
Saleshan flowslide	7 Mar, 1983	China	31	1.0	237	Zhang et al. (2021)
Yigong rockslide-debris flow	9 Apr. 2000	China	100	10.7	unknown	Delaney and Evans (2015)
Frank rock avalanche	29 Apr. 1903	Canada	30	2	70	Cruden and Hungr (1986)
Malpa rock fall–debris flow	8 Aug. 1998	India	1.0	-	221	Paul et al. (2000)
Debris flows at central coast of Venezuela	15–16 Dec. 1999	Venezuela	-	-	30,000	Pérez (2001)

Fig. 1.1 The downtown area of Zhouqu County in Gansu Province, China after the occurrence of the catastrophic debris flow on August 8, 2010. The debris flow is responsible for the deaths of 1557 people. The photo is provided by NASA (https://earthobservatory.nasa.gov/images/45329/landslide-in-zhouqu-china).

There are several good reviews about the current advances in landslide prediction, monitoring, and early warning (Chae et al. 2017, Hürlimann et al. 2019). The main purpose of the present thesis is to study the run-out behavior of rapid flow-like landslides and the related phenomena (bed entrainment, plowing and landslide-structure interaction), so here we will focus mainly on the state-of-the-art of the advances in the study of these related phenomena and the numerical models for simulating them.

Phenomena related to rapid flow-like landslides

A variety of interesting phenomena associated with rapid flow-like landslides were observed in field or in large or small scale physical experiments. Some phenomena, such as the disintegration of rock mass, entrainment, segregation, and the interaction between rapid flow-like landslides and mitigation structures, are recognized as important factors influencing the dynamic characteristics of rapid flow like landslides. Therefore, the advances in these aspects are reviewed below.

Disintegration (or fragmentation), is a remarkable phenomenon in the run-out process of rock avalanches (Crosta et al. 2007) and refers to the dynamic process that the initial intact rock mass disintegrates into rock blocks of various sizes (may range from decimeters to tens of meters). A renowned rock avalanche (the Frank slide) is shown in Fig. 1.2. The grain size was observed to decrease with run-out distance in rock avalanche deposits (Charrière et al. 2016, Locat et al. 2006), indicating disintegration is a gradual process. Abrupt slope change may be an important factor facilitating the disintegration process (De Blasio and Crosta 2015). Disintegration changes the volume and property of the rock avalanche, increasing the difficulty in risk assessment and run-out prediction. Except for field investigation, the studies on rock avalanche fragmentation were mainly conducted through experiments (Haug et al. 2016, Imre et al. 2010) and numerical investigations based on discrete element model (Gao et al. 2020, Zhao et al. 2017). Some progresses have been made to understand the disintegration process. Davies and McSaveney (2009) found that disintegration of grains in force chain can reduce the effective stress and the frictional resistance, which may be a reason for the high mobility of rock avalanche. The experiment conducted by Haug et al. (2016) shows that the run-out distance increases with the degree of fragmentation, while the displacement of the mass center has an opposite tendency, suggesting fragmentation plays a role of energy consumption. However, the mechanism of disintegration is still not fully understood, and further researches should be conducted to illustrate the disintegration mechanism and its influence on the dynamics of rock avalanches.

Fig. 1.2 Panorama of the Frank rock avalanche occurred in British Colombia, Canada in April 1903 which is the deadliest landslide in Canada (https://www.albertasouthwest.com/resources/photo-gallery/frank-slide/).

Entrainment is a prevalent phenomenon associated with rapid flow-like landslides. In a general sense, entrainment refers to the complicated dynamic process of volume expansion of a landslide by entraining, plowing or thrusting the material on the run-out path (Crosta et al. 2015). In the narrow sense, entrainment only denotes basal scouring or bed entrainment. In the present thesis, we regard bed entrainment and frontal plowing as two different processes. The volume of a landslide can expand manifold through bed entrainment. A commonly used index quantifying the volume change is entrainment ratio which is defined as the ratio of the entrained volume to the initial volume (Hungr and Evans 2004). The rock avalanche occurred in Modalen, Norway, had an initial detached rock of 1×10^4 m^3, but the final deposit reached a volume of around 1.15×10^5 m^3 (Hungr and Evans 2004). The Tsing Shan debris flow occurred in Hong Kong had an initial volume of only 400 m^3, but the final volume (20,000 m^3) increased

about 50 times (King 1996). The mobilized rock/soil mass can be significantly different with the initial rock/soil mass in terms of material, water content and the other physical properties. Therefore, bed entrainment may alter the rheological property and mobility of a landslide. Some previous studies indicated that entrainment of dry material will reduce the run-out distance, while entraining saturated mass can increase the mobility (Crosta et al. 2009, Iverson et al. 2011). Iverson et al. (2011) suggested that entrainment of wet material could generate positive excess pore water pressure, thus enhancing the mobility of the landslide, while entraining dry material had an opposite effect. However, the experiment conducted by Mangeney et al. (2010) showed a different conclusion that entrainment of dry material could also enhance the mobility of a landslide. This contradiction indicates that water content may not be the only factor influencing the mobility, other factors like the slope and thickness of the erodible bed, the frictional properties of the material or the interstitial fluid content, could also be crucial in determining the mobility of a flow-like landslide after entrainment (Mangeney 2011). The mechanism of bed entrainment and its influence on landslide mobility are still quite elusive and need further investigation.

Frontal plowing is a phenomenon different with bed entrainment. Normally, plowing occurs at the front of a rapid flow-like landslide where the displaced path material is plowed into and pushed forward by the main body of the landslide. In the plowing process, the landslide generally remains separate with the displaced mass, while in bed entrainment the entrained mass will mix with the original landslide mass. This phenomenon is found to be dominant in some rapid flow-like landslides (McDougall and Hungr 2005). For instance, in the Frank rock avalanche, the plowed alluvium mass caused most of the damage in the town (Cruden and Hungr 1986). The evidence of plowing in rock avalanches is often reflected by the presence of fine-grained splash zones surrounding the margins of the rock avalanche deposits (McDougall and Hungr 2005). In snow avalanches, the frontal plowing is also an importance factor influencing the run-out behavior (Gauer and Issler 2004). The plowing process involves the complex interaction between the landslide and plowed mass. Few previous studies have conducted

in-depth research on this topic, so further investigations are still necessary.

Fig. 1.3 Rock avalanche occurred in Jiangda County, Tibet, China which blocked the Jinsha River (the upper reaches of the Yangtze River) on October 11, 2018, leading to the evacuation of more than 24,600 people. The Photo is from China Daily (http://global.chinadaily.com.cn/a/201810/13/WS5bc13d21a310eff30328222d_1.html).

Segregation is a common and complex phenomenon in both natural (Hutter et al. 1994, Iverson 1997) and industrial granular flows (Ketterhagen et al. 2008, Kudrolli 2004, Rosato et al. 2002) occurring when the granular materials consisted of particles of various sizes are subjected to vibration or shear (Ottino and Khakhar 2000). In segregation process, large particles move toward the free surface and the flow front, while the small ones sink to the bottom. Specifically, in granular flows like debris flows and rock avalanches, particle segregation contributes to

the formation of boulder-enriched levees and fronts (de Haas et al. 2015, Gray and Kokelaar 2010, Johnson et al. 2012), and this special granular structure may determine the dynamic features of these flow-like landslides. Kinetic sieving and squeeze expulsion were recognized as the main mechanisms of particle segregation (Gray 2018, Savage and Lun 1988). According to kinetic sieving theory, the small particles have more chance to percolate downward through the pores formed by big particles, so they tend to sink to the bottom. Meanwhile, large particles are squeezed upward by the small particles while they fill out the pores, which is the so-called squeeze expulsion mechanism. These two processes provide qualitative explanations for particle segregation. However, quantification of segregation is still a long-standing challenge, although some researches have proposed several preliminary models for the calculation of the segregation process (Fan and Hill 2011, Gray and Chugunov 2006, Gray and Thornton 2005, Tunuguntla et al. 2014). To consider segregation in the simulation of real rapid flow-like landslides, more sophisticated models may be required.

Landslide-structure interaction is an important research topic in rapid flow-like landslide mitigation. The mitigation strategies of rapid flow-like landslides can be classified into active and passive measures (Huebl and Fiebiger 2005). The passive measures refer to the non-structural measures, like hazard mapping and land-use planning, are adopting to avoid the direct impact of landslides. Passive measures are more recommended, however, in many cases active measures (constructing of defense structures) are necessary when the passive measures are not feasible. In these situations, a correct understanding of the landslide-structure interaction process is crucial. The purposes of constructing defense structures are to change the direction of the flow or impeding the movement of the flow. The channel works and re-directing obstacles are the measures used to guide the direction of flow-like movement, while check dams, sabo dams and flexible net barriers are adopted to stop the motion or reduce the magnitude of the flow mass. Evaluating the impact force acting on the structure and assessing the efficiency of the

measures are the two major tasks in the design of mitigation measures. To function well, the structures must be strong enough to resist the impact from rapid flow like landslides. At the same time, their performance should be good enough to prevent the possible disasters. Flume tests have been widely adopted in the study of the impact force of debris flow (Armanini 1997, Armanini et al. 2020, Cui et al. 2015, Huebl et al. 2017, Ng et al. 2016, Rossi and Armanini 2019, Sanvitale et al. 2021, Vagnon and Segalini 2016). And the runup and pile-up have been recognized as the two phenomena occurring during the impact process which influence the magnitude of impact force (Choi et al. 2015, Kong et al. 2021). The efficiencies of the mitigation measures cannot be evaluated through small-scale flume experiments, so numerical simulation of the prototype is the main method used to achieve this goal. Some numerical simulations have been conducted regarding the efficiency of defense structures (Chen et al. 2019, Choi et al. 2021, Cuomo et al. 2019, Dai et al. 2017, Kattel et al. 2018). However, the influence of the defense structure on the dynamic and entrainment process of rapid flow-like landslides were not adequately studied, which is still a topic requiring further investigations.

In the above section, we briefly reviewed the state-of-the-art of four important phenomena related to rapid flow-like landslides. In this thesis, entrainment (including frontal plowing) and landslide-structure interaction are the main topics we would like to address, while disintegration and segregation will not be considered.

1.1.2 Modeling methods for rapid flow-like landslides

The modeling methods for rapid flow-like landslides can be classified into three types: 1) the methods based on continuum mechanics, 2) methods based on discrete mechanics; and 3) coupled methods of continuum and discrete

mechanics. In the following section, we will introduce the state-of-the-art of some typical methods adopted in the simulation of rapid flow-like landslides.

Continuum mechanics methods

If we view the landslide mass as a continuum, the governing equations of rapid flow-like landslides can be written as a set of partial difference equations depicting the mass and momentum conservations (sometimes also include energy conservation). In the case of single-phase, the mass and momentum equations can be written as:

$$\frac{\partial \rho}{\partial t} + \nabla \cdot (\rho \vec{v}) = 0 \quad (1.1)$$

$$\frac{\partial \rho \vec{v}}{\partial t} + \nabla \cdot (\rho \vec{v} \otimes \vec{v}) = \nabla \cdot \boldsymbol{\sigma} + \rho \vec{g} \quad (1.2)$$

where ρ is the density; $\vec{v}$ is the velocity vector; ∇ is the divergence operator; $\otimes$ is the dyadic product; $\boldsymbol{\sigma}$ is the Cauchy stress tensor, $\vec{g}$ is the gravitational acceleration.

Mixture theory can be adopted to formulate the governing equations for multi-phase continuum. No matter the continuum is regarded as single-phase or multi-phase material, the governing equations in three-dimensional can be directly discretized by several numerical methods such as the particle finite element method (PFEM), material point method (MPM), smoothed particle hydrodynamics (SPH), finite volume method (FVM), arbitrary lagrangian-eulerian method (ALE), etc., producing three-dimensional models. A brief summary of these numerical methods are listed in Table 1.3. To save computational cost, a popular technology – the depth integration can be used to simplify the equations in the depth direction, obtaining the depth-averaged models (quasi-three dimensional models). The typical three-dimensional models and depth-averaged models will be introduced below.

Three-dimensional models

The traditional finite element method suffers from inaccuracy and instability in the condition of large deformation because of mesh distortion. To overcome this drawback, mesh-free (SPH), re-meshing or moving mesh (PFEM and ALE), and hybrid methods (MPM) are developed for the large deformation problems in continuum mechanics. Therefore, the abovementioned numerical methods for three-dimensional models can be adopted in the analysis of rapid flow-like landslide when suitable rheological/constitutive laws are used.

SPH is an entirely mesh-free method originally proposed to solve the astrophysical problems (Gingold and Monaghan 1977, Lucy 1977). In SPH, the continuum is represented as particle points carrying all the physical properties, and the field functions in governing equations are discretized through two steps: kernel approximation and particle approximation (Liu and Liu 2003). SPH has been implemented in the simulation of rapid flow-like landslides and landslide generated impulsive waves (Bao et al. 2018, Han et al. 2020, Huang et al. 2012, Nikooei and Manzari 2021, Wang et al. 2016). The main merit of SPH over the other methods is that the free surface boundary of the flow can be easily traced by the boundary particles. However, since it is necessary to search a huge number of neighboring particles at each time step, the computational cost can be very expensive, especially if we simulate a large landslide which normally needs millions of particles.

PFEM was proposed by Idelsohn et al. (2004) as an extension of the standard FEM. The material is represented by a set of particles which are regards as the nodes of the finite elements as well. The meshes in PFEM are built or rebuilt via Delaunay triangulation algorithm and alpha shape scheme (Cremonesi et al. 2020). This method can avoid the problem caused by mesh distortion through rebuilding the meshes whenever needed. However, the

re-meshing process also brings errors and additional computational cost because of mapping Gauss points data from old meshes to new meshes. This method has been preliminarily implemented in the simulation of rapid flow-like landslides, landslide-generated water waves and landslide-structure interaction problems (Franci et al. 2020, Franci and Zhang 2018, Salazar et al. 2016, Zhang et al. 2015). On the other hand, the high computational cost and other technological challenges (re-meshing, boundary detection etc.) limit its application in the modeling of large-scale rapid flow-like landslides.

Table 1.3 Typical numerical methods adopted in three-dimensional models for simulating rapid flow-like landslides

Methods	Mesh	Coordinate	Main applications	Typical characteristics
SPH	Meshfree	Lagrangian	Rapid flow-like landslides. Landslide-induced impulsive waves. Fluid-structure interaction.	Free surface can be easily determined, but dealing with contact boundary is challenging. Searching neighboring particles is time-consuming.
PFEM	Re-meshing needed	Lagrangian	Rapid flow-like landslides. Landslide-induced impulsive waves. Fluid-structure interaction.	Re-meshing is time-consuming. Internal and external boundaries are difficult to determine. Mapping Gauss points data can introduce error.
ALE	Moving mesh	Hybrid of Lagrangian and Eulerian	Rapid flow-like landslides. Landslide-induced impulsive waves. Fluid-structure interaction.	The movement of mesh is independent with material producing mapping related error. Boundary is not easy to deal with.
MPM	Background mesh	Lagrangian	Rapid flow-like landslides. Landslide-induced impulsive waves. Fluid-structure interaction.	Mapping information between material points and mesh nodes introduce error. Re-meshing is not necessary. Contact is difficult to detect and calculate.
FVM	Fixed mesh	Eulerian	Rapid flow-like landslides.	Special technologies (e.g., VOF) are needed to deal with the free surface and fluid-solid boundaries. Convection is difficult to deal with. The strain of material cannot be traced.

ALE method is a hybrid Lagrangian and Eulerian method proposed by Noh (1963) to overcome the disadvantages of pure Lagrangian and Eulerian methods in fluid simulation. Then it was applied to the problems in solid

mechanics involving large deformation (Nazem et al. 2009). In ALE, the displacement of material is separate with the mesh displacement, so the problem of mesh distortion can be relieved by adopting this strategy. Crosta et al. (2003) implemented ALE in the simulation of the Val Pola rock avalanche occurred in Italy, which was probably one of the earliest work applying ALE in the simulation of rapid flow-like landslides. Then the method obtained a broader application in the simulation rapid landslide related entrainment, impulsive wave, and landslide-structure interaction problems (Crosta, et al. 2009, Crosta et al. 2016, Luo et al. 2019, Zhao et al. 2020). The ALE method has been incorporated into the commercial software LS-DYNA developed by the Livermore software technology. Several studies have utilized this software to analyze rapid flow-like landslides and landslide–barrier interaction problems, and good predictions were obtained (Kwan et al. 2015, Luo, et al. 2019). However, the accuracy and reliability of ALE models on the simulation of real rapid flow-like landslides still need further investigation. Challenges like modeling entrainment, improving computational efficiency, and contact calculation need to be addressed in the future development of ALE models.

MPM is a relatively new numerical method developed by Sulsky and her co-workers (Sulsky et al. 1994) becoming increasingly popular in solving the problems of large deformation. The idea of MPM was originated from particle-in-cell (PIC) methods for fluid simulation. In MPM, material is represented by a cluster of particles, and all the physical variables (volume, density, velocity, stress, strain, etc.) are carried by the particles. A background mesh is used to discretize the continuous field. The most important merit of MPM is that re-meshing is not necessary, so the difficulty associated with mesh entanglement does not exist. The MPM has been used to simulate large deformation problems in geotechnical engineering such as settlement in landfills over two decades (Fern et al. 2019, Zhou et al. 1999). Until around 10 years ago, some researchers started to implement this method in landslide simulation (Andersen and Andersen 2010). The development of MPM in rapid flow-like simulation progressed

quickly in the last ten years. Nowadays, there are already tens of successful examples of using this method for the simulation of rapid flow-like landslides and their interaction with structures (Cuomo et al. 2021, González Acosta et al. 2021, Li et al. 2020, Mast et al. 2014). On the other hand, challenges like difficulty in contact detection and applying boundary condition need to be overcame in the future to improve the accuracy and applicability. More details related to the recent development of MPM can be found in de Vaucorbeil et al. (2020).

FVM is a commonly-used method in computational fluid dynamics (CFD). The mainstream commercial and open source software in CFD, such as Flow-3D, Fluent and OpenFOAM, are capable of simulating single-phase and multi-phase flows. Up to now these models have been implemented in the simulation of rapid flow-like landslide-generated impulsive waves and air blast (Ersoy et al. 2019, Hu et al. 2020, Rauter et al. 2021, Zhuang et al. 2019). FVM is a Eulerian-based method, so special treatments like volume of fluid (VOF) and cut-in-cell methods are necessary for tracking the free surface and fluid-solid boundary. A full-scale 3D simulation of a large landslide may require millions of meshes which can be very computationally expensive.

In summary, the abovementioned five numerical methods have great application potential in the 3D simulation of rapid flow-like landslide, landslide-induced impulsive waves, and the landslide-structure interaction problems. However, each method has its disadvantages, and the computational costs of these methods are generally high when simulating a large rapid flow-like landslide. Additionally, entrainment, which is a dominant phenomenon in many rapid flow-like landslides, is not easy to be taken into account in these methods.

Depth-averaged models

Depth-averaged models are probably the most popular method in simulation of rapid flow-like landslides because they are more computationally efficient in comparison with the time-consuming 3D simulations. The governing equations of depth-averaged models can be obtained through integrating the 3D governing equations (normally mass and momentum equations) in the depth direction. This depth-integration approach has long been adopted to obtain the so-called shallow water equations or Saint Venant equations in hydraulic channel flows (Pudasaini and Hutter 2007). Savage and Hutter (1989) developed the first generation of depth-integrated model for avalanche, and thus the models developed based on their work are called Savage-Hutter models. Another way to obtain the depth-averaged models is by directly formulating the mass and momentum equations in a soil column via assuming identical horizontal velocity in depth direction. The pioneer model proposed by Sassa (1988) belongs to this type of depth-averaged models. Anyway, the governing equations derived through both methods are basically identical.

Ever since Savage and Hutter, and Sassa proposed their models, the depth-averaged models have developed very quickly and became the mainstream method in the run-out analysis of rapid flow-like landslides. The early depth-averaged models are quite simple. They normally assumed the landslide mass as an incompressible (volume is a constant) and identical single-phase material, and finite difference methods were used to solve the equations. Other numerical methods were also adopted to solve the depth-averaged models. For instance, Chen and Lee (2000) and Denlinger and Iverson (2001) proposed the depth-averaged models solving by FEM and FVM, respectively. However, these early models are quite preliminary because many phenomena associated with rapid flow-like landslides are not considered in the equations. McDougall and Hungr (2003) suggested that a comprehensive model should be capable of 1) considering the non-hydrostatic pressure, 2) taking into account of entrainment, 3) providing a variety of material rheological models, etc. Therefore, a growing number of modified depth-averaged models were proposed to improve the applicability of depth-averaged models. McDougall and Hungr (2005)

proposed a depth-averaged SPH model which considered entrainment and non-hydrostatic lateral pressure. Their model is the well-known DAN3D model which has been widely applied in the simulation of rapid flow-like landslides worldwide (Aaron et al. 2017, Delaney and Evans 2015, Revellino et al. 2013, Xing et al. 2014). Currently, tens of single-phase depth-averaged models have been proposed, some typical models and their characteristics are listed in Table 1.4. As shown in Table. 1.4, various rapid flow-like landslides related phenomena were considered in some of these modified models to improve the performance, such as bed entrainment, centrifugal/centripetal effects caused by curved topography, pore pressure evolution, and effect of barrier.

Apart from single-phase depth-averaged models, two-phase or even multi-phase depth-averaged models have achieved significant advances in the last two decades. These models are generally formulated according to the mixture theory of continuum mechanics. Iverson and Denlinger (2001) proposed one of the earliest quasi two-phase models for debris flow. However, in their model the velocity difference between solid and fluid was not considered. Then Pitman and Le (2005) proposed a two-fluid model in which both solid and fluid phases were regarded as 'fluid'. In the two-fluid model, the velocity difference between solid and fluid phases was considered, but the viscous effect of fluid phase was neglected. To overcome these drawbacks in the previous studies, Pudasaini (2012) derived a more generalized two-phase model for debris flow which considered the viscous effect of fluid, virtual mass, generalized drag, and buoyancy. From then on, more improvements have been made on the early two/multi-phase models. For instance, the effects of evolving dilatancy (Iverson and George 2014), fluid-solid phase transformation in rock/ick avalanches (Pudasaini and Krautblatter 2014) and multi-phase interaction (Kattel et al. 2021) have been incorporated into different models.

In comparison with the single-phase models, the two/multi-phase models are more sophisticated in theory.

Especially in debris flows, the separation of fluid and solid is a dominant phenomenon which cannot be reflected by the single-phase models. On the other hand, the equations of two/multi-phase models are more complex. And more parameters which need calibration are incorporated into the equations, increasing the difficulty of applying these models in the real rapid flow-like landslide cases. By contrast, the calibration of the single-phase models is usually easier because less calibration-based parameters are presented. The simulation results of the single-phase models are normally satisfactory in terms of the simulated run-out distance, impacting area and deposition thickness. Therefore, this thesis mainly focuses on improving the single-phase depth averaged models so that we can extend their applicability in the simulation of rapid flow-like landslides and the related phenomena.

Table 1.4 Comparisons of the features of several single-phase depth-averaged models

Models	Coordinate	Method	Centripetal/centrifugal effect	Entrainment	Pore pressure evolution	Effect of barrier	Reference
FLO-2D	Eulerian	FDM	No	No	No	Yes	O'Brien et al. (1993)
DAN3D	Lagrangian	SPH	Yes	Yes	No	Yes	Hungr and McDougall (2009)
Massflow	Eulerian	FDM	No	Yes	No	No	Ouyang et al. (2013)
RAMMS	Eulerian	FVM	No	Yes	No	Yes	Christen et al. (2010)
Debris-2D	Eulerian	FDM	No	No	No	No	Liu et al. (2013)
RASH3D	Eulerian	FVM	No	Yes	No	Yes	Pirulli and Sorbino (2008)
LS-RAPID	Eulerian	FDM	No	No	No	No	Sassa et al. (2010)
Improved FD model	Eulerian	FDM	Yes	Yes	No	Yes	Shen et al. (2018)
HiPIMS_Landslide	Eulerian	FVM	Yes	No	No	No	Xia and Liang (2018)
GeoFlow-SPH	Lagrangian	SPH	No	Yes	Yes	Yes	Pastor et al. (2009)

Discrete mechanics methods

Granular flows can be view as continuum materials in large scale, but in small scale (the diameter of a particle) they are discrete materials consisting of separated particles. The main parts of some rock avalanches can be regarded as dry granular flows, so we can use the discrete mechanics methods to simulate their run-out behavior. However, the pure discrete methods are not suitable for the simulation of saturated mass movements like debris flows and the flowslides consisting of fine materials (sand, silt, etc.).Discrete element method (DEM) and discontinuous deformation analysis (DDA) are the two discrete mechanics methods currently implemented in the simulation of dry granular flows.

Cundall and Strack (1979) proposed the first version of discrete element model for the simulation of granular particle assembles. In the original discrete element model, the particles are not bonded and they interact with neighboring particles through collision and friction. The governing equation of each particle is formulated simply according to the Newton's Second Law of Motion, with the damping effect being accounted in the equation. Contact detection is necessary in order to calculate the contact forces among particles. Then Potyondy and Cundall (2004) extended the original DEM by bonding the particles, enabling the simulation of the fragmentation process of rock mass. The commercial DEM programs developed by Itasca are probably the most popular DEM software nowadays. These programs include the UDEC in 2D and 3DEC in 3D for the simulation of blocks and PFC2D in 2D and PFC3D in 3D for round particles. Additionally, there are also some open source DEM codes which are easier to extend. These DEM models have been widely applied in the run-out simulation of (earthquake induced) rock avalanches (Lin and Lin 2015, Wu and Hsieh 2021), particle segregation(Zhou and Ng 2010), granular flow-barrier interaction (Law et al. 2015, Shen et al. 2018), fragmentation process (Gao, et al. 2020), and

entrainment (Liu et al. 2020).

DDA is another popular discrete numerical method for the simulation of block assembles. It was originally proposed by Shi (1992). Different with DEM, the governing equations of DDA are formulated according to the minimum principle of the potential energy of the system, so DDA is an implicit numerical method. Another distinct characteristic of DDA is that the blocks (or particle) are deformable rather than the rigid body assumed by DEM. 3D DDA method is still not sophisticated because of the difficulty encountered in 3D contact detection, so the previous studies related to the simulation of rapid flow-like landslides were usually based on the 2D DDA model (Chen et al. 2021, Chen and Wu 2018, Wang et al. 2021).

Coupled methods

The pure continuous mechanic methods and pure discrete mechanic methods have different range of applications. Coupled methods combining the advantages of both continuous and discrete mechanic methods are more powerful in terms of the capability of simulating rapid flow-like landslides (saturated debris flows) related phenomena. One of the most popular coupled methods is the CFD-DEM method. The solid phase of the flow is simulated through DEM, while the fluid phase is simulated via CFD method (FVM). Unlike the two-phase depth-averaged models, CFD-DEM method is a direct approach for the simulation of fluid-solid interaction. Current, the coupled CFD-DEM methods have been mainly implemented in the simulation of landslide-induced impulsive wave (Mao et al. 2020, Shan and Zhao 2014), interaction of debris flow and rigid or flexible barriers (Fang et al. 2021, Li et al. 2020), etc. There are also some other combinations in the coupling methods, such as the SPH-DEM (Hu et al. 2021, Trujillo-Vela et al. 2020, Xu and Dong 2021) and SPH-DDA (Wang et al. 2019) models. These models have similar

applications as the CFD-DEM models. More recently, Liu et al. (2021) established a coupled SPH-DEM-FEM model for the multiple interactions among fluid, particle and structure. An et al. (2021) proposed a coupled depth-averaged method and DEM model for the simulation of two-phase flow. These developments in coupling methods provide the possibility for the more accurate simulation of rapid flow-like landslides and the related phenomena. However, the existing models are still in the early stage of application because of computationally demanding and the difficulties encountered in coupling the methods of different frameworks and foundations.

1.1.3 Brief summary of the state-of-the-art

In Section 1.1 we briefly reviewed the definition of rapid flow-like landslide, the catastrophic rapid flow-like landslide events occurred worldwide, rapid flow-like landslide related phenomena, and the numerical methods for the run-out analysis of this type of landslides.

Four dominate phenomena, namely, disintegration (fragmentation), entrainment (including bed entrainment and frontal plowing), segregation, and landslide-structure interaction, have been identified as the key factors influencing the run-out behavior of rapid flow-like landslides. However, simulating these phenomena is still a big challenge because their mechanisms are not fully understood. In this thesis, we mainly address the topics related to bed entrainment, frontal plowing, and the interaction between debris flow and defense structures. Although the other two factors (disintegration and segregation) are also quite important, they are out of the scope of this thesis.

As reviewed in Section 1.1.2, various numerical methods have been proposed and implemented in the simulation of

the post-failure process of rapid flow-like landslides. The three-dimensional models based on SPH, MPM, PFEM, ALE and FVM are theoretically more sophisticated than the depth-averaged models because the 3D models can provide more detailed information about the internal deformation and stress. However, these 3D models are significantly time-consuming for the simulation of real large-scale rapid flow-like landslides. In addition, these methods have difficulty in simulation entrainment which is probably the most important phenomenon that should not be neglected. The pure discrete mechanic methods like DEM and DDA are also quite computationally demanding and suitable only for dry granular flows. The more advanced coupled methods of continuous and discrete methods are still under the early stage of development, and they are far away from put into practice. Given the above reasons, we choose the most widely used depth-averaged models to conduct the present study. The single-phase depth-averaged models are improved to simulate the frontal plowing, bed entrainment, and debris flow-check dam interaction process.

1.2 Motivation and outline of the thesis

The main motivation of this thesis is to improve the existing depth-averaged models and to apply the improved models in the simulation of rapid flow-like landslide related phenomena like bed entrainment, frontal plowing, and debris flow-check dam interaction.

The thesis consists of six chapters. Chapter 1 introduces the state-of-art and the general guide of this thesis. Chapter 2-5 are four scientific papers. And Chapter 6 is the Conclusions.

In Chapter 1, we firstly reviewed the definition of rapid flow-like landslides and the catastrophic events caused by this type of landslide worldwide. Then we introduced the state-of-the-art of the four dominant phenomena related to rapid flow-like landslides, namely, the disintegration of rock mass, entrainment (bed entrainment and frontal plowing), segregation, and landslide-structure interaction. Finally, the characteristics of the three categories of numerical methods which are currently adopted in the simulation of rapid flow-like landslides were summarized and compared.

In Chapter 2, we addressed the issue of frontal plowing which is an important phenomenon in some rapid flow-like landslides neglected by most previous studies. The related results have been published in the journal - Engineering Geology. In that paper, we developed a new two-layer depth-averaged model for the simulation of frontal flowing. The landslide and the plowed mass were regarded as two separate layers and their interactions were quantified

through the shear and normal forces on the interface of the two layers. The governing equations of this two-layer model were derived and then solved by the finite difference method. The derivation and numerical scheme of the model were presented. Then a typical loess flowslide-the Ximiaodian landslide which is characterized by frontal plowing was analyzed by the new model, and the simulation results were compared with the field data.

In Chapter 3, we investigated the influence of slope gradient and gully channel on the run-out, entrainment and deposition characteristics of a rockslide-debris flow. An improved depth-averaged model proposed by Shen et al. (2018) which has considered bed entrainment was adopted in the run-out analysis of the Verghereto landslide occurred in Italy. Field investigation and unmanned aerial vehicle (UAV) survey were conducted to obtain the digital elevation model for the simulation. The difference of elevation (DOF) before and after the event was generated via the measured data to illustrate the entrainment and deposition characteristics of this landslide, and the DOF was used to validate the simulation results. The relationship between topography (the slope gradient and gully channel) and the deposition and entrainment characteristics of the landslide was analyzed. The effect of gully channel on the run-out (mobility) was discussed. The results have being submitted to the journal - Landslides for peer-review and possible publication.

Chapter 4 and 5 are related to the interaction between debris flows and check dams. In Chapter 4, we proposed an improved depth-averaged model which considered bed entrainment and the impeding effect of check dams. In the improved model, the impeding effect of a check dam was simplified as a rigid constraint, and a new computational scheme was adopted to improve the simulation efficiency. A real debris flow occurred in the Hongchuan gully, Sichuan Province of China, was selected as an example to study the effect of check dams on the dynamic and bed entrainment processes of debris flows. Specifically, we discussed the influence of the check dam locations on the

entrainment characteristics. The results have been published in the journal - Landslides. Then in Chapter 5, this model was implemented in the efficiency assessment of the real constructed check dams in the Hongchun debris flow gully. We analyzed the impeding effect of these check dams on different initial scales of debris flows and investigated the limitations of these check dams. The results have been published in Bulletin of Engineering Geology and the Environment.

In Chapter 6, we reviewed the main conclusions obtained from the above studies. The limitations of the present studies and the possible further developments in the future were also briefly discussed.

1.3 Reference

Aaron J, Hungr O, Stark Timothy D and Baghdady Ahmed K (2017) Oso, washington, landslide of march 22, 2014: Dynamic analysis. Journal of Geotechnical and Geoenvironmental Engineering 143: 05017005. doi: 10.1061/(ASCE)GT.1943-5606.0001748

An H, Ouyang C and Wang D (2021) A new two-phase flow model based on coupling of the depth-integrated continuum method and discrete element method. Computers & Geosciences 146: 104640. doi: https://doi.org/10.1016/j.cageo.2020.104640

Andersen S and Andersen L (2010) Modelling of landslides with the material-point method. Computational Geosciences 14: 137-147. doi: 10.1007/s10596-009-9137-y

Armanini A (1997) On the dynamic impact of debris flows. In: Armanini A and Michiue M (eds) Recent developments on debris flows, Springer Berlin Heidelberg, Berlin, Heidelberg, pp 208-226

Armanini A, Rossi G and Larcher M (2020) Dynamic impact of a water and sediments surge against a rigid wall. Journal of Hydraulic Research 58: 314-325. doi: 10.1080/00221686.2019.1579113

Bao Y, Huang Y, Liu GR and Wang G (2018) Sph simulation of high-volume rapid landslides triggered by earthquakes based on a unified constitutive model. Part i: Initiation process and slope failure. International Journal of Computational Methods 17: 1850150. doi: 10.1142/S0219876218501505

Berti M, Bertello L and Squarzoni G (2019) Surface-wave velocity measurements of shear stiffness of moving earthflows. Landslides 16: 469-484. doi: 10.1007/s10346-018-1102-1

Catane SG, Cabria HB, Tomarong CP, Saturay RM, Zarco MAH and Pioquinto WC (2007) Catastrophic rockslide-debris avalanche at st. Bernard, southern leyte, philippines. Landslides 4: 85-90. doi: 10.1007/s10346-006-0050-3

Chae B-G, Park H-J, Catani F, Simoni A and Berti M (2017) Landslide prediction, monitoring and early warning: A concise review of state-of-the-art. Geosciences Journal 21: 1033-1070. doi: 10.1007/s12303-017-0034-4

Charrière M, Humair F, Froese C, Jaboyedoff M, Pedrazzini A and Longchamp C (2016) From the source area to the deposit: Collapse, fragmentation, and propagation of the frank slide. GSA Bulletin 128: 332-351. doi: 10.1130/B31243.1

Chen G, Xia M, Thuy DT and Zhang Y (2021) A possible mechanism of earthquake-induced landslides focusing on pulse-like ground motions. Landslides 18: 1641-1657. doi: 10.1007/s10346-020-01597-y

Chen H-X, Li J, Feng S-J, Gao H-Y and Zhang D-M (2019) Simulation of interactions between debris flow and check dams on three-dimensional terrain. Engineering Geology 251: 48-62. doi: https://doi.org/10.1016/j.enggeo.2019.02.001

Chen H and Lee CF (2000) Numerical simulation of debris flows. Canadian Geotechnical Journal 37: 146-160. doi: 10.1139/t99-089

Chen K-T and Wu J-H (2018) Simulating the failure process of the xinmo landslide using discontinuous deformation analysis. Engineering Geology 239: 269-281. doi: https://doi.org/10.1016/j.enggeo.2018.04.002

Choi CE, Au-Yeung SCH, Ng CWW and Song D (2015) Flume investigation of landslide granular debris and water runup mechanisms. 5: 28-32. doi: 10.1680/geolett.14.00080

Choi S-K, Park J-Y, Lee D-H, Lee S-R, Kim Y-T and Kwon T-H (2021) Assessment of barrier location effect on debris flow based on smoothed particle hydrodynamics (sph) simulation on 3d terrains. Landslides 18: 217-234. doi: 10.1007/s10346-020-01477-5

Christen M, Kowalski J and Bartelt P (2010) Ramms: Numerical simulation of dense snow avalanches in three-dimensional terrain. Cold Regions Science and Technology 63: 1-14. doi: https://doi.org/10.1016/j.coldregions.2010.04.005

Cremonesi M, Franci A, Idelsohn S and Oñate E (2020) A state of the art review of the particle finite element method (pfem). Archives of Computational Methods in Engineering 27: 1709-1735. doi: 10.1007/s11831-020-09468-4

Crosta GB, De Blasio FV, Locatelli M, Imposimato S and Roddeman D (2015) Landslides falling onto a shallow erodible substrate or water layer: An experimental and numerical approach. IOP Conference Series: Earth and Environmental Science 26: 012004. doi: 10.1088/1755-1315/26/1/012004

Crosta GB, Frattini P and Fusi N (2007) Fragmentation in the val pola rock avalanche, italian alps. Journal of Geophysical Research: Earth Surface 112. doi: https://doi.org/10.1029/2005JF000455

Crosta GB, Imposimato S and Roddeman D (2009) Numerical modelling of entrainment/deposition in rock and debris-avalanches. Engineering Geology 109: 135-145. doi: https://doi.org/10.1016/j.enggeo.2008.10.004

Crosta GB, Imposimato S and Roddeman D (2016) Landslide spreading, impulse water waves and modelling of the vajont rockslide. Rock Mechanics and Rock Engineering 49: 2413-2436. doi: 10.1007/s00603-015-0769-z

Crosta GB, Imposimato S and Roddeman DG (2003) Numerical modelling of large landslides stability and runout. Nat Hazards Earth Syst Sci 3: 523-538. doi: 10.5194/nhess-3-523-2003

Cruden D and Varnes D (1996) Landslide types and processes, special report , transportation research board, national academy of sciences, 247:36-75. Special Report - National Research Council, Transportation Research Board 247: 76.

Cruden DM and Hungr O (1986) The debris of the frank slide and theories of rockslide–avalanche mobility. Canadian Journal of Earth Sciences 23: 425-432. doi: 10.1139/e86-044

Cui P, Zeng C and Lei Y (2015) Experimental analysis on the impact force of viscous debris flow. Earth Surface Processes and Landforms 40: 1644-1655. doi: https://doi.org/10.1002/esp.3744

Cundall PA and Strack ODJg (1979) A discrete numerical model for granular assemblies. 29: 47-65.

Cuomo S, Di Perna A and Martinelli M (2021) Mpm hydro-mechanical modelling of flows impacting rigid walls. Canadian Geotechnical Journal. doi: 10.1139/cgj-2020-0344

Cuomo S, Moretti S and Aversa S (2019) Effects of artificial barriers on the propagation of debris avalanches. Landslides 16: 1077-1087. doi: 10.1007/s10346-019-01155-1

Dai Z, Huang Y, Cheng H and Xu Q (2017) Sph model for fluid–structure interaction and its application to debris flow impact estimation. Landslides 14: 917-928. doi: 10.1007/s10346-016-0777-4

Davies TR and McSaveney MJ (2009) The role of rock fragmentation in the motion of large landslides. Engineering Geology 109: 67-79. doi: https://doi.org/10.1016/j.enggeo.2008.11.004

De Blasio FV and Crosta GB (2015) Fragmentation and boosting of rock falls and rock avalanches. Geophysical Research Letters 42: 8463-8470. doi: https://doi.org/10.1002/2015GL064723

de Haas T, Braat L, Leuven JRFW, Lokhorst IR and Kleinhans MG (2015) Effects of debris flow composition on runout, depositional mechanisms, and deposit morphology in laboratory experiments. Journal of Geophysical Research: Earth Surface 120: 1949-1972. doi: 10.1002/2015JF003525

de Vaucorbeil A, Nguyen VP, Sinaie S and Wu JY (2020) Chapter two - material point method after 25 years: Theory, implementation, and applications. In: Bordas SPA and Balint DS (eds) Advances in applied mechanics, Elsevier, pp 185-398

Delaney KB and Evans SG (2015) The 2000 yigong landslide (tibetan plateau), rockslide-dammed lake and

outburst flood: Review, remote sensing analysis, and process modelling. Geomorphology 246: 377-393. doi: https://doi.org/10.1016/j.geomorph.2015.06.020

Denlinger RP and Iverson RM (2001) Flow of variably fluidized granular masses across three-dimensional terrain: 2. Numerical predictions and experimental tests. Journal of Geophysical Research: Solid Earth 106: 553-566. doi: https://doi.org/10.1029/2000JB900330

Ersoy H, Karahan M, Gelişli K, Akgün A, Anılan T, Sünnetci MO and Yahşi BK (2019) Modelling of the landslide-induced impulse waves in the artvin dam reservoir by empirical approach and 3d numerical simulation. Engineering Geology 249: 112-128. doi: https://doi.org/10.1016/j.enggeo.2018.12.025

Evans SG, Tutubalina OV, Drobyshev VN, Chernomorets SS, McDougall S, Petrakov DA and Hungr O (2009) Catastrophic detachment and high-velocity long-runout flow of kolka glacier, caucasus mountains, russia in 2002. Geomorphology 105: 314-321. doi: https://doi.org/10.1016/j.geomorph.2008.10.008

Fan X, Dufresne A, Siva Subramanian S, Strom A, Hermanns R, Tacconi Stefanelli C, Hewitt K, Yunus AP, Dunning S, Capra L, Geertsema M, Miller B, Casagli N, Jansen JD and Xu Q (2020) The formation and impact of landslide dams – state of the art. Earth-Science Reviews 203: 103116. doi: https://doi.org/10.1016/j.earscirev.2020.103116

Fan Y and Hill KM (2011) Theory for shear-induced segregation of dense granular mixtures. New journal of physics 13: 095009.

Fang J, Wang L, Hong Y and Zhao J (2021) Influence of solid–fluid interaction on impact dynamics against rigid barrier: Cfd–dem modelling. 0: 1-16. doi: 10.1680/jgeot.19.P.160

Fern J, Rohe A, Soga K and Alonso E (2019) The material point method for geotechnical engineering: A practical guide. CRC Press,

Franci A, Cremonesi M, Perego U, Crosta G and Oñate E (2020) 3d simulation of vajont disaster. Part 1: Numerical formulation and validation. Engineering Geology 279: 105854. doi: https://doi.org/10.1016/j.enggeo.2020.105854

Franci A and Zhang X (2018) 3d numerical simulation of free-surface bingham fluids interacting with structures using the pfem. Journal of Non-Newtonian Fluid Mechanics 259: 1-15. doi: https://doi.org/10.1016/j.jnnfm.2018.05.001

Gao G, Meguid Mohamed A, Chouinard Luc E and Xu C (2020) Insights into the transport and fragmentation characteristics of earthquake-induced rock avalanche: Numerical study. International Journal of Geomechanics 20: 04020157. doi: 10.1061/(ASCE)GM.1943-5622.0001800

García-Martínez R and López JL (2005) Debris flows of december 1999 in venezuela. In: Jakob M and Hungr O (eds) Debris-flow hazards and related phenomena, Springer Berlin Heidelberg, Berlin, Heidelberg, pp 519-538

Gauer P and Issler D (2004) Possible erosion mechanisms in snow avalanches. Annals of Glaciology 38: 384-392. doi: 10.3189/172756404781815068

Gingold RA and Monaghan JJ (1977) Smoothed particle hydrodynamics: Theory and application to non-spherical stars. Monthly Notices of the Royal Astronomical Society 181: 375-389. doi: 10.1093/mnras/181.3.375

González Acosta JL, Vardon PJ and Hicks MA (2021) Study of landslides and soil-structure interaction problems using the implicit material point method. Engineering Geology 285: 106043. doi: https://doi.org/10.1016/j.enggeo.2021.106043

Gray JMNT (2018) Particle segregation in dense granular flows. Annual Review of Fluid Mechanics 50: 407-433. doi: 10.1146/annurev-fluid-122316-045201

Gray JMNT and Chugunov VA (2006) Particle-size segregation and diffusive remixing in shallow granular

avalanches. Journal of Fluid Mechanics 569: 365-398. doi: 10.1017/S0022112006002977

Gray JMNT and Kokelaar BP (2010) Large particle segregation, transport and accumulation in granular free-surface flows. Journal of Fluid Mechanics 652: 105-137. doi: 10.1017/S002211201000011X

Gray JMNT and Thornton AR (2005) A theory for particle size segregation in shallow granular free-surface flows. Proceedings of the Royal Society A: Mathematical, Physical and Engineering Sciences 461: 1447-1473. doi: 10.1098/rspa.2004.1420

Han Z, Su B, Li Y, Dou J, Wang W and Zhao L (2020) Modeling the progressive entrainment of bed sediment by viscous debris flows using the three-dimensional sc-hbp-sph method. Water Research 182: 116031. doi: https://doi.org/10.1016/j.watres.2020.116031

Haug ØT, Rosenau M, Leever K and Oncken O (2016) On the energy budgets of fragmenting rockfalls and rockslides: Insights from experiments. Journal of Geophysical Research: Earth Surface 121: 1310-1327. doi: https://doi.org/10.1002/2014JF003406

Hu KH, Cui P and Zhang JQ (2012) Characteristics of damage to buildings by debris flows on 7 august 2010 in zhouqu, western china. Nat Hazards Earth Syst Sci 12: 2209-2217. doi: 10.5194/nhess-12-2209-2012

Hu Y-x, Yu Z-y and Zhou J-w (2020) Numerical simulation of landslide-generated waves during the 11 october 2018 baige landslide at the jinsha river. Landslides 17: 2317-2328. doi: 10.1007/s10346-020-01382-x

Hu Y-x, Zhu Y-g, Li H-b, Li C-j and Zhou J-w (2021) Numerical estimation of landslide-generated waves at kaiding slopes, houziyan reservoir, china, using a coupled dem-sph method. Landslides. doi: 10.1007/s10346-021-01718-1

Huang Y, Zhang W, Xu Q, Xie P and Hao L (2012) Run-out analysis of flow-like landslides triggered by the ms 8.0 2008 wenchuan earthquake using smoothed particle hydrodynamics. Landslides 9: 275-283. doi: 10.1007/s10346-011-0285-5

Huebl J and Fiebiger G (2005) Debris-flow mitigation measures. In: Jakob M and Hungr O (eds) Debris-flow hazards and related phenomena, Springer Berlin Heidelberg, Berlin, Heidelberg, pp 445-487

Huebl J, Nagl G, Suda J and Rudolf-Miklau F (2017) Standardized stress model for design of torrential barriers under impact by debris flow (according to austrian standard regulation 24801). International Journal of Erosion Control Engineering 10: 47-55. doi: 10.13101/ijece.10.47

Hungr O and Evans SG (2004) Entrainment of debris in rock avalanches: An analysis of a long run-out mechanism. GSA Bulletin 116: 1240-1252. doi: 10.1130/B25362.1

Hungr O, Leroueil S and Picarelli L (2014) The varnes classification of landslide types, an update. Landslides 11: 167-194. doi: 10.1007/s10346-013-0436-y

Hungr O and McDougall S (2009) Two numerical models for landslide dynamic analysis. Computers & Geosciences 35: 978-992. doi: https://doi.org/10.1016/j.cageo.2007.12.003

Hürlimann M, Coviello V, Bel C, Guo X, Berti M, Graf C, Hübl J, Miyata S, Smith JB and Yin H-Y (2019) Debris-flow monitoring and warning: Review and examples. Earth-Science Reviews 199: 102981. doi: https://doi.org/10.1016/j.earscirev.2019.102981

Hutter K, Svendsen B and Rickenmann D (1994) Debris flow modeling: A review. Continuum Mechanics and Thermodynamics 8: 1-35. doi: 10.1007/BF01175749

Idelsohn SR, Oñate E and Pin FD (2004) The particle finite element method: A powerful tool to solve incompressible flows with free-surfaces and breaking waves. International Journal for Numerical Methods in Engineering 61: 964-989. doi: https://doi.org/10.1002/nme.1096

Imre B, Laue J and Springman SM (2010) Fractal fragmentation of rocks within sturzstroms: Insight derived from physical experiments within the eth geotechnical drum centrifuge. Granular Matter 12: 267-285. doi:

10.1007/s10035-009-0163-1

Iverson RM (1997) The physics of debris flows. Reviews of Geophysics 35: 245-296. doi: 10.1029/97RG00426

Iverson RM and Denlinger RP (2001) Flow of variably fluidized granular masses across three-dimensional terrain: 1. Coulomb mixture theory. Journal of Geophysical Research: Solid Earth 106: 537-552. doi: https://doi.org/10.1029/2000JB900329

Iverson RM and George DL (2014) A depth-averaged debris-flow model that includes the effects of evolving dilatancy. I. Physical basis. Proceedings of the Royal Society A: Mathematical, Physical and Engineering Sciences 470: 20130819. doi: 10.1098/rspa.2013.0819

Iverson RM, Reid ME, Logan M, LaHusen RG, Godt JW and Griswold JP (2011) Positive feedback and momentum growth during debris-flow entrainment of wet bed sediment. Nature Geoscience 4: 116-121. doi: 10.1038/ngeo1040

Johnson CG, Kokelaar BP, Iverson RM, Logan M, LaHusen RG and Gray JMNT (2012) Grain-size segregation and levee formation in geophysical mass flows. Journal of Geophysical Research: Earth Surface 117. doi: 10.1029/2011JF002185

Kattel P, Kafle J, Fischer J-T, Mergili M, Tuladhar BM and Pudasaini SP (2018) Interaction of two-phase debris flow with obstacles. Engineering Geology 242: 197-217. doi: https://doi.org/10.1016/j.enggeo.2018.05.023

Kattel P, Khattri KB and Pudasaini SP (2021) A multiphase virtual mass model for debris flow. International Journal of Non-Linear Mechanics 129: 103638. doi: https://doi.org/10.1016/j.ijnonlinmec.2020.103638

Ketterhagen WR, Curtis JS, Wassgren CR and Hancock BC (2008) Modeling granular segregation in flow from quasi-three-dimensional, wedge-shaped hoppers. Powder Technology 179: 126-143. doi: https://doi.org/10.1016/j.powtec.2007.06.023

King JJCED (1996) The tsing shan debris flow, special project report spr 6/96, hong kong: Geotechnical engineering office.

Kong Y, Li X and Zhao J (2021) Quantifying the transition of impact mechanisms of geophysical flows against flexible barrier. Engineering Geology 289: 106188. doi: https://doi.org/10.1016/j.enggeo.2021.106188

Kudrolli A (2004) Size separation in vibrated granular matter. Reports on Progress in Physics 67: 209-247. doi: 10.1088/0034-4885/67/3/r01

Kwan JSH, Koo RCH and Ng CWW (2015) Landslide mobility analysis for design of multiple debris-resisting barriers. Canadian Geotechnical Journal 52: 1345-1359. doi: 10.1139/cgj-2014-0152

Law RPH, Choi CE and Ng CWW (2015) Discrete-element investigation of influence of granular debris flow baffles on rigid barrier impact. Canadian Geotechnical Journal 53: 179-185. doi: 10.1139/cgj-2014-0394

Li X, Yan Q, Zhao S, Luo Y, Wu Y and Wang D (2020) Investigation of influence of baffles on landslide debris mobility by 3d material point method. Landslides 17: 1129-1143. doi: 10.1007/s10346-020-01346-1

Li X, Zhao J and Kwan JSH (2020) Assessing debris flow impact on flexible ring net barrier: A coupled cfd-dem study. Computers and Geotechnics 128: 103850. doi: https://doi.org/10.1016/j.compgeo.2020.103850

Lin C-H and Lin M-L (2015) Evolution of the large landslide induced by typhoon morakot: A case study in the butangbunasi river, southern taiwan using the discrete element method. Engineering Geology 197: 172-187. doi: https://doi.org/10.1016/j.enggeo.2015.08.022

Liu C, Yu Z and Zhao S (2021) A coupled sph-dem-fem model for fluid-particle-structure interaction and a

case study of wenjia gully debris flow impact estimation. Landslides 18: 2403-2425. doi: 10.1007/s10346-021-01640-6

Liu G-R and Liu MB (2003) Smoothed particle hydrodynamics: A meshfree particle method. World scientific,

Liu K-F, Wu Y-H, Chen Y-C, Chiu Y-J and Shih S-S (2013) Large-scale simulation of watershed mass transport: A case study of tsengwen reservoir watershed, southwest taiwan. Natural Hazards 67: 855-867. doi: 10.1007/s11069-013-0611-4

Liu Z, Su L, Zhang C, Iqbal J, Hu B and Dong Z (2020) Investigation of the dynamic process of the xinmo landslide using the discrete element method. Computers and Geotechnics 123: 103561. doi: https://doi.org/10.1016/j.compgeo.2020.103561

Locat P, Couture R, Leroueil S, Locat J and Jaboyedoff M (2006) Fragmentation energy in rock avalanches. Canadian Geotechnical Journal 43: 830-851. doi: 10.1139/t06-045

Lucy LBJTaj (1977) A numerical approach to the testing of the fission hypothesis. 82: 1013-1024.

Luo HY, Zhang LL and Zhang LM (2019) Progressive failure of buildings under landslide impact. Landslides 16: 1327-1340. doi: 10.1007/s10346-019-01164-0

Mangeney A (2011) Landslide boost from entrainment. Nature Geoscience 4: 77-78. doi: 10.1038/ngeo1077

Mangeney A, Roche O, Hungr O, Mangold N, Faccanoni G and Lucas A (2010) Erosion and mobility in granular collapse over sloping beds. Journal of Geophysical Research: Earth Surface 115. doi: https://doi.org/10.1029/2009JF001462

Mao J, Zhao L, Di Y, Liu X and Xu W (2020) A resolved cfd–dem approach for the simulation of landslides and impulse waves. Computer Methods in Applied Mechanics and Engineering 359: 112750. doi: https://doi.org/10.1016/j.cma.2019.112750

Mast CM, Arduino P, Miller GR and Mackenzie-Helnwein P (2014) Avalanche and landslide simulation using the material point method: Flow dynamics and force interaction with structures. Computational Geosciences 18: 817-830. doi: 10.1007/s10596-014-9428-9

McDougall S and Hungr O (2003) Objectives for the development of an integrated three-dimensional continuum model for the analysis of landslide runout. Debris-flow Hazards Mitigation: Mechanics, Prediction, and Assessment: Proceedings of the 3rd International DFHM Conference, Davos, Switzerland, edited by: Rickenmann, D and Chen, CL, pp 481-490

McDougall S and Hungr O (2005) Dynamic modelling of entrainment in rapid landslides. Canadian Geotechnical Journal 42: 1437-1448. doi: 10.1139/t05-064

Nazem M, Carter JP and Airey DW (2009) Arbitrary lagrangian–eulerian method for dynamic analysis of geotechnical problems. Computers and Geotechnics 36: 549-557. doi: https://doi.org/10.1016/j.compgeo.2008.11.001

Ng CWW, Song D, Choi CE, Liu LHD, Kwan JSH, Koo RCH and Pun WK (2016) Impact mechanisms of granular and viscous flows on rigid and flexible barriers. Canadian Geotechnical Journal 54: 188-206. doi: 10.1139/cgj-2016-0128

Nikooei M and Manzari MT (2021) Investigating the effect of mixing layer rheology on granular flow over entrainable beds using sph method. Computers & Geosciences 155: 104792. doi: https://doi.org/10.1016/j.cageo.2021.104792

Noh WF (1963) Cel: A time-dependent, two-space-dimensional, coupled eulerian-lagrange code. Lawrence Radiation Lab., Univ. of California, Livermore,

O'Brien JS, Julien PY and Fullerton WT (1993) Two-dimensional water flood and mudflow simulation. Journal of Hydraulic Engineering 119: 244-261. doi: 10.1061/(ASCE)0733-9429(1993)119:2(244)

Ottino JM and Khakhar DV (2000) Mixing and segregation of granular materials. Annual Review of Fluid

Mechanics 32: 55-91. doi: 10.1146/annurev.fluid.32.1.55

Ouyang C, He S, Xu Q, Luo Y and Zhang W (2013) A maccormack-tvd finite difference method to simulate the mass flow in mountainous terrain with variable computational domain. Computers & Geosciences 52: 1-10. doi: https://doi.org/10.1016/j.cageo.2012.08.024

Pastor M, Haddad B, Sorbino G, Cuomo S and Drempetic V (2009) A depth-integrated, coupled sph model for flow-like landslides and related phenomena. International Journal for Numerical and Analytical Methods in Geomechanics 33: 143-172. doi: https://doi.org/10.1002/nag.705

Paul SK, Bartarya SK, Rautela P and Mahajan AK (2000) Catastrophic mass movement of 1998 monsoons at malpa in kali valley, kumaun himalaya (india). Geomorphology 35: 169-180. doi: https://doi.org/10.1016/S0169-555X(00)00032-5

Pérez FL (2001) Matrix granulometry of catastrophic debris flows (december 1999) in central coastal venezuela. CATENA 45: 163-183. doi: https://doi.org/10.1016/S0341-8162(01)00149-7

Pirulli M and Sorbino G (2008) Assessing potential debris flow runout: A comparison of two simulation models. Nat Hazards Earth Syst Sci 8: 961-971. doi: 10.5194/nhess-8-961-2008

Pitman EB and Le L (2005) A two-fluid model for avalanche and debris flows. Philosophical Transactions of the Royal Society A: Mathematical, Physical and Engineering Sciences 363: 1573-1601. doi: 10.1098/rsta.2005.1596

Potyondy DO and Cundall P (2004) A bonded-particle model for rock. International journal of rock mechanics and mining sciences 41: 1329-1364.

Pudasaini SP (2012) A general two-phase debris flow model. Journal of Geophysical Research: Earth Surface 117. doi: https://doi.org/10.1029/2011JF002186

Pudasaini SP and Hutter K (2007) Avalanche dynamics: Dynamics of rapid flows of dense granular avalanches. Springer Science & Business Media,

Pudasaini SP and Krautblatter M (2014) A two-phase mechanical model for rock-ice avalanches. Journal of Geophysical Research: Earth Surface 119: 2272-2290. doi: https://doi.org/10.1002/2014JF003183

Rauter M, Hoße L, Mulligan RP, Take WA and Løvholt F (2021) Numerical simulation of impulse wave generation by idealized landslides with openfoam. Coastal Engineering 165: 103815. doi: https://doi.org/10.1016/j.coastaleng.2020.103815

Revellino P, Guerriero L, Grelle G, Hungr O, Fiorillo F, Esposito L and Guadagno FM (2013) Initiation and propagation of the 2005 debris avalanche at nocera inferiore (southern italy). Italian Journal of Geosciences 132: 366-379. doi: 10.3301/IJG.2013.02

Rosato AD, Blackmore DL, Zhang N and Lan Y (2002) A perspective on vibration-induced size segregation of granular materials. Chemical Engineering Science 57: 265-275. doi: https://doi.org/10.1016/S0009-2509(01)00380-3

Rossi G and Armanini A (2019) Impact force of a surge of water and sediments mixtures against slit check dams. Science of The Total Environment 683: 351-359. doi: https://doi.org/10.1016/j.scitotenv.2019.05.124

Salazar F, Irazábal J, Larese A and Oñate E (2016) Numerical modelling of landslide-generated waves with the particle finite element method (pfem) and a non-newtonian flow model. International Journal for Numerical and Analytical Methods in Geomechanics 40: 809-826. doi: https://doi.org/10.1002/nag.2428

Sanvitale N, Bowman E and Cabrera MA (2021) Experimental investigation on the impact dynamics of saturated granular flows on rigid barriers. Environmental and Engineering Geoscience 27: 127-138. doi: 10.2113/EEG-D-20-00033

Sassa K (1988) Special lecture: Geological model for the motion of landslides. International symposium on

landslides 5, pp 37-55

Sassa K, Nagai O, Solidum R, Yamazaki Y and Ohta H (2010) An integrated model simulating the initiation and motion of earthquake and rain induced rapid landslides and its application to the 2006 leyte landslide. Landslides 7: 219-236. doi: 10.1007/s10346-010-0230-z

Savage SB and Hutter K (1989) The motion of a finite mass of granular material down a rough incline. Journal of Fluid Mechanics 199: 177-215. doi: 10.1017/S0022112089000340

Savage SB and Lun CKK (1988) Particle size segregation in inclined chute flow of dry cohesionless granular solids. Journal of Fluid Mechanics 189: 311-335. doi: 10.1017/S002211208800103X

Shan T and Zhao J (2014) A coupled cfd-dem analysis of granular flow impacting on a water reservoir. Acta Mechanica 225: 2449-2470. doi: 10.1007/s00707-014-1119-z

Shen W, Li T, Li P and Guo J (2018) A modified finite difference model for the modeling of flowslides. Landslides 15: 1577-1593. doi: 10.1007/s10346-018-0980-6

Shen W, Zhao T, Zhao J, Dai F and Zhou GGD (2018) Quantifying the impact of dry debris flow against a rigid barrier by dem analyses. Engineering Geology 241: 86-96. doi: https://doi.org/10.1016/j.enggeo.2018.05.011

Shi GH (1992) Discontinuous deformation analysis: A new numerical model for the statics and dynamics of deformable block structures. Engineering Computations 9: 157-168. doi: 10.1108/eb023855

Sulsky D, Chen Z and Schreyer HL (1994) A particle method for history-dependent materials. Computer Methods in Applied Mechanics and Engineering 118: 179-196. doi: https://doi.org/10.1016/0045-7825(94)90112-0

Tang C, Rengers N, van Asch TWJ, Yang YH and Wang GF (2011) Triggering conditions and depositional characteristics of a disastrous debris flow event in zhouqu city, gansu province, northwestern china. Nat Hazards Earth Syst Sci 11: 2903-2912. doi: 10.5194/nhess-11-2903-2011

Trujillo-Vela MG, Galindo-Torres SA, Zhang X, Ramos-Ca ñón AM and Escobar-Vargas JA (2020) Smooth particle hydrodynamics and discrete element method coupling scheme for the simulation of debris flows. Computers and Geotechnics 125: 103669. doi: https://doi.org/10.1016/j.compgeo.2020.103669

Tunuguntla DR, Bokhove O and Thornton AR (2014) A mixture theory for size and density segregation in shallow granular free-surface flows. Journal of Fluid Mechanics 749: 99-112. doi: 10.1017/jfm.2014.223

Vagnon F and Segalini A (2016) Debris flow impact estimation on a rigid barrier. Nat Hazards Earth Syst Sci 16: 1691-1697. doi: 10.5194/nhess-16-1691-2016

Varnes DJ (1978) Slope movement types and processes. Special report 176: 11-33.

Wang GL (2013) Lessons learned from protective measures associated with the 2010 zhouqu debris flow disaster in china. Natural Hazards 69: 1835-1847. doi: 10.1007/s11069-013-0772-1

Wang J, Zhang Y, Chen Y, Wang Q, Xiang C, Fu H, Wang P, Zhao JX and Zhao L-h (2021) Back-analysis of donghekou landslide using improved dda considering joint roughness degradation. Landslides 18: 1925-1935. doi: 10.1007/s10346-020-01586-1

Wang W, Chen G, Han Z, Zhou S, Zhang H and Jing P (2016) 3d numerical simulation of debris-flow motion using sph method incorporating non-newtonian fluid behavior. Natural Hazards 81: 1981-1998. doi: 10.1007/s11069-016-2171-x

Wang W, Yin K, Chen G, Chai B, Han Z and Zhou J (2019) Practical application of the coupled dda-sph method in dynamic modeling for the formation of landslide dam. Landslides 16: 1021-1032. doi: 10.1007/s10346-019-01143-5

WP/WLI (1995) International geotechnical societies' unesco working party on world landslide inventory. Working group on rate of movement (chairman: Ch bonnard) a suggested method for describing the rate

of movement of a landslide. Bull Eng Geol Environ 52: 75-78.

Wu J-H and Hsieh P-H (2021) Simulating the postfailure behavior of the seismically- triggered chiu-fen-erh-shan landslide using 3dec. Engineering Geology 287: 106113. doi: https://doi.org/10.1016/j.enggeo.2021.106113

Xia X and Liang Q (2018) A new depth-averaged model for flow-like landslides over complex terrains with curvatures and steep slopes. Engineering Geology 234: 174-191. doi: https://doi.org/10.1016/j.enggeo.2018.01.011

Xing AG, Wang G, Yin YP, Jiang Y, Wang GZ, Yang SY, Dai DR, Zhu YQ and Dai JA (2014) Dynamic analysis and field investigation of a fluidized landslide in guanling, guizhou, china. Engineering Geology 181: 1-14. doi: https://doi.org/10.1016/j.enggeo.2014.07.022

Xu W-J and Dong X-Y (2021) Simulation and verification of landslide tsunamis using a 3d sph-dem coupling method. Computers and Geotechnics 129: 103803. doi: https://doi.org/10.1016/j.compgeo.2020.103803

Zhang F, Peng J, Wu X, Pan F, Jiang Y, Kang C, Wu W and Ma W (2021) A catastrophic flowslide that overrides a liquefied substrate: The 1983 saleshan landslide in china. Earth Surface Processes and Landforms n/a. doi: https://doi.org/10.1002/esp.5144

Zhang X, Krabbenhoft K, Sheng D and Li W (2015) Numerical simulation of a flow-like landslide using the particle finite element method. Computational Mechanics 55: 167-177. doi: 10.1007/s00466-014-1088-z

Zhao L, He JW, Yu ZX, Liu YP, Zhou ZH and Chan SL (2020) Coupled numerical simulation of a flexible barrier impacted by debris flow with boulders in front. Landslides 17: 2723-2736. doi: 10.1007/s10346-020-01463-x

Zhao T, Crosta GB, Utili S and De Blasio FV (2017) Investigation of rock fragmentation during rockfalls and rock avalanches via 3-d discrete element analyses. Journal of Geophysical Research: Earth Surface 122: 678-695. doi: https://doi.org/10.1002/2016JF004060

Zhou GGD and Ng CWW (2010) Numerical investigation of reverse segregation in debris flows by dem. Granular Matter 12: 507-516. doi: 10.1007/s10035-010-0209-4

Zhou S, Stormont J and Chen Z (1999) Simulation of geomembrane response to settlement in landfills by using the material point method. International Journal for Numerical and Analytical Methods in Geomechanics 23: 1977-1994. doi: https://doi.org/10.1002/(SICI)1096-9853(19991225)23:15<1977::AID-NAG45>3.0.CO;2-3

Zhuang Y, Xu Q and Xing A (2019) Numerical investigation of the air blast generated by the wenjia valley rock avalanche in mianzhu, sichuan, china. Landslides 16: 2499-2508. doi: 10.1007/s10346-019-01253-0

2. PAPER 1

A two-layer numerical model for simulating the frontal plowing phenomenon of flow-like landslides

Wei Shen[1], Tonglu Li[2*], Ping Li[2], Matteo Berti[1], Yueqiang Shen[2], Jian Guo[2]
*Correspondence author

1 Department of Biological, Geological and Environmental Sciences, University of Bologna, Italy, 40126
2 Department of Geological Engineering, Chang'an University, Xi'an, China, 710064

Paper has been published in Engineering Geology

Engineering Geology 259 (2019) 105168

Contents lists available at ScienceDirect

Engineering Geology

journal homepage: www.elsevier.com/locate/enggeo

A two-layer numerical model for simulating the frontal plowing phenomenon of flow-like landslides

Wei Shen[a], Tonglu Li[b,*], Ping Li[b], Matteo Berti[a], Yueqiang Shen[b], Jian Guo[b]

[a] Dipartimento di Scienze Biologiche, Geologiche e Ambientali, Università di Bologna, 67-40126, Italy
[b] Department of Geological Engineering, Chang'an University, Xi'an 710064, China

ARTICLE INFO

Keywords:
Flow-like landslides
Numerical simulation
Finite difference method
Two-layer model
Landslide entrainment

ABSTRACT

Many flow-like landslides entrain material from their paths during motion. At the flow front and along the lateral margins the sliding mass can plow into the path material pushing or entraining the existing soil. Although plowing can be a dominant mechanism for landslide mobility, little attention has been paid to this phenomenon in comparison with other entraining mechanism such as basal scouring. Therefore, establishing a suitable mathematical description is still a challenge. In this paper, a two-layer finite difference model is proposed to simulate frontal plowing. The frontal erodible mass and the sliding mass are simplified as two separate layers based on the assumption that they are immiscible in their propagation processes. The interaction (i.e., thrusting and shear) between the two layers is simulated by the normal force and shear force acting on the two-layer interface. The governing equations for the two-layer model are deduced from the mass and momentum conservations of a soil column and transformed into a finite difference form for numerical solving. Then the proposed model is tested in the back analysis of the Ximiaodian landslide which is a typical loess flow-like landslide located at the south bank of the Jing River, China. The modeling results show that frontal plowing has significant influence on the propagation of this landslide, especially on the final topography of the deposit. Without considering this effect, the thickness of the final deposit tends to be underestimated, while the propagation duration, area and distance are likely to be overestimated. The proposed model can provide more accurate and reliable simulations for rapid flow-like landslides with frontal plowing phenomenon.

1. Introduction

Flow-like landslides are commonly characterized by high speed and long run-out distance (Legros, 2002; Pudasaini and Miller, 2013). Debris avalanches, debris flows and mudflows are typical flow-like landslides (Hungr et al., 2014). They frequently occur in many mountainous regions across the world and are responsible for thousands of casualties and huge property loss (Zhang and Wang, 2007; Huang, 2009; Evans et al., 2009; Iverson et al., 2015; Haque et al., 2016; Mergili et al., 2018). The physical mechanism of these landslides is rather complex and still not fully understood. Past studies showed that many factors, such as heavy precipitation (Wang and Sassa, 2003; Xing et al., 2014; Peng et al., 2015), earthquake (Okada et al., 2008; Wang et al., 2014) and entrainment (Iverson et al., 2011; Cuomo et al., 2014) can trigger a flow-like landslide. In particular, entraining of saturated materials along the landslide path maybe the factor that most influences the mobility of flow-like landslides (Hungr and Evans, 2004; Crosta et al., 2009; Mangeney, 2011; Iverson and Ouyang, 2015; Pudasaini and Fischer, 2016). According to the existing literatures, landslide entrainment is a multiple process consisting of shearing, dragging and plowing (Crosta et al., 2017; de Haas and van Woerkom, 2016). The volume of a flow-like landslide can increase many folds through entrainment (Wang et al., 2003; Hungr and Evans, 2004), and the run-out distance is likely to be significantly influenced by entrainment (Shen et al., 2018a, 2018b; Pudasaini and Fischer, 2016). For many flow-like landslides, entrainment consists of two separate processes, namely bed entrainment/basal scouring and frontal plowing (McDougall, 2006). Bed entrainment and frontal plowing are two substantially different processes. Bed entrainment occurs when a landslide moves on a weak substrate, and the material in the substrate will be entrained by (incorporated into) the sliding mass under the long-term effect of basal scouring. However, in the process of frontal plowing, the sliding mass mainly pushes the plowing mass forward, and they basically remain separate (only limited mixing occurs) in this

* Corresponding author.
E-mail addresses: wei.shen@studio.unibo.it (W. Shen), dcdgx08@chd.edu.cn (T. Li), dcdgx07@chd.edu.cn (P. Li), matteo.berti@unibo.it (M. Berti), 2017226065@chd.edu.cn (Y. Shen), 2018026022@chd.edu.cn (J. Guo).

https://doi.org/10.1016/j.enggeo.2019.105168
Received 3 October 2018; Received in revised form 30 May 2019; Accepted 30 May 2019
Available online 04 June 2019
0013-7952/

process. Most previous studies focused on the numerical or experimental studies of bed entrainment (Mcdougall and Hungr, 2005; Cuomo et al., 2016; Crosta et al., 2017), so much progresses have been made in modeling bed entrainment. In comparison, only very limited studies (Cascini et al., 2013; Christen et al., 2010) have tried to quantify the phenomenon of frontal plowing, so establishing a suitable mathematical description for this phenomenon remains a challenge in landslide modeling. However, frontal plowing may play a dominate role in the propagation of rapid flow-like landslides. For example, in the 1903 Frank landslide, the frontal plowing of the alluvium was responsible for most of the damages in Frank town (Cruden and Hungr, 1986). Neglecting frontal plowing may be an importance source of error in numerical simulation, so it should be considered when this phenomenon is obvious.

Numerical models of flow-like landslides developed quickly in last few decades (Pirulli et al., 2015; Mergili et al., 2017, 2018; Scaringi et al., 2018). On the other hand, the existing models, either based on empirical methods (Berti and Simoni, 2014) or numerical methods (Crosta et al., 2003; Hungr and McDougall, 2009; Liu et al., 2009; Sassa et al., 2010; Ouyang et al., 2013; Pastor et al., 2014; Pudasaini, 2012; Pudasaini, 2014; Shen et al., 2018a), do not include frontal plowing. This is because in these models all masses (sliding mass and erodible mass) are in a same computational layer. A possible way to address this problem is to propose a two-layer model to describe the motions of both the sliding mass and the frontal plowing mass, like the techniques adopted in modeling landslide-induced water wave (Sassa et al., 2016).

In this study, we propose a new mathematical model to describe the frontal plowing phenomenon in flow-like landslides. In comparison with traditional one-layer models, the sliding mass and the frontal plowing mass are in two different layers and are immiscible, and the interactions between them are considered by the normal and shear forces on the two-layer interface. The present model highlights in extending the applications of the depth-averaged models, and it can reflect the interactive process between the sliding mass and the plowing mass. In the following sections, the governing equations for the mathematical model are deduced first, and then transformed into the finite difference forms. The propagation of the Ximiandian landslide is analyzed by the model to validate its accuracy and effectiveness. Finally, the performance of the model is discussed and compared with the traditional one-layer models.

2. Mathematical model of frontal plowing

2.1. Conceptual representation

In our model, the landslides are assumed to have a two-layer structure, consisting of a thick sliding mass layer (layer 2) and a thin plowing mass layer (layer 1), as shown in Fig. 1. The two layers are assumed to be immiscible in their propagation processes. In nature, the sliding mass usually thrusts into the frontal mass like a plow, and then pushes the plowing mass forward. Therefore, this process is called frontal plowing (McDougall, 2006). Fig. 1 gives a schematic depiction of the typical frontal plowing phenomenon in flow-like landslides. The interaction between the two layers is simplified as the shear and normal forces acting on the two-layer interface (Fig. 1b).

Based on the abovementioned assumptions, the governing equations for the two-layer model are deduced in a fixed soil column in a Cartesian coordinate system, following Sassa et al. (2010) and Shen et al. (2018a). The coordinate and the forces acting on the column are shown in Fig. 2. For both layers, four forces act on the column: the weight W, lateral pressure P, normal force N and shear resistance S. Specifically, for layer 2, the normal force and shear resistance on the

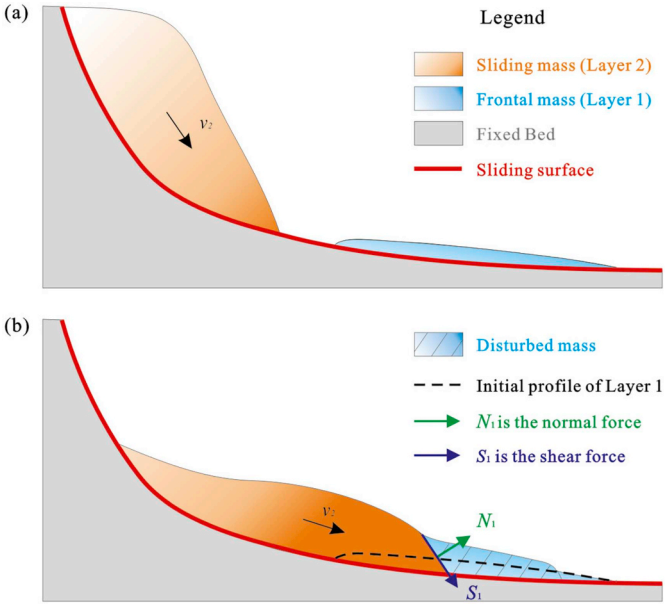

Fig. 1. Schematic diagram of the two-layer structure of flow-like landslides. **a** Before frontal plowing, and **b** after frontal plowing.

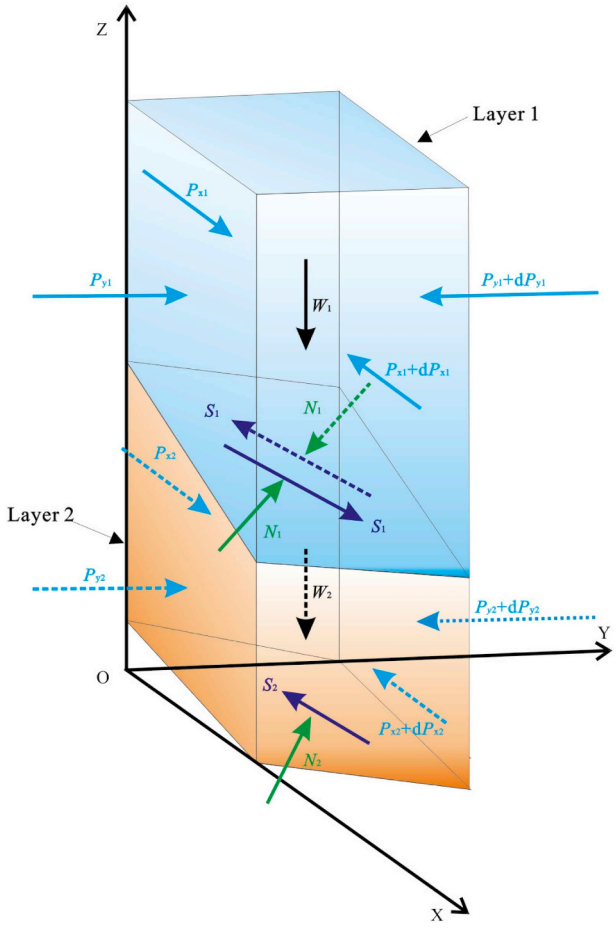

Fig. 2. Coordinate setup for the model and forces acting on the two-layer soil column. W is the weight, P is the lateral pressure, N is the normal force, and S is the shear resistance.

bottom surface of layer 1 are regarded as the additional external forces acting on the top surface of layer 2. In addition, the shear resistance forces acting on the lateral surfaces of these columns are neglected according to the shallow water assumption. This simplification is justified to be reasonable since the width and length of a flow-like landslide is usually much larger than its depth.

2.2. Continuity and momentum equations

Both layer 1 and layer 2 are assumed to be incompressible. Since this paper focuses on studying frontal plowing, bed entrainment is not considered. Therefore, the continuity equations for both layers can be expressed as.

$$\frac{\partial h_i}{\partial t} + \frac{\partial Q_{xi}}{\partial x} + \frac{\partial Q_{yi}}{\partial y} = 0 \tag{1}$$

where h is the height of a soil column, $Q_x = v_x h$ and $Q_y = v_y h$ are the flow quantities in the x and y directions, respectively, v_x and v_y are the depth-averaged velocities of the soil column in the x and y directions, respectively, and the subscript i of each variable refers to layer i (i = 1 or 2). The above continuity equation reflects the mass conservation in both soil columns.

The momentum equations are deduced according to the momentum conservation of a soil column. For simplicity, the deducing process is briefly introduced here (Appendix A), and the details can be found in Shen et al. (2018a). For example, the kinematic equations for layer 1 and layer 2 in the x direction can be written as.

$$a_{x1} = \frac{\partial v_{x1}}{\partial t} + v_{x1}\frac{\partial v_{x1}}{\partial x} + v_{y1}\frac{\partial v_{x1}}{\partial y} = \frac{-dP_{x1}}{m_1} + \frac{N_{x1}}{m_1} + \frac{S_{x1}}{m_1} \tag{2}$$

$$a_{x2} = \frac{\partial v_{x2}}{\partial t} + v_{x2}\frac{\partial v_{x2}}{\partial x} + v_{y2}\frac{\partial v_{x2}}{\partial y} = \frac{-dP_{x2}}{m_2} + \frac{N_{x2}}{m_2} + \frac{S_{x2}}{m_2} - \frac{m_1}{m_2}\left(\frac{N_{x1}}{m_1} + \frac{S_{x1}}{m_1}\right) \tag{3}$$

where m_1 and m_2 are the masses of layer 1 and layer 2, respectively, a is the acceleration, P is the lateral pressure, N is the normal force, S is the shear resistance. Eq. (2) and Eq. (3) are the equilibrium equations for layer 1 and layer 2 in the x direction, respectively. For each layer, P, N and S contribute to the momentum change of the layer. The interaction between the two layers is produced by N_{x1} and S_{x1}. Therefore, Eq. (3) has an additional term (the second term) on its right side. The kinematic equations of layer 1 and layer 2 in the y direction have similar forms as in Eqs. (2)–(3). The momentum equations of the two-layer model can be obtained by combining the kinematic equations with the continuity equation (e.g., the momentum equation of layer 1 can be obtained by combining Eq. (2) with Eq. (1)).

2.2.1. Momentum equations for layer 1

The momentum equations for layer 1 are given by.

$$\frac{\partial Q_{x1}}{\partial t} + \frac{\partial {Q_{x1}}^2/h_1}{\partial x} + \frac{\partial Q_{x1}Q_{y1}/h_1}{\partial y} = -B_{x1} + A_1\frac{\tan\alpha_1}{G_1} - \frac{D_{x1}h_1}{m_1}S_1 \tag{4}$$

$$\frac{\partial Q_{y1}}{\partial t} + \frac{\partial {Q_{y1}}^2/h_1}{\partial y} + \frac{\partial Q_{x1}Q_{y1}/h_1}{\partial x} = -B_{y1} + A_1\frac{\tan\beta_1}{G_1} - \frac{D_{y1}h_1}{m_1}S_1 \tag{5}$$

where B_x and B_y represent the contributions of the lateral pressure P (corresponding to dP_{x1} in Eq. (2)) to the momentum in the x and y directions, respectively, A represents the contribution of the normal force N (corresponding to N_{x1} in Eq. (2)), S (corresponding to S_{x1} in Eq. (2)) is the shear resistance, D_x and D_y are the operators projecting S in the x and y directions, respectively, α and β represent the dip angles of the sliding surface in the x and y directions, respectively, and G is the geometric parameter related to α and β. The expressions of B_{x1}, B_{y1}, A_1, D_{x1}, D_{y1}, and G_1 are given by Eqs. (6)–(11)

$$B_{x1} = k_1 g h_1 \frac{\partial h_1}{\partial x} \tag{6}$$

$$B_{y1} = k_1 g h_1 \frac{\partial h_1}{\partial y} \tag{7}$$

$$A_1 = B_{x1}\tan\alpha_1 + B_{y1}\tan\beta_1 + g h_1 \tag{8}$$

$$D_{x1} = \frac{v_{x1} - v_{x2}}{\sqrt{(v_{x1} - v_{x2})^2 + (v_{y1} - v_{y2})^2 + {v_{z1}}^2}} \tag{9}$$

$$D_{y1} = \frac{v_{y1} - v_{y2}}{\sqrt{(v_{x1} - v_{x2})^2 + (v_{y1} - v_{y2})^2 + {v_{z1}}^2}} \tag{10}$$

$$G_1 = \tan^2\alpha_1 + \tan^2\beta_1 + 1 \tag{11}$$

where $v_{z1} = -(v_{x1} - v_{x2})\tan\alpha_1 - (v_{y1} - v_{y2})\tan\beta_1$, and k is the lateral pressure coefficient. Eq. (4) and (5) are very similar to the momentum equations of the traditional one-layer models. However, the expressions of D_{x1} and D_{y1} are slightly different with their traditional counterparts in one-layer models. In one-layer models absolute velocities (v_{x1} and v_{y1}) are used to calculate D_{x1} and D_{y1}, while the relative velocities (v_{x1} - v_{x2} and $v_{y1} - v_{y2}$) are adopted in Eq. (9) and (10) because the direction of the shear resistance S_1 is opposite to the direction of the relative velocity of the two layers.

2.2.2. Momentum equations for layer 2

The momentum equations for layer 2 are given by.

$$\frac{\partial Q_{x2}}{\partial t} + \frac{\partial {Q_{x2}}^2/h_2}{\partial x} + \frac{\partial Q_{x2}Q_{y2}/h_2}{\partial y} = -B_{x2} + A_2\frac{\tan\alpha_2}{G_2} - \frac{D_{x2}h_2}{m_2}S_2 - \frac{\rho_1}{\rho_2}\left(A_1\frac{\tan\alpha_1}{G_1} - \frac{D_{x1}h_1}{m_1}S_1\right) \tag{12}$$

$$\frac{\partial Q_{y2}}{\partial t} + \frac{\partial {Q_{y2}}^2/h_2}{\partial y} + \frac{\partial Q_{x2}Q_{y2}/h_2}{\partial x} = -B_{y2} + A_2\frac{\tan\beta_2}{G_2} - \frac{D_{y2}h_2}{m_2}S_2 - \frac{\rho_1}{\rho_2}\left(A_1\frac{\tan\beta_1}{G_1} - \frac{D_{y1}h_1}{m_1}S_1\right) \tag{13}$$

where ρ_1 and ρ_2 are the bulk densities of layer 1 and layer 2, respectively. The first three terms on the right sides of Eq. (12) and (13) have similar forms with Eq. (4) and (5) (corresponding to the first three terms on the right hand side of Eq. (3)), while the last terms of Eq. (12) and (13) (corresponding to the last term in Eq. (3)) reflect the

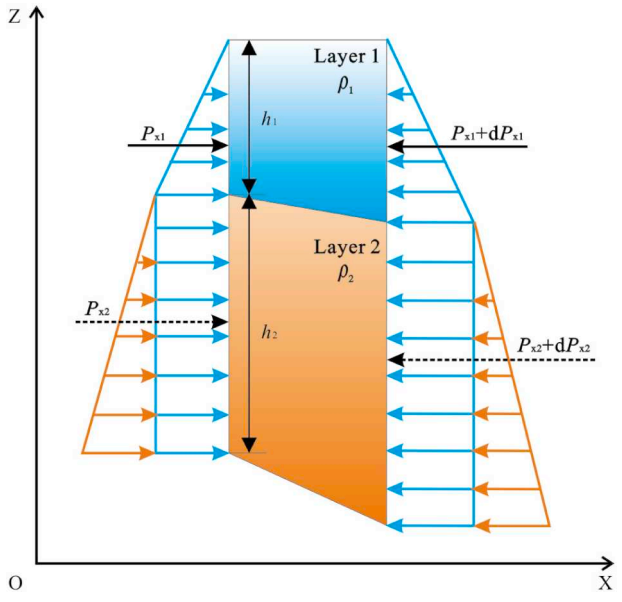

Fig. 3. Distribution of the lateral pressure in a soil column in the x direction.

interaction between the two layers. In addition, the lateral pressure of layer 2 has different expression with that of layer 1 because layer 2 is buried by layer 1 in the interactive areas. The lateral pressure in a soil column in the x direction is shown in Fig. 3. The lateral pressure is assumed to increase linearly with soil depth.

The expressions of B_{x2}, B_{y2}, A_2, D_{x2}, D_{y2}, and G_2 are given by Eqs. (14)–(19)

$$B_{x2} = k_1 g \frac{\rho_1}{\rho_2}\left(h_1 \frac{\partial h_2}{\partial x} + h_2 \frac{\partial h_1}{\partial x}\right) + k_2 g h_2 \frac{\partial h_2}{\partial x} \tag{14}$$

$$B_{y2} = k_1 g \frac{\rho_1}{\rho_2}\left(h_1 \frac{\partial h_2}{\partial y} + h_2 \frac{\partial h_1}{\partial y}\right) + k_2 g h_2 \frac{\partial h_2}{\partial y} \tag{15}$$

$$A_2 = B_{x2}\tan\alpha_2 + B_{y2}\tan\beta_2 + g h_2 \tag{16}$$

$$D_{x2} = \frac{v_{x2}}{\sqrt{{v_{x2}}^2 + {v_{y2}}^2 + {v_{z2}}^2}} \tag{17}$$

$$D_{y2} = \frac{v_{y2}}{\sqrt{{v_{x2}}^2 + {v_{y2}}^2 + {v_{z2}}^2}} \tag{18}$$

$$G_2 = \tan^2\alpha_2 + \tan^2\beta_2 + 1 \tag{19}$$

where $v_{z2} = -v_{x2}\tan\alpha_2 - v_{y2}\tan\beta_2$. Eq. (14) and (15) can be transformed into Eq. (6) and (7) in areas where only layer 2 exists.

2.2.3. Expression of the shear resistance S

The shear resistance S can be determined by different rheological laws. Most frequently-used rheological laws for flow-like landslides are the Voellmy model and the Mohr-Coulomb criterion. In the present study, the Mohr-Coulomb criterion is selected to simulate of the Ximiaodian landslide for its simplicity. In addition, since the sliding mass of the Ximiaodian landslide mainly consists of pure loess and the main material in the terrace is gravel, the Mohr-Coulomb criterion is suitable for depicting the rheology of these types of soils, which is given by

$$S_i = N_i(1 - r_{ui})\tan\varphi_i + c_i A_{ri} \tag{20}$$

where r_u is the pore pressure coefficient, φ and c are the effective friction angle and cohesion, respectively, and $A_r(\tan\alpha_1 i + \tan\beta_1 j + k)/\sqrt{G_1}$ is the bottom area of the soil columns.

In summary, the governing equations of the two-layer model consist of Eq. (1), (4), (5), (12) and (13). The basic variables in these equations are h_1, h_2, Q_{x1}, Q_{y1}, Q_{x2}, and Q_{y2}.

3. Model setup and numerical scheme

3.1. Initial and boundary conditions

The sliding mass and frontal plowing mass are static at first. Each part of the two layers can start moving only if the external forces (e.g., pressure gradient and normal force) overcome the basal resistance. Taking the initial condition in the x direction as an example, for the static erodible mass in layer 1, the following initial condition should be satisfied

$$\left|-B_{x1} + A_1\frac{\tan\alpha_1}{G_1}\right| > \left|\frac{D_{x1}h_1}{m_1}S_1\right| \tag{21}$$

While for layer 2, the initial condition is given by

$$\left|-B_{x2} + A_2\frac{\tan\alpha_2}{G_2} - \frac{\rho_1}{\rho_2}\left(A_1\frac{\tan\alpha_1}{G_1} - \frac{D_{x1}h_1}{m_1}S_1\right)\right| > \left|\frac{D_{x2}h_2}{m_2}S_2\right| \tag{22}$$

There are two types of boundaries in the present study. One is the free surface boundary, which is automatically determined by the calculated thickness of the sliding mass layer and plowing mass layer. Another one is the moving boundary. For each layer (the sliding mass layer or the plowing mass layer), the moving boundary is the boundary between the moving mass and the static mass (or the dry bed). On the moving boundary, the velocity of the sliding (plowing) mass is zero ($v = 0$). If it is dry bed, the height is also zero ($h = 0$). For a flow-like landslide, the computational region is set to be big enough so that the landslide will move within this region in simulation.

3.2. Numerical scheme

The governing equations of the two-layer model are discretized in fixed rectangular cells, following Shen et al. (2018a). Height h is discretized at the center of these cells and velocity v is discretized at the surfaces of these cells. For the temporal terms in the governing equations, the one-order forward difference method is utilized

$$\frac{\partial f}{\partial t} \approx \frac{f_{i,j}^{t+1} - f_{i,j}^{t}}{\Delta t} \tag{23}$$

where f is the variable being discretized (i.e., h, Q_x and Q_y), the subscripts i and j represent cell (i, j), the superscript t represent time, and Δt is the time step. For the convective terns (the second and third terms on the left sides of Eq. (4), (5), (12) and (13)), the first-order upwind method is adopted according to the direction of the velocity. For other spatial terms in the governing equations, central difference scheme is adopted

$$\frac{\partial f}{\partial x_i} \approx \frac{f_{i+1/2,j}^{t} - f_{i-1/2,j}^{t}}{dx_i} \tag{24}$$

where dx_i is the length of a cell. The governing equations are transformed into finite difference equations through the above difference scheme. Then these equations can be solved using an explicit method. The numerical scheme adopted here has first-order accuracy in time and second-order accuracy in space. To achieve higher computational resolution, some high-resolution and highly-efficient difference schemes (Pudasaini and Hutter, 2007; Mergili et al., 2017) can also be used to discretize these governing equations.

The time step is calculated by the following equation

$$\Delta t = \min\left(\min\left(\frac{dx}{\omega \max|v_{xi}|}, \frac{dy}{\omega \max|v_{yi}|}\right), \Delta t_s\right) \tag{25}$$

where $\omega = 5$ is adopted here to guarantee the stability of the numerical scheme; Δt_s is the initial time step.

4. Case study of the Ximiaodian Landslide

4.1. Introduction of the Ximiaodian landslide

The Ximiaodian landslide (E 108° 45′ 42.81″, N 34° 30′ 9.65″) is a typical flow-like landslide in the Miaodian Village, Shaanxi Province, China. It is located at the north side of a loess tableland and adjacent to the Jing River (see Fig. 4). In recent three decades, many similar landslides were triggered by irrigation or canal leakage on the top of this loess tableland (Zhang et al., 2009; Xu et al., 2011; Shen et al., 2016; Leng et al., 2018; Peng et al., 2018; Hou et al., 2018), which have caused serious casualties and economic losses. The local hydrogeological data showed that the water table in the side slopes of this loess tableland increased steady in last 30 years (Leng et al., 2018), which finally induced the Ximiaodian landslide in July 2015. Field survey and mapping was conducted a few days after this landslide.

Fig. 5 is the panorama view of the Ximiaodian landslide. According to our field observation, the plowing phenomenon is very obvious in this landslide. The original loess landslide and the frontal plowing mass basically remain unmixed after the landslide, which is clearly shown by the distinct boundary between them. Based on this feature, the landslide can be divided into two different parts: the first part is the yellow loess deposit (i.e., the rear part of this landslide without many plants),

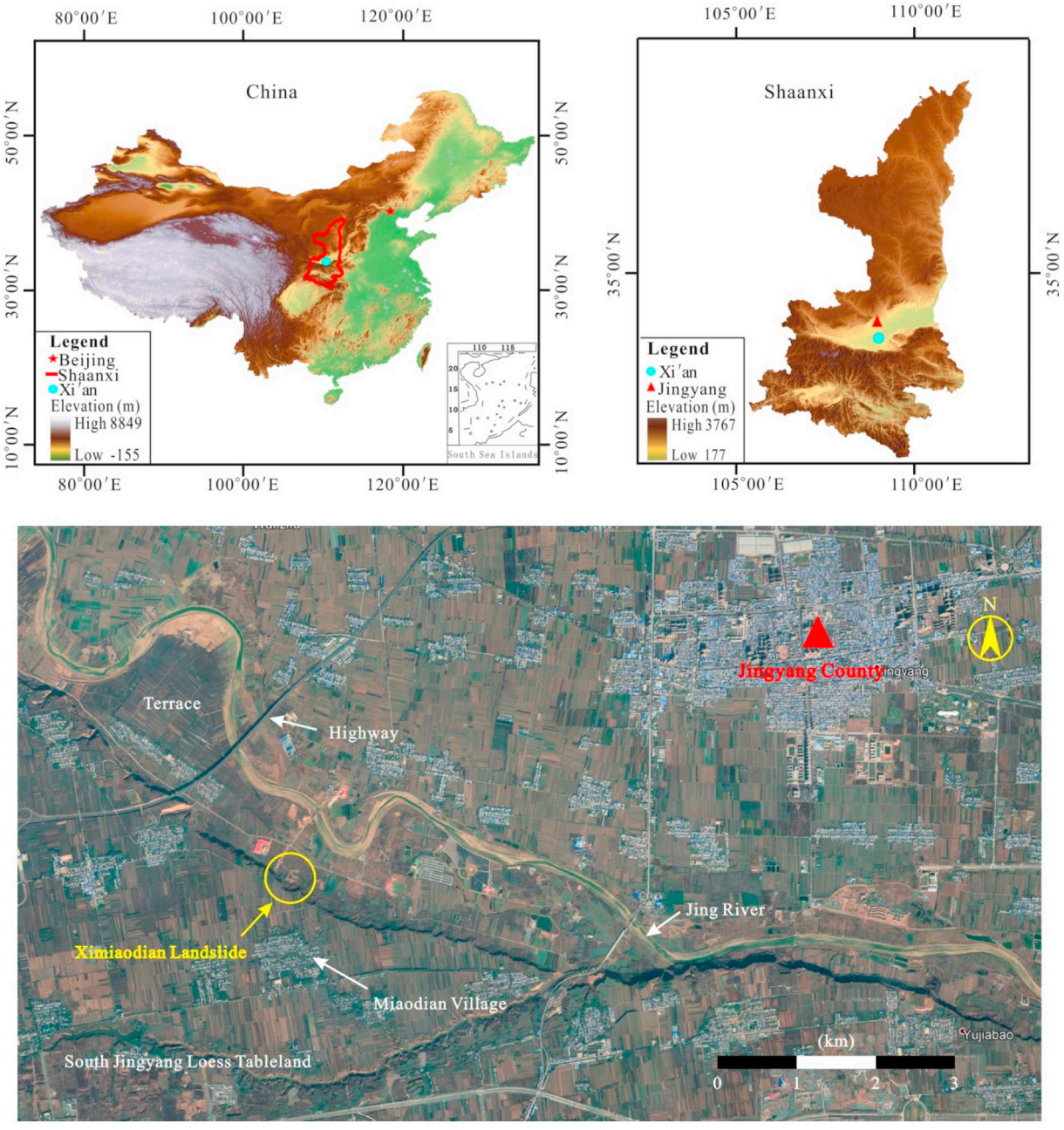

Fig. 4. Location of the Ximiaodian landslide in the study area.

and the second part is the entrained terrace materials with green trees. The entrained terrace material mainly consisted of gravel and was pushed forward by the loess landslide, leading to a significant lateral spreading of the terrace deposit. It also shows that some small compression ridges form in the middle part of the gravel deposit under the passive thrusting of the loess landslide. This feature can be helpful in understanding the plowing process of this landslide. However, the present two-layer model is not capable of reflecting such a subtle feature. This is mainly caused by the discrepancy between the model and the reality. The saturated gravel mass behaves like a flow-like material, even though there are differences with respect to a pure fluid. Therefore, the passive ridges in the gravel are likely to be smoothed when using the current depth-averaged governing equations and numerical method.

The geological cross-section (I-I′) in Fig. 5 is depicted according to the field survey data, as shown in Fig. 6. The landslide mass mainly consists of loess (from the loess slope) and gravel (from the terrace). The volume of the loess sliding mass is about 435,000 m^3. After failure, the volume of the final deposit (about 456, 000 m^3) is slightly larger than the original value, which is probably caused by the fissures in the deposit. The original height of the loess slope is 63 m, and the initial slope angle is about 50°. The horizontal run-out distance of this landslide is about 290 m. The gravel at the foot of the loess slope was pushed forward by the landslide for about 100 m and propagated in a flow-like motion. The frontal plowing phenomenon is obvious in this landslide, forming a ridge between the loess deposit and the gravel deposit (indicated by the dark dashed line in Fig. 5). The original thickness of the terrace is about 4 m, while that of the loess sliding mass is much thicker with an average thickness of about 30 m. Therefore, the loess sliding mass can easily plow into the terrace.

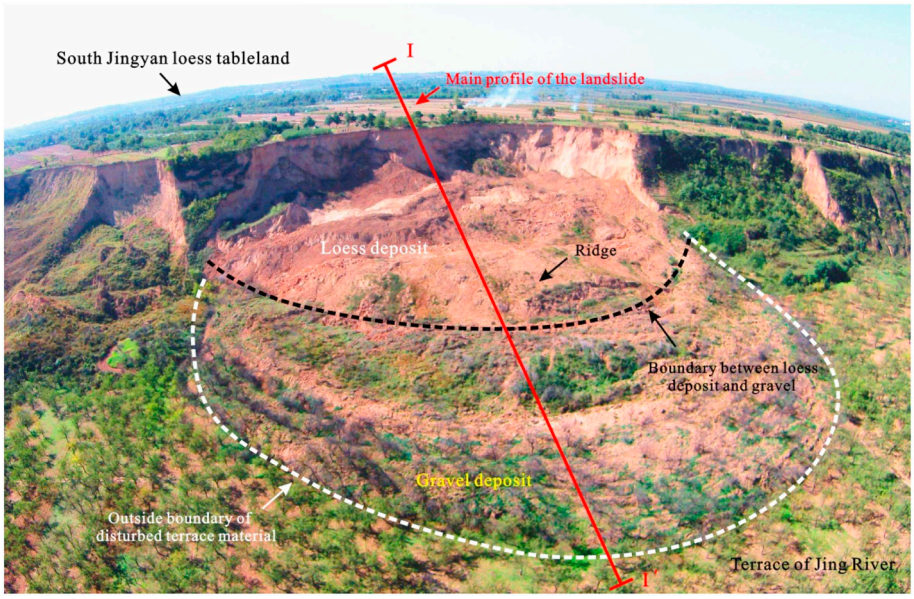

Fig. 5. Panorama view of the Ximiaodian landslide. The terrace material of the Jing River was pushed forward by this loess landslide for about 100 m.

4.2. Simulation setup

The computational region is 505 m in length and 435 m in width. The length of each cell is 5 m in both the x and y directions, so the computational region is divided into 8787 cells. Three different situations are simulated by the proposed model to study the influence of frontal plowing on the propagation of this landslide. In situation 1, the frontal plowing effect is considered and simulated by the two-layer model. In situation 2, the entrainment of the terrace is not considered, so only the propagation of the loess sliding mass is simulated. In situation 3, both the terrace mass and the loess mass are regarded as the sliding mass layer (layer 2). In situation 2 and 3, since the plowing mass layer does not exist, the two-layer model is transformed into a traditional one-layer model. For situation 1, the rheological parameters of the sliding mass and plowing mass take those of the loess and gravel, respectively. However, for situation 2 and 3, the rheological parameters take those of the loess in the loess zone and those of the gravel in the terrace zone. The initial time step is 0.01 s in these simulations.

Table 1 gives the parameters used in these simulations. The density of the gravel and loess are determined by in-situ and laboratory testing, respectively. Four intact loess specimens were taken at the foot of the backscarp of the landslide (about 15 m below the top of the tableland), and these specimens were used to determine the effective frictional angle and cohesion of the loess. The specimens of the gravel were taken at the front part of the terrace about 1.5 m below the ground, and the effective frictional angle and cohesion of the gravel are determined by ring shear tests. The lateral pressure coefficient k is set to be the static lateral pressure coefficient. The excess pore pressure coefficient r_u (defined as a ratio between the total pore pressure and the total overburden pressure) is estimated according to the saturate degree of the sliding mass and its drainage conditions. For the loess, r_u has a relative low value because part of the loess mass is unsaturated. While since the terrace gravel is saturated in nature and the drainage condition is probably undrained given the rapid propagation of this landslide, its r_u value is relatively high. One drawback of single-phase models is that the r_u value of the soil is an empirical parameter, which is kept constant during the run-out process of a landslide. In comparison, the evolution of the pore water pressure can be simulated by two-phase models (Pudasaini, 2012), which represents the advantage distinguishing them from single-phase models.

Table 1
Parameters used in simulating the Ximiaodian landslide.

Soil type	Lateral pressure coefficient	Density	Frictional angle	Cohesion	Excess pore pressure coefficient
	k	ρ (g/cm^3)	φ (°)	c (kPa)	r_u
Loess	0.58	1.80	25.0	15.0	0.6
Gravel	0.52	2.00	29.0	5.0	0.9

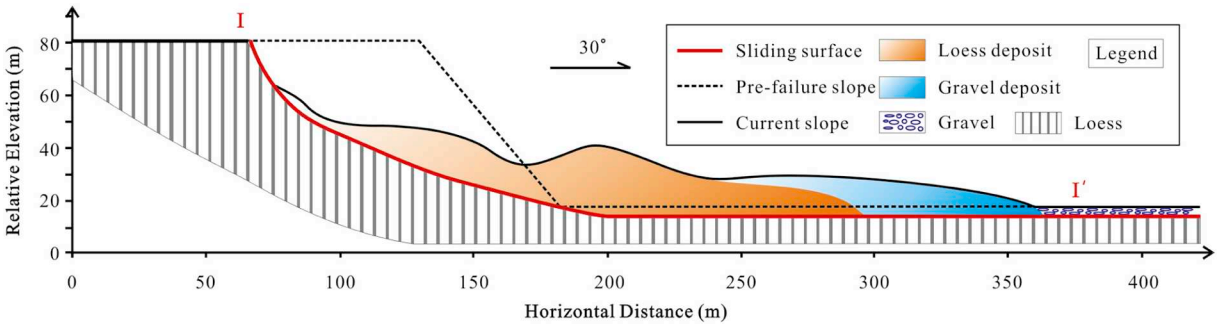

Fig. 6. Geological cross-section of profile I-I′.

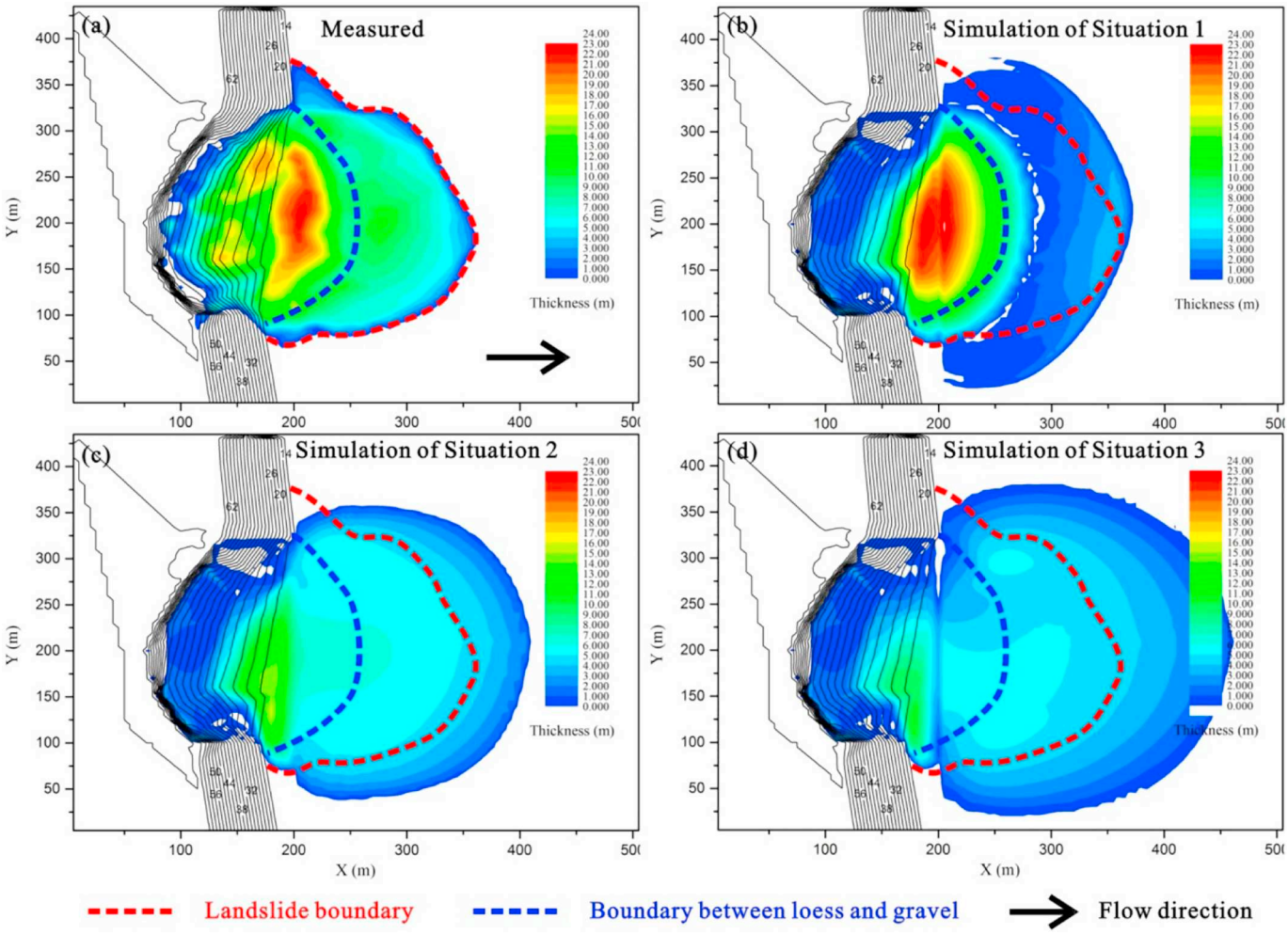

Fig. 7. Comparison of the simulated final topography of the three situations with the measured topography. **a** Measured topography, **b** result of situation 1 by the two-layer model, **c** result of situation 2 in which entrainment is not considered, and **d** result of situation 3 in which both loess mass and gravel are in the sliding mass layer (layer 2).

5. Results and discussions

5.1. Comparison of the simulation results

The simulated final topography of these three situations is shown and compared with the measured data in Fig. 7. It shows that the result of the two-layer model agrees best with the measured result, while those of the other two situations significantly overestimated the propagation area. As can be seen in Fig. 7a, the loess deposit has an average thickness of 20 m, and the thickest part of the deposit is about 24 m, forming a bulb-shaped ridge between the loess deposit and the gravel deposit. The simulated results of the two-layer model (Fig. 7b) somehow reflect these features, and the bulb-shaped ridge is also captured well. However, in the other two situations, the landslide propagate too far because lacking resistance from the frontal gravel mass, so the final shape of the deposit becomes too flat.

On the other hand, it is also noted that the simulated lateral spreading of the gravel mass is overestimated by the two-layer model. This error is probably caused by the simplification made in this model with respect to the two-layer interaction. In fact, the frontal plowing is

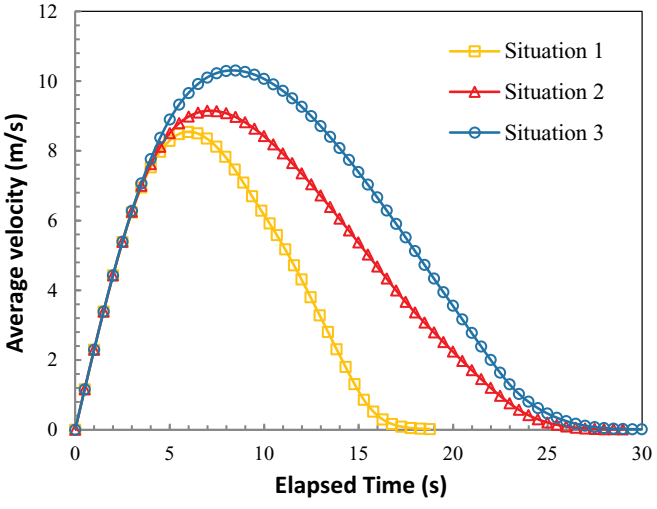

Fig. 8. Simulated average velocity of the sliding mass in the three situations.

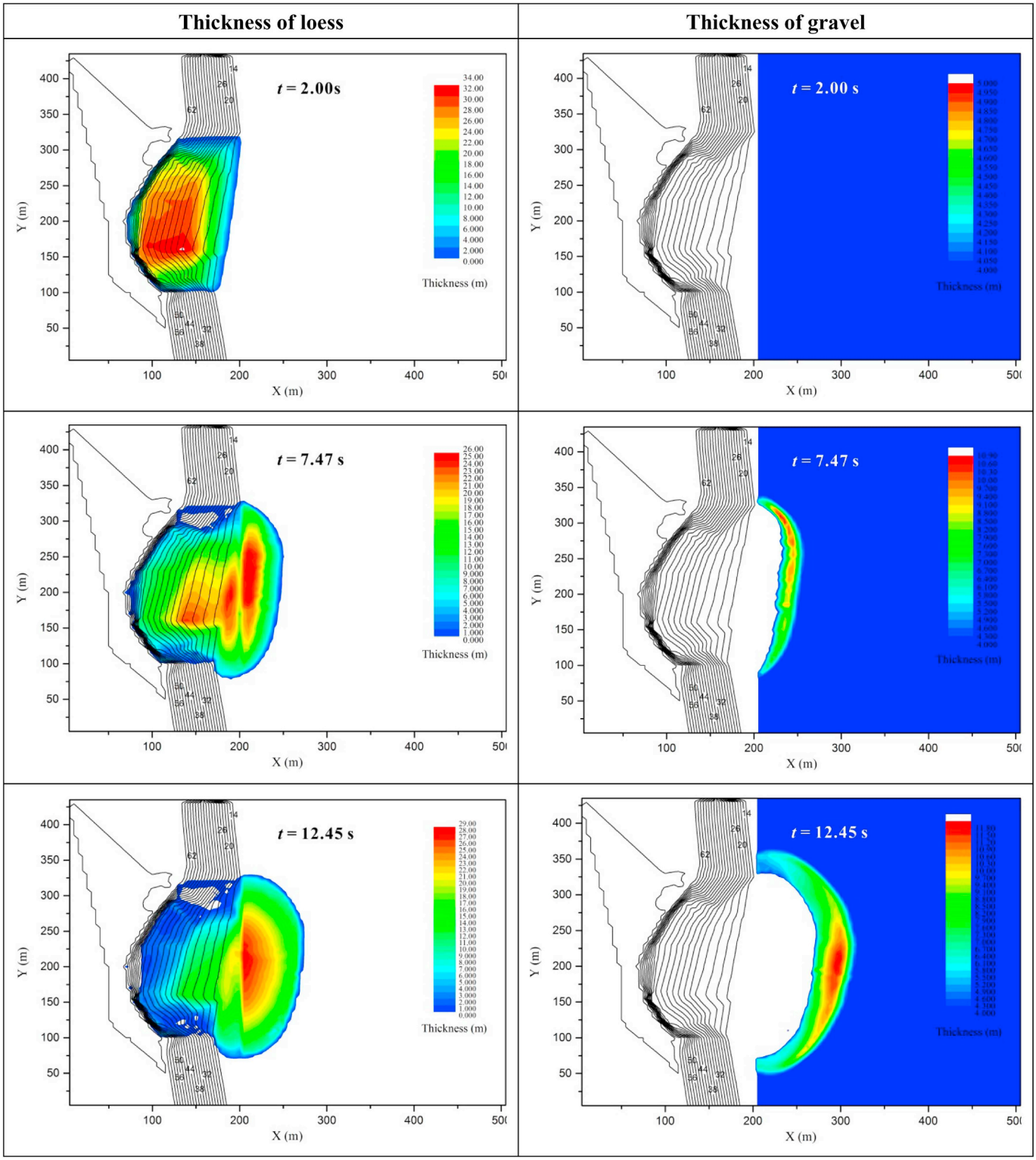

Fig. 9. Simulated thicknesses of the loess mass and gravel mass at different propagation stages by the two-layer model.

a very complex physical phenomenon involving thrusting, shearing and pushing of the frontal material (Crosta et al., 2017). It is almost impossible to account for such a phenomenon in a numerical model without taking simplifications and assumptions. Therefore, this phenomenon is simplified as shear and normal force acting on the interface in the present study. Nevertheless, in comparison with the other traditional one-layer models (Sassa et al., 2010; Ouyang et al., 2013; Shen et al., 2018a), the proposed two-layer model can basically reflect the frontal plowing phenomenon. Therefore, the present two-layer model is able to provide more reasonable and accurate simulation results for these kinds of flow-like landslides.

The simulated average velocity of the sliding mass is also outputted (Fig. 8). It shows that situation 1 has the shortest propagation time (about 18.76 s), while situation 3 has the longest one (about 29.48 s). This shows the same tendency with the propagation distance shown in Fig. 7: the longer the propagation time, the larger the propagation

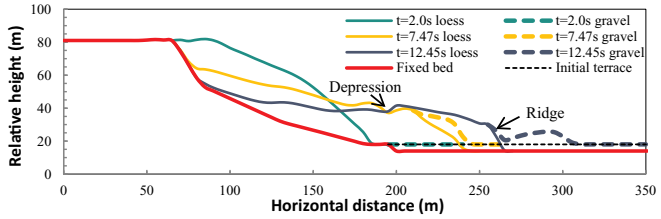

Fig. 10. Topography of the loess sliding mass and terrace plowing mass in profile I-I′ at three times.

distance. The turning point of situation 1 on the velocity-time curve is also the earliest (t = 5.50 s) and the lowest (v = 8.79 m/s). Frontal plowing impedes the movement of the sliding mass, so more energy is consumed by the two-layer interaction. The proposed model can correctly reflect this principle. In comparison, since situation 2 and situation 3 do not consider frontal plowing, more potential energy will transform into kinetic energy, resulting in a larger propagation area and distance.

5.2. Propagation characters of the Ximiaodian landslide

The simulated results at three times (t = 2.00 s, 7.47 s and 12.45 s) are selected to analysis the propagation characters of the Ximiaodian landslide, as shown in Fig. 9. These three times represent the early, middle and later stages of the propagation process, respectively. At t = 2.00 s, the landslide starts moving and propagating forward from the rear part to the front. The average thickness of the loess mass is about 25–30 m. The movement mainly occurs within the sliding mass, and the gravel layer is undisturbed at this time. At t = 7.47 s, about half of the loess mass propagates to the terrace and spreads forward in a bulb shape. The average thickness of the loess mass decreases from about 30 m to about 20 m and the thickest part of it reaches the terrace, forming a ridge at the front. At the same time, the frontal part of the loess mass plows into the gravel layer and pushes the gravel mass forward. Part of the gravel mass accumulates on the loess ridge due to inertia, forming a curved gravel belt with an average thickness of about 9 m on the terrace. At t = 12.45 s, most of the loess mass deposits on the terrace, and the height of the ridge reaches about 29 m. The loess mass keeps moving forward and laterally, but its velocity decreases quickly due to the frontal plowing resistance. The gravel mass quickly propagates forward like a water wave under the effect of the gravity and plowing force, and the thickest part of the gravel mass (about 12 m) is in the middle of the gravel belt. According to the above analysis, the frontal plowing process of this landslide can be divided into three stages: 1) The loess landslide plows into the gravel layer and starts to push the gravel mass forward. 2) The loess mass decelerates quickly under the frontal plowing resistance caused by the gravel mass, forming a ridge in its frontal part. At the same time, the gravel mass accumulates on this ridge since its velocity is lower than that of the sliding mass. 3) The gravel mass propagates quickly forward in a wave-like motion under the impacts of gravity and plowing force.

Fig. 10 shows the thicknesses of the loess mass and gravel mass in profile I-I′ (Fig. 5) at the three times. Before frontal plowing occurs (t = 2.00 s), the shape of the loess mass is relatively smooth. In the plowing process (t = 7.47 s and 12.45 s), the velocity of the frontal part of the loess mass decreases and forms a ridge under the resistance of the gravel, and the shape of the loess mass in the middle part becomes fluctuant under the impact of the frontal resistance, forming a valley in the rear part. The frontal gravel accumulates at the ridge at 7.47 s, and departs from the ridge at 12.45 s.

The velocity of the loess mass and gravel mass at t = 7.47 s and 12.45 s in the profile I-I′ is shown in Fig. 11. It shows that frontal plowing has significant influence on the velocity of both the loess mass and gravel mass. The velocity of the loess mass fluctuates and decelerates quickly due to the plowing resistance, which may contribute to the formation of the frontal ridge. The velocity of the gravel mass is about the same of the loess mass at 7.47 s (corresponding to the second stage of the plowing process), while its velocity is larger than that of the loess mass at 12.45 s (corresponding to the third stage of the plowing process). It indicates that the energy is transferred by the loess mass to the gravel mass through this interactive process.

6. Conclusion

In this paper, a two-layer model is proposed to simulate the frontal plowing phenomenon in flow-like landslides. The model is deduced according to the momentum and mass conservations of the sliding mass and erodible mass, and is solved by the finite difference method. A real flow-like landslide in the Chinese loess plateau is analyzed by the proposed model, and the simulation results are compared with the traditional one-layer models. The following conclusions are obtained.

(1) The frontal plowing process in flow-like landslides can be divided into three stages: 1) The sliding mass plows into the frontal erodible mass and pushes it forward. 2) The frontal sliding mass decelerates quickly and forms a ridge in the interactive area due to the plowing

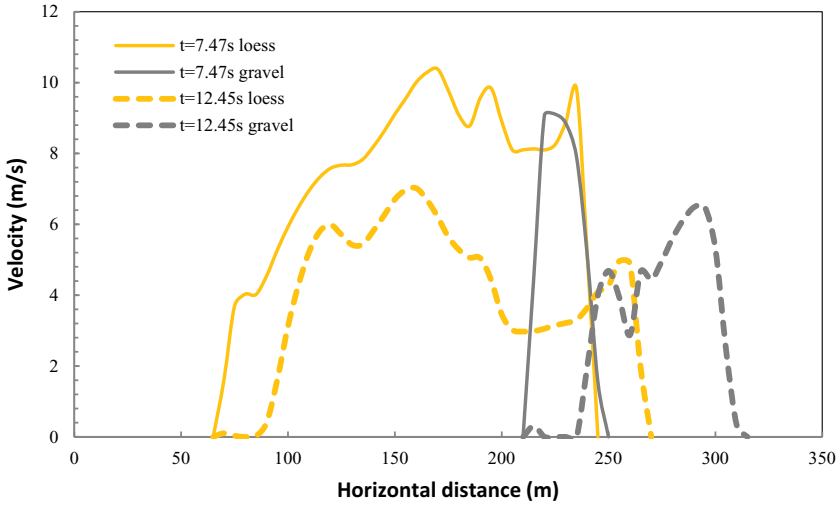

Fig. 11. Velocity of the loess sliding mass and the terrace plowing mass in profile I-I′ at t = 7.47 s and 12.45 s.

resistance, and the erodible mass accumulates on the ridge since it moves slower than the sliding mass. 3) The erodible mass accelerates under the influence of the gravity and plowing force, and moves forward quickly in a flow-like way.

(2) The frontal plowing phenomenon has significant influence on the propagation of flow-like landslides. Without considering its effect, the propagation velocity, distance and duration of a flow-like landslide are likely to be overestimated, while the thickness of the final deposit tends to be underestimated. In comparison with the traditional one-layer models, the proposed two-layer model can properly reflect the frontal plowing phenomenon in flow-like landslides, and can provide more reliable and accurate simulation results.

Acknowledgement

Authors acknowledge the fund received from the National Key R&D Program of China (2017YFC1501302), the China Scholarship Council (CSC) – University of Bologna Joint Scholarship (File No. 201806560011), and the National Natural Science Foundation of China (No. 41877242)which supported this study.

Appendix A. Derivation of the momentum equations

The deducing procedures of the momentum equations in the x direction are presented here, and those in the y direction are similar. The sizes of the soil columns are dx and dy in the x and y directions, respectively.

For layer 1, lateral pressure P_{x1} can be written as

$$P_{x1} = \frac{k_1 \rho_1 g h_1^2 dy}{2} \tag{A1}$$

Assuming k_1 is constant. Substituting Eq. (A1) into the first term (pressure term) on the right side of Eq. (2) gives the following expression

$$\frac{-dP_{x1}}{m_1} = \frac{-1}{\rho_1 h_1 dx dy}\frac{\partial P_{x1}}{\partial x}dx = -k_1 g\frac{\partial h_1}{\partial x} \tag{A2}$$

Similarly, the pressure term of layer 1 in the y direction can be written as

$$\frac{-dP_{y1}}{m_1} = -k_1 g\frac{\partial h_1}{\partial y} \tag{A3}$$

Normal force of layer 1 can be obtained according to force equilibrium condition in the normal direction of the sliding surface. The unit normal vector of the sliding surface of layer 1 is given by

$$\boldsymbol{n}_1 = \frac{(\tan\alpha_1 \mathbf{i} + \tan\beta_1 \mathbf{j} + \mathbf{k})}{\sqrt{G_1}} \tag{A4}$$

where **i**, **j** and **k** are the unit vectors in the x, y and z directions, respectively. The equilibrium condition on the sliding surface is given by

$$N_{x1} = ((\mathrm{d}P_{x1}\mathbf{i} + \mathrm{d}P_{y1}\mathbf{j} + W_1\mathbf{k})\bullet\mathbf{n}_1)\mathbf{n}_1\bullet\mathbf{i} \tag{A5}$$

Therefore, the second term (normal force term) on the right side of layer 1 can be written as

$$\frac{N_{x1}}{m_1} = \frac{(\mathrm{d}P_{x1}\tan\alpha_1 + \mathrm{d}P_{y1}\tan\beta_1 + m_1 g)}{m_1}\frac{\tan\alpha_1}{G_1} \tag{A6}$$

Substituting Eqs. (A2) and (A3) into the above equation gives the following expression

$$\frac{N_{x1}}{m_1} = \left(k_1 g\frac{\partial h_1}{\partial x}\tan\alpha_1 + k_1 g\frac{\partial h_1}{\partial y}\tan\beta_1 + g\right)\frac{\tan\alpha_1}{G_1} \tag{A7}$$

The sliding surface of layer 1 is the top surface of layer 2 (Fig. 1). Therefore, the direction of the resistance S_1 on the sliding surface of layer 1 should be opposite to the direction of the total relative velocity (which is assumed to be parallel to the sliding surface). The unit vector in the direction of resistance is given by

$$\boldsymbol{s}_1 = -\frac{((v_{x1} - v_{x2})\mathbf{i} + (v_{y1} - v_{y2})\mathbf{j} + v_{z1}\mathbf{k})}{\sqrt{(v_{x1} - v_{x2})^2 + (v_{y1} - v_{y2})^2 + {v_{z1}}^2}} \tag{A8}$$

The third term (resistance term) on the right side of layer 1 can be written as

$$\frac{S_{x1}}{m_1} = S_1\boldsymbol{s}_1\bullet\mathbf{i} = -\frac{v_{x1} - v_{x2}}{\sqrt{(v_{x1} - v_{x2})^2 + (v_{y1} - v_{y2})^2 + {v_{z1}}^2}}\frac{S_1}{m_1} \tag{A9}$$

Substituting Eqs. (A2), (A7) and (A9) into Eq. (2) gives the following equation

$$\frac{\partial v_{x1}}{\partial t} + v_{x1}\frac{\partial v_{x1}}{\partial x} + v_{y1}\frac{\partial v_{x1}}{\partial y} = -k_1 g\frac{\partial h_1}{\partial x} + \left(k_1 g\frac{\partial h_1}{\partial x}\tan\alpha_1 + k_1 g\frac{\partial h_1}{\partial y}\tan\beta_1 + g\right)\frac{\tan\alpha_1}{G_1} - \frac{v_{x1} - v_{x2}}{\sqrt{(v_{x1} - v_{x2})^2 + (v_{y1} - v_{y2})^2 + {v_{z1}}^2}}\frac{S_1}{m_1} \tag{A10}$$

Combining Eqs. (A9) and (2) produces the momentum equation of layer 1 in the x direction (Eq.(4)), and that in the y direction (Eq. (5)) can be obtained by applying similar procedures.

For layer 2, pressure P_{x2} can be written as

$$p_{x2} = k_1 \rho_1 g h_1 h_2 dy + \frac{k_2 \rho_2 g h_2^2 dy}{2} \tag{A11}$$

Assuming both k_1 and k_2 are constant and substituting Eq. (A11) into the first term on the right side of Eq. (3) produce the following equation

$$\frac{-dP_{x2}}{m_2} = \frac{-1}{\rho_2 h_2 dxdy}\frac{\partial P_{x2}}{\partial x}dx = -k_1 g\frac{\rho_1}{\rho_2}\left(\frac{h_1}{h_2}\frac{\partial h_2}{\partial x} + \frac{\partial h_1}{\partial x}\right) - k_2 g\frac{\partial h_2}{\partial x} \tag{A12}$$

Similarly, the pressure term of layer 2 in the y direction can be written as

$$\frac{-dP_{y2}}{m_2} = -k_1 g\frac{\rho_1}{\rho_2}\left(\frac{h_1}{h_2}\frac{\partial h_2}{\partial y} + \frac{\partial h_1}{\partial y}\right) - k_2 g\frac{\partial h_2}{\partial y} \tag{A13}$$

The derivation procedures of the second term on the right side of Eq. (3) are similar to those of layer1, and its expression is given by

$$\frac{N_{x2}}{m_2} = \left(\left(k_1 g\frac{\rho_1}{\rho_2}\left(\frac{h_1}{h_2}\frac{\partial h_2}{\partial x} + \frac{\partial h_1}{\partial x}\right) + k_2 g\frac{\partial h_2}{\partial x}\right)\tan\alpha_1 + \left(k_1 g\frac{\rho_1}{\rho_2}\left(\frac{h_1}{h_2}\frac{\partial h_2}{\partial y} + \frac{\partial h_1}{\partial y}\right) + k_2 g\frac{\partial h_2}{\partial y}\right)\tan\beta_1 + g\right)\frac{\tan\alpha_2}{G_2} \tag{A14}$$

Due to the siding surface of layer 2 is static, the unit vector in the direction of the resistance S_2 is given by

$$\boldsymbol{s}_2 = -\frac{(v_{x2}\mathbf{i} + v_{y2}\mathbf{j} + v_{z2}\mathbf{k})}{\sqrt{{v_{x2}}^2 + {v_{y2}}^2 + {v_{z2}}^2}} \tag{A15}$$

Therefore, the third term on the right side of Eq. (3) can be rewritten as

$$\frac{S_{x2}}{m_2} = S_2\boldsymbol{s}_2\bullet\mathbf{i} = -\frac{v_{x2}}{\sqrt{{v_{x2}}^2 + {v_{y2}}^2 + {v_{z2}}^2}}\frac{S_2}{m_2} \tag{A16}$$

Substituting Eqs. (A7) and (A9) into the last term on the right side of Eq. (3) produce the following expression

$$\frac{m_1}{m_2}\left(\frac{N_{x1}}{m_1} + \frac{S_{x1}}{m_1}\right) = \frac{\rho_1}{\rho_2}\frac{1}{h_2}\left(\left(k_1 g\frac{\partial h_1}{\partial x}h_1\tan\alpha_1 + k_1 g h_1\frac{\partial h_1}{\partial y}\tan\beta_1 + g h_1\right)\frac{\tan\alpha_1}{G_1} - \frac{v_{x1} - v_{x2}}{\sqrt{(v_{x1} - v_{x2})^2 + (v_{y1} - v_{y2})^2 + {v_{z1}}^2}}\frac{S_1 h_1}{m_1}\right) \tag{A17}$$

Finally, the momentum equation of layer 2 in the x direction (Eq. (12)) can be obtained by substituting Eqs. (A13), (A14), (A16) and (A17) into Eq. (3) and then combining it with Eq. (1). The momentum equation of layer 2 in the y direction (Eq. (13)) can be deduced by adopting similar procedures.

References

Berti, M., Simoni, A., 2014. DFLOWZ: a free program to evaluate the area potentially inundated by a debris flow. Comput. Geosci. 67, 14–23.

Cascini, L., Cuomo, S., Pastor, M., 2013. Inception of debris avalanches: remarks on geomechanical modelling. Landslides 10, 701–711.

Christen, M., Kowalski, J., Bartelt, P., 2010. RAMMS: Numerical simulation of dense snow avalanches in three-dimensional terrain. Cold Reg. Sci. Technol. 63, 1–14.

Crosta, G.B., Imposimato, S., Roddeman, D.G., 2003. Numerical modelling of large landslides stability and runout. Nat. Hazards Earth Syst. Sci. 3, 523–538.

Crosta, G.B., Imposimato, S., Roddeman, D., 2009. Numerical modelling of entrainment/deposition in rock and debris-avalanches. Eng. Geol. 109, 135–145.

Crosta, G.B., De Blasio, F.V., De Caro, M., Volpi, G., Imposimato, S., Roddeman, D., 2017. Modes of propagation and deposition of granular flows onto an erodible substrate: experimental, analytical, and numerical study. Landslides 14, 47–68.

Cruden, D.M., Hungr, O., 1986. The debris of the Frank Slide and theories of rockslide-avalanche mobility. Can. J. Earth Sci. 23, 425–432.

Cuomo, S., Pastor, M., Cascini, L., Castorino, G.C., 2014. Interplay of rheology and entrainment in debris avalanches: a numerical study. Can. Geotech. J. 51, 1318–1330.

Cuomo, S., Pastor, M., Capobianco, V., Cascini, L., 2016. Modelling the space–time evolution of bed entrainment for flow-like landslides. Eng. Geol. 212, 10–20.

de Haas, T., van Woerkom, T., 2016. Bed scour by debris flows: experimental investigation of effects of debris-flow composition. Earth Surf. Process. Landf. 41, 1951–1966.

Evans, S.G., Roberts, N.J., Ischuk, A., Delaney, K.B., Morozova, G.S., Tutubalina, O., 2009. Landslides triggered by the 1949 Khait earthquake, Tajikistan, and associated loss of life. Eng. Geol. 109, 195–212.

Haque, U., Blum, P., da Silva, P.F., et al., 2016. Fatal landslides in Europe. Landslides 13, 1545–1554.

Hou, X.K., Vanapalli, S.K., Li, T.L., 2018. Water infiltration characteristics in loess associated with irrigation activities and its influence on the slope stability in Heifangtai, loess highland, China. Eng. Geol. 234, 27–37.

Huang, R., 2009. Some catastrophic landslides since the twentieth century in the southwest of China. Landslides 6, 69–81.

Hungr, O., Evans, S.G., 2004. Entrainment of debris in rock avalanches: an analysis of a long run-out mechanism. GSA Bull. 116, 1240–1252.

Hungr, O., McDougall, S., 2009. Two numerical models for landslide dynamic analysis. Comput. Geosci. 35, 978–992.

Hungr, O., Leroueil, S., Picarelli, L., 2014. The Varnes classification of landslides types, an update. Landslides 11, 167–194.

Iverson, R.M., Ouyang, C., 2015. Entrainment of bed material by earth-surface mass flows: review and reformulation of depth-integrated theory. Rev. Geophys. 53, 27–58.

Iverson, R.M., Reid, M.E., Logan, M., LaHusen, R.G., Godt, J.W., Griswold, J.P., 2011. Positive feedback and momentum growth during debris-flow entrainment of wet bed sediment. Nat. Geosci. 4, 116–121.

Iverson, R.M., George, D.L., Allstadt, K., et al., 2015. Landslide mobility and hazards: implications of the 2014 Oso disaster. Earth Planet. Sci. Lett. 412, 197–208.

Legros, F., 2002. The mobility of long-runout landslides. Eng. Geol. 63, 301–331.

Leng, Y.Q., Peng, J.B., Wang, Q.Y., Meng, Z.J., Huang, W.L., 2018. A fluidized landslide occurred in the Loess Plateau: a study on loess landslide in south Jingyang tableland. Eng. Geol. 236, 129–136.

Liu, K.F., Li, H.C., Hsu, Y.C., 2009. Debris flow hazard assessment with numerical simulation. Nat. Hazards 49, 137–161.

Mangeney, A., 2011. Geomorphology: landslide boost from entrainment. Nat. Geosci. 4, 77–78.

McDougall, S., 2006. A New Continuum Dynamic Model for the Analysis of Extremely Rapid Landslide Motion across Complex 3D Terrain. PhD thesis. University of British Columbia, Vancouver, B.C., Canada.

Mcdougall, S., Hungr, O., 2005. Dynamic modelling of entrainment in rapid landslides. Can. Geotech. J. 42, 1437–1448.

Mergili, M., Fischer, J.T., Krenn, J., Pudasaini, S.P., 2017. r.avaflow v1, an advanced open-source computational framework for the propagation and interaction of two-phase mass flows. Geosci. Model Dev. 10, 553–569.

Mergili, M., Emmer, A., Juřicová, A., Cochachin, A., Fischer, J.T., Huggel, C., Pudasaini, S.P., 2018. How well can we simulate complex hydro-geomorphic process chains? The 2012 multi-lake outburst flood in the Santa Cruz Valley (Cordillera Blanca, Perú). Earth Surf. Process. Landf. 43, 1373–1389.

Okada, Y., Ochiai, H., Kurokawa, U., Ogawa, Y., Asano, S., 2008. A channelised long run-out debris slide triggered by the Noto Hanto earthquake in 2007, Japan. Landslides 5, 235–239.

Ouyang, C.J., He, S.M., Xu, Q., Luo, Y., Zhang, W.C., 2013. A MacCormack-TVD finite difference method to simulate the mass flow in mountainous terrain with variable computational domain. Comput. Geosci. 52, 1–10.

Pastor, M., Blanc, T., Haddad, B., et al., 2014. Application of a SPH depth-integrated model to landslide run-out analysis. Landslides 11, 793–812.

Peng, J.B., Fan, Z.J., Wu, D., Zhuang, J., Dai, F., Chen, W., Zhao, C., 2015. Heavy rainfall triggered loess-mudstone landslide and subsequent debris flow in Tianshui, China. Eng. Geol. 186, 79–90.

Peng, D.L., Xu, Q., Liu, F.Z., et al., 2018. Distribution and failure modes of the landslides in Heitai terrace, China. Eng. Geol. 236, 97–110.

Pirulli, M., Scavia, C., Tararbra, M., 2015. On the use of Numerical Models for Flow-like Landslide simulation. In: Lollino, G. (Ed.), Engineering Geology for Society and Territory. vol. 2. Springer, Cham, pp. 1625–1628.

Pudasaini, S.P., 2012. A general two-phase debris flow model. J. Geophys. Res. Earth Surf. 117, F03010.

Pudasaini, S.P., 2014. Dynamics of submarine debris flow and tsunami. Acta Mech. 225, 2423–2434.

Pudasaini, S.P., Fischer, J.T., 2016. A Mechanical Erosion Model for Two-Phase Mass Flows. arXiv:1610.01806.

Pudasaini, S.P., Hutter, K., 2007. Avalanche Dynamics: Dynamics of Rapid Flows of Dense Granular Avalanches. Springer, Berlin, pp. 329–342.
Pudasaini, S.P., Miller, S.A., 2013. The hypermobility of huge landslides and avalanches. Eng. Geol. 157, 124–132.
Sassa, K., Nagai, O., Solidum, R., Yamazaki, Y., Ohta, H., 2010. An integrated model simulating the initiation and motion of earthquake and rain induced rapid landslides and its application to the 2006 Leyte landslide. Landslides 7, 219–236.
Sassa, K., Dang, K., Yanagisawa, H., He, B., 2016. A new landslide-induced tsunami simulation model and its application to the 1792 Unzen-mayuyama landslide-and-tsunami disaster. Landslides 13, 1–15.
Scaringi, G., Fan, X.M., Xu, Q., et al., 2018. Some considerations on the use of numerical methods to simulate past landslides and possible new failures: the case of the recent Xinmo landslide (Sichuan, China). Landslides 15, 1359–1375.
Shen, W., Zhai, Z.H., Li, T.L., Zhao, Q.L., Wang, F.W., 2016. Simulation of propagation process for the Dabaozi rapid long run-out loess landslide in the south bank of the Jing River, Shaanxi Province. J. Eng. Geol. 24, 1309–1317 (in Chinese with English abstract).
Shen, W., Li, T.L., Li, P., Guo, J., 2018a. A modified finite difference model for the modeling of flowslides. Landslides 15, 1577–1593.
Shen, W., Li, T.L., Li, P., Shen, Y.Q., Lei, Y.L., Guo, J., 2018b. The influence of the bed entrainment-induced rheology and topography changes on the propagation of flow-like landslides: a numerical investigation. Bull. Eng. Geol. Environ. https://doi.org/10.1007/s10064-018-01447-1.
Wang, G.H., Sassa, K., 2003. Pore-pressure generation and movement of rainfall-induced landslides, effects of grain size and fine-particle content. Eng. Geol. 69, 109–125.
Wang, G.H., Sassa, K., Fukuoka, H., 2003. Downslope volume enlargement of a debris slide-debris flow in the 1999 Hiroshima, Japan, rainstorm. Eng. Geol. 69, 309–330.
Wang, G.H., Zhang, D.X., Furuya, G., Yang, J., 2014. Pore-pressure generation and fluidization in a loess landslide triggered by the 1920 Haiyuan earthquake, China: a case study. Eng. Geol. 174, 36–45.
Xing, A.G., Wang, G.H., Yin, Y.P., et al., 2014. Dynamic analysis and field investigation of a fluidized landslide in Guanling, Guizhou, China. Eng. Geol. 181 (1–14).
Xu, L., Dai, F.C., Tham, L.G., et al., 2011. Field testing of irrigation effects on the stability of a cliff edge in loess, north-West China. Eng. Geol. 120, 10–17.
Zhang, D.X., Wang, G.H., 2007. Study of the 1920 Haiyuan earthquake-induced landslides in loess (China). Eng. Geol. 94, 76–88.
Zhang, D.X., Wang, G.H., Luo, C.Y., Chen, J., Zhou, Y.X., 2009. A rapid loess flowslide triggered by irrigation in China. Landslides 6, 55–60.

3. PAPER 2

The influence of slope gradient and gully channel on the run-out behavior of rockslide-debris flow: an analysis on the Verghereto landslide in Italy

Wei Shen[1], Matteo Berti[1], Tonglu Li[2,3], Andrea Benini[4], Zhitian Qiao[1*]

*Correspondence author

1 Department of Biological, Geological and Environmental Sciences, University of Bologna, Italy, 40126

2 Department of Geological Engineering, Chang'an University, Xi'an, China, 710064

3 Water Cycle and Geological Environment Observation and Research Station for the Chinese Loess Plateau,Ministry of Education, Gansu 745399, China

4 Servizio Tecnico Bacino Romagna Regione Emilia-Romagna

Paper submitted to “Landslides” for review and possible publication

Abstract:

Rockslide-debris flow is a hybrid type of mass movement occurring when a rockslide transforms into a debris flow. This type of mass movement may cause catastrophic damages because of its high speed and long run-out distance. To achieve a better understanding toward the run-out behavior of this type of landslide, a recent rockslide-debris flow occurred in Verghereto (Northern Apennines of Italy) is studied through field investigation and numerical simulation. The run-out process of this landslide is simulated by an improved depth-averaged model, paying special attention to analyzing the influence of slope gradient and gully channel. The results show that the depth-averaged model can correctly simulate the entrainment and deposition characteristic of this landslide by adopting different basal friction strengths for rockslide region and debris flow region. Entrainment occurs in both high and low slope gradient zones. However, entrainment can only be observed in the high slope gradient zones, while in the low gradient zones the post-failure topography shows accumulation and deposition. Numerical modelling also demonstrates that the presence of a gully channel is a key factor in determining landslide mobility and run-out distance. In comparison to a landslide with similar size and geological settings but without a gully channel, the run-out distance is much less and the landslide does not develop into a flow.

Keywords: Rockslide-debris flow, Numerical simulation, Solid-fluid transformation, Run-out analysis, Bed entrainment

1. Introduction

A rockslide may transform into a debris flow when it disintegrates and propagates along a confined channel, and this hybrid mass movement is named as rockslide-debris flow. The term “debris flow” indicates partially or fully saturated flow-like movement propagating in gully channel (Hungr et al. 2014) and is distinguished from “rock avalanche” which describes the flow-like movement of essentially dry debris on unconfined slope. A rockslide-debris flow is typically characterized by the presence of a gully channel on the run-out path and it is renowned for the solid-fluid transformation (SFT) occurring during the run-out process. The SFT contributes to the high mobility of these types of landslides. Several factors, such as the disintegration of rock mass (Bowman et al. 2012, Crosta et al. 2007, Davies and McSaveney 2009), entrainment (Aaron and McDougall 2019, Dufresne and Geertsema 2020, Hungr and Evans 2004), and excess pore pressure (Collins and Reid 2019, Sassa and Wang 2005, Wang et al. 2002), have been identified as the possible reasons for the SFT, but the mechanism is still largely elusive because of the complexity of the geo-materials.

Numerous rockslide-debris flows have been reported around the world. Some typical events, such as the Ponti Peak landslide in India (Shugar et al. 2021), the Dujiangyan landslide (Yin et al. 2016) and Jiweishan landslide in China (Xu et al. 2010), and the Mount Meager landslide in Canada (Guthrie et al. 2012), have caused serious economic losses or death tolls to the local communities. Rockslide-debris flows tend to have catastrophic consequences because they are commonly characterized by extremely high speed (a few to tens of meters per second) and long run-out distance (several to tens of kilometers). These catastrophic events remind us the significance of making accurate risk assessment for the potential rockslide-debris flows, and this goal can be achieved only if we have a correct understanding of and can make accurate predictions for the run-out process of these landslides.

Numerical simulation is an efficient tool for the run-out analysis and prediction of rockslide-debris flow, and a variety of physically-based models have been adopted to simulate the run-out process of

real landslide events. The models generally in use belong to three categories: 1) depth-averaged models based on the finite difference method (FDM) (O'Brien et al. 1993, Ouyang et al. 2013, Sassa et al. 2010, Shen et al. 2019, Shen et al. 2018), finite volume method (FVM) (Christen et al. 2010, Mangeney et al. 2003, Xia and Liang 2018), or smoothed particle hydrodynamics (SPH) (Hungr and McDougall 2009, Pastor et al. 2009); 2) discrete models originated from the discrete element method (DEM) (Gao et al. 2021, Wu et al. 2018); and 3) three-dimensional models formulated according to the SPH (Dai et al. 2017, Ghaʹtanellis et al. 2021), particle finite element method (PFEM) (Zhang et al. 2015, Zhang et al. 2020) or material point method (MPM) (Li et al. 2021, Soga et al. 2016, Xu et al. 2018). Among these models, the depth-averaged models are probably the most sophisticated and frequently-used in the run-out analysis of real rockslide-debris flow events, mainly because they are more time efficient. Specifically, the depth-averaged model can easily consider entrainment (Cuomo et al. 2016, Iverson and Ouyang 2015, McDougall and Hungr 2005) which is an important phenomenon in rockslide-debris flow modeling. The main difficulty in modeling rockslide-debris flow is how to account for the SFT process. As mentioned above, the mechanism of SFT is still quite elusive, so nearly no existing models can reflect the real physical process of this phenomenon as far as we concerned. However, ignoring the influence of SFT may lead to a wrong prediction of landslide mobility. A simple approach has been adopted in some depth-averaged models to account for the influence of SFT by adopting different rheological models for rockslide and debris flow (Gao et al. 2017, McDougall et al. 2006), and this strategy performed well in improving the simulation results. Due to the above reasons, the depth-averaged models should be more suitable choices for the run-out analysis of the rockslide-debris flow in this study.

Although many studies have analyzed the run-out processes of real rockslide-debris flow events around the world (Gao, et al. 2017, Liang et al. 2020, McDougall, et al. 2006, Xing et al. 2014), few of them have investigated the influence of the geomorphological factors such as slope gradient and gully channel. Moreover, most of these studies did not provide in-depth analysis on the performance of the models according to field measurements of entrainment and deposition.

In this paper we investigate a rockslide-debris flow event recently occurred in the Northern Apennines of Italy (the Verghereto landslide). The landslide was surveyed soon after the failure and a detailed map of entrainment and deposition was obtained from drone surveys. These data allow validating an improved depth-average model capable of reproducing the complex behavior of the landslide. The model considers entrainment and the influence of SFT is taken into account by changing the basal frictional strength. The influences of slope gradient and the presence of a gully channel on the run-out behavior are discussed, and some insightful conclusions are obtained.

2. The Verghereto landslide

2.1 Geological settings

The Verghereto landslide is located in the Northern Apennines of Italy, approximately 40 km to the south of Cesena City. The area is characterized by steep slopes and deeply incised valleys carved by rivers, with altitudes ranging from 600 m to 900 m above the sea level (Fig. 1).

The bedrock consists of deep marine flysch deposits belonging to the Marnoso-Arenacea Formation. The Marnoso-Arenacea Formation is a turbidite succession representing the filling of the Miocene Apennine foredeep complex, which deposited between the Langhian and the Tortonian (Lucchi and Valmori 1980). It consists of alternating sandstones and marls layers in variable proportion (Fig. 2a). In the study area, the ratio between coarse and fine strata is about 1/3 and the average bed thickness varies from 0.5 m to 2 m. Both sandstones and marls are strong rocks characterized by high resistance to compression (the uniaxial compressive strength of intact rock specimens typically ranges from 40 MPa to 60 MPa) and high resistance to weathering. When the bedding planes are horizontal or dip into the slope, the high strength of the rock mass ensures the stability of the slopes and supports subvertical cliffs (Fig. 2b). Instead, large failures may occur when the strata dip out of the slope. In this case the rock mass can slide along one controlling bedding plane generating

127 massive rockslides.

128

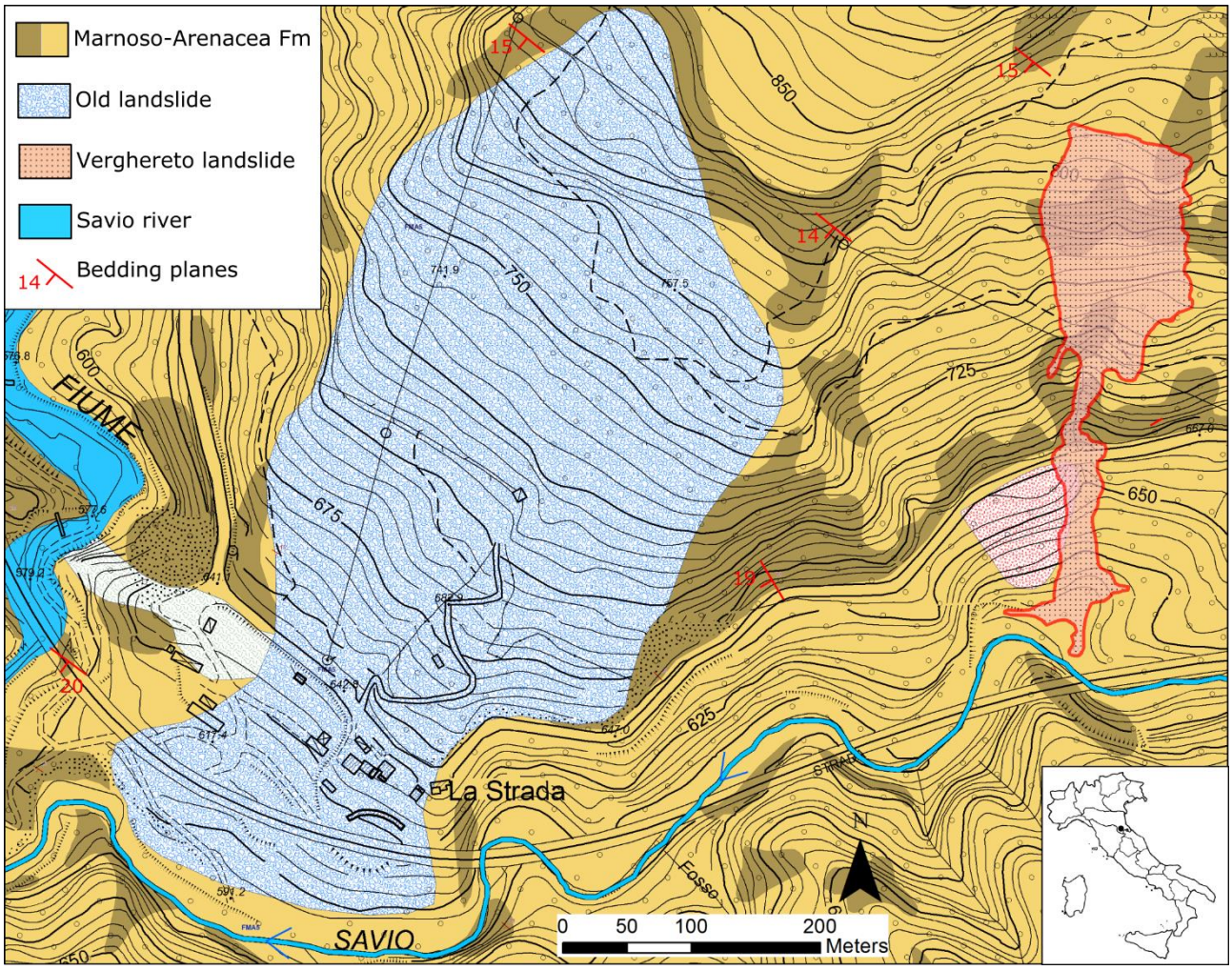

129

130 Fig. 1 Geological map of the study area and the locations of the Verghereto rockslide-debris flow
131 and a giant old rockslide-avalanche adjacent to this landslide

132

133 Rockslides are the predominant form of instability in the area and are very common on cataclinal
134 slopes where bedding dip is less than slope angle. These failures can occur on bed gradients less
135 than 10 °, which is approximately equal to half of the fully-softened angle of shearing resistance of
136 the marls (Berti et al. 1994, Berti et al. 1996). In most cases the failed mass moves as a nearly intact
137 block for a few tens of meters, retaining the original appearance and succession. Less commonly,
138 the failed mass collapses generating dangerous flow-like landslide. In the study area both cases are
139 present. The large landslide shown in the map of Fig. 1 is an old rockslide that did not turn into a

flow, as suggested by the rectangular shape of the deposit and by lack of a transportation channel. Instead, the Verghereto landslide (in red) mobilized into a flow that advanced down a gully to the foot of the slope.

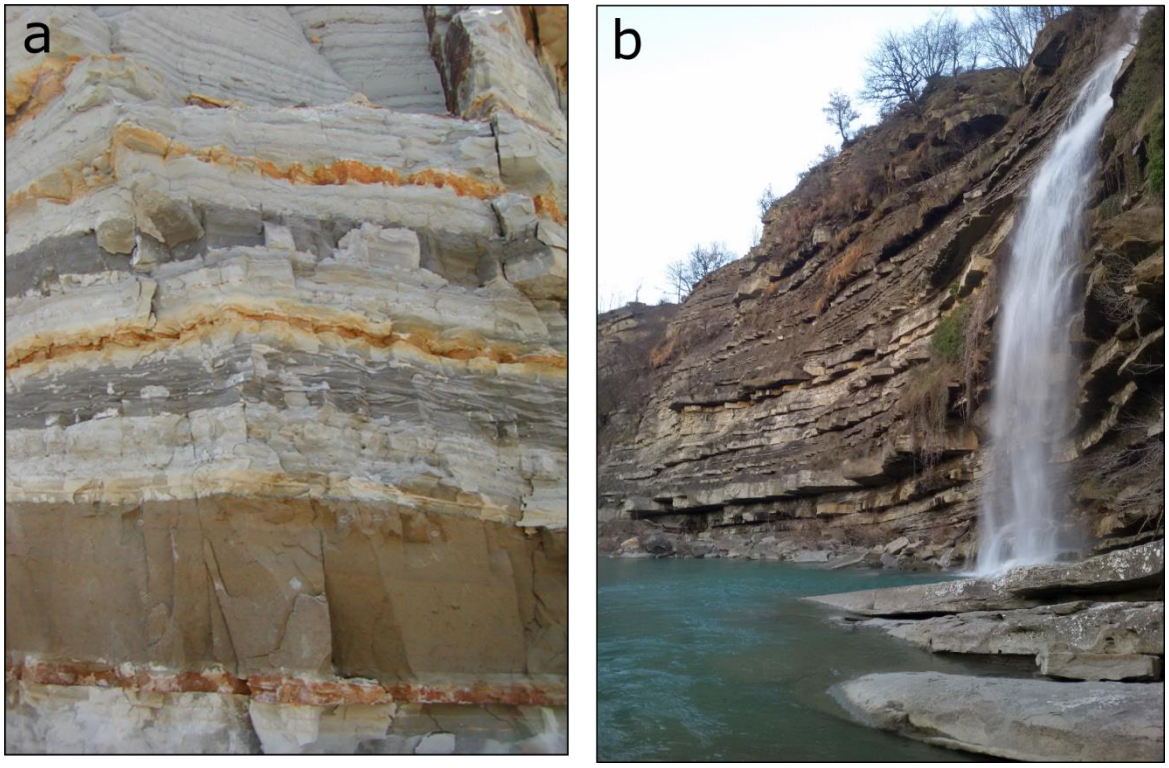

Fig. 2 Alternating sandstone and marls layers which consist of the sliding mass of the Verghereto rockslide-debris flow

2.2 The landslide

The Verghereto landslide occurred around 5:00 a.m. in the morning of May 13, 2019. A rock mass with a volume of nearly 40,000 m^3 detached from the upper part of the slope sliding along a gently dipping bedding plane. The toe of the failed mass came out the slope, disintegrated into rock debris, and transformed into a debris flow that traveled downslope for about 300 m reaching the main river (Fig. 3a). The landslide destroyed a local road, 2.4 hectares of forest, and threatened the pylons of the highway that passes on the valley floor.

The map in Fig. 4 shows the three geomorphological zones that were identified in the field soon after the event. Zone A is the source area of the landslide. It consisted of a rockslide that moved essentially as a rigid block. Apparently, the slide did not acquire enough momentum to carry all the rock mass beyond the foot of the slope, and about one third of the mass stopped at 30-40 m from the detachment scarp. Sliding took place at a depth of about 10 m below the ground surface, at the top of a marlstone layer dipping 15 ° to southwest (Fig. 3b). The rock exposed on the sliding surface was fresh and stiff and we did not notice any appreciable difference with the other marls layers outcropping on the trench walls. The lack of previous landslides indicated that the slide was a first-time failure.

The front part of the rockslide collapsed and dropped about 28,000 m^3 of fragmented rock to the slope below (zone B in Fig. 4; Fig. 3d). Just below the source area, the slope is very steep (over 35 ° degrees). Here the landslide stripped the vegetation and the soil cover over an area of about 4500 m^2, leaving evident scratches on the rock surface. Further downhill the slope angle decreases to less than 30 ° allowing some crushed rocks and coarse debris to accumulate loosely in the lower part of the zone.

Part of the landslide material then entered a small, ephemeral gully incised in colluvium and mobilized into a debris flow (zone C in Fig. 4). Along the steep reach of the gully the debris flow showed significant bulking by scouring and erosion and created a channel 15 m wide and 2-3 m deep (Fig. 3c). As the gradient decreased to 20 °-25 °, the flow started to deposit within the channel and came to rest at the foot of the slope. In the accumulation lobe the debris was on average 1-3 m thick with an overall volume of approximately 15,000-20,000 m^3. The presence of scouring, lateral levees, and trees damaged by the impact with debris indicate that the flow was extremely rapid.

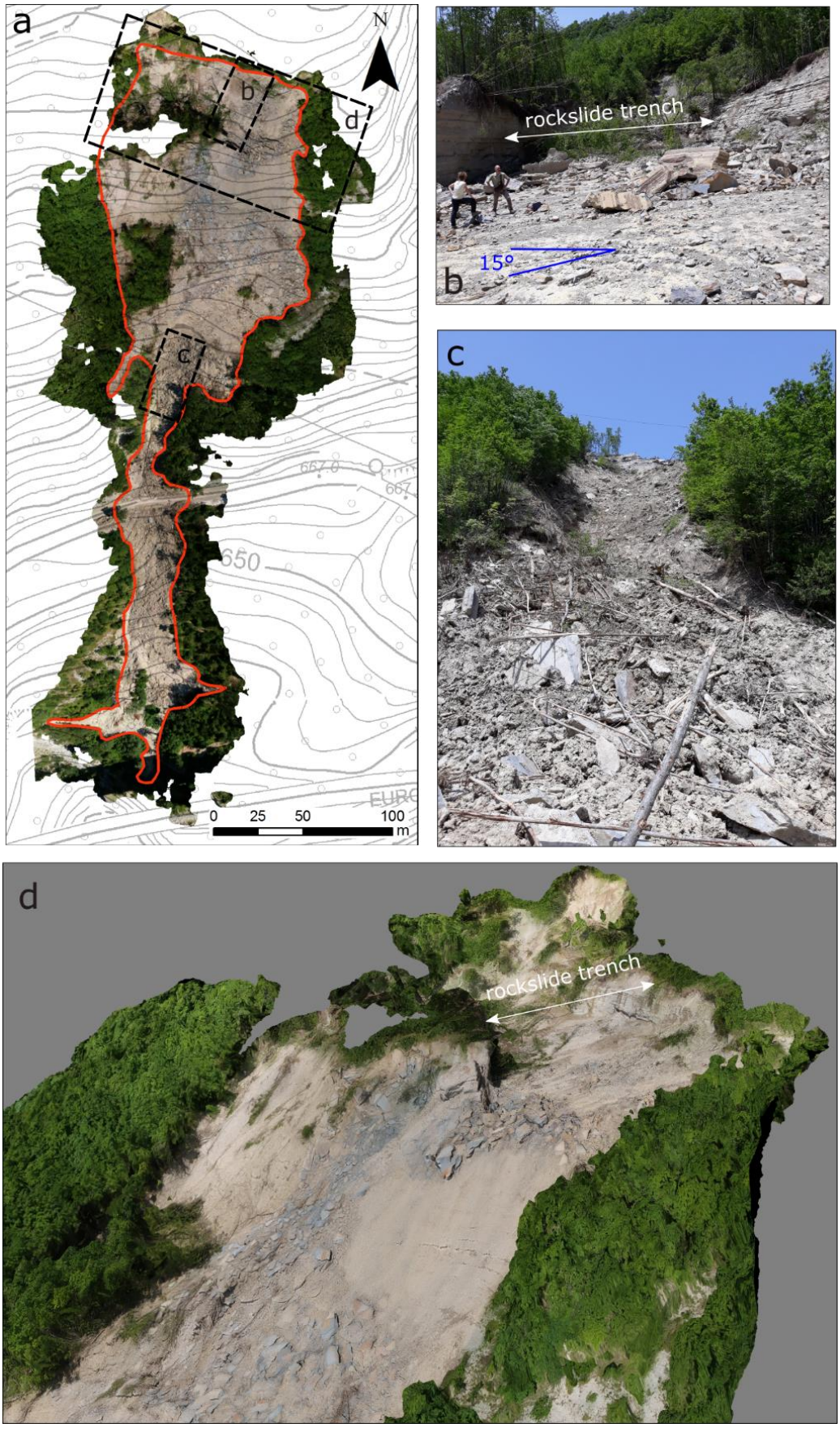
a
N
b
d
c
667.0
667
650
0 25 50 100
m
rockslide trench
15°
b
c
d
rockslide trench

184

Fig. 3 a) Top view of the rockslide, b) the trench exposed in the source zone after the occurrence of the rockslide, c) debris deposit in the channel, and d) the steep slope below the source zone

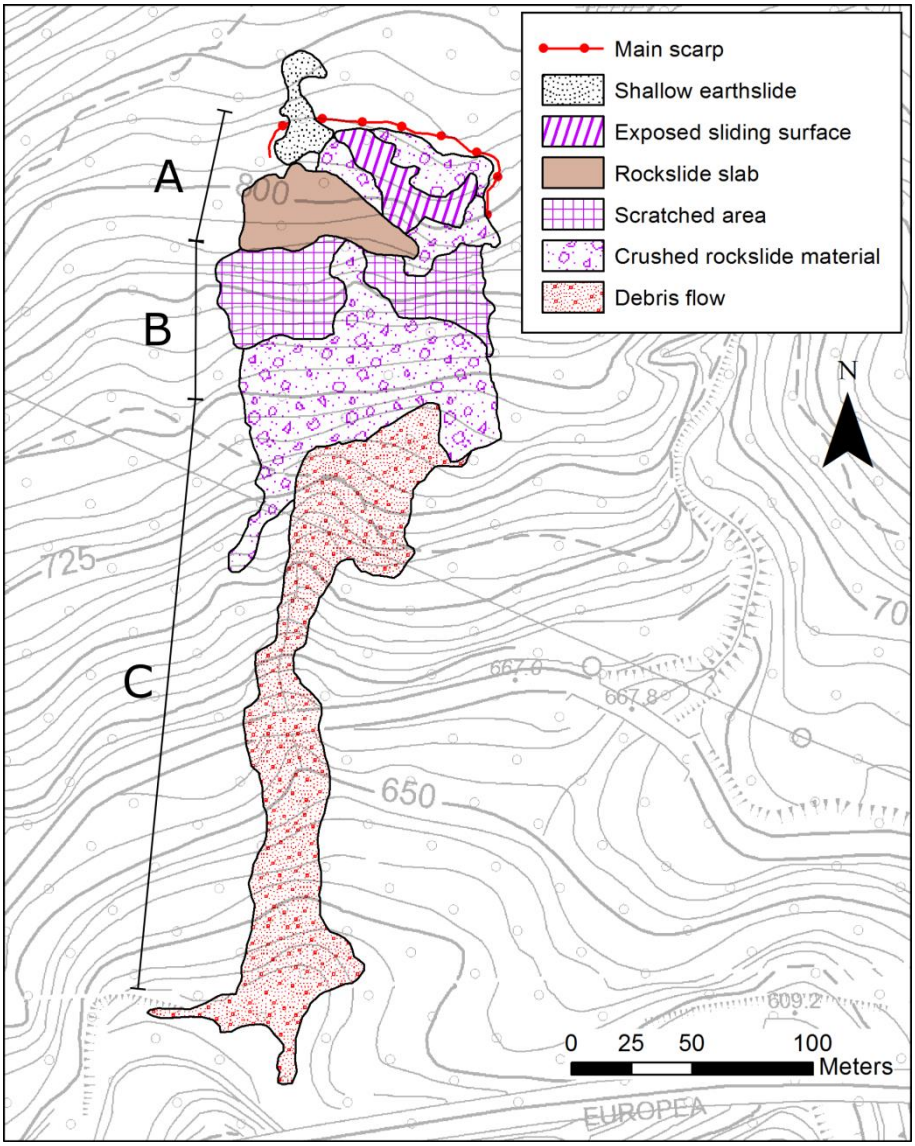

Fig. 4 Characteristics of the deposit in different regions of the landslide influenced zone and the three geomorphological zones identified after the event. A is the source area of the landslide, B is the transformation zone, and C is the debris flow zone

3. Methodology

3.1 Numerical model

An improved finite difference model (Shen, et al. 2018) is adopted to simulate the run-out process of the Verghereto landslide. This model is built in a global Cartesian coordinate, with the positive direction of z axis parallel to the opposite direction of gravity. Similar to the typical depth-averaged models, this model consists of one mass balance equation and two momentum balance equations, which are given by:

$$\frac{\partial h}{\partial t}+\frac{\partial Q_x}{\partial x}+\frac{\partial Q_y}{\partial y}=-\frac{\partial Z}{\partial t}=\frac{\tau_b-\tau_e}{\rho_e\sqrt{v_x{}^2+v_y{}^2}} \tag{1}$$

$$\frac{\partial Q_x}{\partial t}+\frac{\partial Q_x{}^2/h}{\partial x}+\frac{\partial Q_xQ_y/h}{\partial y}=-\frac{\partial k_x gh^2/2}{\partial x}+\frac{(Ag+B)h\tan\alpha}{\tan^2\alpha+\tan^2\beta+1}-\frac{\tau_b A_b h v_x}{m\sqrt{v_x{}^2+v_y{}^2+v_z{}^2}} \tag{2}$$

$$\frac{\partial Q_y}{\partial t}+\frac{\partial Q_xQ_y/h}{\partial x}+\frac{\partial Q_y{}^2/h}{\partial y}=-\frac{\partial k_y gh^2/2}{\partial y}+\frac{(Ag+B)h\tan\beta}{\tan^2\alpha+\tan^2\beta+1}-\frac{\tau_b A_b h v_y}{m\sqrt{v_x{}^2+v_y{}^2+v_z{}^2}} \tag{3}$$

where: h is flow depth; $Q_x = v_x h$ and $Q_y = v_y h$ are mass fluxes in x and y directions; v_x, v_y and v_z are depth-averaged velocities in x, y and z directions; k_x and k_y are lateral pressure coefficients in x and y directions determined according to soil state (Ouyang et al. 2015); g is gravitational acceleration; A and B are terms related to static and centrifugal/centripetal normal forces on bed; α and β are dip angles in x and y directions; τ_b is the basal shear stress of flow; τ_e is the shear stress in erodible mass; ρ_e is the bulk density of entrained mass; A_b is the bottom area of a control volume; m is the mass of flow in the control volume. The expressions of A, B, A_b, τ_b and τ_e are given by:

$$A=1+\frac{\partial k_x h^2/2}{\partial x}\tan\alpha+\frac{\partial k_y h^2/2}{\partial y}\tan\beta \tag{4}$$

$$B=\frac{C_x}{\cos\alpha}\left(\frac{v_x}{\cos\alpha}\right)^2+\frac{C_y}{\cos\beta}\left(\frac{v_y}{\cos\beta}\right)^2 \tag{5}$$

$$A_b=\Delta x\Delta y\sqrt{\tan^2\alpha+\tan^2\beta+1} \tag{6}$$

$$\tau_b=\sigma(1-r_{ub})\tan\varphi_b'+c_b' \tag{7}$$

$$\tau_e=\sigma(1-r_{ue})\tan\varphi_e'+c_e' \tag{8}$$

in which: C_x and C_y are bed curvatures in x and y directions; Δx, Δy are the sizes of a control volume in x and y directions; σ is the normal stress on bed; r_{ub} and r_{ue} are the pore pressure coefficients (the ratio of the pore pressure to the total normal stress) in flow bottom and erodible mass; φ' and c' are effective frictional angle and cohesion. The subscripts b and e refer to flow bottom and erodible mass, respectively.

A finite difference scheme is utilized to solve the above governing equations, and the details of the numerical scheme could be found in Shen, et al. (2018).

3.2 Simulation setup

The pre-failure digital elevation model (DEM) of the landslide area was available by the Regional Technical Map with a 5 m resolution, while the post-failure DEM at 1 m resolution has been obtained through unmanned aerial vehicle (UAV) survey. Within the area we selected a region which covers the whole run-out zone of the landslide as the computational domain. The size of this domain is 522 m in x direction (N-S) and 291 m in y direction (E-W). Uniform computational grids 3 m long in both x and y directions are adopted in the present study, and the maximum time step is 0.02 s.

According to the landslide characteristic described in Section 2, we divided the computational domain into two regions (Fig. 5). The first region is the area above the gully head (x < 270 m), which include the source zone of the rockslide and the steep slope below (zones A and B in Fig. 3). The second region is the zone below the gully head, where the rockslide turned into a debris flow (zone C in Fig. 3). According to our field observations, the landslide essentially moved like a solid in the first region and like a flow in the gully.

Although the transformation of rockslide and debris flow is gradual rather than sudden, in order to simulate the complex behavior of the Verghereto landslide with a single-phase model, we must

necessarily assume different material properties in the two regions. A simple way to do it is to assign a high frictional strength in region 1 (where the landslide moved like a slide) and a low frictional strength in region 2 (where the landslide moved like a flow). Different values of the frictional strength were obtained by adopting different values of the pore pressure coefficient r_u in the two regions. In particular, we used a pore pressure coefficient of zero to simulate the high frictional strength at the base of the landslide, and a pore pressure coefficient of 0.3 to simulate low frictional strength.

This assumption is basically reasonable, since the basal pore pressure is usually higher when a landslide is in fluid state than in solid state. All the other model parameters (density, friction and cohesion) were assumed to be identical in the whole domain.

Based on these assumptions, three groups of simulation were conducted using the parameters listed in Table 1. According to field investigation, the thickness of erodible soil cover was set to be 1.5 m in the whole region except in the source zone of the rockslide where the bedrock outcrops. The erodible mass is required to have a higher pore pressure than the sliding mass in order to be entrained. Here, erodible mass is assumed to have the same effective strength parameters (c' and φ') as the sliding mass, while its pore pressure coefficient r_{ue} takes a higher value (r_u=0.8).

Table 1 Parameters for simulating the Verghereto landslide

Group	**Pore pressure coefficient in R1** r_{u1}	**Pore pressure coefficient in R2** r_{u2}	**Basal effective cohesion** c' (kPa)	**Basal effective friction angle** φ'
S1	0.0	0.0	5	30
S2	0.3	0.3	5	30
S3	0.0	0.3	5	30

Notes: R1 and R2 refer to Region 1 and Region 2, respectively.

4. Results

4.1 Depositional characteristics

In Fig. 5, we illustrate the difference between the pre-failure and post-failure topography obtained from simulations (a-b-c) and measurements (d). The analysis S1 simulates a landslide with high frictional resistance at the base (r_u=0 in the whole domain). In this scenario, the landslide stops in the upper part of the slope and reaches a much smaller run-out distance than that observed in the field. However, the computed depositional pattern agrees well with the survey data in Zone A and B (comparing simulation results with Fig. 4 and Fig.3d). As mentioned above, in region 1 the landslide caused erosion on steep slopes and deposition on gentle slopes. The model captures this spatial variability, showing entrainment on the steep slopes right below the source zone (negative DEM difference ranges from -1.0 m to -1.5 m) and deposition on the gentle slopes further downhill (positive DEM difference ranges from 4.0 m to 5.0 m).

By assuming low frictional strength in the whole domain (r_u=0.3; simulation S2) the model predicts a larger mobility of the landslide (Fig. 5b). In this case, the landslide spreads over a much broader region than the measured one, leading to a significantly inaccurate prediction of the run-out. In particular, the landslide runs downslope laterally rather than flowing into the gully (Fig. 5b). These results indicate that in region 1 the frictional strength at the base of the landslide should be relatively high, so that most of the fragmented material can come to rest in this area.

This is confirmed by the results of simulation S3, which provides the best agreement with reality. By adopting a high friction in region 1 and a low friction in region 2 simultaneously, part of the material stops below the source area and part continues downslope as a flow. With this combination of r_u the model can simulate the debris flow (zone C in Fig. 4) and the landslide reaches a run-out distance similar to the measured one (Fig. 5d). Moreover, the model correctly predicts erosion in the

upper reach of the channel and deposition in the lower reach, where the slope becomes gentle (Fig. 5c). The above analysis indicates that friction change caused by the SFT plays a significant role in the run-out behavior of this landslide. And we may not be able to correctly simulate the run-out process if the SFT is neglected. Additionally, although the single-phase model cannot actually depict the complicated physical process of the SFT, the above simple method could improve the simulation results of those landslides involving such a complex SFT phenomenon by adopting frictional strengths for the sliding mass under the two different states (solid and fluid states).

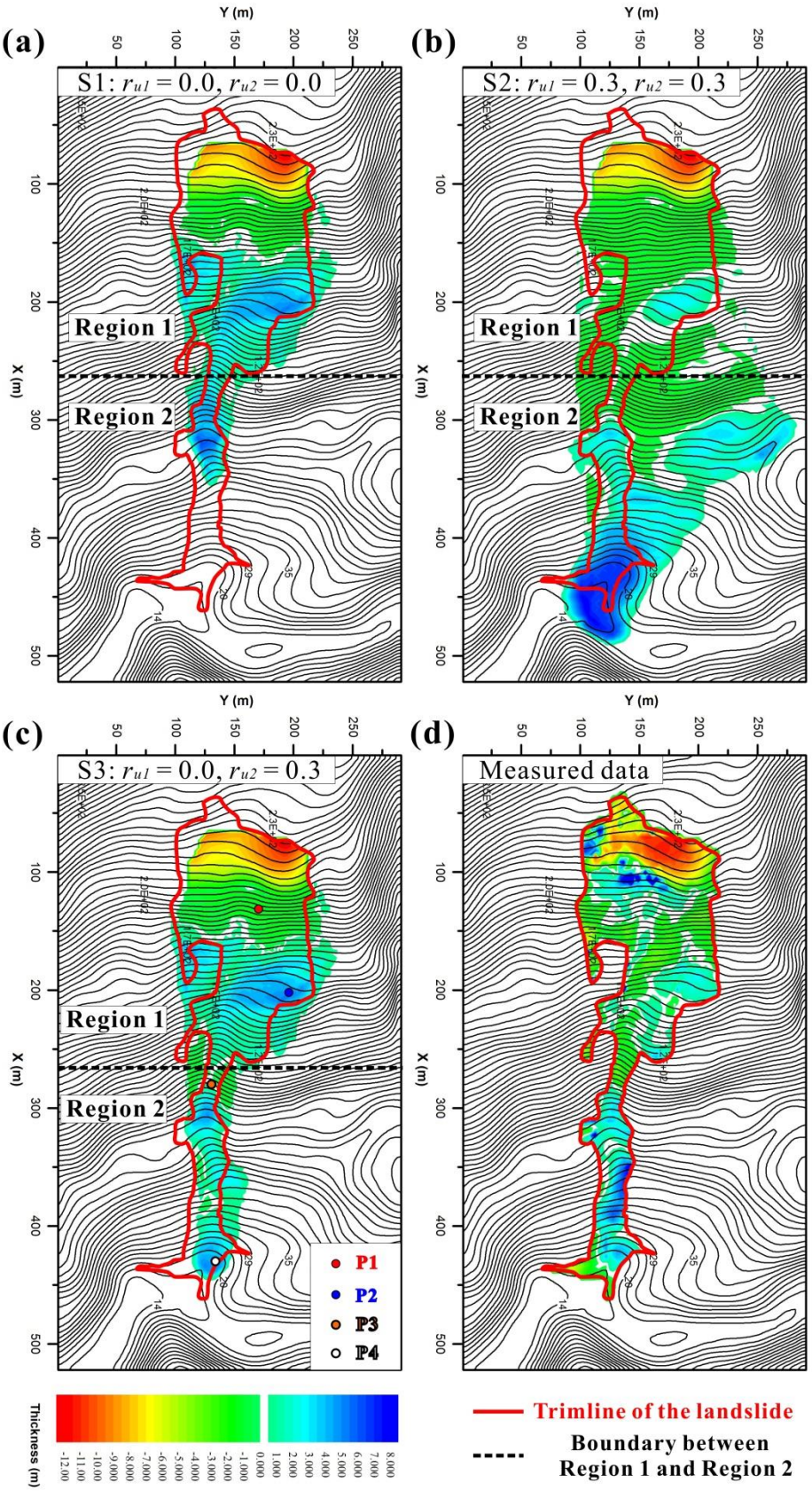

300

301 **Fig. 5** Digital elevation differences between pre-failure and post-failure topographies in the

landslide zone obtained from simulations and field survey

4.2 Velocity and entrainment

The total average velocity and entrainment time curves of the landslide in the three simulations (S1-S3) are illustrated in Fig. 6. The four turning points shown on the average velocity curve of simulation S3 (Fig. 6a) indicate the first velocity peak (t_1), the turning point between the first deceleration stage and the second acceleration stage (t_2), the second velocity peak (t_3), and the time when the motion of the landslide basically stops (t_4). From 0 s to t_1, the landslide accelerates rapidly after it detaches from the bedrock and propagates to the steep slope just below the detachment area. Then the landslide reaches a low slope gradient area (lower part of zone B, Fig. 4), resulting in a dramatic drop of the average velocity from t_1 to t_2. The landslide enters the gully head at around t_2. Here the model predicts a second slight acceleration stage (from t_2 to t_3) which should be attributed to both SFT and the steep topography in the downstream part of the gully head. Finally (from t_3 to t_4) the landslide comes to rest gradually. The difference between simulations S1 and S3 is that the second acceleration stage does not exist in S1, since in this case the reduction in frictional strength is not taken into account. Therefore, in S1 the landslide stops quickly after entering the gully showing a small run-out distance. By contrast, in S2 the landslide runs too fast and too distant, and the predicted velocity and entrainment are clearly overestimated.

The total volume curve of simulation S3 (Fig. 6b) indicates that the landslide is likely to have entrained a large amount of loose soil before reaching to the gully head. This extra volume from entrainment may potentially generate the source material for the mass flow in the gully. The volume of the landslide probably doubled (from approximately 28,000 m^3 to around 56,000 m^3) through entrainment.

The thickness and entrainment distributions of the landslide (in group S3) at the above four moments (t_1-t_4) are presented in Fig. 7. The thickness distributions at the four moments support our

above analysis toward the velocity change process of the landslide. By contrast, the entrainment distribution characteristic of the landslide is relatively simple (Fig. 7), indicating the landslide may entrain almost all the superficial loose mass on the slope wherever the landslide runs over.

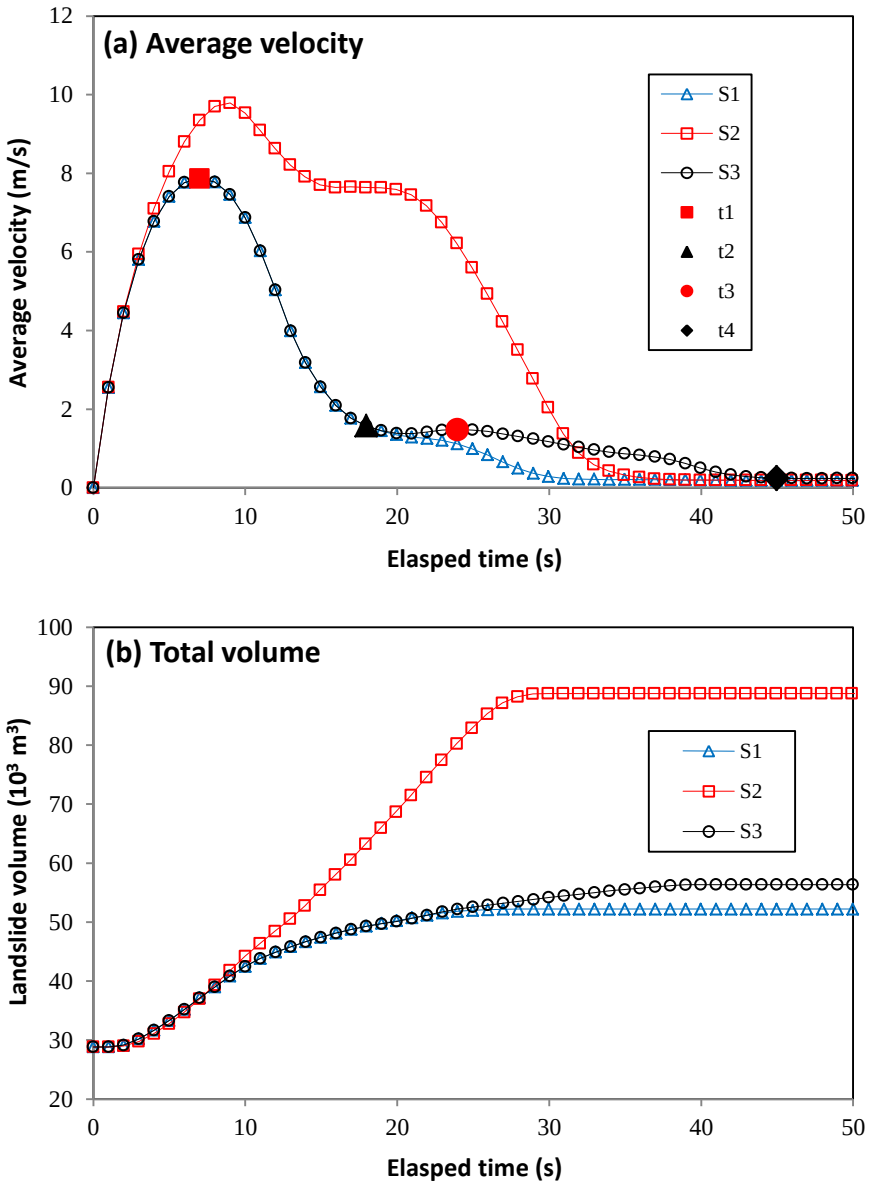

Fig.6 Simulated time curves of the (a) average velocity and (b) total volume of the Verghereto landslide

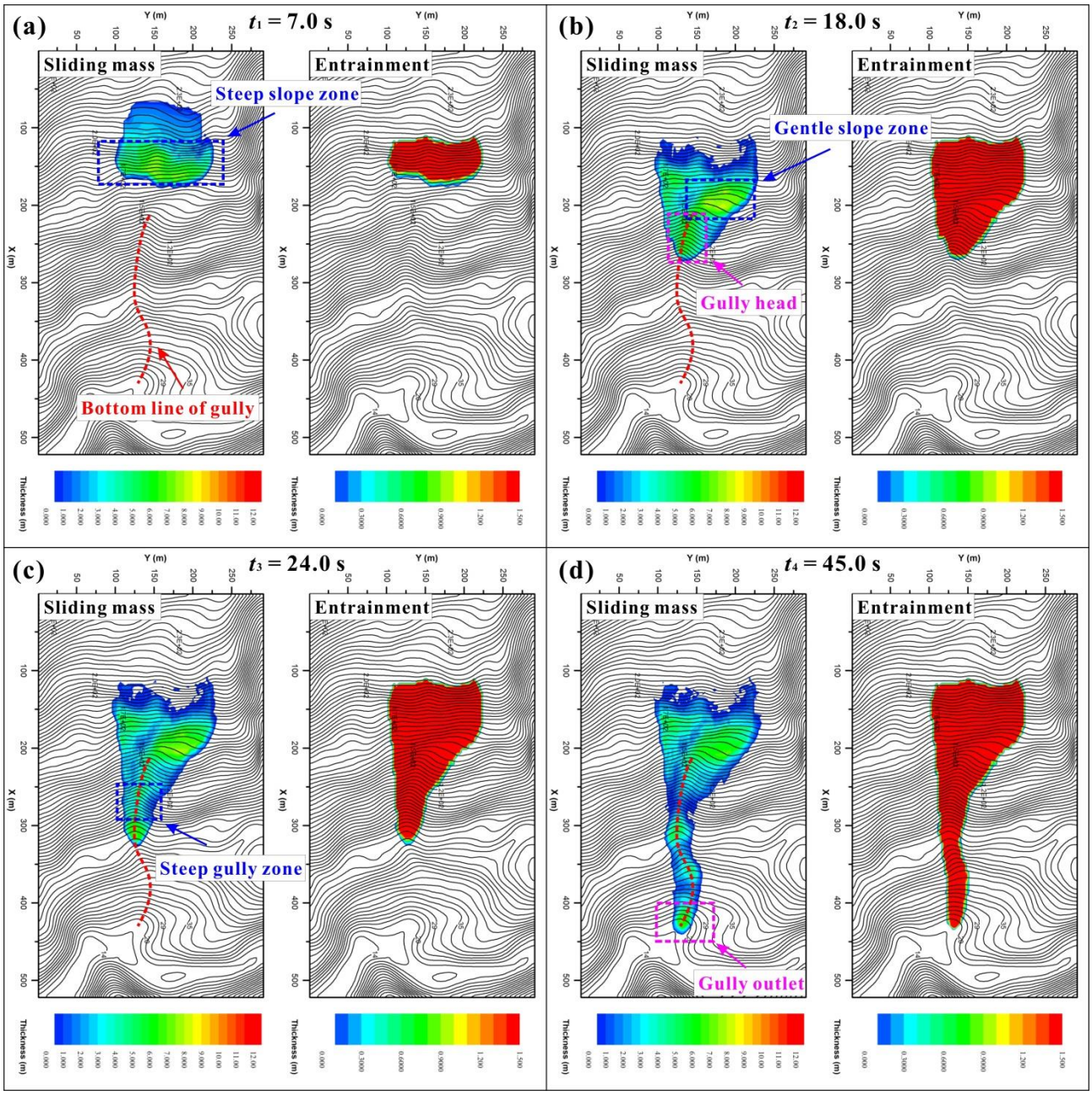

Fig. 7 Thickness and entrainment distributions of the landslide at four moments in S3. t_1 corresponds to the time when the landslide has the highest kinetic energy, t_2 is the time when part of the landslide starts to enter the gully head, t_3 is the time when the landslide reaches the second velocity peak, and t_4 corresponds to the time when the landslide basically comes to rest.

4.3 Influence of topography

Four numerical gauge points (P1-P4) in the landslide area are selected to analyze the influence of

topography (slope gradient and gully channel) on the simulated dynamic characteristics (thickness, velocity and Froude number) of the landslide at four different locations, and the simulation results of group S3 is used to conduct this analysis. The locations of these gauge points are shown in Fig. 5c. P1 and P2 are located in region 1 where the landslide is in 'solid state', while P3 and P4 are points located in region 2 where the landslide has transformed into a debris flow. P1 and P3 are approximately in the middle part of the steep slope gradient zones in region 1 and region 2 (in gully), respectively. For comparison, P2 and P4 are selected from the low slope gradient zones in region 1 and region 2, respectively. The flow thickness *h* and depth-averaged velocity *v* are directly available from the simulation results, while the Froude (Fr) number is calculated using $\mathrm{Fr} = v/\sqrt{gh}$. Fr number is a dimensionless variable reflecting the relationship between flow inertia and gravity. At P1 and P3 where the slopes are steep, the thickness of the landslide (Fig. 8a) increases fast when the front of the landslide arrives, and then decreases gradually to less than 1 m. The final DEM differences (net change in elevation) in these zones are less than zero, so the deposit there has an appearance of entrainment. However, at P2 and P4 the sliding mass accumulates and finally stops propagating, demonstrating an opposite appearance of deposition. Actually, entrainment should occur in both steep and gentle slope gradient regions, but the apparent entrainment is only revealed in steep slope zones. The thickness of the landslide at P3 remains at a relatively stable and thin level (about 1.5 m) which lasts for around 15 s after the arrival of landslide front, while at P1, the thickness decreases quickly after the arrival of landslide front. These different thickness curves indicate that on the steep slopes in Region 1 (P1) the landslide propagates like a surge wave, while on the steep slopes in Region 2 (P3), the landslide probably behaves like a plug flow due to the confinement of lateral propagation from the gully channel. The velocity curves (Fig. 8b) illustrate that the velocity of landslide is generally higher when it propagates on steep slopes than on gentle slopes (Fig. 8b). And the peak velocity of landslide on steep slopes (around 8.0 to 9.0 m/s) is about twice of the peak value on gentle slopes (approximately 4.0 to 5.0 m/s). The Fr number curves at P2 and P4 are similar. At P2 and P4, the Fr number peaks at the arrival of landslide front, and then decreases quickly because the sliding mass accumulates and comes to rest on the gentle slopes. By

contrast, the Fr numbers at P1 and P3 show some different tendencies. At P1 and P3, the Fr number peaks when the landslide front arrives, and then the number drops quickly until it rises up again. After reaching at the first valley value, at P1 the Fr number increases rapidly to a second peak larger than the first one, and then the number slumps to a low value. However, at P3 the Fr number increases only slightly until reaching at a relatively steady value (around 1.5) which lasts approximately 10 s, and then gradually decreases to a low value. These difference tendencies on Fr number between P1 and P3 is probably caused by the presence of the gully channel and its influence on the dynamic process of a landslide. This influence from gully will be discussed in the Discussion section. In summary, the topography on the path has a significant influence on the dynamic characteristic of this landslide. At locations on steep slopes, the landslide passes over quickly and finally shows entrainment. Conversely, at low slope gradients regions, the landslide comes to rest fast and eventually produces deposition. The existence of a gully channel also alters the dynamic characteristic of the landslide.

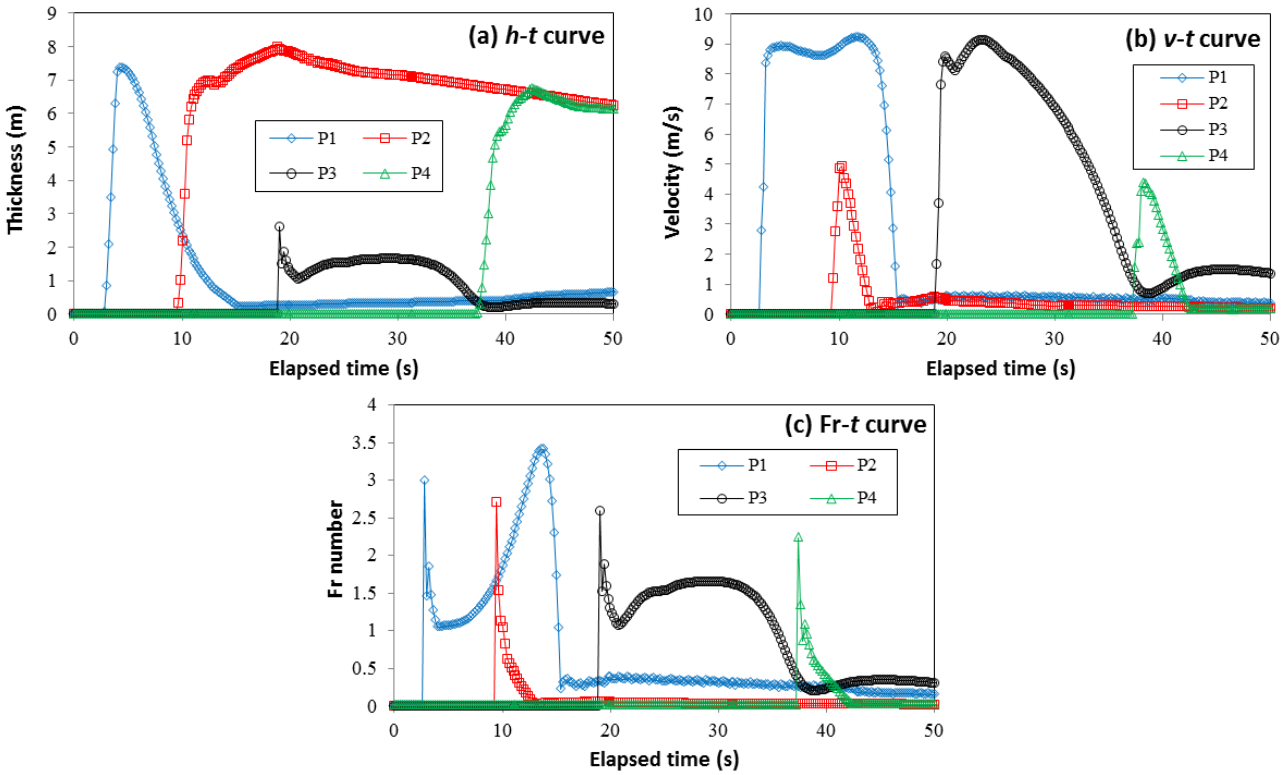

Fig. 8 Time curves of thickness, velocity and Froude (*Fr*) number of sliding mass at four locations

P1 to P4. P1 is on the steep slope of Region 1, P2 on the low slope gradient zone in Region 1, P3 on the steep slope at the gully head and P4 on gully outlet.

5. Discussion

As mentioned above, the existence of a gully channel may play an important role in determining the dynamic characteristic of a landslide. In field, we observed an interesting phenomenon that the existence of a gully seems to increase the final run-out distance of a rockslide. In rockslides with similar geological setting, those rockslides have a gully on the slope, similar to the Verghereto landslide in this study, tends to have a larger run-out distance which usually extends to the slope toe, while the rockslides without a gully normally deposit in the middle part of the slope which is far away from the slope toe.

To illustrate the influence from channel, in this section we simulate the Verghereto landslide in the condition of without a channel. Then four imaginary numerical tests (S1-nTnG, S2-nTwG, S3-wTnG and S4-wTwG) are conducted to investigate the generalized scenarios.

The simulation setups of the Verghereto landslide without the presence of a channel are the same as those in S3 expect for the topography. In this simulation, the channel on the slope is artificially removed by adjusting the elevation around the gully. The result is present in Fig. 9, which obviously shows a reduction in the run-out distance due to the absence of a channel.

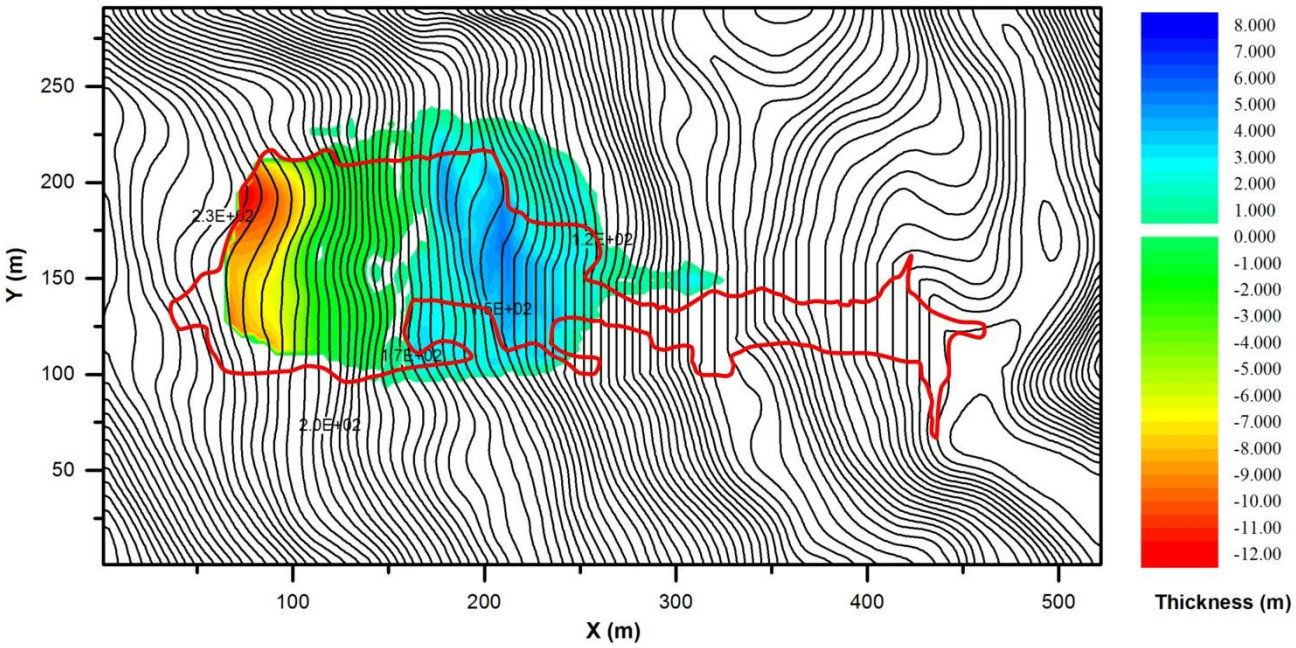

Fig. 9 Simulation result of the Verghereto landslide in the condition without the presence of a channel on the slope

The simulation setups for the other four generalized numerical tests are listed in Table 2. The schematic diagram of these numerical tests is shown in Fig. 10. In these tests, a 10 m thick, 80 m wide and 60 m long rock block is assumed to detach from the bedrock in a rock scarp and forms a rockslide. Then the rockslide propagates on a 25 °slope next to the rock scarp. The landslide area is divided into two regions similar to what we have done in the simulation of the Verghereto landslide. The slope above the gully head (x > 200 m) is region 1, while the slope below the gully head is region 2. The pore pressure coefficients in these two regions have different combinations in different groups (Table 2).

Table 2 Parameters for simulating ideal soil collapse experiments

Group	**Existence of A channel**	**Pore pressure Coefficient in R1** r_{u1}	**Pore pressure Coefficient in R2** r_{u2}	**Basal effective cohesion** c' (kPa)	**Basal effective friction angle** φ'
S1-nTnG	No	0.25	0.25	5	30

S2-nTwG	Yes	0.25	0.25	5	30
S4-wTnG	No	0.25	0.40	5	30
S4-wTwG	Yes	0.25	0.40	5	30

Notes: R1 and R2 refer to Region 1 and Region 2, respectively.

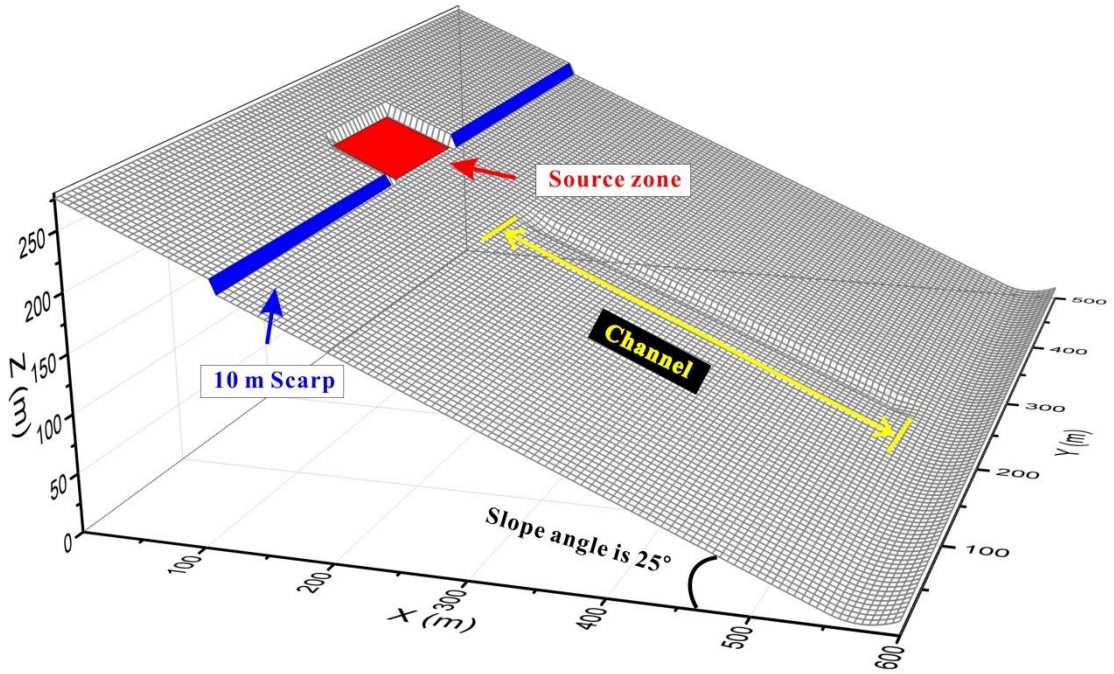

Fig. 10 Schematic diagram of the ideal rock collapse experiment with a channel on the slope

The simulation results illustrate that the existence of a channel can obviously increase the run-out distance (Fig. 11), no matter there is SFT or not. Without SFT and the channel (Fig.11a), the front of final deposit reaches to x = 280 m, while the final landslide front can reach to x = 360 m if there is a channel on the slope (Fig. 11b). Similarly, when there is SFT, the rockslide will has a larger run-out distance than that one without SFT (Fig. 11a), but the movement of the rockslide still will stop on the middle part of the slope while there is no channel on the slope (Fig. 11c). By contrast, the landslide may reach to the slope toe if there is a channel (Fig. 11d). These results indicate that SFT may not be the only factor contributing to the large run-out distance of the landslide. The existence of a gully can also promote the run-out distance. The promotion effect of a gully on the run-out

distance of a landslide may simply because the gully constrained the lateral spreading of the landslide. When the landslide propagates on a relatively uniform slope (Fig. 11a and 11c), it propagates forward and laterally simultaneously. The lateral spreading process will consume part of the kinetic energy, so the deposit has a smaller run-out distance but a larger lateral spreading area. Conversely, the channel reduces the lateral spreading and the energy consumption caused by it, so the landslide reaches a larger run-out distance but a much smaller lateral spreading area. This conclusion could be helpful for us to conduct a quick prediction on the risk of potential rockslides similar to the Verghereto rockslide. Those with a gully channel on the slope may pose higher risk on the infrastructures in the gully outlet (slope toe), while the potential rockslides without a gully on slope mainly endanger the properties in the middle part of the slope. The average velocity curves of these numerical tests agree with the above analysis (Fig. 12). The existence of a channel can reduce the rate of deceleration and produce a larger run-out distance.

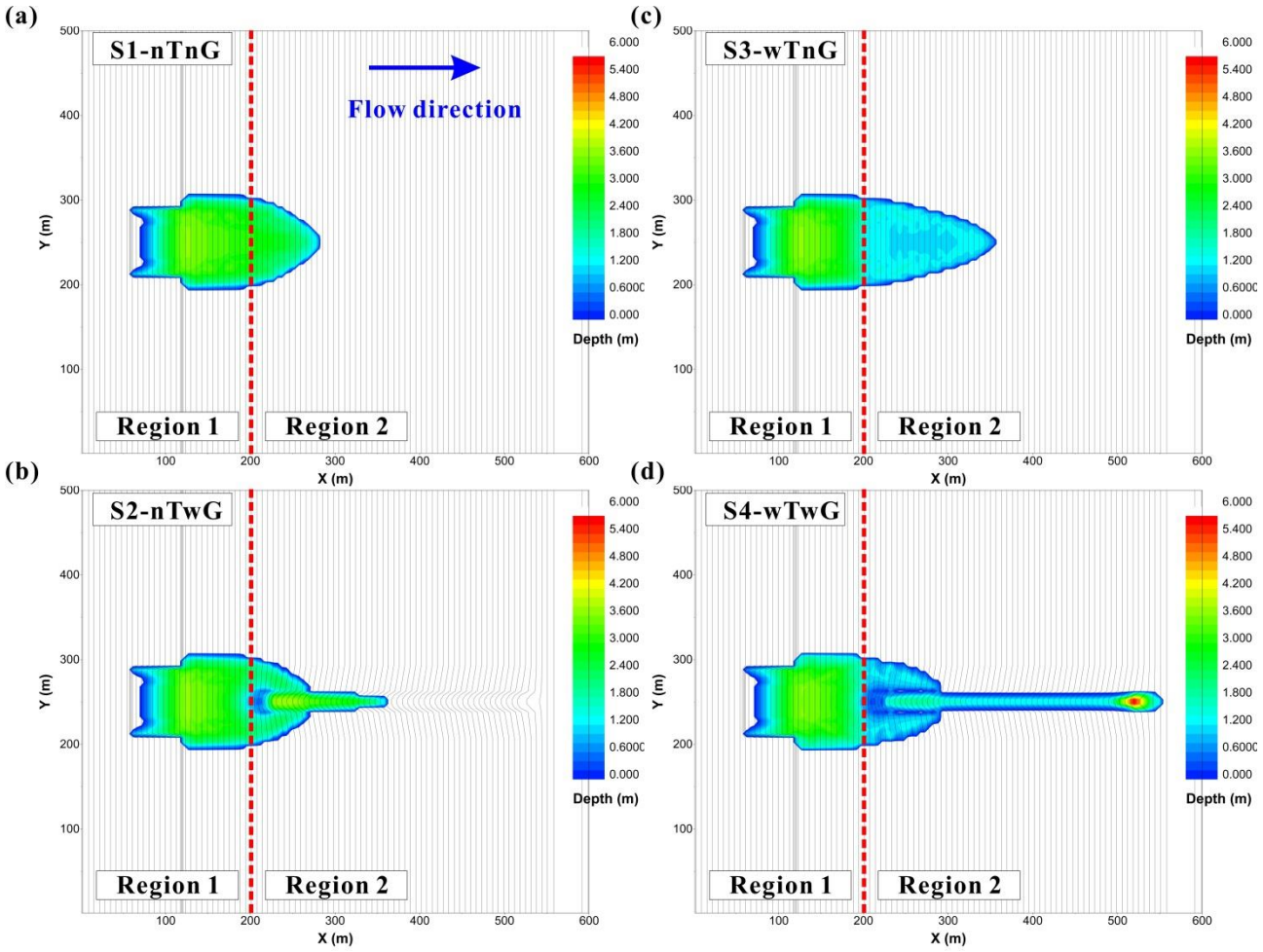

Fig. 10 Simulation results of ideal rockslides on a slope with different parametric and topographic conditions. The four graphs correspond to (a) without both SFT a channel and, (b) without SFT but with a channel, (c) with SFT but without a channel, and (d) with both SFT a channel

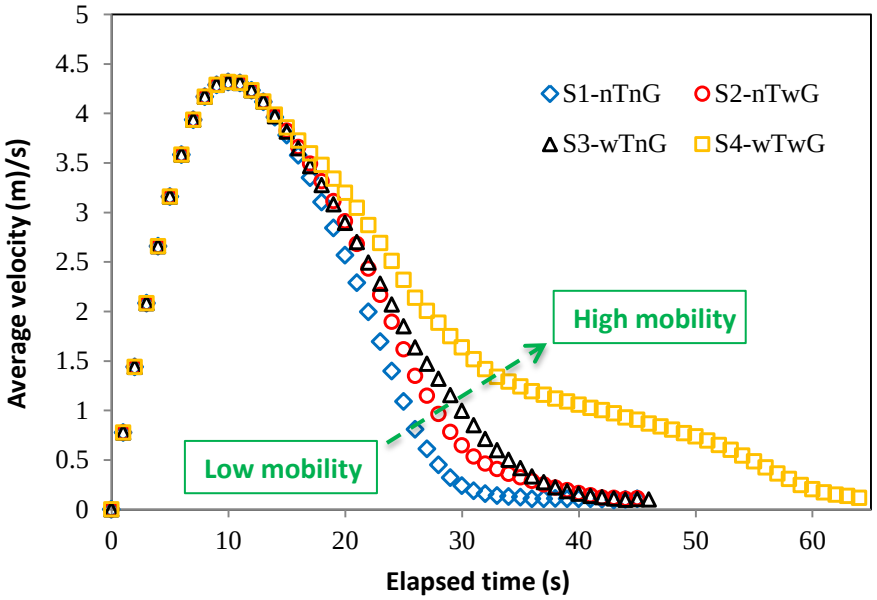

Fig. 11 Average velocity-time curves of the collapsed soil in the four simulation conditions. From S1 to S4 the mobility of the sliding mass increases gradually

6. Conclusions

The run-out process of a rockslide-debris flow in a layered rock slope is studied by an improved finite difference model. Field investigation and numerical simulations on this landslide are conducted to interpret the propagation process, and we obtain the following conclusions.

(1) The run-out process of the Verghereto landslide can be divided into three stages. In the first stage, the landslide detached from the bed rock sliding on the relatively gentle surface in the source zone. Then in the second stage, the landslide descended quickly in the steep slope zone next to the source zone before slumping heavily on the low slope gradient zone, and in the meantime, the volume of the landslide increased by entraining the loose mass on the slope and the rock mass disintegrated quickly. In the final stage, the disintegrated rock mass converged into the gully and transformed into a debris flow, and then the flow propagated along the gully until it stopped at the outlet of the gully.

(2) Simulation results show that the frictional strength change produced by the SFT process probably performs an important role in determining the dynamic characteristics of this landslide. The run-out behavior and depositional characteristic of the landslide can be correctly simulated if we properly consider this friction strength change of sliding mass. The depth-averaged single-phase model adopted in this study performs well in the simulation of the Verghereto rockslide-debris flow.

(3) Topography may have a dominant impact on the depositional characteristic of the Verghereto landslide. In the landslide area where the slope is relatively steep, the final digital elevation difference shows entrainment. By contrast, in low slope gradient zones, the deposit shows accumulation and deposition. However, bed entrainment should occur on both steep and gentle slopes. Additionally, the existence of a gully channel on the slope could enlarge the run-out distance of the landslide. In the potential rockslides similar to the Verghereto landslide, those with a gully on the slope may pose higher risk to the infrastructures in the outlet of the gully (at slope toe).

Acknowledgement

We would like to thank the anonymous referees for careful reading the manuscript and providing constructive comments to help us improve the quality of this paper. This research is funded by the National Key R&D Program of China (2021YFE0111900), the Fundamental Research Funds for the Central Universities, CHD（300102261507）, and the China Scholarship Council (CSC) – University of Bologna Joint Scholarship (File No. 201806560011).

Reference

Aaron J and McDougall S (2019) Rock avalanche mobility: The role of path material. Engineering Geology 257: 105126. doi: https://doi.org/10.1016/j.enggeo.2019.05.003

Berti M, Cuzzani MG, Vai GB, Landuzzi A, Taviani M and Aharon P (1994) Hydrocarbon-derived imprints in olistostromes of the early serravallian marnoso-arenacea formation, romagna apennines (northern italy). Geo-Marine Letters 14: 192-200. doi: 10.1007/BF01203731

Berti M, Genevois R, Ghirotti M and Tecca PR (1996) Mechanical characteristics and behaviour of a complex formation by landslide investigations and analyses. ISL'96 : International Symposium on landslides (7 ; Trondheim 1996-06-17), A.A. Balkema, Rotterdam, pp 1155-1162.

Bowman ET, Take WA, Rait KL and Hann C (2012) Physical models of rock avalanche spreading behaviour with dynamic fragmentation. Canadian Geotechnical Journal 49: 460-476. doi: 10.1139/t2012-007

Christen M, Kowalski J and Bartelt P (2010) Ramms: Numerical simulation of dense snow avalanches in three-dimensional terrain. Cold Regions Science and Technology 63: 1-14. doi: https://doi.org/10.1016/j.coldregions.2010.04.005

Collins BD and Reid ME (2019) Enhanced landslide mobility by basal liquefaction: The 2014 state route 530 (oso), washington, landslide. GSA Bulletin 132: 451-476. doi: 10.1130/B35146.1

Crosta GB, Frattini P and Fusi N (2007) Fragmentation in the val pola rock avalanche, italian alps. Journal of Geophysical Research: Earth Surface 112. doi: 10.1029/2005JF000455

Cuomo S, Pastor M, Capobianco V and Cascini L (2016) Modelling the space–time evolution of bed entrainment for flow-like landslides. Engineering Geology 212: 10-20. doi: 10.1016/j.enggeo.2016.07.011

Dai Z, Huang Y, Cheng H and Xu Q (2017) Sph model for fluid–structure interaction and its application to debris flow impact estimation. Landslides 14: 917-928. doi: 10.1007/s10346-016-0777-4

Davies TR and McSaveney MJ (2009) The role of rock fragmentation in the motion of large landslides. Engineering Geology 109: 67-79. doi: https://doi.org/10.1016/j.enggeo.2008.11.004

Dufresne A and Geertsema M (2020) Rock slide–debris avalanches: Flow transformation and hummock formation, examples from british columbia. Landslides 17: 15-32. doi: 10.1007/s10346-019-01280-x

Gao G, Meguid MA, Chouinard LE and Zhan W (2021) Dynamic disintegration processes accompanying transport of an earthquake-induced landslide. Landslides 18: 909-933. doi:

10.1007/s10346-020-01508-1

Gao Y, Yin Y, Li B, Feng Z, Wang W, Zhang N and Xing A (2017) Characteristics and numerical runout modeling of the heavy rainfall-induced catastrophic landslide–debris flow at sanxicun, dujiangyan, china, following the wenchuan ms 8.0 earthquake. Landslides 14: 1361-1374. doi: 10.1007/s10346-016-0793-4

Ghaťanellis A, Violeau D, Liu PLF and Viard T (2021) Sph simulation of the 2007 chehalis lake landslide and subsequent tsunami. Journal of Hydraulic Research: 1-25. doi: 10.1080/00221686.2020.1844814

Guthrie RH, Friele P, Allstadt K, Roberts N, Evans SG, Delaney KB, Roche D, Clague JJ and Jakob M (2012) The 6 august 2010 mount meager rock slide-debris flow, coast mountains, british columbia: Characteristics, dynamics, and implications for hazard and risk assessment. Nat Hazards Earth Syst Sci 12: 1277-1294. doi: 10.5194/nhess-12-1277-2012

Hungr O and Evans SG (2004) Entrainment of debris in rock avalanches: An analysis of a long run-out mechanism. GSA Bulletin 116: 1240-1252. doi: 10.1130/B25362.1

Hungr O, Leroueil S and Picarelli L (2014) The varnes classification of landslide types, an update. Landslides 11: 167-194. doi: 10.1007/s10346-013-0436-y

Hungr O and McDougall S (2009) Two numerical models for landslide dynamic analysis. Computers & Geosciences 35: 978-992. doi: 10.1016/j.cageo.2007.12.003

Iverson RM and Ouyang C (2015) Entrainment of bed material by earth-surface mass flows: Review and reformulation of depth-integrated theory. Reviews of Geophysics 53: 27-58. doi: 10.1002/2013RG000447

Li X, Tang X, Zhao S, Yan Q and Wu Y (2021) Mpm evaluation of the dynamic runout process of the giant daguangbao landslide. Landslides 18: 1509-1518. doi: 10.1007/s10346-020-01569-2

Liang H, He S and Liu W (2020) Dynamic simulation of rockslide-debris flow based on an elastic–plastic framework using the sph method. Bulletin of Engineering Geology and the Environment 79: 451-465. doi: 10.1007/s10064-019-01537-8

Lucchi FR and Valmori E (1980) Basin-wide turbidites in a miocene, over-supplied deep-sea plain:

A geometrical analysis. Sedimentology 27: 241-270. doi: https://doi.org/10.1111/j.1365-3091.1980.tb01177.x

Mangeney CA, Vilotte JP, Bristeau MO, Perthame B, Bouchut F, Simeoni C and Yerneni S (2003) Numerical modeling of avalanches based on saint venant equations using a kinetic scheme. Journal of Geophysical Research: Solid Earth 108. doi: https://doi.org/10.1029/2002JB002024

McDougall S, Boultbee N, Hungr O, Stead D and Schwab JW (2006) The zymoetz river landslide, british columbia, canada: Description and dynamic analysis of a rock slide–debris flow. Landslides 3: 195. doi: 10.1007/s10346-006-0042-3

McDougall S and Hungr O (2005) Dynamic modelling of entrainment in rapid landslides. Canadian Geotechnical Journal 42: 1437-1448. doi: 10.1139/t05-064

O'Brien JS, Julien PY and Fullerton WT (1993) Two‐dimensional water flood and mudflow simulation. Journal of Hydraulic Engineering 119: 244-261. doi: 10.1061/(ASCE)0733-9429(1993)119:2(244)

Ouyang C, He S and Tang C (2015) Numerical analysis of dynamics of debris flow over erodible beds in wenchuan earthquake-induced area. Engineering Geology 194: 62-72. doi: 10.1016/j.enggeo.2014.07.012

Ouyang C, He S, Xu Q, Luo Y and Zhang W (2013) A maccormack-tvd finite difference method to simulate the mass flow in mountainous terrain with variable computational domain. Computers & Geosciences 52: 1-10. doi: 10.1016/j.cageo.2012.08.024

Pastor M, Haddad B, Sorbino G, Cuomo S and Drempetic V (2009) A depth-integrated, coupled sph model for flow-like landslides and related phenomena. International Journal for Numerical and Analytical Methods in Geomechanics 33: 143-172. doi: 10.1002/nag.705

Sassa K, Nagai O, Solidum R, Yamazaki Y and Ohta H (2010) An integrated model simulating the initiation and motion of earthquake and rain induced rapid landslides and its application to the 2006 leyte landslide. Landslides 7: 219-236. doi: 10.1007/s10346-010-0230-z

Sassa K and Wang Gh (2005) Mechanism of landslide-triggered debris flows: Liquefaction phenomena due to the undrained loading of torrent deposits. In: Jakob M and Hungr O (eds)

584 Debris-flow hazards and related phenomena, Springer Berlin Heidelberg, Berlin, Heidelberg,
585 pp 81-104. doi: 10.1007/3-540-27129-5_5
586 Shen W, Li T, Li P, Berti M, Shen Y and Guo J (2019) A two-layer numerical model for simulating
587 the frontal plowing phenomenon of flow-like landslides. Engineering Geology 259: 105168.
588 doi: 10.1016/j.enggeo.2019.105168
589 Shen W, Li T, Li P and Guo J (2018) A modified finite difference model for the modeling of
590 flowslides. Landslides 15: 1577-1593. doi: 10.1007/s10346-018-0980-6
591 Shugar DH, Jacquemart M, Shean D, Bhushan S, Upadhyay K, Sattar A, Schwanghart W, McBride
592 S, de Vries MVW, Mergili M, Emmer A, Deschamps-Berger C, McDonnell M, Bhambri R,
593 Allen S, Berthier E, Carrivick JL, Clague JJ, Dokukin M, Dunning SA, Frey H, Gascoin S,
594 Haritashya UK, Huggel C, Kääb A, Kargel JS, Kavanaugh JL, Lacroix P, Petley D, Rupper S,
595 Azam MF, Cook SJ, Dimri AP, Eriksson M, Farinotti D, Fiddes J, Gnyawali KR, Harrison S,
596 Jha M, Koppes M, Kumar A, Leinss S, Majeed U, Mal S, Muhuri A, Noetzli J, Paul F,
597 Rashid I, Sain K, Steiner J, Ugalde F, Watson CS and Westoby MJ (2021) A massive rock
598 and ice avalanche caused the 2021 disaster at chamoli, indian himalaya. Science 373: 300.
599 doi: 10.1126/science.abh4455
600 Soga K, Alonso E, Yerro A, Kumar K and Bandara S (2016) Trends in large-deformation analysis of
601 landslide mass movements with particular emphasis on the material point method.
602 Géotechnique 66: 248-273. doi: 10.1680/jgeot.15.LM.005
603 Wang FW, Sassa K and Wang G (2002) Mechanism of a long-runout landslide triggered by the
604 august 1998 heavy rainfall in fukushima prefecture, japan. Engineering Geology 63:
605 169-185. doi: https://doi.org/10.1016/S0013-7952(01)00080-1
606 Wu J-H, Lin W-K and Hu H-T (2018) Post-failure simulations of a large slope failure using 3dec:
607 The hsien-du-shan slope. Engineering Geology 242: 92-107. doi:
608 https://doi.org/10.1016/j.enggeo.2018.05.018
609 Xia X and Liang Q (2018) A new depth-averaged model for flow-like landslides over complex
610 terrains with curvatures and steep slopes. Engineering Geology 234: 174-191. doi:
611 https://doi.org/10.1016/j.enggeo.2018.01.011

612 Xing AG, Wang G, Yin YP, Jiang Y, Wang GZ, Yang SY, Dai DR, Zhu YQ and Dai JA (2014)
613 Dynamic analysis and field investigation of a fluidized landslide in guanling, guizhou, china.
614 Engineering Geology 181: 1-14. doi: https://doi.org/10.1016/j.enggeo.2014.07.022
615 Xu Q, Fan X, Huang R, Yin Y, Hou S, Dong X and Tang M (2010) A catastrophic rockslide-debris
616 flow in wulong, chongqing, china in 2009: Background, characterization, and causes.
617 Landslides 7: 75-87. doi: 10.1007/s10346-009-0179-y
618 Xu X, Jin F, Sun Q, Soga K and Zhou GGD (2018) Three-dimensional material point method
619 modeling of runout behavior of the hongshiyan landslide. Canadian Geotechnical Journal 56:
620 1318-1337. doi: 10.1139/cgj-2017-0638
621 Yin Y, Cheng Y, Liang J and Wang W (2016) Heavy-rainfall-induced catastrophic rockslide-debris
622 flow at sanxicun, dujiangyan, after the wenchuan ms 8.0 earthquake. Landslides 13: 9-23.
623 doi: 10.1007/s10346-015-0554-9
624 Zhang X, Krabbenhoft K, Sheng D and Li W (2015) Numerical simulation of a flow-like landslide
625 using the particle finite element method. Computational Mechanics 55: 167-177. doi:
626 10.1007/s00466-014-1088-z
627 Zhang X, Wang L, Krabbenhoft K and Tinti S (2020) A case study and implication: Particle finite
628 element modelling of the 2010 saint-jude sensitive clay landslide. Landslides 17: 1117-1127.
629 doi: 10.1007/s10346-019-01330-4
630

4. PAPER 3

The effect of check dams on the dynamic and bed entrainment processes of debris flows

Wei Shen[1], Dongpo Wang[2*], Huanan Qu[2], Tonglu L[3]
*Correspondence author

1 Department of Biological, Geological and Environmental Sciences, University of Bologna, Italy, 40126
2 State Key Laboratory of Geohazard Prevention and Geoenvironment Protection, Chengdu University of Technology, Chengdu, China, 610059
3 Department of Geological Engineering, Chang'an University, Xi'an, China, 710064

Paper has been published in Landslides

Landslides (2019) 16:2201–2217
DOI 10.1007/s10346-019-01230-7
Received: 1 April 2019
Accepted: 18 June 2019
Published online: 10 July 2019

Wei Shen · Dongpo Wang · Huanan Qu · Tonglu Li

The effect of check dams on the dynamic and bed entrainment processes of debris flows

Abstract Bed entrainment plays a significant role in the formational process of a debris flow. Thus the influence of bed entrainment may be an important factor which cannot be neglected when assessing the prevention effect of check dams. However, since few studies have investigated the interaction between check dams and debris flows with considering bed entrainment, the interactive effect of check dams on the dynamic and bed entrainment processes of debris flows remains unclear. Therefore, in this paper, an improved depth-averaged model is proposed to overcome this weakness. In the improved model, the impeding effect of a check dam is simplified as a rigid constraint, and a new computational scheme is adopted to improve the simulation efficiency. Using this model, the dynamic and bed entrainment processes of the catastrophic 2010 Hongchun gully debris flow are analyzed, and the effects of check dams on this debris flow are studied. The results show that the present model can properly depict the dynamic and bed entrainment processes of the Hongchun gully debris flow. Without bed entrainment, the flow quantity tends to decrease gradually from the upstream to the downstream, while the flow quantity will show an opposite tendency if bed entrainment is considered. The check dams can largely reduce the bed entrainment scale and flow quantity of this debris flow. Additionally, the prevention effect of check dams tends to be better when they are constructed at the upper part of the gully by constraining bed entrainment.

Keywords Disaster prevention · Debris flow · Numerical simulation · Check dam · Bed entrainment

Introduction

Debris flows are saturated poorly sorted two-phase flows. These flows are usually characterized by high velocity, huge impact force, and long run-out distance, making them one of the most dangerous landslide types (Jakob and Hungr 2005). As world-wide hazardous phenomena, debris flows can occur in any mountainous areas with steep terrain, channelized path, and sufficient rainfall. Additionally, they are distinct from other types of landslides by periodically occurring in the same channels (Hungr et al. 2014). Due to the above characteristics, debris flows have caused enormous economic loss and casualties to human communities around the world (Evans et al. 2009; García-Martínez and López 2005; Ren 2014; Takahashi 2009).

Generally, debris flows fall into two categories according to their initiation mechanisms, namely landslide-induced debris flows (Iverson et al. 1997; Scott et al. 2001) and runoff-induced debris flows (Berti and Simoni 2005; Hu et al. 2016). For runoff-induced debris flows, apart from intensive rainfall, abundant loose material is also a prerequisite for their formations. The huge earthquake happened in Wenchuan County of China in 2008 triggered thousands of landslides, with a total volume of more than five billion cubic meters (Parker et al. 2011). These landslide deposits became the main source of loose materials of the runoff-induced debris flows in the earthquake impacted area (Huang and Li 2014; Tang et al. 2012a). As a consequence, the frequency and magnitude of debris flows increased dramatically in this area, while in the meantime the precipitation threshold for triggering a debris flow decreased significantly (Tang et al. 2011; Xu et al. 2012). More seriously, more than 2000 people died or disappeared in some huge debris flow events after the earthquake (Tang et al. 2012a). To mitigate this situation, millions of dollars were allocated by the Chinese government to construct countermeasures such as check dams in some gullies (e.g., the Wenjia and Hongchun gullies). Despite all of these efforts, catastrophic debris flows still occurred due to the inadequate effect of some of these mitigation measures (Chen et al. 2015). Furthermore, since in this area debris flows are expected to occur frequently in 5–15 years after the earthquake (Cui et al. 2011), the risk of occurring catastrophic debris flows is still very high. Therefore, it is an urgent mission and of great importance to develop some useful methods for effectively designing and assessing these mitigation measures.

Currently, experiment and numerical simulation are the two main approaches for studying the dynamics of debris flows. Many experiments (most are flume tests) have been conducted in the past few decades. These tests were mainly utilized in illustrating the initial mechanism (Hu et al. 2016), the dynamic characteristics (Iverson et al. 2010) and the impact forces of debris flows (Armanini 1997; Cui et al. 2015; Wang et al. 2018). Experiments are very useful method in terms of helping scientists understand some basic physics of debris flows, but their drawbacks are also obvious, such as having size effect, being expensive, and being time-consuming. These disadvantages limit their applications in assessing the effect of mitigation measures when the prototype debris flow is huge. In comparison, numerical simulation does not suffer from these weaknesses, making them more suitable for mitigation measure design and assessment. Plenty of numerical models have been proposed for simulating the dynamic process of flow-like motions like debris flows (Crosta et al. 2009; Huang et al. 2015; Hungr and McDougall 2009; Liu and Huang 2006; Liu et al. 2016; Ouyang et al. 2013; Pastor et al. 2009; Pitman and Le 2005; Sassa et al. 2010; Shen et al. 2018a). Additionally, since the substantial influence of bed entrainment on the mobility of flow-like landslides is gradually recognized by researchers in this field (Hungr and Evans 2004; Iverson 2012; Iverson and Ouyang 2015), a growing number of models start to consider bed entrainment either by adopting empirically based or mechanically based entrainment methods (Cuomo et al. 2016; Frank et al. 2015; Liu and He 2016; McDougall and Hungr 2005; Ouyang et al. 2015; Pirulli and Pastor 2012; Shen et al. 2018b). Specially, for runoff-induced debris flows, bed entrainment contributes greatly to their formations. Sometimes most mass in a debris flow may come from entraining loose materials along the path, so under such a circumstance bed entrainment cannot be neglected. Although many

progresses have been made in bed entrainment modeling as mentioned above, these previous studies simulated the bed entrainment process of debris flows in a green field (i.e., without barriers along the path), and few studies considered bed entrainment when assessing the prevention effect of check dams on debris flows. More recently, some researchers have implemented numerical models in studying the effects of artificial barriers on flow-like landslides (Chen et al. 2019; Cuomo et al. 2019; Dai et al. 2017; Gao et al. 2017; Kattel et al. 2018; Liu et al. 2013). These studies mainly focused on exploring the mechanical impacts of debris flows on the structures or the impeding effect of artificial barriers. On the other hand, almost none of them considered bed entrainment in their studies and its interactive influences with debris flow dynamics under the effect of check dams. Therefore, some aspects remain unclear in this field, for instance, how check dams affect the bed entrainment process (which will alter debris flow dynamics in turn), and how to quantify and consider their influence when designing check dams in a debris flow gully with obvious bed entrainment phenomenon, etc.

Based on the above analysis, this paper aims at proposing a simple but efficient method for assessing the effect of check dams on the dynamics of debris flows with taking bed entrainment into account. The present study highlights in extending the application of the depth-averaged models from risk assessment of debris flows on green field to the design of mitigation measures (e.g., check dams). The improved model is able to provide more reasonable guides for constructing check dams in debris flow gullies. In the following sections, the basic principles of the improved method are introduced first. Then it is applied in modeling the dynamic process of the catastrophic Hongchun gully debris flow in southwest China. Totally 20 groups of simulations representing different scenarios are conducted to explore the influences of check dams on the bed entrainment and dynamic processes of this debris flow. Afterwards, the simulation results are presented and discussed in detail, and finally, conclusions are drawn according to the results.

Basic principles of the method

Governing equations

The governing equations adopted in this paper consist of one continuity equation and two momentum equations. These equations are deduced according to the mass and momentum conservations of a small rectangular soil column in a Cartesian coordinate system. Bed entrainment is incorporated into these equations as a source term. For simplicity, these equations are only briefly introduced here, and detailed derivations can be found in Shen et al. (2018a). The governing equations are given by.

$$\frac{\partial h}{\partial t}+\frac{\partial Q_x}{\partial x}+\frac{\partial Q_y}{\partial y}-E_r=0 \tag{1}$$

$$\frac{\partial Q_x}{\partial t}+\frac{\partial {Q_x}^2/h}{\partial x}+\frac{\partial Q_xQ_y/h}{\partial y}=-\left(k_xhg\frac{\partial h}{\partial x}+g\frac{h^2}{2}\frac{\partial k_x}{\partial x}\right)+(Ag+B)\frac{h\tan\beta}{\tan^2\alpha+\tan^2\beta+1}-\frac{\tau_bA_bhv_x}{m\sqrt{{v_x}^2+{v_y}^2+{v_z}^2}} \tag{2}$$

$$\frac{\partial Q_y}{\partial t}+\frac{\partial Q_xQ_y/h}{\partial x}+\frac{\partial {Q_y}^2/h}{\partial y}=-\left(k_yhg\frac{\partial h}{\partial y}+g\frac{h^2}{2}\frac{\partial k_y}{\partial y}\right)+(Ag+B)\frac{h\tan\beta}{\tan^2\alpha+\tan^2\beta+1}-\frac{\tau_bA_bhv_y}{m\sqrt{{v_x}^2+{v_y}^2+{v_z}^2}} \tag{3}$$

where h is the thickness of the debris flow, $Q_x=v_xh$ and $Q_y=v_yh$ are the flow quantities in the x and y directions, respectively, v_x and v_y are the flow velocities in the x and y directions, respectively, E_r is the entrainment rate, k_x and k_y are the lateral pressure coefficients in the x and y directions, respectively, which evolve according to the pressure state (active state or passive state) of the soil (Ouyang et al. 2013; Savage and Hutter 1989), g is the gravitational acceleration, A and B are the parameters related to the static and centrifugal supporting forces, respectively, α and β are the dip angles of the sliding mass in the x and y directions, respectively, τ_b is the basal shear stress, A_b is the area of the bottom surface of the soil column, and m is the mass of the soil column. The expressions of A, B and A_b are given by.

$$A=1+\left(k_x\frac{\partial h}{\partial x}+\frac{h}{2}\frac{\partial k_x}{\partial x}\right)\tan\alpha+\left(k_y\frac{\partial h}{\partial y}+\frac{h}{2}\frac{\partial k_y}{\partial y}\right)\tan\beta \tag{4}$$

$$B=\frac{C_x}{\cos\alpha}\left(\frac{v_x}{\cos\alpha}\right)^2+\frac{C_y}{\cos\beta}\left(\frac{v_y}{\cos\beta}\right)^2 \tag{5}$$

$$A_b=dxdy\sqrt{\tan^2\alpha+\tan^2\beta+1} \tag{6}$$

where C_x and C_y are the curvature of the bed in the x and y directions, respectively, dx and dy are the sizes of the soil column in the x and y directions, respectively.

In some models, two additional momentum production terms (E_rv_{bx} and E_rv_{by}) may appear in the momentum equations (Eqs. (2)–(3)). However, since the erodible mass are usually assumed to be static ($v_{bx}=v_{by}=0$) before being entrained, these momentum productions terms are removed from the momentum equations in this paper.

Rheological law and entrainment model

The governing equations are not closed before E_r and τ_b are determined by some kinds of models. The widely used Voellmy model is adopted to calculate the basal shear stress of the debris flow.

$$\tau_b=\sigma(1-r_{ub})\tan\phi_s+\rho_sg\frac{{v_x}^2+{v_y}^2}{\xi} \tag{7}$$

where σ is the normal stress on the bed, r_{ub} is the pore water pressure coefficient on the bed, ϕ_s is the effective friction angle of the debris flow, ρ_s is the bulk density of the debris flow, and ξ is the turbulence coefficient. To determine E_r, a mechanically based model proposed by Fraccarollo and Capart (Fraccarollo and Capart 2002) is adopted given it has clear physical meaning

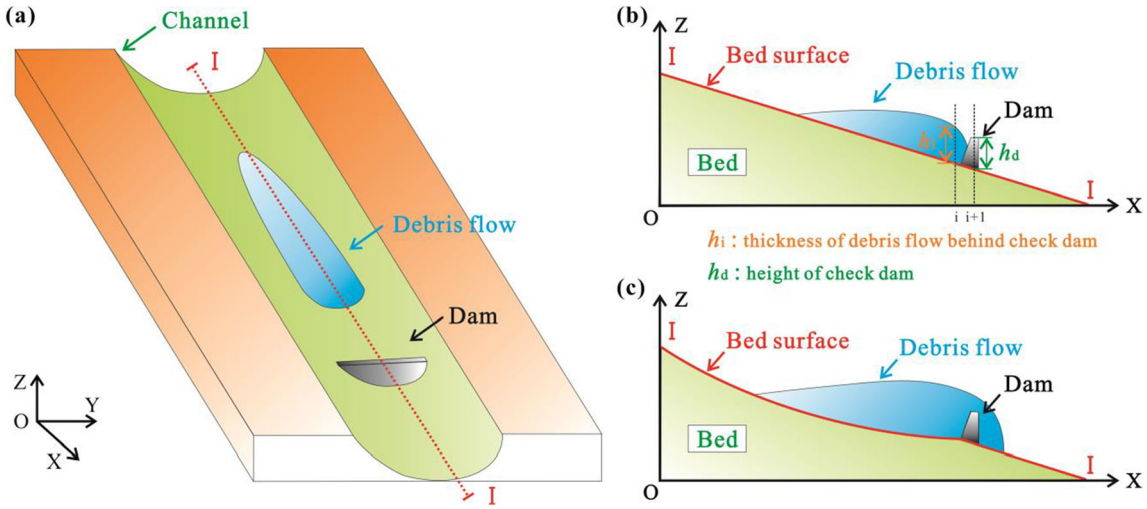

Fig. 1 Schematic diagram of the interaction between channelized debris flow and check dam. **a** Three-dimensional view before interaction, **b** result after interaction without entrainment, and **c** result after interaction with entrainment

$$E_r = -\frac{\partial Z}{\partial t} = \frac{\tau_b - \tau_e}{\rho_e \sqrt{v_x^2 + v_y^2}} \tag{8}$$

where Z is the elevation of the bed, τ_e is the resistant shear stress in the erodible mass, and ρ_e is the bulk density of the erodible mass. τ_e is calculated according to the Mohr-Coulomb model

$$\tau_e = \sigma(1 - r_{ue})\tan\phi_e + c_e \tag{9}$$

where r_{ue} is the pore water pressure coefficient in the erodible mass, ϕ_e is the effective friction angle of the erodible mass, and c_e is the cohesion of the erodible mass. Substituting Eq. (7) and (9) into Eq. (8), the following entrainment model can be obtained

$$E_r = -\frac{\partial Z}{\partial t} = \left(\sigma(1 - r_{ub})\tan\phi_s + \rho_s g \frac{v_x^2 + v_y^2}{\xi} - \sigma(1 - r_{ue})\tan\phi_e - c_e\right) \frac{1}{\rho_e \sqrt{v_x^2 + v_y^2}} \tag{10}$$

Equation (10) is utilized to determine the entrainment rate in this paper. This equation is similar to the entrainment model adopted in Ouyang et al. (2015), and it takes advantages of both the Voellmy model and the Mohr-Coulomb model.

Constraint of check dams and computational scheme

To reflect the restraining impact of check dams on debris flows, check dams are taken as a kind of rigid constraint, as shown in Fig. 1. Therefore, the failure of check dams is not considered in the present study. Those computational cells with a dam inside are marked, and their neighboring cells are also identified. Assuming the height of the dam is h_d, and the thickness of the debris flow in an cell next to the dam (at the upstream side, see Fig. 1b) is h_i, then the following velocity constraint is imposed to the upstream cells next to the dam

$$v = \begin{cases} 0 & if \quad h_i < h_d \\ calculate \quad value & if \quad h_i >= h_d \end{cases} \tag{11}$$

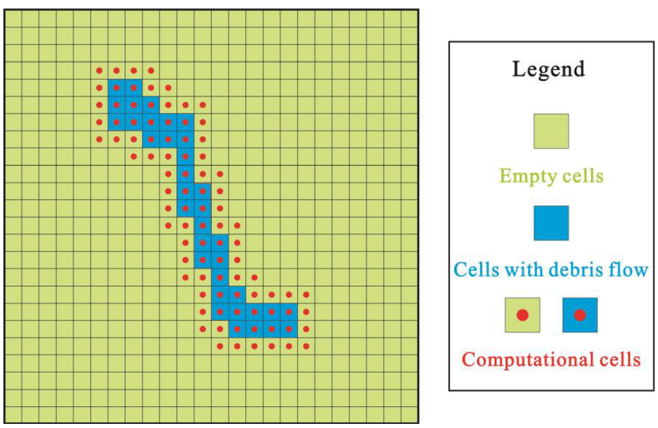

Fig. 2 Dynamic computational cells used in the model to reduce computational consumption

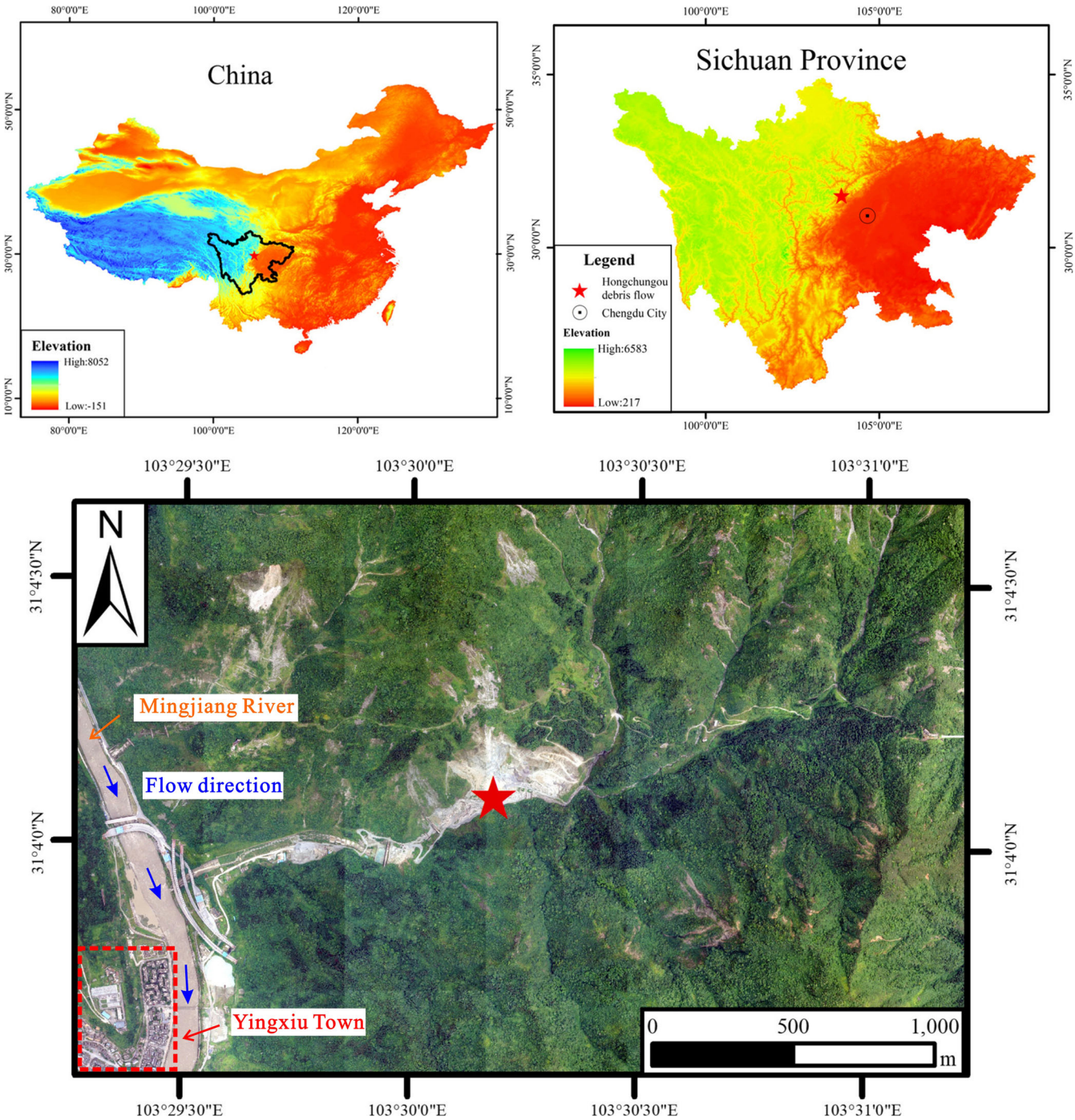

Fig. 3 Location of the Hongchun gully in China (N 31°04′01.1″, E 103°29′32.7″)

Equation (11) implies that when the thickness of the debris flow is lower than the height of the dam, it will not be able to flood over the top of the dam. In this situation, the debris flow will accumulate behind the dam, until it becomes thick enough to surpass the dam to a certain extent. By this way, the impeding effect of the dam can naturally be reflected. Figure 1 also schematically illustrates the importance of considering bed entrainment. The outcomes are likely to be totally different when considering or not considering bed entrainment. As illustrated by Fig.1, the outcome without considering bed entrainment shows that the check dam succeeds in preventing the debris flow (Fig. 1b), while the result of that considering entrainment is totally opposite (Fig. 1c). Therefore, it is necessary to take bed entrainment into account when assessing the effect of check dams.

Noticeably, debris flows usually propagate along long, narrow and meandering gullies. Therefore, only a small area in the channels is occupied by the debris mass. However, when simulating the dynamic process of a huge debris flow, a large rectangular computational region

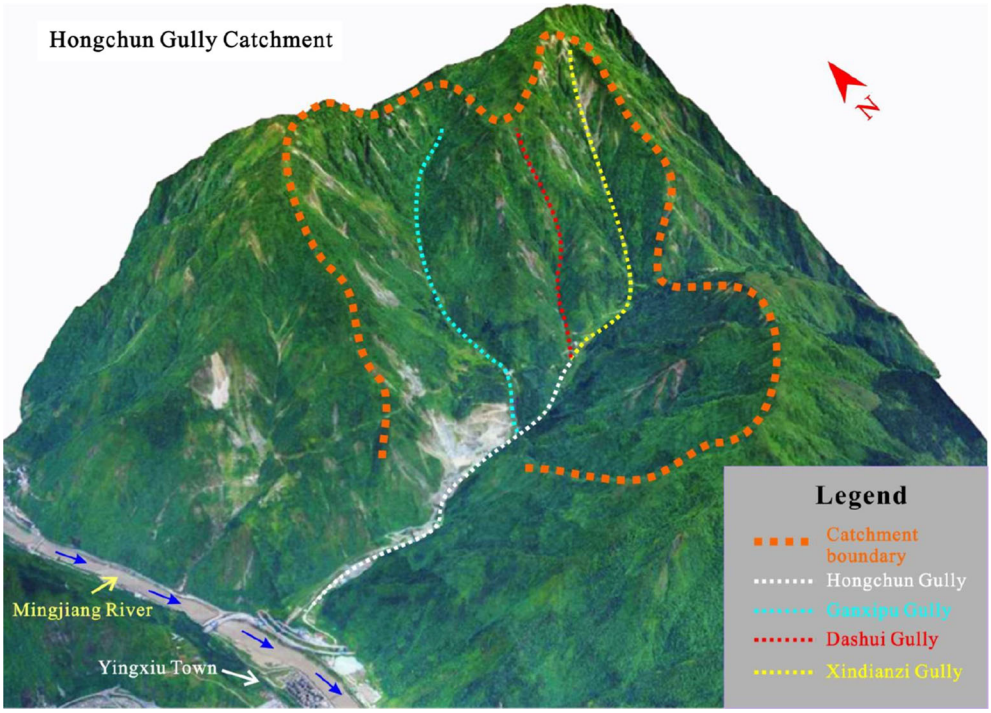

Fig. 4 Panorama of the Hongchun gully catchment

which should contain all the debris flow gullies is usually selected for conducting the simulation. This means that most cells in the computational region are empty and theoretically unnecessary to participate in calculation. In the traditional computational scheme (Ouyang et al. 2013; Shen et al. 2018a), most of these cells still involve in calculation, resulting in a large waste of computational resources and times. To make the model more suitable for simulating huge debris flows, an improved computational scheme is adopted in this paper, as shown in Fig. 2. In the new scheme, the computational cells evolve automatically according to the propagation of a debris flow. Only those cells with debris mass inside participate in the simulation. This method could reduce the computational effort to almost the minimum level, and it can easily achieve by applying the following logical condition

$$\text{condition} = \begin{cases} \text{skip} & \text{if } h(i,j) = 0 \text{ and with empty neighbors} \\ \text{calculate} & \text{if otherwise} \end{cases} \tag{12}$$

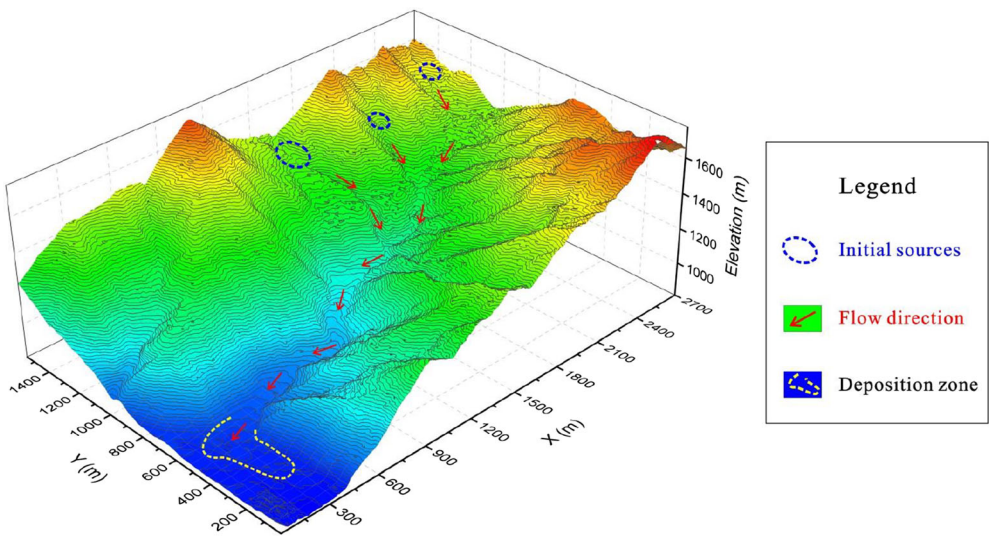

Fig. 5 3D digital elevation model, coordinates setup and initial debris mass distributions in the simulation

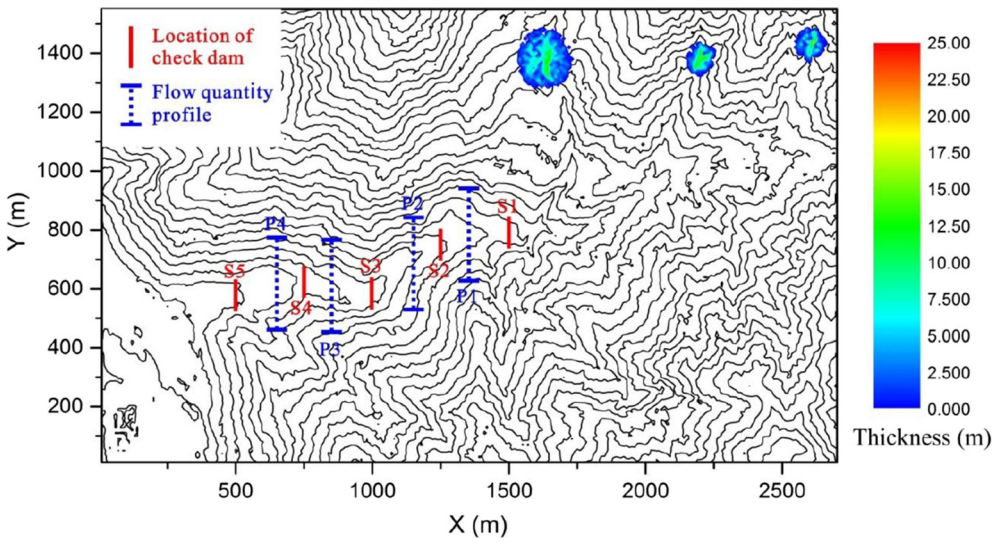

Fig. 6 Locations of the check dams and the profiles for monitoring flow quantity

Equation (12) indicates that all those empty cells whose all neighbors are also empty will be skipped in the calculation.

The constraint of the check dam and the new computational scheme are incorporated into a modified finite difference code developed by Shen et al. (2018a, b) to formulate an improved depth-averaged model. This improved model is designed for modeling long run-out debris flows with accounting for the influences of bed entrainment and check dams, and it is applied in modeling the following debris flow case.

Modeling of the Hongchun gully debris flow

Introduction of the Hongchun gully debris flow

The Hongchun gully is a debris flow gully about 500 m to the northeast of the Yingxiu Town — the epicentral zone of the 2008 huge Wenchuan earthquake, as shown in Fig. 3. The outlet of the gully is next to the Mingjiang River, and the Yingxiu Town is located at the west bank of the river.

During August 12 to 14, 2010, this region experienced a heavy rainfall event with an accumulative precipitation of 162.1 mm (Xu et al. 2012). This rainfall finally triggered hundreds of channelized debris flows (Tang et al. 2012b) near the Yingxiu Town. Among them, the Hongchun gully debris flow occurred on August 14 at 3 a.m. may be the most disastrous one in terms of its huge scale and serious consequence. This debris flow was initiated by the runoff erosion of the landslide deposits in the three branch channels of the Hongchun gully. An estimated total volume of 700,000–800,000 m^3 of debris mass involved in this event, and about half of the debris mass (350,000–400,000 m^3) rushed out the outlet of the gully and blocked the Mingjiang River. As a consequence, the Mingjiang River changed its course, causing a flood in the newly reconstructed Yingxiu Town (Tang et al. 2011) and the deaths or disappearances of 17 people.

Figure 4 is the panorama of the Hongchun gully catchment. The total area of this catchment is 5.35 km^2, and the length of the main gully is about 3.6 km. The elevation of the gully is between 880 m and 1700 m, and it has an average slope gradient of about 36%. The upstream of the Hongchun gully consists of three branch channels. They are the Ganxipu gully, the Dashui gully and the Xindianzi gully from west to east, respectively. All these gullies involved in the August 14 event (Ouyang et al. 2015), and the initial volumes of the debris mass in these three gullies were 112,000 m^3 (Ganxipu gully), 39,000 m^3 (Dashui gully), and 32,000 m^3 (Xindianzi gully), respectively. Therefore, the initial total volume of this debris flow was estimated to be about 183,000 m^3, and about 517,000–617,000 m^3 of debris mass was entrained along the path. Field survey shows that the phenomenon of bed entrainment is very obvious along the gully, and a maximum entrainment depth of about 20 m occurred in this gully (Ouyang et al. 2015).

Simulation set-ups

A digital elevation model (DEM) with a resolution of 10 m is built up according to the surveying data. The DEM, coordinates setup, and initial distributions of debris mass in the simulation are illustrated in Fig. 5. The computational region is 2700 m in the x direction and 1550 m in the y direction. The sizes of cells in both the x and y directions are 10 m. The maximum time step for simulating this case is 0.02 s.

To study the influence of check dam location on the dynamic and entrainment processes of the Hongchun gully debris flow, five locations along the main gully are selected as the possible locations for constructing check dams. These locations represent five

Table 1 Locations of check dams

Dam location	S1	S2	S3	S4	S5
Center coordinates	X = 1500 m Y = 780 m	X = 1250 m Y = 740 m	X = 1000 m Y = 580 m	X = 750 m Y = 620 m	X = 500 m Y = 570 m

Table 2 Locations of profiles for monitoring flow quantity

Profile	P1	P2	P3	P4
Location	X = 1350 m	X = 1150 m	X = 850 m	X = 650 m

different scenarios of check dam setups: constructing at upper gully, upper and middle gully, middle gully, middle and lower gully, and lower gully, respectively. Four profiles are selected to monitoring the changes of flow quantity under the effect of check dams. The locations of check dams and monitoring profiles are illustrated in Fig. 6, and their coordinates are given in Tables 1 and 2, respectively.

Totally 20 groups of simulations are conducted, and the simulation setups for all these groups are listed in Table 3. Among them, NE and WE represent the situations before constructing check dams, and they are used to calibrate the rheological parameters and analyze the influence of bed entrainment on the August 14 debris flow event. All other groups represent the situations with imaginary check dams, and they are utilized to explore the possible influences of check dams on the dynamic and entrainment processes of this debris flow.

The parameters adopted in these simulations are given in Table 4. Among these parameters, the value of the basal frictional angle, turbulent coefficient (its value here corresponds to a Chezy coefficient value of 12), internal frictional angle and bulk density of the Hongchun gully debris flow are given according to Ouyang et al. (2015). The erodible mass is assumed to have similar property with the debris flow, so its basal friction angle and bulk density values take the same values as those of the debris flow. The pore pressure coefficient r_u represents the ratio of the pore pressure to the total stress in the soil. However, the pore pressure in a debris flow is usually much larger than the static pore water pressure because excess pore water pressure will generate in the rapid motion. The value of the pore pressure coefficient takes 0.8 for the debris flow, which is a typical value according to debris flow experiments. A relatively higher pore pressure coefficient value is allocated to the erodible mass given it tends to be in undrained condition under rapid shear action. In addition, a small cohesion value is given to the erodible mass to prevent materials on steep slopes being entrained (Ouyang et al. 2015).

Simulation results

Simulation results of the August 14 event

The simulated run-out processes of the debris flow in group NE and WE are shown in Fig. 7. The simulated distributions of debris mass at two times are compared. These two times represent the middle and final stages of the debris flow motion, respectively. At $t = 100$ s, the run-out distance in WE is obviously larger (about 200 m) than that in NE, indicating than bed entrainment

Table 3 Setups in different simulation groups

Simulation groups	Entrainment	Dam numbers	Dam height	Dam position
NE	No	0	–	–
WE	Yes	0	–	–
G0	No	1	20 m	S2
G1	Yes	1	10 m	S1
G2	Yes	1	10 m	S2
G3	Yes	1	10 m	S3
G4	Yes	1	10 m	S4
G5	Yes	1	10 m	S5
G6	Yes	1	20 m	S1
G7	Yes	1	20 m	S2
G8	Yes	1	20 m	S3
G9	Yes	1	20 m	S4
G10	Yes	1	20 m	S5
G11	Yes	2	20 m	S1 and S3
G12	Yes	2	20 m	S1 and S4
G13	Yes	2	20 m	S1 and S5
G14	Yes	2	20 m	S2 and S4
G15	Yes	2	20 m	S2 and S5
G16	Yes	2	20 m	S3 and S5
G17	Yes	3	20 m	S1, S3, and S5

Table 4 Parameters used in simulating the Hongchun gully debris flow

Parameters	Pore pressure coefficient r_u	Basal friction angle ϕ (°)	Turbulent coefficient ξ	Basal cohesion c (kPa)	Internal friction angle ϕ_i (°)	Bulk density ρ (g/cm^3)
Debris mass	0.8	12	2850	–	35	2.02
Erodible mass	0.95	12	–	2.1	–	2.02

significantly facilitates the motion of this debris flow. In addition, the thickness of the debris flow along the main gully in WE (Fig. 7c) is also much thicker than that of NE (Fig. 7a), which means that a noticeable expansion of the scale of the debris flow occurs due to entrainment. At $t = 1000$ s, the main propagation process has finished in both WE and NE, but the simulated final deposits of them show totally different characters. Although the debris flow rushes out from the outlet in both situations, the volume of the rushing out debris mass in WE (about 349,000 m^3, see Fig. 7d) is about ten times as much as that in NE (about 35,000 m^3, see Fig. 7b). Without considering bed entrainment, the debris flow turns out to be incapable of blocking the Mingjiang River. In

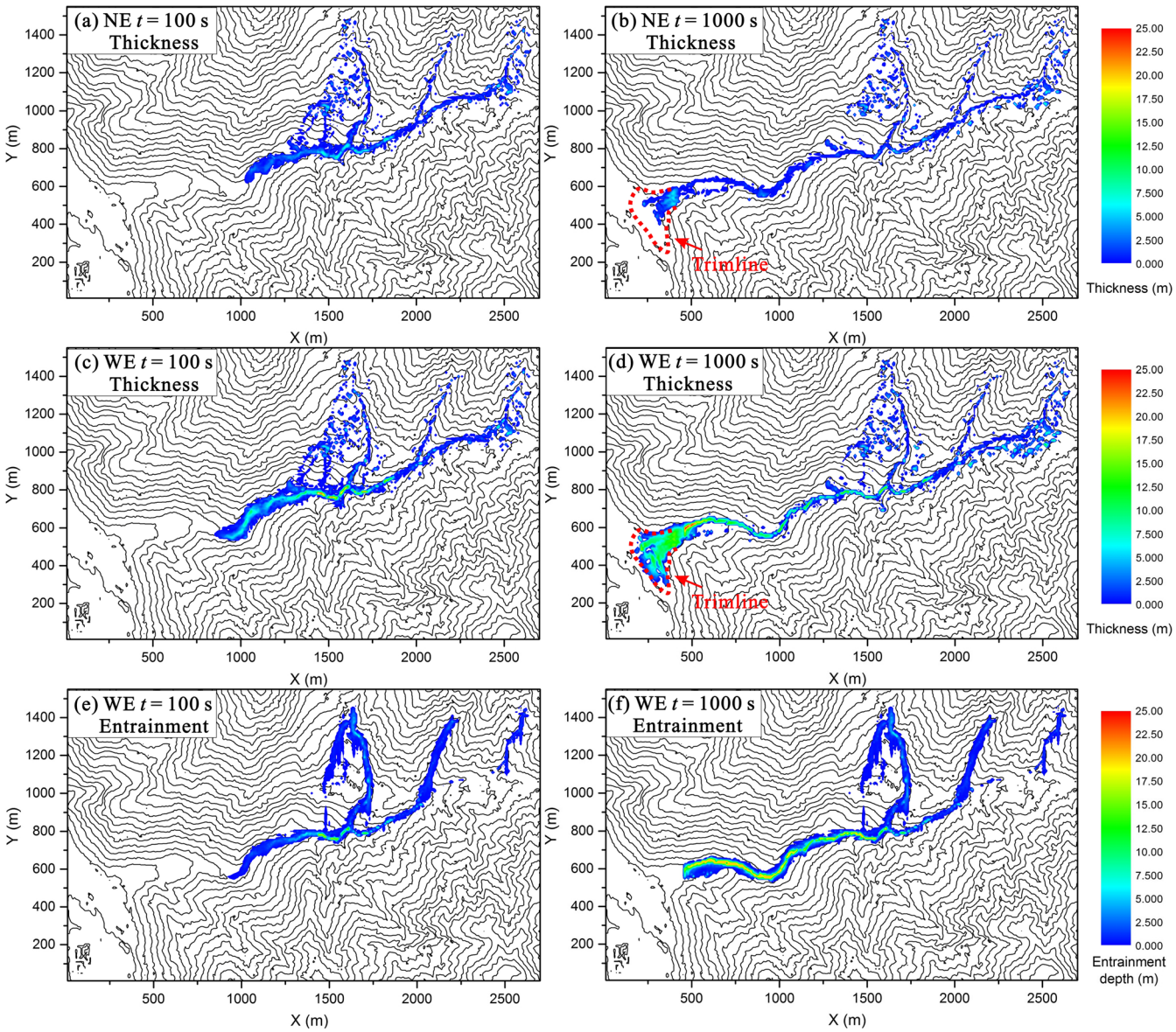

Fig. 7 Simulated deposition and entrainment processes without check dams. **a** and **b** are the thicknesses of debris flow at $t = 100$ s and 1000 s without considering entrainment (NE), respectively, **c** and **d** are the thicknesses of debris flow at $t = 100$ s and 1000 s considering entrainment (WE), respectively, and **e** and **f** are the entrainment depths at $t = 100$ s and 1000 s, respectively

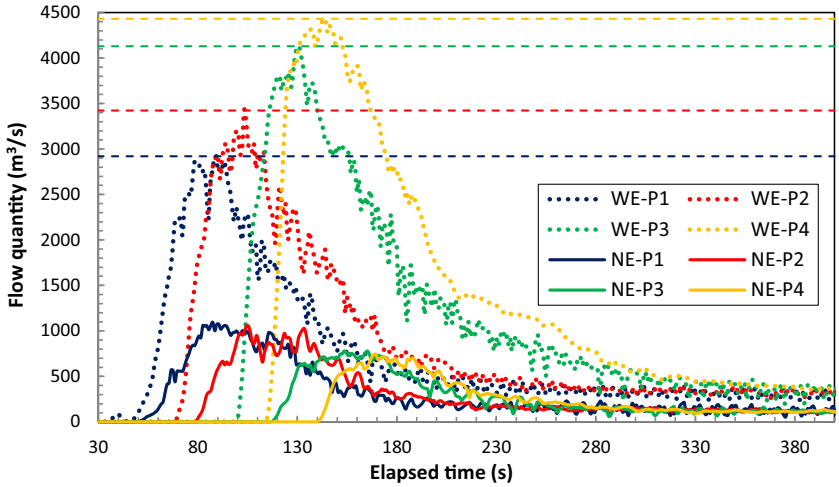

Fig. 8 Simulated flow quantities at four profiles along the gully without check dams, WE: considering bed entrainment, NE: without bed entrainment

comparison, the simulated final deposit considering bed entrainment matches quite well with the measured data in terms of run-out distance, covering area, and the shape and thickness (about 5–10 m) of the debris dam. The entrainment depths in WE at the two times are also presented in Fig. 7. It shows that the peak entrainment depth (about 20 m) appears at the bottom of the main gully, while the entrainment depth decreases gradually from the gully bottom to the lateral slopes. According to field observation, the most apparent bed entrainment occurred in the middle section of the main gully, with an average thickness of 6–10 m and the maximum depth about 20 m (Ouyang et al. 2015), while the entrainment depth in the three branch gullies are relatively insignificant with an average thickness of only 1–2 m. The simulated entrainment distribution (Fig. 7d) shows good accordance with

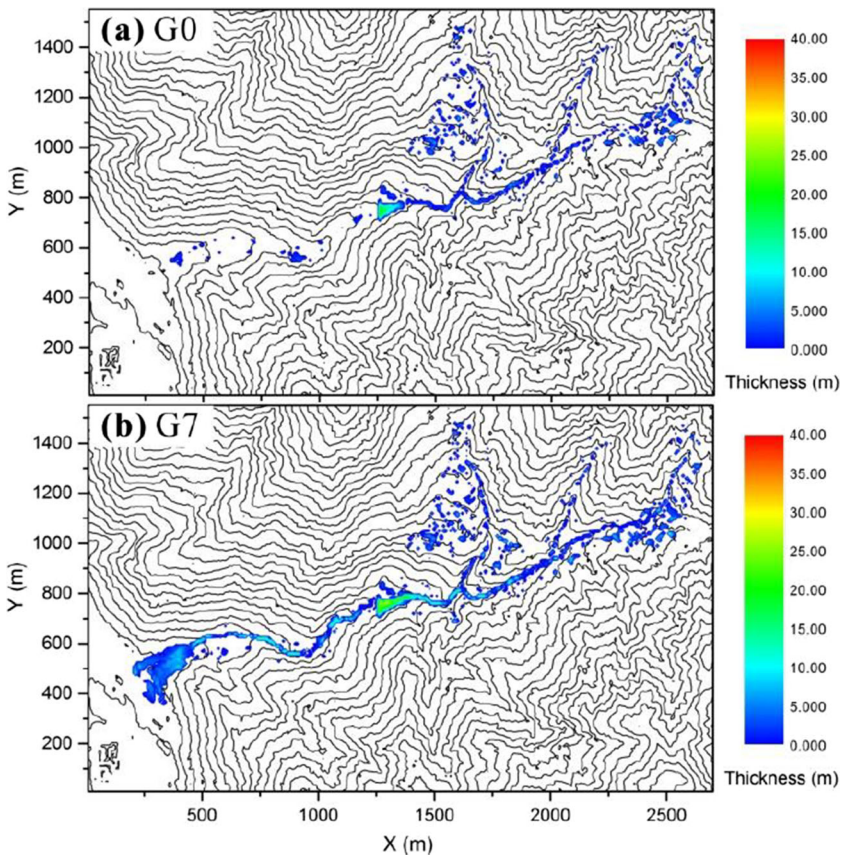

Fig. 9 Comparison of the prevention effect of check dam between G0 (with a 20 m check dam at S2 and without entrainment) and G7 (with a check dam 20 m high at S2 and considering entrainment)

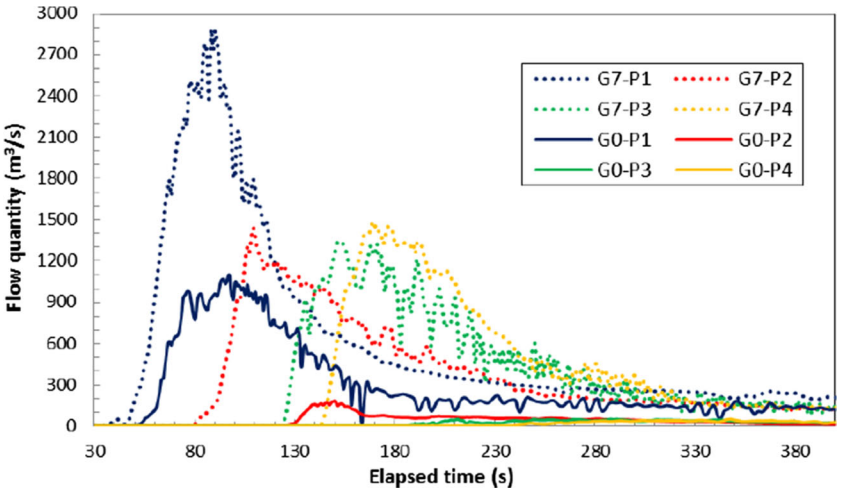

Fig. 10 Comparison of the flow quantities at four profiles between G0 (not considering entrainment) and G7 (considering entrainment)

this observation. The final volume of the debris flow reaches 763,000 m^3, this value also agrees well with the estimated final volume of 700,000 m^3 to 800,000 m^3. The above analysis indicates the improved model adopted here can properly depict the entrainment process of the Hongchun gully debris flow, and the simulation accuracy is quite good.

The simulated flow quantities at the four monitoring profiles in these two groups are compared in Fig. 8. The results of the two groups show totally opposite patterns. When considering bed entrainment, the peak flow quantity values increase gradually from upstream to downstream. This is because the thickness of the debris flow grows quickly by entraining loose materials. However, the peak values show a decreasing tendency when without obtaining new mass by entrainment, because in this situation the thickness of the debris flow is likely to become thinner at downstream. In general, it illustrates that bed entrainment boosts the magnitude of the flow quantity by 3 (P1) to 6 (P4) times in this gully. Additionally, in WE the arrival times of the debris flow at the four profiles are also earlier than their counterparts in NE, which means the debris flow will run faster under the influence of bed entrainment.

Simulation results with the effect of check dam

The results of G7 and G0 are compared first to check the influence of check dam on the dynamic process of this debris flow in the situations considering and not considering bed entrainment. In G7 and G0, a check dam (20 m high) is built up at the upper and middle gully (S2). The results show that in both groups the check dam has an obvious impeding effect on the debris flow, but their outcomes are different. When neglecting bed entrainment (G0, see Fig. 9a), the check dam is shown to perform quite well in preventing the debris flow. Although a small volume of debris mass overrides the dam, almost no debris mass rushes out the outlet. However, an opposite conclusion is illustrated by the result of considering entrainment (G7). In spite of a large amount of the debris mass has been resisted by the dam, the rest debris mass surpassed the dam still turns into a relatively large debris flow by entrainment. The results above indicate that the prevention effect of a check dam is likely to be overestimated if the bed entrainment is not taken into account, which may result in the inadequate design of prevention measures.

The flow quantities at the monitoring profiles in G0 and G7 are compared in Fig. 10. The results show that check dam can significantly reduce the flow quantity of the debris flow at the downstream side of the dam in both situations. In G7, the flow quantity of the debris flow decreases sharply first when it passes the dam under the hindering effect, and then its value increases gradually after surmounting the dam due to entrainment. This explains why the final scale of the debris flow is still big despite a great amount of debris mass has been stopped by the dam. However, the results of G0 show that the flow quantity continuously decreases after overriding the dam.

To further investigate the influence of the locations of check dams on the dynamic and bed entrainment processes of this debris flow, the simulation results of different situations with single dam and multiple dams constructing at different locations are analyzed and presented (Fig. 11).

Figure 11a–c are the results of the situations with one check dam of 20 m high located at S1 (upper gully), S3 (middle gully) and S5 (lower gully), respectively. The performance of the check dam is best when it is located at downstream. Two factors are likely to contribute to this result. The first one is that the velocity of the debris flow at downstream is relatively smaller than that at upstream. Another reason is that the topography at downstream is wider and plainer, so the volume capacity of the check dam is larger than that at upstream. The result of G8 is the worst. This is because the volume capacity of the check dam reservoir at the middle stream is not big, while at the same time the velocity of debris flow is relatively high. In comparison, the check dam achieves a modest effect because it constrains the entrainment scale of the debris flow by reducing the flow quantity at an early stage.

The results of multiple dams (Fig. 11d-h) show similar patterns. When the check dams are constructed at relatively upper parts of the gully (G11 and G14), the prevention effect tends to be better than other situations (G16 and G13) due to the scale of bed entrainment is effectively constrained by the dams. In contrast, the prevention effects of check dams constructing at relatively lower parts of the gully (G16 and G13) is relatively weak, since the scale of the debris flow has already boosted by entraining the loose materials at upstream.

In order to show the impact of check dam on the final entrainment scale of the debris flow, the simulated entrainment depths in

G6, G10, and G11 are presented in Fig. 12. The results agree with the above analysis that constructing check dam at upstream performs better in controlling the final entrainment scale.

The flow quantities at the monitoring profiles in G6, G8, G10, and G14 are compared to reveal the influence of check dam on the flow quantity of this debris flow (Fig. 13). In these situations, the constraining effect of check dam significantly reduces the magnitude of the flow quantity at the downstream of the dam. This reducing effect tends to be stronger when the dam is located at upstream (Fig. 13c) rather than at middle stream (Fig. 13b) and downstream (Fig. 13a).

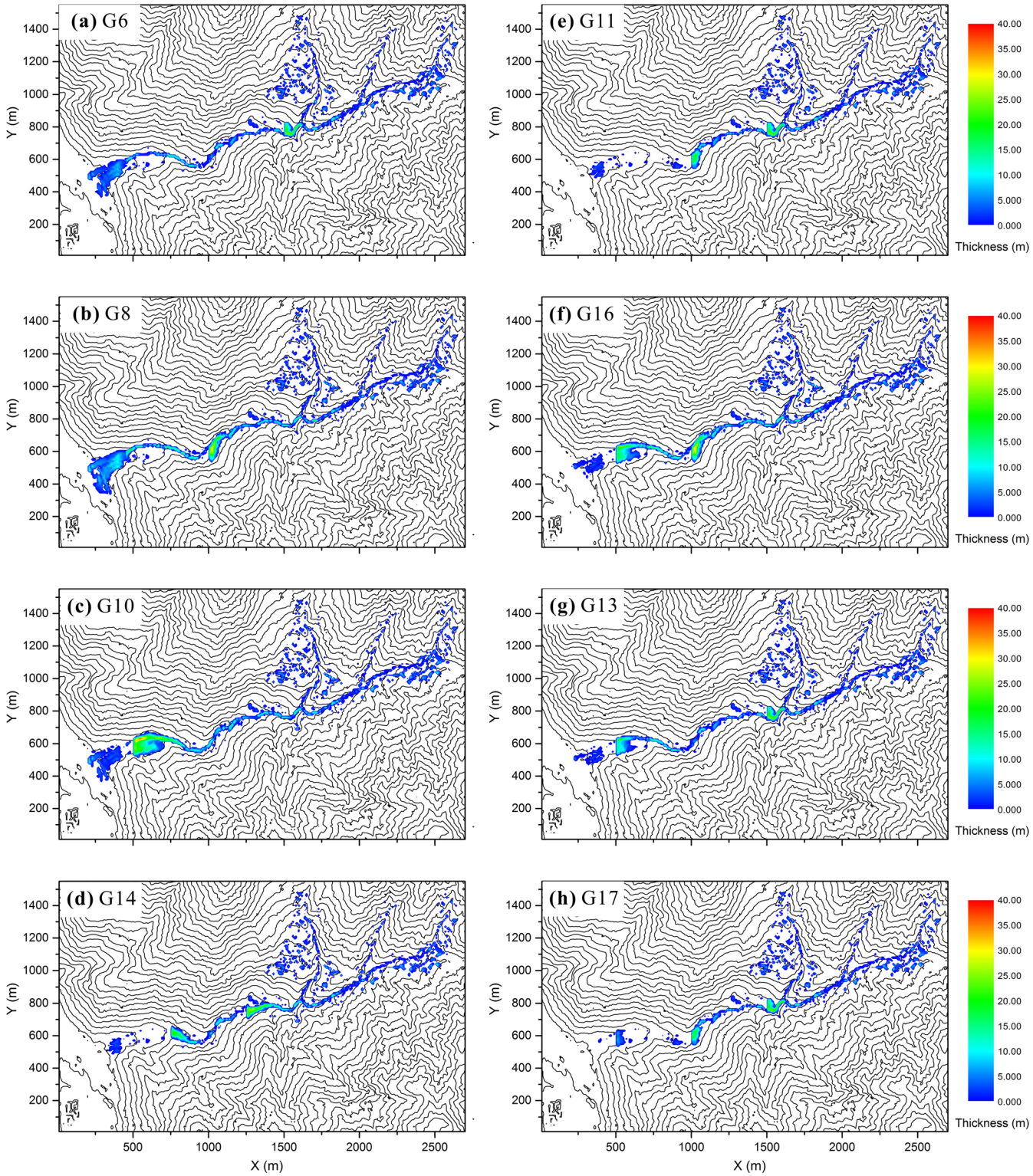

Fig. 11 Simulated final thickness of the debris deposit under the influence of check dam in several different situations

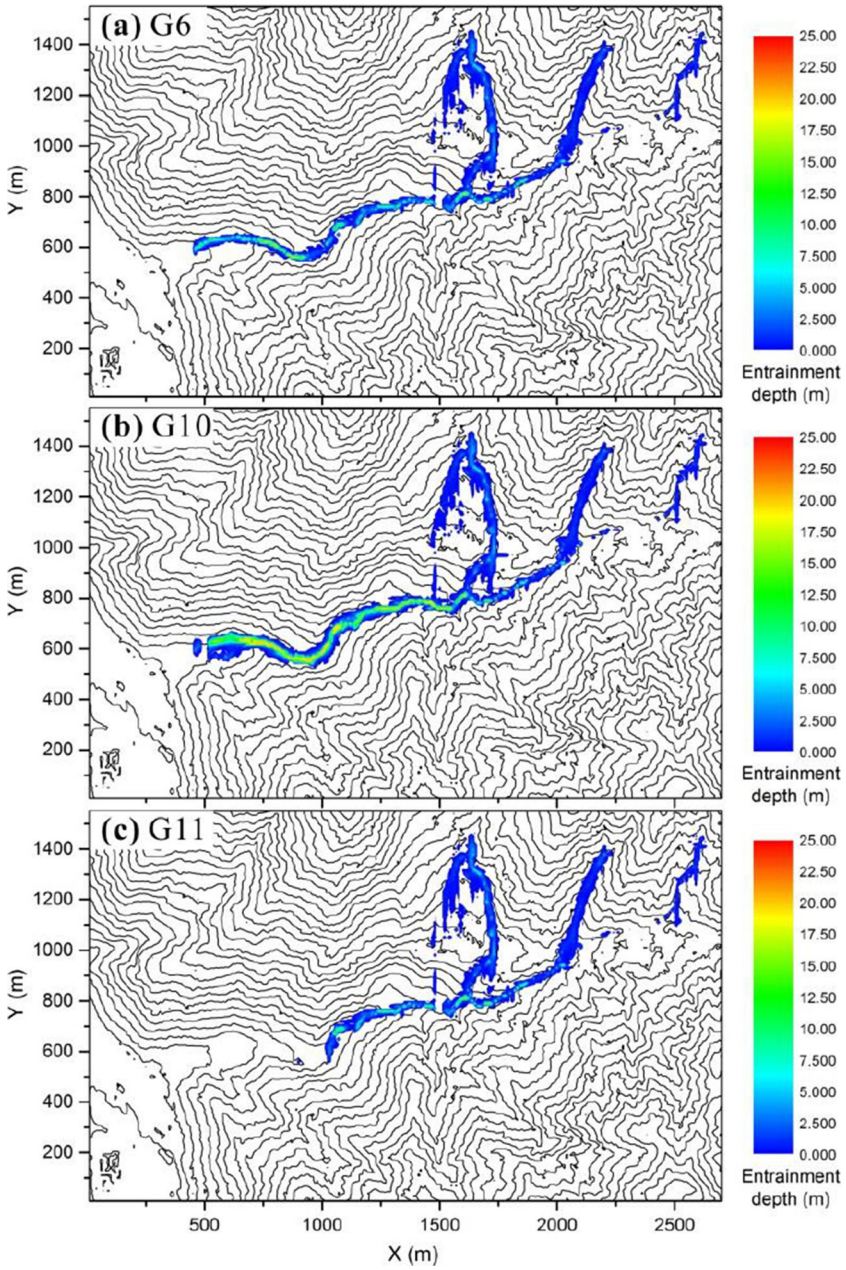

Fig. 12 Simulated entrainment depths in the catchment in G6, G10, and G11

Apart from that, this constraining effect delays the arrival time of the debris flow at downstream (P4), and it shows that the arrival time tends to be later when the check dam is constructed at upstream instead of at downstream. For example, the arrival time at P4 in G6 is 150.3 s, while those in G8 and G10 are 141.1 s and 116.1 s, respectively.

Some simulated characteristic data in all these simulation groups, including the entrainment volume, volume of the deposit rushing out the gully, and peak flow quantities and arrival times of the debris flow at the monitoring profiles, are provided in Table 5. These data agree well with the above analysis regarding to the simulation results with the effect of check dam.

Finally, the total volume evolution processes of the debris flow under the effect of bed entrainment in several different groups are compared in Fig. 14. It also shows that the dam does have great influence on the entrainment rate of the debris flow. The groups constructing the check dams at the upper gully tend to have a smaller total volume of final debris deposit. In addition, the data in Table 5 show that those groups with less bed entrainment volume (or total volume) tend to have less debris mass rushing out the outlet of the gully.

Discussions

Twenty groups of simulations with different bed entrainment and check dam setups are conducted by using the improved model proposed in this paper. The debris flow event occurred in the Hongchun gully in 2010 is analyzed by the model, and the results of considering and not considering bed entrainment are compared. It shows that bed entrainment has a dominant influence on the final scale and dynamics

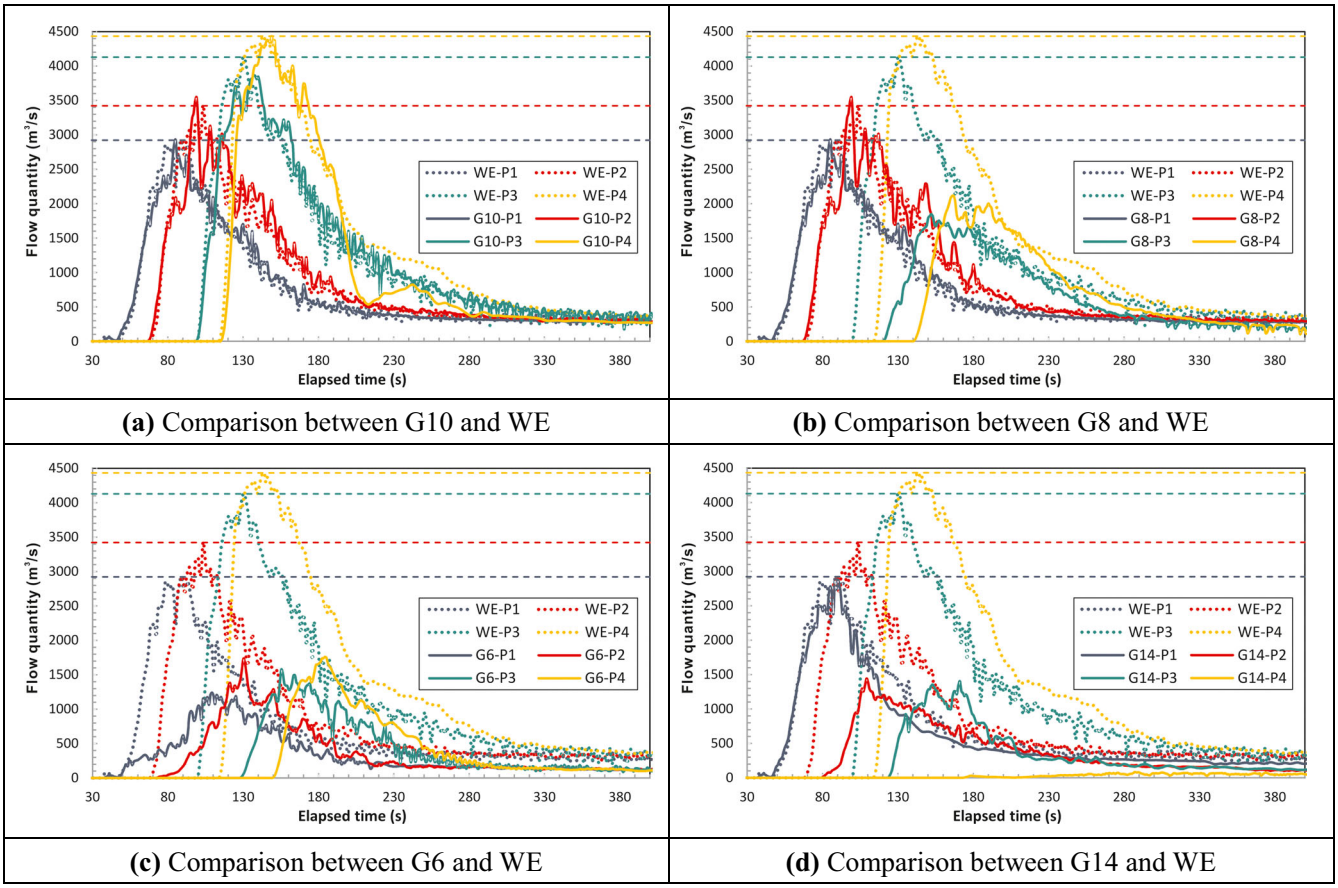

(a) Comparison between G10 and WE

(b) Comparison between G8 and WE

(c) Comparison between G6 and WE

(d) Comparison between G14 and WE

Fig. 13 Influence of check dam on the flow quantities at four profiles

of this debris flow. Without bed entrainment, this debris flow could not develop into a huge catastrophic event which blocked the Mingjiang River. The simulation result of considering bed entrainment matches quite well with the field data, demonstrating that the model performs well in modeling this debris flow. In addition, the scale of this debris flow and its flow quantity in the gully expand violently by entraining loose materials along the gully, so it is necessary to account for bed entrainment when designing check dams in this gully. Otherwise, the prevention effect of a check dam may be significantly overestimated, thus leading to an inadequate design of prevention measures. The results of those groups with check dams inside the gully indicate that the check dams can obviously alter the bed entrainment character and the dynamic process of this debris flow. The flow quantity at the downstream of the dam and the entrainment scale will be reduced greatly due to the impeding effect of the dam, while the arrival time at downstream of the gully will be delayed.

In the improved model, the effect of dam is taken as a velocity constraint which is imposed on the upstream cells next to the dam (Eq. (11)). Actually, the interactive process between a debris flow and a dam is much complicated. During the first few seconds when the debris flow impacts on the wall of the dam, it may produce a vertical jet-like bulge (Armanini 1997), or even be reflected back by the wall, turning the flow into a very complex turbulence. This phenomenon is important for analyzing the mechanical impact of the debris flow on structures (Wang et al. 2018), and need to be accounted when designing the structure strength of the check dams. However, the main purpose of this paper is to study the prevention effect of check dam and its interactive influences with bed entrainment and the dynamics of a debris flow, so the check dams are simply taken as a rigid body here. Furthermore, although the vertical surging process may transport part of the debris mass over the check dam, the amount is quite limited because this process is usually very short. The main body will accumulate behind the dam until surpassing the top of the dam. Therefore, the rigid constraint assumption about the check dam is reasonable for the present study, and it shows a good numerical effect in reflecting the impeding effect of the check dams according to the simulation results. Comparing with some other widely used depth-averaged models (Hungr and McDougall 2009; Ouyang et al. 2013; Pastor et al. 2009; Sassa et al. 2010), our model is similar to them in terms of the basic governing equations for depicting the run-out process of debris flows. However, these models are mainly designed to simulate and assess the run-out processes of rapid flow-like landslides on green field without artificial barriers, and the impeding effect of check dams cannot be properly reflected by them. By contrast, the improved model here introduces a rigid constraint condition to account for the effect of check dams, expanding the application range of the depth-averaged models from risk assessment to the design and assessment of check dams in debris flow gullies. Additionally, although a few other previous studies (Chen et al. 2019; Cuomo et al. 2019; Dai et al. 2017; Liu et al. 2013) have accounted for the effect of artificial barriers on the

Table 5 Simulation results of entrainment, deposition and flow characters at monitoring profiles in different groups

Simulation 7groups	Entrainment volume (m^3)	Deposit rushing out outlet(m^3)	Peak volume flow quantity (m^3/s)				Arrival time of debris flow (s)			
			P1	P2	P3	P4	P1	P2	P3	P4
NE	0	35,000	1095	1055	778	743	46.6	78.5	117.5	140.5
WE	580,000	349,000	2921	3422	4129	4432	35.5	68.4	99.2	114.2
G0	0	2000	1097	182	50	49	47.5	125.4	187.4	239.4
G1	466,000	241,000	1878	2348	2689	3053	37.5	71.3	106.2	123.2
G2	515,000	266,000	2993	2865	2893	3103	35.5	71.3	103.2	119.2
G3	539,000	287,000	2921	3381	3481	3328	35.5	68.4	103.2	118.2
G4	515,000	235,000	2921	3422	3947	2793	35.5	68.4	99.2	116.1
G5	552,000	234,000	2921	3422	4129	4468	35.5	68.4	99.2	114.1
G6	272,000	92,000	1240	1739	1577	1761	37.5	72.3	128.3	150.3
G7	334,000	103,000	2875	1442	1345	1489	36.5	80.2	124.1	143.2
G8	458,000	171,000	2928	3543	1848	2114	36.5	67.3	119.1	141.1
G9	442,000	129,000	2928	3544	3983	1341	36.5	67.3	99.2	125.1
G10	543,000	50,000	2928	3544	3864	4434	36.5	67.3	99.2	116.1
G11	187,000	9000	1240	1724	203	141	37.5	72.3	195.3	235.3
G12	214,000	5000	1240	1739	1464	78	37.5	72.3	128.3	174.3
G13	263,000	11,000	1240	1739	1577	1754	37.5	72.3	128.3	150.3
G14	271,000	10,000	2875	1442	1402	83	36.5	80.2	124.2	174.2
G15	324,000	13,000	2875	1442	1361	1613	36.5	80.2	124.2	144.2
G16	428,000	16,000	2928	3541	2056	2203	36.5	67.3	119.1	140.1
G17	187,000	1000	1240	1724	203	141	37.5	72.3	195.3	235.3

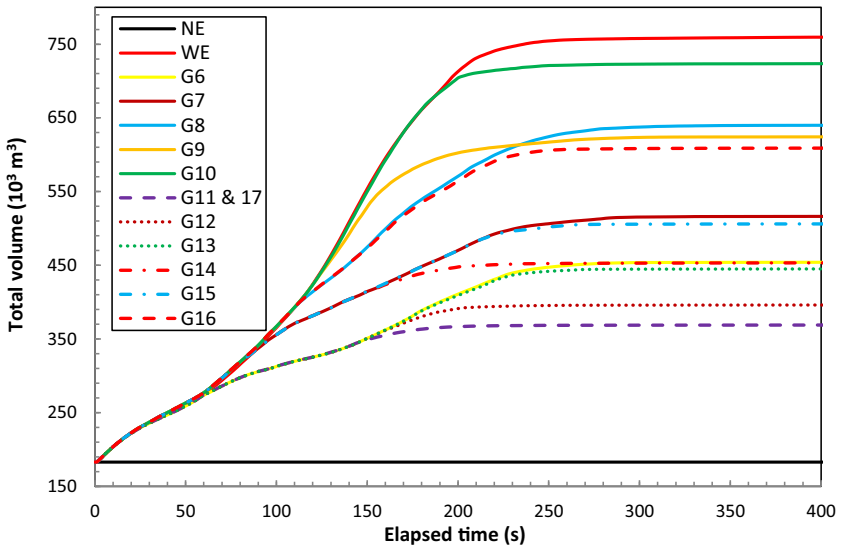

Fig. 14 Simulated total volume evolution curves of the debris flow in different groups

dynamics of flow-like landslides, they did not consider bed entrainment or did not account for its interactive effects with check dams. Therefore, this paper is also helpful in better understanding the effects of check dams on the bed entrainment and dynamic processes of debris flows. Another improvement adopted in this paper regarding computational scheme performs well in promoting computational efficiency. In some models (Sassa et al. 2010), the computational region is a fixed rectangular area with debris flows run inside it, while in some other models (Liu and Huang 2006; Ouyang et al. 2013; Shen et al. 2018a) the computational region is a dynamic rectangular area whose size changes with the propagation of debris flows. In both cases, plenty of empty cells will involve in the calculation, resulting in the waste of a great amount of computational time. In comparison, the improved computation method adopted here only calculates the cells with debris mass in them, so that it can greatly reduce the computational cost. The total computational time for calculating 50,000 time steps in simulating the present debris flow (cell numbers are 41,850) is about 3 h and 15 min, while the time consumption is more than 6 times (20 h and 40 min) of the new scheme if the old scheme (Ouyang et al. 2013, Shen et al. 2018a) is adopted. These two improvements make the new model more suitable for modeling the dynamic process of a long run-out debris flow with obviously bed entrainment phenomenon and check dams in the gully. The current simulations were conducted on an ordinary desktop with a CUP produced by Intel (Intel (R) Core (TM) i7-4770 @ 3.40 GHz). The computation time can be further reduced by adopting high-performance server with better CPU or adopting parallel computing techniques, which will not be addressed this paper.

On the other hand, since the interaction between debris flows and check dams is a very complex phenomenon, it is still far from being fully understood currently. For instance, it is possible that the property (i.e., bulk density, components, and rheology) of a debris flow will change after surpassing a check dam. Such a complex process is very difficult to consider in a numerical model, so in the present study it is neglected for simplicity. The phenomena such as the property change of a debris flow due to the filtering effect of check dams are out of the scope of this paper, while further researches about them are needed in the future in order to improve the applicability of this model.

Conclusions

An improved numerical model is proposed in this paper to study the influence of check dams on the dynamic and bed entrainment processes of debris flow. The run-out process of the 2010 catastrophic Hongcuan gully debris flow is simulated by the new model, and the effects of check dams on the dynamic and bed entrainment processes of this debris flow are analyzed. The simulation results are presented and discussed, and following conclusions can be obtained.

(1). Bed entrainment plays a dominant role in the formational and run-out processes of the Hongchun gully debris flow. Without bed entrainment, this debris flow could not evolve into a huge debris flow that blocked the Mingjiang River. The simulation results of the debris flow when considering bed entrainment agree well with the field data, indicating that the improved model has good numerical accuracy in modeling this debris flow.

(2). Bed entrainment significantly alters the flow characters of this debris flow. Without bed entrainment, the peak value of flow quantity tends to decrease gradually from the upstream of the gully to the downstream, while the peak value will show an opposite tendency if bed entrainment is significant. Therefore, bed entrainment should be considered in assessing the prevention effect of check dams to prevent inadequate design of them.

(3). Check dams can greatly change the dynamic and bed entrainment processes of this debris flow. They reduce the flow quantity and bed entrainment scale of the debris flow at the downstream side of the check dam, delaying the arrival time of the debris flow at downstream. Additionally, by effectively constraining the bed entrainment scale, the prevention effect of check dams tends to be better when they are constructed at the upper part of the gully.

(4). The improved model is shown to be able to properly reflect the impeding effect of check dams, and the new computational scheme adopted in this model can significantly

improve the computation efficiency. These improvements make the present model more suitable in assessing the prevention effect of check dams on huge debris flows with obvious bed entrainment phenomenon.

Acknowledgments

We would like to thank the anonymous referees for careful reading the manuscript and providing insightful comments to help us improve the quality of this paper.

Funding information

This research is funded by the National Key R&D Program of China (Grant No. 2017YFC1501000, 2017YFC1501302), the Natural Science Foundation of China (Grant No. 41790433, 41877266), the State Key Laboratory of Geohazard Prevention and Geoenvironment Protection Independent Research Project (Grant No. SKLGP2016Z014), and the China Scholarship Council (CSC) — University of Bologna Joint Scholarship (File No. 201806560011).

References

Armanini A (1997) On the dynamic impact of debris flows. In: Armanini A, Michiue M (eds) Recent developments on debris flows. Springer, Berlin Heidelberg, pp 208–226. https://doi.org/10.1007/BFb0117770

Berti M, Simoni A (2005) Experimental evidences and numerical modelling of debris flow initiated by channel runoff. Landslides 2:171–182. https://doi.org/10.1007/s10346-005-0062-4

Chen X, Cui P, You Y, Chen J, Li D (2015) Engineering measures for debris flow hazard mitigation in the Wenchuan earthquake area. Eng Geol 194:73–85. https://doi.org/10.1016/j.enggeo.2014.10.002

Chen H-X, Li J, Feng S-J, Gao H-Y, Zhang D-M (2019) Simulation of interactions between debris flow and check dams on three-dimensional terrain. Eng Geol 251:48–62. https://doi.org/10.1016/j.enggeo.2019.02.001

Crosta GB, Imposimato S, Roddeman D (2009) Numerical modelling of entrainment/deposition in rock and debris-avalanches. Eng Geol 109:135–145. https://doi.org/10.1016/j.enggeo.2008.10.004

Cui P, Chen X-Q, Zhu Y-Y, Su F-H, Wei F-Q, Han Y-S, Liu H-J, Zhuang J-Q (2011) The Wenchuan earthquake (may 12, 2008), Sichuan province, China, and resulting geohazards. Nat Hazards 56:19–36. https://doi.org/10.1007/s11069-009-9392-1

Cui P, Zeng C, Lei Y (2015) Experimental analysis on the impact force of viscous debris flow. Earth Surf Process Landf 40:1644–1655. https://doi.org/10.1002/esp.3744

Cuomo S, Pastor M, Capobianco V, Cascini L (2016) Modelling the space–time evolution of bed entrainment for flow-like landslides. Eng Geol 212:10–20. https://doi.org/10.1016/j.enggeo.2016.07.011

Cuomo S, Moretti S, Aversa S (2019) Effects of artificial barriers on the propagation of debris avalanches. Landslides. 16:1077–1087. https://doi.org/10.1007/s10346-019-01155-1

Dai Z, Huang Y, Cheng H, Xu Q (2017) Sph model for fluid–structure interaction and its application to debris flow impact estimation. Landslides 14:917–928. https://doi.org/10.1007/s10346-016-0777-4

Evans SG, Tutubalina OV, Drobyshev VN, Chernomorets SS, McDougall S, Petrakov DA, Hungr O (2009) Catastrophic detachment and high-velocity long-runout flow of Kolka Glacier, caucasus mountains, Russia in 2002. Geomorphology 105:314–321. https://doi.org/10.1016/j.geomorph.2008.10.008

Fraccarollo L, Capart H (2002) Riemann wave description of erosional dam-break flows. J Fluid Mech 461:183–228. https://doi.org/10.1017/S0022112002008455

Frank F, McArdell BW, Huggel C, Vieli A (2015) The importance of entrainment and bulking on debris flow runout modeling: examples from the swiss alps. Nat Hazards Earth Syst Sci 15:2569–2583. https://doi.org/10.5194/nhess-15-2569-2015

Gao L, Zhang LM, Chen HX (2017) Two-dimensional simulation of debris flow impact pressures on buildings. Eng Geol 226:236–244. https://doi.org/10.1016/j.enggeo.2017.06.012

García-Martínez R, López JL (2005) Debris flows of december 1999 in Venezuela. In: Debris-flow hazards and related phenomena. Springer, Berlin Heidelberg, pp 519–538. https://doi.org/10.1007/3-540-27129-5_20

Hu W, Dong XJ, Xu Q, Wang GH, van Asch TWJ, Hicher PY (2016) Initiation processes for run-off generated debris flows in the wenchuan earthquake area of China. Geomorphology 253:468–477. https://doi.org/10.1016/j.geomorph.2015.10.024

Huang R, Li W (2014) Post-earthquake landsliding and long-term impacts in the Wenchuan earthquake area, China. Eng Geol 182:111–120. https://doi.org/10.1016/j.enggeo.2014.07.008

Huang Y, Cheng H, Dai Z, Xu Q, Liu F, Sawada K, Moriguchi S, Yashima A (2015) Sph-based numerical simulation of catastrophic debris flows after the 2008 Wenchuan earthquake. Bull Eng Geol Environ 74:1137–1151. https://doi.org/10.1007/s10064-014-0705-6

Hungr O, Evans SG (2004) Entrainment of debris in rock avalanches: an analysis of a long run-out mechanism. GSA Bull 116:1240–1252. https://doi.org/10.1130/B25362.1

Hungr O, McDougall S (2009) Two numerical models for landslide dynamic analysis. Comput Geosci 35:978–992. https://doi.org/10.1016/j.cageo.2007.12.003

Hungr O, Leroueil S, Picarelli L (2014) The Varnes classification of landslide types, an update. Landslides 11:167–194. https://doi.org/10.1007/s10346-013-0436-y

Iverson RM (2012) Elementary theory of bed-sediment entrainment by debris flows and avalanches. J Geophys Res Earth Surf 117:F03006. https://doi.org/10.1029/2011JF002189

Iverson RM, Ouyang C (2015) Entrainment of bed material by earth-surface mass flows: review and reformulation of depth-integrated theory. Rev Geophys 53:27–58. https://doi.org/10.1002/2013RG000447

Iverson RM, Reid ME, LaHusen RG (1997) Debris-flow mobilization from landslides. Annu Rev Earth Planet Sci 25:85–138. https://doi.org/10.1146/annurev.earth.25.1.85

Iverson RM, Reid ME, Logan M, LaHusen RG, Godt JW, Griswold JP (2010) Positive feedback and momentum growth during debris-flow entrainment of wet bed sediment. Nat Geosci 4:116–121. https://doi.org/10.1038/ngeo1040

Jakob M, Hungr O (2005) Introduction. In: Debris-flow hazards and related phenomena. Springer, Berlin Heidelberg, pp 1–7. https://doi.org/10.1007/3-540-27129-5_1

Kattel P, Kafle J, Fischer J-T, Mergili M, Tuladhar BM, Pudasaini SP (2018) Interaction of two-phase debris flow with obstacles. Eng Geol 242:197–217. https://doi.org/10.1016/j.enggeo.2018.05.023

Liu W, He S (2016) A two-layer model for simulating landslide dam over mobile river beds. Landslides 13:565–576. https://doi.org/10.1007/s10346-015-0585-2

Liu K-F, Huang MC (2006) Numerical simulation of debris flow with application on hazard area mapping. Comput Geosci 10:221–240. https://doi.org/10.1007/s10596-005-9020-4

Liu J, Nakatani K, Mizuyama T (2013) Effect assessment of debris flow mitigation works based on numerical simulation by using kanako 2d. Landslides 10:161–173. https://doi.org/10.1007/s10346-012-0316-x

Liu W, He S, Li X, Xu Q (2016) Two-dimensional landslide dynamic simulation based on a velocity-weakening friction law. Landslides 13:957–965. https://doi.org/10.1007/s10346-015-0632-z

McDougall S, Hungr O (2005) Dynamic modelling of entrainment in rapid landslides. Can Geotech J 42:1437–1448. https://doi.org/10.1139/t05-064

Ouyang C, He S, Xu Q, Luo Y, Zhang W (2013) A maccormack-tvd finite difference method to simulate the mass flow in mountainous terrain with variable computational domain. Comput Geosci 52:1–10. https://doi.org/10.1016/j.cageo.2012.08.024

Ouyang C, He S, Tang C (2015) Numerical analysis of dynamics of debris flow over erodible beds in Wenchuan earthquake-induced area. Eng Geol 194:62–72. https://doi.org/10.1016/j.enggeo.2014.07.012

Parker RN, Densmore AL, Rosser NJ, de Michele M, Li Y, Huang R, Whadcoat S, Petley DN (2011) Mass wasting triggered by the 2008 Wenchuan earthquake is greater than orogenic growth. Nat Geosci 4:449–452. https://doi.org/10.1038/ngeo1154

Pastor M, Haddad B, Sorbino G, Cuomo S, Drempetic V (2009) A depth-integrated, coupled SPH model for flow-like landslides and related phenomena. Int J Numer Anal Methods Geomech 33:143–172. https://doi.org/10.1002/nag.705

Pirulli M, Pastor M (2012) Numerical study on the entrainment of bed material into rapid landslides. Géotechnique 62:959–972. https://doi.org/10.1680/geot.10.P.074

Pitman EB, Le L (2005) A two-fluid model for avalanche and debris flows. Philos Trans R Soc A Math Phys Eng Sci 363:1573–1601. https://doi.org/10.1098/rsta.2005.1596

Ren D (2014) The devastating zhouqu storm-triggered debris flow of august 2010: likely causes and possible trends in a future warming climate. J Geophys Res-Atmos 119:3643–3662. https://doi.org/10.1002/2013jd020881

Sassa K, Nagai O, Solidum R, Yamazaki Y, Ohta H (2010) An integrated model simulating the initiation and motion of earthquake and rain induced rapid landslides and its

application to the 2006 Leyte landslide. Landslides 7:219–236. https://doi.org/10.1007/s10346-010-0230-z
Savage SB, Hutter K (1989) The motion of a finite mass of granular material down a rough incline. J Fluid Mech 199:177–215. https://doi.org/10.1017/S0022112089000340
Scott KM, Macias JL, Naranjo JA, Rodriguez S and McGeehin JP (2001) Catastrophic debris flows transformed from landslides in volcanic terrains: mobility, hazard assessment and mitigation strategies. Professional paper, – edn., doi: https://doi.org/10.3133/pp1630
Shen W, Li T, Li P, Guo J (2018a) A modified finite difference model for the modeling of flowslides. Landslides 15:1577–1593. https://doi.org/10.1007/s10346-018-0980-6
Shen W, Li T, Li P, Shen Y, Lei Y, Guo J (2018b) The influence of the bed entrainment-induced rheology and topography changes on the propagation of flow-like landslides: a numerical investigation. Bull Eng Geol Environ. https://doi.org/10.1007/s10064-018-01447-1
Takahashi T (2009) A review of Japanese debris flow research. Int J Eros Cont Eng 2:1–14. https://doi.org/10.13101/ijece.2.1
Tang C, Zhu J, Ding J, Cui XF, Chen L, Zhang JS (2011) Catastrophic debris flows triggered by a 14 august 2010 rainfall at the epicenter of the Wenchuan earthquake. Landslides 8:485–497. https://doi.org/10.1007/s10346-011-0269-5
Tang C, van Asch TWJ, Chang M, Chen GQ, Zhao XH, Huang XC (2012a) Catastrophic debris flows on 13 august 2010 in the qingping area, southwestern China: the combined effects of a strong earthquake and subsequent rainstorms. Geomorphology 139-140:559–576. https://doi.org/10.1016/j.geomorph.2011.12.021
Tang C, Zhu J, Chang M, Ding J, Qi X (2012b) An empirical–statistical model for predicting debris-flow runout zones in the Wenchuan earthquake area. Quat Int 250:63–73. https://doi.org/10.1016/j.quaint.2010.11.020
Wang D, Chen Z, He S, Liu Y, Tang H (2018) Measuring and estimating the impact pressure of debris flows on bridge piers based on large-scale laboratory experiments. Landslides 15:1331–1345. https://doi.org/10.1007/s10346-018-0944-x
Xu Q, Zhang S, Li W, Van Asch TW (2012) The 13 august 2010 catastrophic debris flows after the 2008 Wenchuan earthquake, China. Nat Hazards Earth Syst Sci 12:201–216. https://doi.org/10.5194/nhess-12-201-2012

W. Shen · D. Wang (✉) · H. Qu
State Key Laboratory of Geohazard Prevention and Geoenvironment Protection,
Chengdu University of Technology,
Chengdu, 610059, Sichuan, China
Email: wangdongpo2014@cdut.edu.cn

W. Shen
e-mail: shenweichd@qq.com

H. Qu
e-mail: 871781461@qq.com

W. Shen
Department of Biological, Geological and Environmental Sciences,
University of Bologna,
40126, Bologna, Italy

T. Li
Department of Geological Engineering,
Chang'an University,
Xi'an, 710054, China
e-mail: dcdgx08@chd.edu.cn

5. PAPER 4

Numerical assessment of the impeding effect of check dams in the Hongchun debris flow gully, Sichuan Province, China

Wei Shen[1], Dongpo Wang[2*], Siming He[3,4], Tonglu L[5]
*Correspondence author

1 Department of Biological, Geological and Environmental Sciences, University of Bologna, Italy, 40126
2 State Key Laboratory of Geohazard Prevention and Geoenvironment Protection, Chengdu University of Technology, Chengdu, China, 610059
3 Key Laboratory of Mountain Hazards and Surface Process, Instituteof Mountain Hazards and Environment, Chinese Academy of Sciences, Chengdu, China, 610041
4 Center for Excellence in Tibetan Plateau Earth Sciences, Chinese Academy of Sciences, Beijing, China
5 Department of Geological Engineering, Chang'an University, Xi'an, China, 710064

Paper has been published in Bulletin of Engineering Geology and the Environment

Bulletin of Engineering Geology and the Environment
https://doi.org/10.1007/s10064-020-01755-5

ORIGINAL PAPER

Numerical assessment of the impeding effect of check dams in the Hongchun debris flow gully, Sichuan Province, China

Wei Shen [1,2] · Dongpo Wang [1] · Siming He [3,4] · Tonglu Li [5]

Received: 18 August 2019 / Accepted: 17 February 2020

Abstract

To mitigate potential damage from debris flows, numerous check dams have been constructed in thousands of debris flow gullies all over the world. However, the efficiencies of these check dams are largely unknown because they are normally designed based on empirical methods. This paper presents an assessment of the impeding effect of check dams constructed in the Hongchun debris flow gully in Sichuan Province, China by using an improved finite difference model. Compared with other models, the improved model can consider both the impeding effect of check dams and bed entrainment. We analyzed the impeding effect of these check dams on different initial scales of debris flows. The results show that these check dams perform quite well in constraining bed entrainment downstream of the gully. The average velocity, peak discharge, and final scale of a debris flow in the gully can be substantially reduced by constructed check dams. The impeding effect is sufficient when the initial volume of the debris flow is less than 1.5 times that of the catastrophic debris flow event that occurred in this gully on 14 August 2010. This study improves our understanding of the influence of check dams on the dynamic and bed entrainment processes of debris flows. The model adopted in this study can be a robust tool to quantify the efficiencies of existing check dams and provide reasonable guidance in the design of check dams in debris flow gullies.

Keywords Natural hazards · Numerical simulation · Debris flow · Check dams · Bed entrainment

Introduction

Debris flows are poorly sorted two-phase geophysical flows that occur frequently in mountainous areas. Distinct from other types of flow-like landslides (e.g., rock avalanches, mudflows, earthflows etc.), debris flows occur suddenly and periodically in established channels and tend to have higher mobility and destructive power (Hungr et al. 2014; Iverson 1997; Takahashi and Das 2014). The formation of a debris flow usually requires three basic conditions: sufficient precipitation, abundant loose materials, and steep topography. In regions meeting these conditions, debris flows occur frequently and can seriously impact the local community (García-Martínez and López 2005; Sidle and Chigira 2004; Tang et al. 2011a; Wieczorek et al. 2001). Natural debris flows generally have three origins. Some debris flows are triggered

✉ Dongpo Wang
wangdongpo2014@cdut.edu.cn

Wei Shen
shenweichd@qq.com

Siming He
hsm@imde.ac.cn

Tonglu Li
dcdgx08@chd.edu.cn

[1] State Key Laboratory of Geohazard Prevention and Geoenvironment Protection, Chengdu University of Technology, Chengdu 610059, Sichuan, China

[2] Department of Biological, Geological and Environmental Sciences, University of Bologna, 40126 Bologna, Italy

[3] Key Laboratory of Mountain Hazards and Surface Process, Institute of Mountain Hazards and Environment, Chinese Academy of Sciences, Chengdu 610041, China

[4] Center for Excellence in Tibetan Plateau Earth Sciences, Chinese Academy of Sciences, Beijing, China

[5] Department of Geological Engineering, Chang'an University, Xi'an 710064, China

Published online: 26 February 2020

by the erosion of loose material from runoff (Berti and Simoni 2005; Breien et al. 2008), while some are directly transformed from a landslide (Guthrie et al. 2012; Iverson et al. 1997). Additionally, the failure of a landslide dam can also trigger a catastrophic debris flow (Fan et al. 2019; Ouyang et al. 2019; Takahashi and Das 2014; Zhou et al. 2013). A distinct characteristic of runoff-induced debris flows is that most of the debris mass may come from entraining loose material along the path. As such, bed entrainment has been identified as a dominant factor determining the mobility of this type of debris flow (Hungr et al. 2005; Iverson et al. 2010b; Shen et al. 2019b). This needs consideration when designing countermeasures in debris flow gullies (Shen et al. 2019c).

There have been a lot of advances in debris flow research in recent decades. A variety of field monitoring techniques were developed to obtain field data of debris flows and provide instant early warning information (Berger et al. 2011; Berti et al. 2000; Cui et al. 2018). Plenty of flume tests were conducted to understand the physics of debris flows (Iverson et al. 2010a; Iverson et al. 2010b; Wang et al. 2018). Various numerical models have also been utilized to analyze the propagation processes of debris flows (Berti and Simoni 2014; Huang et al. 2015; Koo et al. 2017a; Kwan and Sun 2006; Mergili et al. 2017; Nakatani et al. 2008; Ouyang et al. 2013; Sassa et al. 2010; Shen et al. 2018). Nonetheless, the mitigation of debris flows is still a critical challenge in practice. Many engineering countermeasures have been developed to mitigate debris flow disasters, including check dams, slit dams, channel works, and wire nets etc. (Ikeya 1989; Mizuyama 2008; Takahashi and Das 2014). Check dams may be the most widely used countermeasure, with numerous check dams having been constructed in thousands of debris flow gullies around the world to prevent potential disasters. However, these check dams are usually designed using empirical methods, and their actual efficiencies remain uncertain until a debris flow event occurs. As it turned out, the efficiency of many check dams did not meet the design intent and they failed to prevent some debris flow events (Chen et al. 2015; Mizuyama 2008; Tang et al. 2011a). This design inadequacy is a waste of public resources and poses a considerable public safety risk to local residents. Therefore, it has become increasingly critical to improve the accuracy and efficiency of the methods for the design and assessment of check dams.

The rapid development of numerical modeling methods enables quantitative assessment of the efficiencies of debris flow countermeasures. Currently, both single-phase (Hungr and McDougall 2009; Iverson and Ouyang 2015; Ouyang et al. 2017; Pastor et al. 2009; Sassa et al. 2010; Shen et al. 2019a; Shen et al. 2018) and two-phase depth-averaged models (Heß et al. 2019; Tai et al. 2019) have been successfully applied in simulating flow-like movements such as debris flows. In addition, a growing number of depth-averaged models have begun to incorporate bed entrainment into their equations as the importance of bed entrainment on the mobility of debris flows has been acknowledged (McDougall and Hungr 2005; Ouyang et al. 2015; Pirulli and Pastor 2012). Depth-averaged models are very efficient in terms of computational cost, and can achieve satisfactory simulation results. As such, they remain the most commonly used tools in debris flow simulations. However, most of these models did not consider the effect of check dams as they were originally designed for simulating flow-like movements which propagate on natural topography. This drawback limits their application. Recently, investigative researches have been conducted on the interaction between debris flows and artificial structures (Choi et al. 2014; Cuomo et al. 2019; Dai et al. 2017; Kattel et al. 2018; Kwan et al. 2015; Kwan et al. 2018; Liu et al. 2013; Xiong et al. 2016). These studies improved the techniques for the design of debris flow prevention work. However, few of them considered bed entrainment when assessing the impact of artificial barriers. When bed entrainment is not considered, the assessment results tend to be questionable as bed entrainment has a substantial influence on the final magnitude and mobility of a runoff-induced debris flow.

This paper presents an assessment of the impeding effect of the check dams in the Hongchun debris flow gully, Sichuan province, China using an improved depth-averaged single-phase model (Shen et al. 2019c). Compared to other models, the single-phase model used in this research considers bed entrainment and the impeding effect of check dams, making it more suitable for this study. The debris flow event of interest in this study occurred in the Hongchun gully on 14 August 2010. It was studied by Ouyang et al. (2015) under the condition of green ground. More recently, Shen et al. (2019c) discussed the dynamic and bed entrainment characteristics of the debris flow event in the Hongchun gully under the influence of imaginary check dams. However, these studies did not consider the actual engineering layout of the check dams and the influence of debris flow magnitude. As such, the efficiency of the check dams in this gully is still unknown. To address these gaps, this study analyzed the efficiency of the check dams in the Hongchun gully by considering the actual engineering layout and debris flow magnitude simultaneously.

This paper has been structured into four sections: (1) background and context on the Hongchun debris flow gully; (2) basic principles of the numerical model and the simulation settings; (3) presentation of simulation results and discussion of results; and (4) final conclusions.

Introduction of the Hongchun debris flow gully

On 12 May 2008, a catastrophic earthquake of M 8.0 occurred in Wenchuan County, Sichuan Province, China. The earthquake triggered more than 15,000 geo-hazards, including

landslide types such as rock avalanches, rockslides, and debris flows (Cui et al. 2011). There were thousands of casualties and widespread damage to infrastructure as a direct result of these landslides. Additionally, these landslides produced more than five billion m^3 of loose deposit (i.e., a mixture of boulder, gravel, silt etc.), magnifying the frequency and magnitude of debris flow disasters. In the ten years after the earthquake, massive catastrophic debris flows occurred in the earthquake-impact areas. For instance, on 24 September 2008, a heavy rainstorm triggered 72 debris flow events in Beichuan County, leading to 42 deaths and serious damage to reconstructed infrastructure (Cui et al. 2011). On 14 August 2010, another intense rainfall induced 21 debris flow events in Yingxiu Town, near the epicenter of the earthquake. Out of the 14 August 2010 debris flow events, the huge debris flow that occurred in the Hongchun gully was catastrophic as it blocked the Mingjiang River, changing the course of this river (Tang et al. 2011b). This caused flooding which inundated the newly reconstructed Yingxiu Town and led to 17 fatalities.

An aerial view of the Hongchun gully catchment is shown in Fig. 1. The Hongchun gully is located at the east bank of the Mingjiang River, and the outlet of this gully is approximately 500 m away from the eastern outskirt of the Yingxiu Town. This catchment has a total area of 5.35 km^2 (Xu et al. 2012), and Hongchun gully is the primary gully with a length of approximately 3.6 km. Upstream of Hongchun gully are three tributaries; from west to east there is the Ganxipu gully, Dashui gully, and Xindianzi gully. Prior to the 2008 Wenchuan earthquake, only two small-scale debris flow events occurred in this gully sometime in the 1930s and in 1962, no damages were reported for either of these events. After the earthquake, the loose material in this catchment increased dramatically from about 1000,000 to 4000,000 m^3 (Gan et al. 2012; Tang et al. 2011b; Xu et al. 2012). As a result, the magnitude of debris flow in this gully increased dramatically. The 14 August 2010 debris flow may have been the largest that has ever occurred in this gully.

All three tributaries contributed to the 14 August 2010 debris flow event (Ouyang et al. 2015). The initial total volume of mobilized debris mass was approximately 183,000 m^3, in which 112,000, 39,000, and 32,000 m^3 originated from Ganxipu gully, Dashui gully, and Xindianzi gully, respectively. Additionally, an estimated 500,000–600,000 m^3 of loose material along the path was entrained by the debris flow, and approximately half of the debris (350,000–400,000 m^3) flowed out of the gully outlet, forming a 100 m wide and 350–400 m long dam that blocked the Mingjiang River. Based on field observations (Ouyang et al. 2015), the entrainment mainly occurred in Hongchun gully, averaging a depth between 6 and 10 m with a maximum entrainment depth of approximately 20 m in the middle and lower streams of the gully. The entrainment extent in the three tributaries was smaller, approximately 1–2 m.

After the 14 August 2010 event, the volume of the loose material that could be mobilized in the catchment had reduced to an estimated 3100,000 m^3 (Li et al. 2012). However, it was still a much larger volume than that prior to the earthquake. Thus, the risk of catastrophic debris flow events reoccurring is still very high. To address this, the Chinese government allocated millions of dollars to construct engineering countermeasures in the catchment. The prevention project in this catchment mostly consisted of the installation of four check dams in the middle and upper streams of the main gully in conjunction with several small check dams in the three tributaries. Figure 2

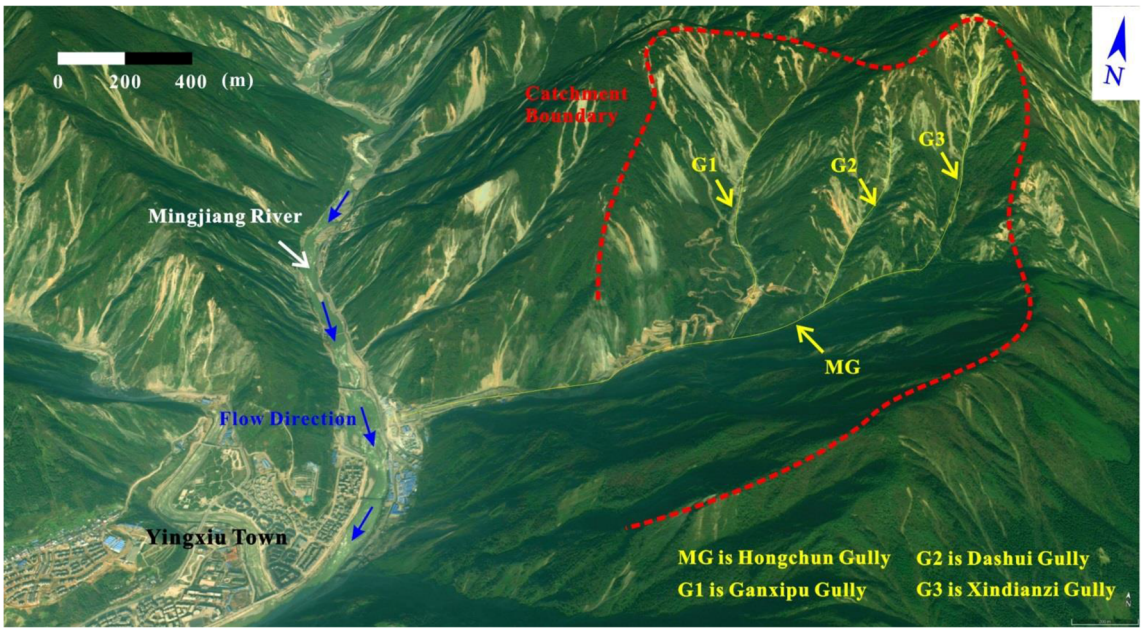

Fig. 1 Aerial view of the Hongchun gully catchment (N 31°04′01.1″, E 103°29′32.7″, from Google Earth)

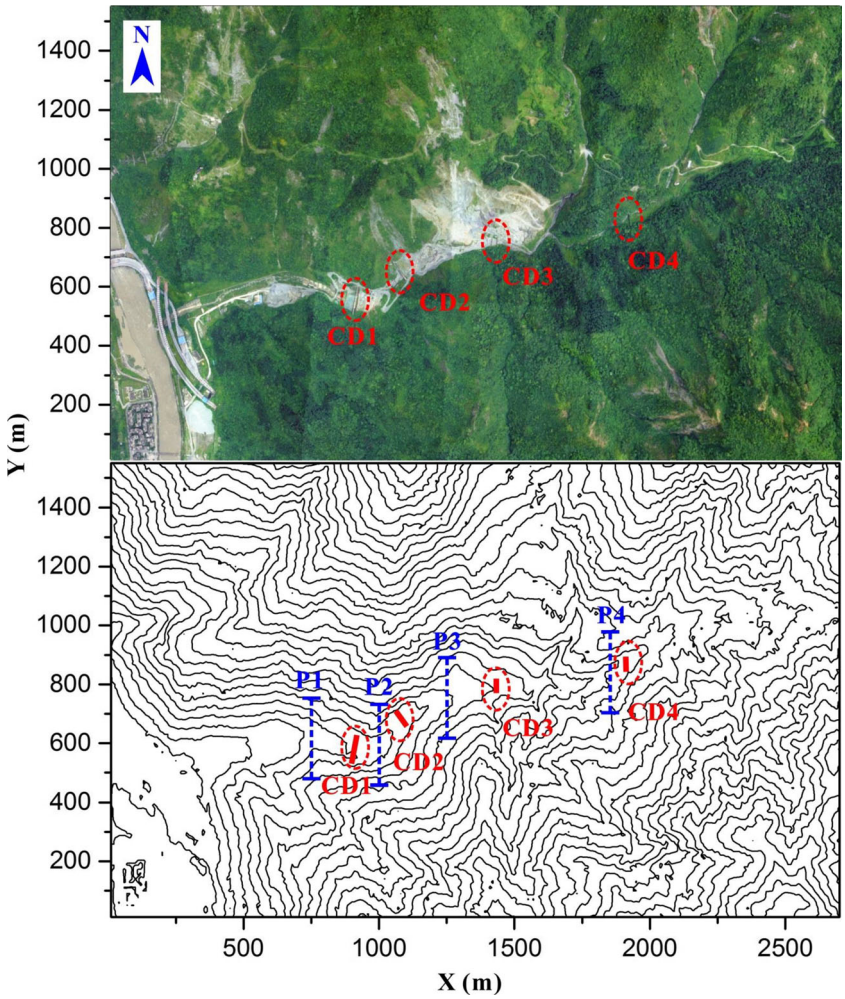

Fig. 2 Locations of the four check dams in Hongchun gully and the discharge monitoring profiles. CD1–CD4 represents the four check dams. P1–P4 is the four profiles selected to monitor discharge during simulation

illustrates the locations of the four check dams in the main gully, and Table 1 details their engineering layouts. These four check dams are marked CD1–CD4 (downstream to upstream). CD4 was designed to capture debris mass flowing out from the Dashui and Xindianzi gullies, while the other dams were intended to control the movement of the remaining debris mass from the three tributaries. We have only considered these four dams in the simulations as they are designed to play a major role in preventing debris flows in Hongchun gully catchment. Their impeding effect is checked by the improved model.

Table 1 Locations and engineering layouts of the check dams in Hongchun gully

Dam labels	CD1	CD2	CD3	CD4
Center coordinates (m)	$X=910$ $Y=600$	$X=1070$ $Y=690$	$X=1440$ $Y=800$	$X=1910$ $Y=890$
Height (m)	20	18	10	8
Length (m)	105	68.5	43	41
Width (m)	1.5	1.5	1.5	1.5

Principles of the numerical model

Governing equations

The governing equations in the model consist of one mass balance equation and two momentum equations, representing the mass and momentum conservations in a control volume, respectively. The detailed derivations of these equations are provided in Shen et al. (2018). The governing equations are given by

$$\frac{\partial h}{\partial t}+\frac{\partial Q}{\partial x}+\frac{\partial Q_y}{\partial y}=E_r \tag{1}$$

$$\frac{\partial Q}{\partial t}+\frac{\partial Q_x^2/h}{\partial x}+\frac{\partial Q_xQ_y/h}{\partial y}=\frac{\partial k_x g h^2/2}{\partial x}+\frac{(Ag+B)}{\tan^2 a+\beta+1}-\frac{\tau_b A_b h v_x}{m\sqrt{v_x^2+v_y^2+v_z^2}} \tag{2}$$

$$\frac{\partial Q_y}{\partial t}+\frac{\partial Q_xQ_y/h}{\partial x}+\frac{\partial Q_y^2/h}{\partial y}=\frac{\partial k_y g h^2/2}{\partial y}+\frac{(Ag+B)}{\tan^2 a+\tan^2\beta+1}-\frac{\tau_b A_b h v_y}{m\sqrt{v_x^2+v_y^2+v_z^2}} \tag{3}$$

where h is the flow depth in the control volume; $Q_x=hv_x$ and $Q_y=hv_y$ are the mass fluxes in the x and y directions,

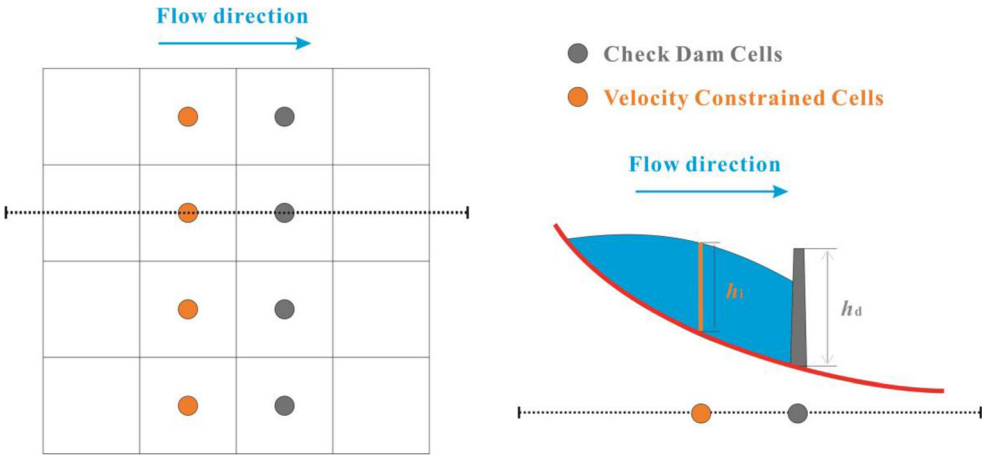

Fig. 3 Schematic diagram of check dam cells (CDCs) and the velocity constrained cells (VCCs)

respectively; v_x, v_y, and v_z are the depth-averaged velocities in the x, y, and z directions, respectively; E_r is the entrainment rate; k_x and k_y are the lateral pressure coefficients in the x and y directions, respectively, related to the internal frictional and basal frictional angles and evolve with the pressure state of the debris mass (Ouyang et al. 2015); A and B are the terms related to the static and centrifugal normal forces on the basal flow boundary, respectively; g is gravitational acceleration; α and β are the dip angles of the sliding mass in the x and y directions, respectively; τ_b is the shear stress of the debris flow on the basal boundary; A_b is the bottom area of the control volume; and m is the mass. Expressions for A, B, A_b, and E_r can be given as

$$A = 1 + \frac{\partial k_x h^2/2}{\partial x}\tan a + \frac{\partial k_y h^2/2}{\partial y}\tan\beta \tag{4}$$

$$B = \frac{C_x}{\cos a}\left(\frac{v_x}{\cos a}\right)^2 + \frac{C_y}{\cos\beta}\left(\frac{v_y}{\cos\beta}\right)^2 \tag{5}$$

$$A_b = dxdy\sqrt{\tan^2 a + \tan^2\beta + 1} \tag{6}$$

$$E_r = \frac{\partial Z}{\partial t} = \frac{\tau_b - \tau_e}{\rho_e\sqrt{v_x^2 + v_y^2}} \tag{7}$$

where C_x and C_y are the bed curvatures in the x and y directions, respectively; dx and dy are the sizes of the control volume in the x and y directions, respectively; Z is the elevation of the bed; ρ_e is the bulk density of the entrained debris; and τ_e is the resistant shear stress in the static bed material. To calculate the basal shear stress in debris flow τ_b, we use the Voellmy model; the Mohr-Coulomb model is adopted to determine τ_e.

Table 2 Locations of discharge monitoring profiles in simulation

Coordinate	P1	P2	P3	P4
X (m)	750	1000	1250	1850
Y (m)	600	580	750	850

Their expressions are given by

$$\tau_b = \sigma(1-r_{ub})\tan\phi_s' + \rho_s g\frac{v_x^2 + v_y^2}{\xi} \tag{8}$$

$$\tau_e = \sigma(1-r_{ue})\tan\phi_e' + c_e' \tag{9}$$

where r_{ub} and r_{ue} are the pore pressure coefficients of debris flow and bed material, respectively; φ'_d and φ'_e are the effective frictional angles of debris flow and bed material, respectively; ρ_s is the bulk density of the debris flow; ξ is the turbulent coefficient; and c'_e is the effective cohesion of bed material.

Equation (7) is a physically based entrainment model describing the momentum conservation of the bed material. This equation is adopted in this numerical study as it has clear physical meaning compared with empirical models (Iverson and Ouyang 2015; Ouyang et al. 2015; Shen et al. 2019b; Shen et al. 2019c).

Effect of check dams and numerical scheme

This study's primary focus is to investigate the impeding effect of check dams on debris flows. Therefore, the effect of check dams is simplified as a rigid constraint here, and failure of the check dam is not considered. The computational cells containing the check dams are marked as check dam cells (CDCs). The cells upstream and close to these check dam cells are identified as velocity constrained cells (VCCs). If the flow depth in a VCC (h_i) is less than the height of the dam in the adjoining CDC, then the debris in the VCC will remain static until its flow depth surpasses the height of the dam (Fig. 3). This enables the accommodation of the impeding effect of a check dam (Shen et al. 2019c).

To ensure debris flows move within the outside computational boundary, a rectangular computational region which is usually larger than the debris flow impact area will be typically adopted in simulation. This treatment simplifies the complexity of dealing with a boundary condition but may increase the computational cost. Debris flows usually move in a long, narrow, and

Table 3 Simulation conditions in different groups

Group names	WD	$V_i = V$	$V_i = 1.5\ V$	$V_i = 2\ V$	$V_i = 3\ V$	$V_i = 4\ V$
Initial volume (m^3)	183,000	183,000	274,500	366,000	549,000	732,000
Check dam	No	Yes	Yes	Yes	Yes	Yes

meandering gully; therefore, its impact area is generally considerably smaller than the computational region. Including empty cells within the computational region would result in large computational time. As such, only cells that contain debris mass are included in simulation to save computational cost.

We adopted an improved finite difference code that had incorporated the above check dam constraints and numerical scheme to assess the impeding effect of the check dams in Hongchun gully.

Simulation settings

The computational region was a rectangular area, with a width of 2700 m (x direction) and a length of 1550 m (y direction). The coordinates for this region are shown in Fig. 2. Field survey data were used to generate a digital elevation model (DEM) of the computational region. Computational cells were 10 m in the x and y directions. The maximum time step in simulation was 0.02 s. Four cross-sections (P1–P4) downstream of each check dam were selected to monitor the influence of these dams on debris flow discharge. The locations of these cross-sections within the computational region are given in Table 2. Six groups of simulations were conducted to investigate the impeding effect of the check dams on debris flows of different scales. Table 3 provides details on the setups of these simulations. In group WD (see Table 3), check dams were not present, and the initial volume of the debris flow was equivalent to the initial volume from the 14 August 2010 debris flow event. The setups of check dams in the main gully were the same for the remaining five groups, and the configuration of these dams are given in Table 1. To investigate the influence of debris flows of different magnitudes, different initial debris volumes were used in these five groups.

Table 4 details the values of parameters required in these simulations. The values of the effective friction angle, turbulent coefficient, internal friction angle, and the bulk density of the debris flow were assigned as per Ouyang et al. (2015). The effective friction angle and bulk density of the bed material were assumed to be equivalent to those of the debris flow. The r_{ub} value of debris flow was 0.8, which was the typical value assigned based on the results of flume tests. A higher bed erodible material r_{ue} value was assumed to be entrained by the debris flow. A small cohesion value was allocated to the erodible mass to prevent the debris flow from entraining material on steep slopes (Ouyang et al. 2015). The above parameters were determined after several trials so that the simulation results representing the 14 August 2010 event (i.e., the simulation results of WD) matched the field observations (Ouyang et al. 2015; Shen et al. 2019c).

Results and discussions

Impeding effect analysis

Figure 4 illustrates the simulated thickness distributions of the final deposit in the six groups. It indicates that the check dams in the main gully have a clear impeding impact on the movement of debris flow. These check dams perform well in preventing a debris flow with an initial volume less than 1.5 times the volume of the 14 August 2010 event. The first three dams upstream are successful in the prevention of a debris flow with an equivalent magnitude to the 14 August 2010 event ($V_i = V$), and virtually no debris is able to reach CD1. In this simulation, the average thickness of debris flow deposits trapped behind CD2–CD4 is approximately 5–10 m. When the magnitude of the debris flow increases to 1.5 times that of the 14 August 2010 event, part of the debris flow will surmount CD2, but no debris mass is able to flow over CD1. In $V_i = 1.5\ V$, the average thickness of the deposit captured by each dam increases to approximately 15–20 m. If the initial volume of the debris flow is larger than twice that of the 14 August 2010 event, the debris flow will rush out from the outlet of the gully, and there will be a very high risk of blocking the Mingjiang River. If debris flow has an initial

Table 4 Parameters for simulating the Hongchun gully debris flow

Parameters	Pore pressure coefficient r_u	Effective friction angle φ'	Turbulent coefficient ξ	Effective cohesion c'	Internal friction angle φ_i	Bulk density ρ
	–	°	–	kPa	°	g/cm^3
Debris mass	0.8	12	2850	–	35	2.02
Erodible mass	0.95	12	–	2.1	–	2.02

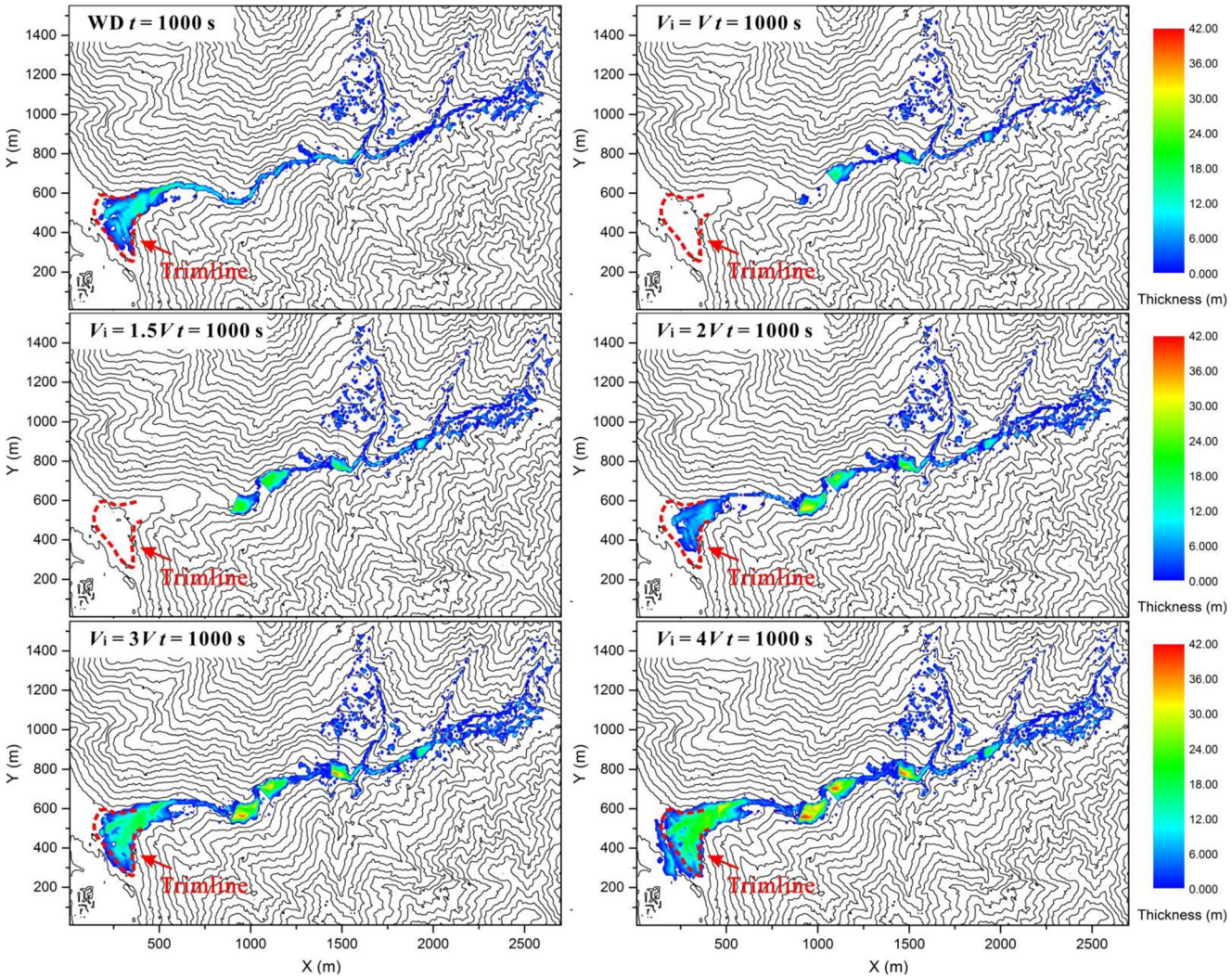

Fig. 4 Thickness distribution of the final debris deposit for different simulation groups

volume larger than three times that of the 14 August 2010 event, the impeding effect of the check dam will be inadequate, and the debris flow will certainly block the Mingjiang River. Figure 4 also demonstrates that the thickness of the deposit captured by each dam increases with the magnitude of debris flow. This is likely to be due to the increased entrainment extent with debris flow magnitude.

The corresponding final entrainment depths for different simulation groups are illustrated in Fig. 5. The figure shows that these check dams can substantially reduce the total extent of entrainment. The entrainment extent is less than that of the 14 August 2010 event when the initial volume of debris flow is less than 1.5 times this event. However, these check dams will no longer be able to control the entrainment extent of debris flow if the initial scale of debris flow is greater than 2–3 times that of the 14 August 2010 event. The check dams in the gully also drastically change the entrainment distributions in the gully. Prior to the construction of these check dams, the entrainment extent in the middle and downstream areas of this gully is much larger than those upstream. Following the installation of these check dams, the entrainment extent downstream will substantially decrease, while the regions behind the dams will be subject to extreme bed entrainment. This is because these check dams increase the thickness of debris mass captured behind the dam.

The discharge curves for the four monitoring profiles are illustrated in Fig. 6. This figure illustrates that peak discharge will increase upstream to downstream without the influence of check dams (Fig. 6a). However, the reverse will occur in the absence of entrainment (Shen et al. 2019c). A comparison between Fig. 6 a and b indicates that the constructed check dams can largely reduce discharge in the gully and delay the arrival time of the debris flow. In $V_i = V$, the peak discharges at P3 and P4 reduce to less than half those of the 14 August 2010 event due to the resistance of the check dams. There is hardly any debris mass passing through P1 and P2. The peak discharge at each profile increases with debris flow magnitude. When the initial volume of debris flow increases to 1.5 times that of the

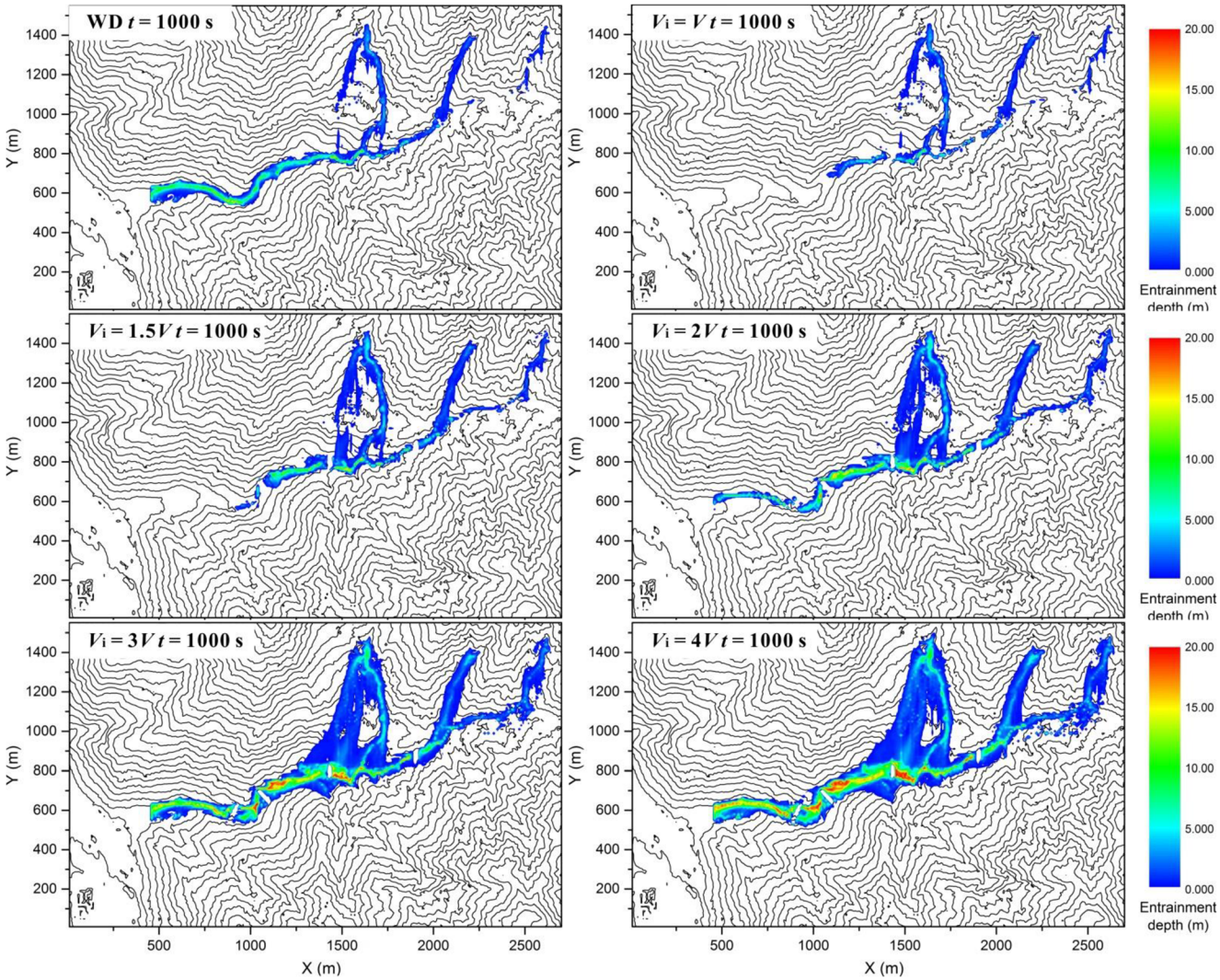

Fig. 5 Final entrainment depth distributions in the gully for different simulation groups

14 August 2010 event (Fig. 6c), the peak discharges at P3 and P4 almost recover to pre-check dam levels. However, the peak discharges downstream are still lower than those prior to check dam construction. Until the initial volume of the debris flow is three times that of the 14 August 2010 event, the peak discharge downstream (P4) recovers to the corresponding discharge value prior to check dam construction. These results suggest that these check dams perform very well in reducing peak discharge in the gully. Previous researches investigating the impeding effect of multiple barriers without considering bed entrainment also reported similar results in terms of the time delay of debris flow (Kwan et al. 2015).

Propagation and entrainment processes of the debris flow

Three points of time (t = 50, 150, and 250 s), representing the early, middle, and later stages of debris flow movement are selected to analyze the propagation and entrainment characteristics. In the early stage, the debris flow primarily propagates in the three tributaries. In contrast, the debris flow converges in the main gully during the middle stage, while most debris mass deposits in the accumulation zone during the later stage. As the result of group $V_i = 1.5\ V$ is similar to that of $V_i = V$; and the results of groups $V_i = 3\ V$ and $V_i = 4\ V$ are similar to that of $V_i = 2\ V$; only the results of groups WD, $V_i = V$, and $V_i = 2\ V$ are presented for simplicity. In these groups, WD represents the no check dam scenario, $V_i = V$ represents a scenario where the check dams succeed in impeding the debris flow, and $V_i = 2\ V$ represents a scenario where the check dams fail in impeding the debris flow.

Figure 7 shows the simulated thickness distributions of debris flow in groups WD, $V_i = V$, and $V_i = 2\ V$ at the three aforementioned points of time. At the early stage (t = 50 s), the debris flow arrives at CD3 and CD4 in WD and $V_i = V$, while a large volume of debris flow has already been captured by CD3 in $V_i = 2\ V$. This is because propagation is typically faster for a larger debris flow compared with a small debris

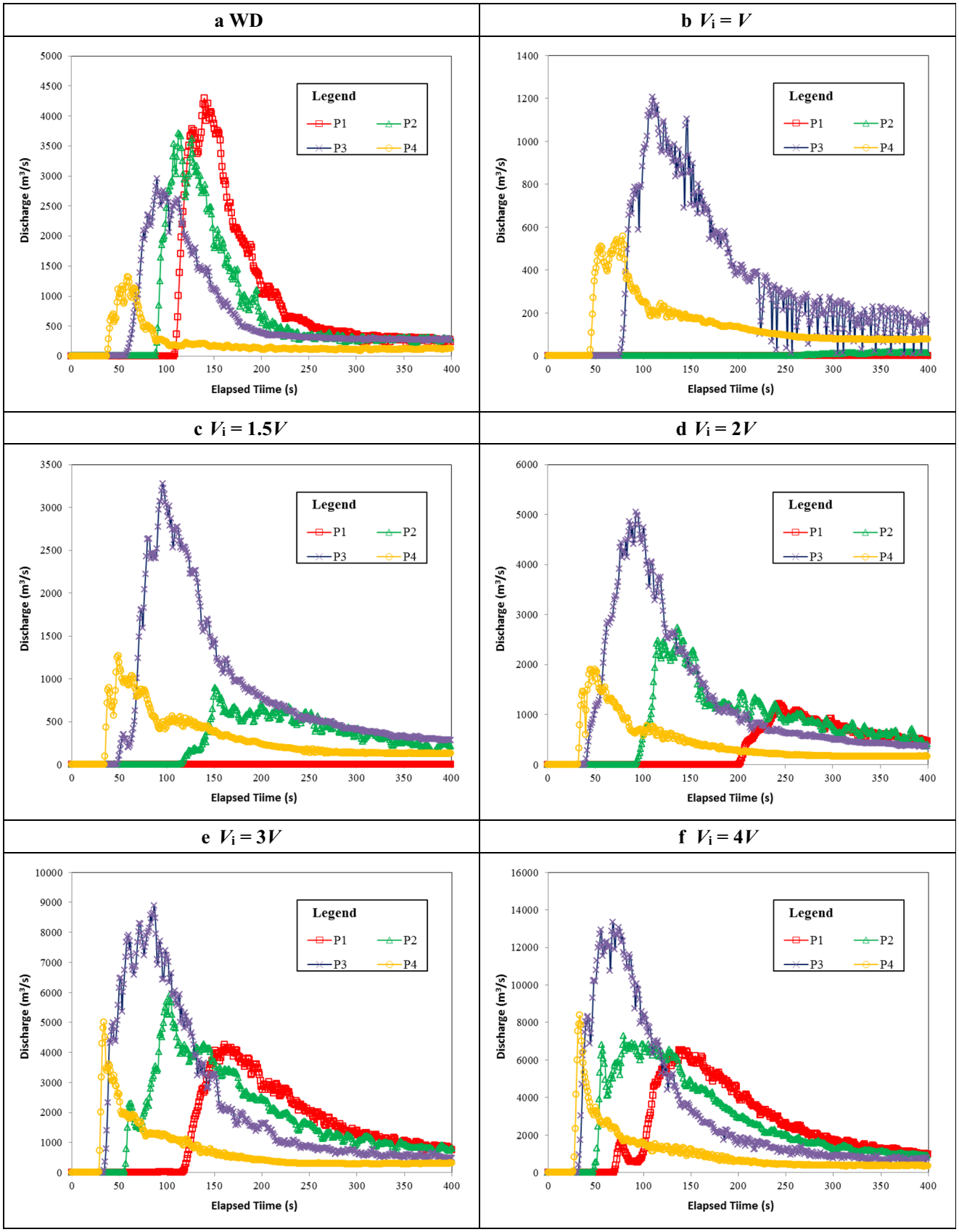

Fig. 6 Simulated discharge process curves at the four monitoring profiles for different simulation groups

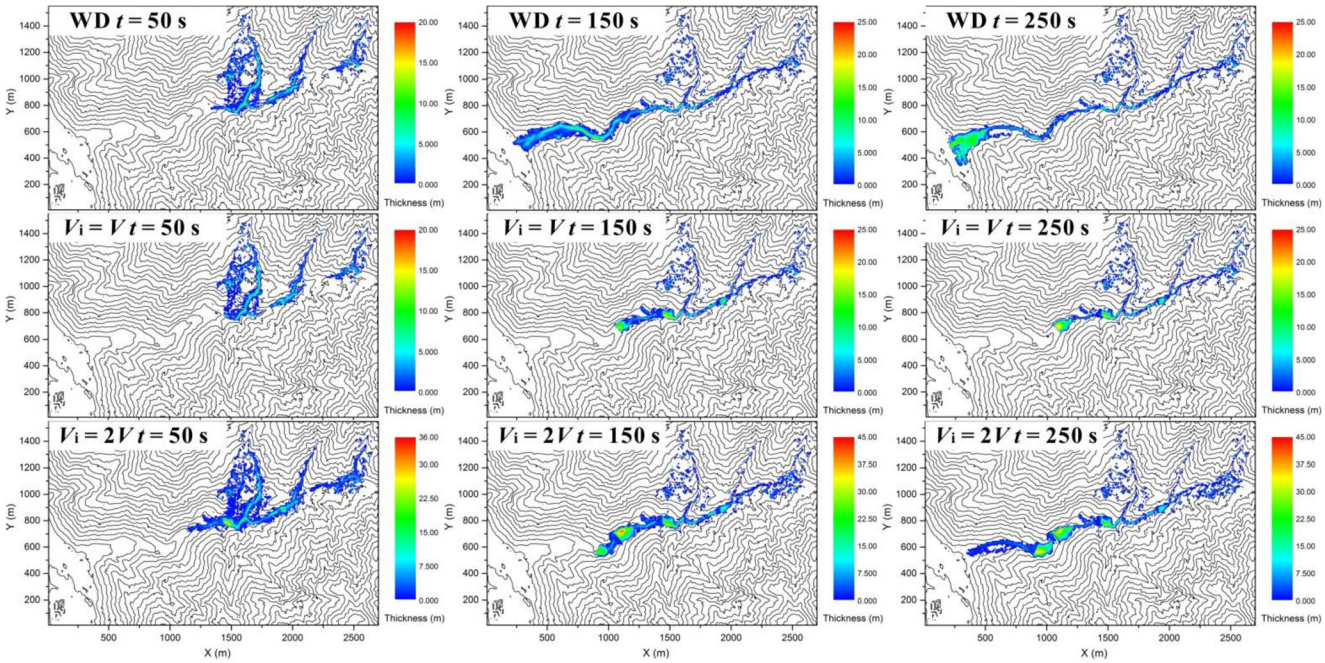

Fig. 7 Propagation characteristics of the debris flow at three points in time for groups WD, $V_i = V$, and $V_i = 2\ V$

flow. At the middle stage ($t = 150$ s), the debris flow in WD has reached the outlet of the gully. The debris flows in $V_i = V$ and $V_i = 2\ V$ have only arrived at the middle section of the main gully, with a growing amount of debris mass accumulating behind the dams. This is due to the impeding effect of the check dams. At the later stage ($t = 250$ s), the deposition process is almost complete for each group. At this stage, the debris flow in WD forms a fan-shaped dam that can block the Mingjiang River. In contrast, for $V_i = V$ and $V_i = 2\ V$, most debris mass has been successfully captured by these check dams. The corresponding entrainment processes of the debris flow in these three situations are shown in Fig. 8. The results also demonstrate that the check dams are able to reduce the entrainment extent downstream but may also increase the entrainment extent behind the dams.

The simulated average velocities of the debris flow in the six situations are presented in Fig. 9. The average velocity of debris flow experiences two peaks in WD. The first peak is

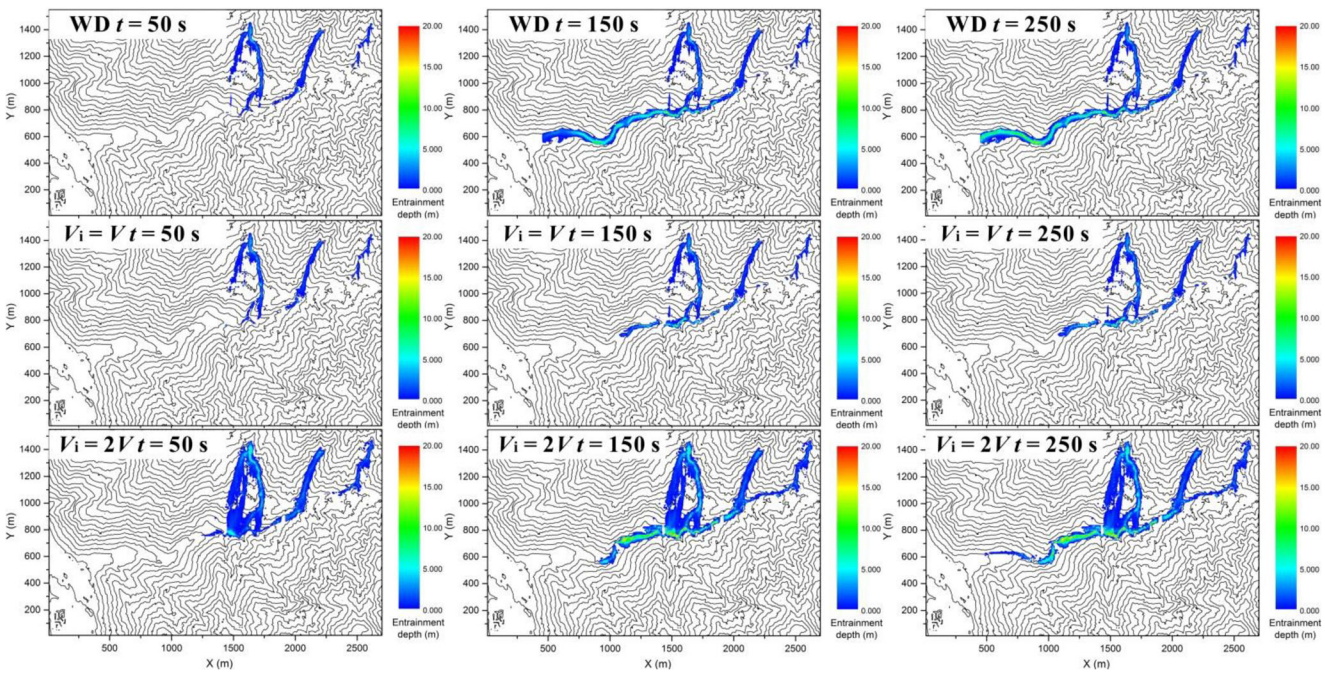

Fig. 8 Entrainment depths of the debris flow at three points in time for groups WD, $V_i = V$, and $V_i = 2\ V$

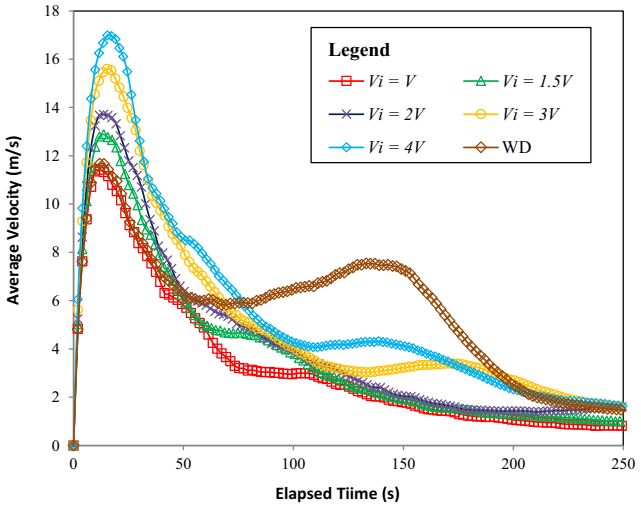

Fig. 9 Average velocity curves of debris flow for the six different simulation groups

produced as the debris flow moves through the steep source zone at the early stage. During this time, the gravitational potential of the debris flow consistently transfers into kinematic energy. The acceleration stage ends when the debris flow arrives at the transportation zone that has a gentler gradient. The second peak may be caused by bed entrainment, as entraining saturated loose material will reduce basal resistance. In scenarios where check dams are present in the gully, the peak average velocity of the debris flow increases with the initial magnitude of debris flow. However, the average velocity will remain considerably lower than a scenario with no check dams due to the impeding effect of the check dams. These results indicate that check dams in this gully are able to reduce the average velocity of the debris flow by constraining the extent of bed entrainment to the downstream area of the gully. Previous experimental studies have also

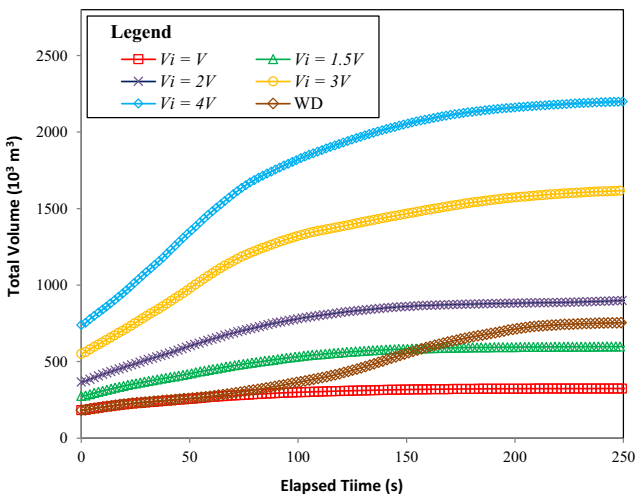

Fig. 10 Total volume bulking curves of debris flow for the six different simulation groups

reported on the attenuation effect of check dams on velocity of debris flow (Koo et al. 2017b).

The total debris flow volumes in these simulations are shown in Fig. 10. The results demonstrate that check dams can greatly constrain the total entrainment volume in the gully. However, the entrainment control effect of these dams will decrease when the initial debris flow volume increases. If this initial volume increases to more than twice that of the 14 August 2010 event, these check dams are likely to have little impact on controlling the final magnitude of bed entrainment.

Table 5 details the simulated final entrainment volumes, deposition volumes (i.e., the volume of the debris exiting the outlet of the main gully), and the peak discharges at the four monitoring profiles for the six different simulation groups. The total entrainment volume increases with the magnitude of the initial mobilized debris flow. The entrainment volume in $V_i = 2\ V$ is essentially equivalent to that of WD, while the deposition volume in $V_i = 2\ V$ is only about half that of WD. This suggests that these dams can effectively minimize the consequence of a debris flow and reduce the risk of damming the Mingjiang River. The value of peak discharge at each profile increases with the initial magnitude of debris flow, but these dams can substantially reduce the discharge in the gully. Additionally, the dams can change the discharge characteristics of the debris flow in this gully. The peak discharge increases consistently as it travels upstream to downstream in the absence of check dams. In contrast, the peak discharge with the influence of check dams does the reverse, indicating that these check dams have a clear impeding effect on the propagation of a debris flow.

Conclusions

The impeding effect of check dams in the Hongchun debris gully was assessed using an improved finite difference model. Based on the results of this assessment, the following conclusions can be made:

1) The check dams in Hongchun gully perform well in controlling the bed entrainment extent in the downstream part of the gully, which helps to reduce the average velocity, peak discharge, and final magnitude of debris flow. These check dams can successfully prevent a debris flow with an initial volume less than 1.5 times that of the 14 August 2010 event. However, these dams may lose their efficacy if the initial debris flow volume exceeds 2–3 times that of the 14 August 2010 event.
2) These check dams change the bed entrainment characteristics of Hongchun gully. Prior to check dam construction, the largest entrainment extent occurs in the middle and downstream sections of the main gully, whereas there is only a slight entrainment extent upstream. Following

Table 5 Simulated entrainment volumes and deposit volumes of debris flow, and the peak discharges at the four monitoring profiles for the six different simulation groups

Simulation groups	Entrainment volume (10^3 m^3)	Deposition volume (10^3 m^3)	Peak discharge (m^3/s)			
			P1	P2	P3	P4
WD	580	349	4298	3710	2943	1324
$V_i = V$	141	0	0	19	1205	558
$V_i = 1.5\ V$	329	0	0	896	3279	1272
$V_i = 2\ V$	586	185	1221	2749	5046	1909
$V_i = 3\ V$	1105	643	4250	5926	8885	4999
$V_i = 4\ V$	1495	1012	6543	7275	13,344	8378

check dam construction, the entrainment extent behind the dams is found to be the highest, while the entrainment extent downstream is largely reduced.

3) The model adopted here performs well in assessing the impeding effect of check dams in Hongchun gull. As such, it may be an effective tool to guide the construction and assessment of check dams in debris flow gullies.

Acknowledgments We would like to thank the anonymous referees for carefully reading the manuscript and providing constructive comments to help us improve the quality of this paper.

Funding information This research is funded by the Natural Science Foundation of China (Grant No. 41877266, 41790433), the National Key R&D Program of China (Grant No. 2017YFC1501000, 2017YFC1501302), and the China Scholarship Council (CSC) – University of Bologna Joint Scholarship (File No. 201806560011).

References

Berger C, McArdell BW, Schlunegger F (2011) Direct measurement of channel erosion by debris flows, Illgraben, Switzerland. J Geophys Res Earth Surf 116(F1)

Berti M, Simoni A (2005) Experimental evidences and numerical modelling of debris flow initiated by channel runoff. Landslides 2(3):171–182

Berti M, Simoni A (2014) DFLOWZ: a free program to evaluate the area potentially inundated by a debris flow. Comput Geosci 67:14–23

Berti M, Genevois R, LaHusen R, Simoni A, Tecca PR (2000) Debris flow monitoring in the Acquabona watershed on the Dolomites (Italian alps). Phys Chem Earth B Hydrol Oceans Atmos 25(9): 707–715

Breien H, De Blasio FV, Elverhøi A, Høeg K (2008) Erosion and morphology of a debris flow caused by a glacial lake outburst flood, Western Norway. Landslides 5(3):271–280

Chen X, Cui P, You Y, Chen J, Li D (2015) Engineering measures for debris flow hazard mitigation in the Wenchuan earthquake area. Eng Geol 194:73–85

Choi CE, Ng CWW, Law RPH, Song D, Kwan JSH, Ho KKS (2014) Computational investigation of baffle configuration on impedance of channelized debris flow. Can Geotech J 52(2):182–197

Cui P, Chen X-Q, Zhu Y-Y, Su F-H, Wei F-Q, Han Y-S, Liu H-J, Zhuang J-Q (2011) The Wenchuan earthquake (may 12, 2008), Sichuan Province, China, and resulting geohazards. Nat Hazards 56(1):19–36

Cui P, Guo X, Yan Y, Li Y, Ge Y (2018) Real-time observation of an active debris flow watershed in the Wenchuan earthquake area. Geomorphology 321:153–166

Cuomo S, Moretti S, Aversa S (2019) Effects of artificial barriers on the propagation of debris avalanches. Landslides 16(6):1077–1087

Dai Z, Huang Y, Cheng H, Xu Q (2017) SPH model for fluid–structure interaction and its application to debris flow impact estimation. Landslides 14(3):917–928

Fan X, Scaringi G, Korup O, West AJ, van Westen CJ, Tanyas H, Hovius N, Hales TC, Jibson RW, Allstadt KE, Zhang L, Evans SG, Xu C, Li G, Pei X, Xu Q, Huang R (2019) Earthquake-induced chains of geologic hazards: patterns, mechanisms, and impacts. Rev Geophys 57(2):421–503

Gan J, Sun H, Huang R, Tan Y, Fang C, Li Q, Xu X (2012) Study on mechanism of formation and river blocking of Hongchungou giant debris flow at Yingxiu of Wenchuan County. J Catastrophol 27(1): 5–9 (in Chinese)

García-Martínez R, López JL (2005) Debris flows of December 1999 in Venezuela. In: Debris-flow hazards and related phenomena. Springer, Berlin, pp 519–538

Guthrie RH, Friele P, Allstadt K, Roberts N, Evans SG, Delaney KB, Roche D, Clague JJ, Jakob M (2012) The 6 August 2010 Mount Meager rock slide-debris flow, Coast Mountains, British Columbia: characteristics, dynamics, and implications for hazard and risk assessment. Nat Hazards Earth Syst Sci 12(5):1277–1294

Heß J, Tai Y-C, Wang Y (2019) Debris flows with pore pressure and intergranular friction on rugged topography. Comput Fluids 190: 139–155

Huang Y, Cheng H, Dai Z, Xu Q, Liu F, Sawada K, Moriguchi S, Yashima A (2015) SPH-based numerical simulation of catastrophic debris flows after the 2008 Wenchuan earthquake. Bull Eng Geol Environ 74(4):1137–1151

Hungr O, McDougall S (2009) Two numerical models for landslide dynamic analysis. Comput Geosci 35(5):978–992

Hungr O, McDougall S, Bovis M (2005) Entrainment of material by debris flows. In: Jakob M, Hungr O (eds) Debris-flow hazards and related phenomena. Springer, Berlin, pp 135–158

Hungr O, Leroueil S, Picarelli L (2014) The Varnes classification of landslide types, an update. Landslides 11(2):167–194

Ikeya H (1989) Debris flow and its countermeasures in Japan. Bulletin of the International Association of Engineering Geology - Bulletin de l'Association Internationale de Géologie de l'Ingénieur 40(1):15–33

Iverson RM (1997) The physics of debris flows. Rev Geophys 35(3): 245–296

Iverson RM, Ouyang C (2015) Entrainment of bed material by earth-surface mass flows: review and reformulation of depth-integrated theory. Rev Geophys 53(1):27–58

Iverson RM, Reid ME, LaHusen RG (1997) Debris-flow mobilization from landslides. Annu Rev Earth Planet Sci 25(1):85–138

Iverson RM, Logan M, LaHusen RG, Berti M (2010a) The perfect debris flow? Aggregated results from 28 large-scale experiments. J Geophys Res Earth Surf 115(F3)

Iverson RM, Reid ME, Logan M, LaHusen RG, Godt JW, Griswold JP (2010b) Positive feedback and momentum growth during debris-flow entrainment of wet bed sediment. Nat Geosci 4:116

Kattel P, Kafle J, Fischer J-T, Mergili M, Tuladhar BM, Pudasaini SP (2018) Interaction of two-phase debris flow with obstacles. Eng Geol 242:197–217

Koo RCH, Kwan JSH, Lam C, Goodwin GR, Choi CE, Ng CWW, Yiu J, Ho KKS, Pun WK (2017a) Back-analysis of geophysical flows using three-dimensional runout model. Can Geotech J 55(8):1081–1094

Koo RCH, Kwan JSH, Ng CWW, Lam C, Choi CE, Song D, Pun WK (2017b) Velocity attenuation of debris flows and a new momentum-based load model for rigid barriers. Landslides 14(2):617–629

Kwan JSH, Sun HW (2006) An improved landslide mobility model. Can Geotech J 43(5):531–539

Kwan JSH, Koo RCH, Ng CWW (2015) Landslide mobility analysis for design of multiple debris-resisting barriers. Can Geotech J 52(9): 1345–1359

Kwan JSH, Sze EHY, Lam C (2018) Finite element analysis for rockfall and debris flow mitigation works. Can Geotech J:1–26

Li D, Xu X, Hao H (2012) Formation conditions and the movement characteristics of "8.14" giant debris flow in Yingxiu town, Wenchuan County, Sichuan Province. Chinese J Geol Hazard Control 23(3):32–38 (in Chinese)

Liu J, Nakatani K, Mizuyama T (2013) Effect assessment of debris flow mitigation works based on numerical simulation by using Kanako 2D. Landslides 10(2):161–173

McDougall S, Hungr O (2005) Dynamic modelling of entrainment in rapid landslides. Can Geotech J 42(5):1437–1448

Mergili M, Fischer JT, Krenn J, Pudasaini SP (2017) R.avaflow v1, an advanced open-source computational framework for the propagation and interaction of two-phase mass flows. Geosci Model Dev 10(2):553–569

Mizuyama T (2008) Structural countermeasures for debris flow disasters. Int J Erosion Control Eng 1(2):38–43

Nakatani K, Wada T, Satofuka Y, Mizuyama T (2008) Development of “Kanako 2D (Ver.2.00),” a user-friendly one- and two-dimensional debris flow simulator equipped with a graphical user interface. Int J Erosion Control Eng 1(2):62–72

Ouyang C, He S, Xu Q, Luo Y, Zhang W (2013) A MacCormack-TVD finite difference method to simulate the mass flow in mountainous terrain with variable computational domain. Comput Geosci 52:1–10

Ouyang C, He S, Tang C (2015) Numerical analysis of dynamics of debris flow over erodible beds in Wenchuan earthquake-induced area. Eng Geol 194:62–72

Ouyang C, Zhao W, He S, Wang D, Zhou S, An H, Wang Z, Cheng D (2017) Numerical modeling and dynamic analysis of the 2017 Xinmo landslide in Maoxian County, China. J Mt Sci 14(9):1701–1711

Ouyang C, An H, Zhou S, Wang Z, Su P, Wang D, Cheng D, She J (2019) Insights from the failure and dynamic characteristics of two sequential landslides at Baige village along the Jinsha River, China. Landslides 16(7):1397–1414

Pastor M, Haddad B, Sorbino G, Cuomo S, Drempetic V (2009) A depth-integrated, coupled SPH model for flow-like landslides and related phenomena. Int J Numer Anal Methods Geomech 33(2):143–172

Pirulli M, Pastor M (2012) Numerical study on the entrainment of bed material into rapid landslides. Géotechnique 62(11):959–972

Sassa K, Nagai O, Solidum R, Yamazaki Y, Ohta H (2010) An integrated model simulating the initiation and motion of earthquake and rain induced rapid landslides and its application to the 2006 Leyte landslide. Landslides 7(3):219–236

Shen W, Li T, Li P, Guo J (2018) A modified finite difference model for the modeling of flowslides. Landslides 15(8):1577–1593

Shen W, Li T, Li P, Berti M, Shen Y, Guo J (2019a) A two-layer numerical model for simulating the frontal plowing phenomenon of flow-like landslides. Eng Geol 259:105168

Shen W, Li T, Li P, Shen Y, Lei Y, Guo J (2019b) The influence of the bed entrainment-induced rheology and topography changes on the propagation of flow-like landslides: a numerical investigation. Bull Eng Geol Environ 78(7):4771–4785

Shen W, Wang D, Qu H, Li T (2019c) The effect of check dams on the dynamic and bed entrainment processes of debris flows. Landslides 16(11):2201–2217

Sidle RC, Chigira M (2004) Landslides and debris flows strike Kyushu, Japan. EOS Trans Am Geophys Union 85(15):145–151

Tai Y-C, Heß J, Wang Y (2019) Modeling two-phase debris flows with grain-fluid separation over rugged topography: application to the 2009 Hsiaolin event, Taiwan. J Geophys Res Earth Surf 124(2): 305–333

Takahashi T, Das DK (2014) Debris flow: mechanics, prediction and countermeasures. CRC press

Tang C, Rengers N, van Asch TWJ, Yang YH, Wang GF (2011a) Triggering conditions and depositional characteristics of a disastrous debris flow event in Zhouqu city, Gansu Province, northwestern China. Nat Hazards Earth Syst Sci 11(11):2903–2912

Tang C, Zhu J, Ding J, Cui XF, Chen L, Zhang JS (2011b) Catastrophic debris flows triggered by a 14 August 2010 rainfall at the epicenter of the Wenchuan earthquake. Landslides 8(4):485–497

Wang D, Chen Z, He S, Liu Y, Tang H (2018) Measuring and estimating the impact pressure of debris flows on bridge piers based on large-scale laboratory experiments. Landslides 15(7):1331–1345

Wieczorek GF, Larsen MC, Eaton LS, Morgan BA, Blair JL (2001) Debris-flow and flooding hazards associated with the December 1999 storm in coastal Venezuela and strategies for mitigation. US Geological Survey. Open-File Report: 2001–144

Xiong M, Meng X, Wang S, Guo P, Li Y, Chen G, Qing F, Cui Z, Zhao Y (2016) Effectiveness of debris flow mitigation strategies in mountainous regions. Prog Phys Geogr Earth Environ 40(6):768–793

Xu Q, Zhang S, Li W, Van Asch TW (2012) The 13 August 2010 catastrophic debris flows after the 2008 Wenchuan earthquake, China. Nat Hazards Earth Syst Sci 12:201–216

Zhou GGD, Cui P, Chen HY, Zhu XH, Tang JB, Sun QC (2013) Experimental study on cascading landslide dam failures by upstream flows. Landslides 10(5):633–643

6. CONCLUSIONS

In this thesis, we have investigated three key phenomena (frontal plowing, bed entrainment and landslide-check dam interaction) related to flow-like landslides using three improved depth-averaged models. The following conclusions are obtained:

In Chapter 2 (Paper 1), we proposed a new two-layer depth-averaged model for the simulation of frontal plowing. The landslide mass and the frontal displaced mass were assumed to be two separate materials (layers), and the governing equations for each layer were formulated according to the mass and momentum conservation principles. The interaction between the landslide mass and the frontal displaced mass were simplified as the shear and normal forces acting on the interface of the two layers. The two-layer model was then used to simulate the Ximiaodian loess landslide which has obvious frontal plowing phenomenon indicating by the obvious dividing line between the loess landslide and the terrace material. We derived that:

- The frontal plowing process of the Ximiaodian landslide could be divided into three stages: 1) The landslide plowed into the frontal terrace mass and pushed it forward. 2) The front part of the landslide decelerated quickly and formed a ridge in the interactive area due to the plowing resistance, and the displaced mass accumulated on the ridge since it moved slower than the landslide. 3) The displaced mass accelerated under the influence of the gravity and plowing force, and moved forward quickly in a flow-like way.
- Frontal plowing had a dominant influence on the run-out behavior of the Ximiaodian landslide and the geomorphological characteristics of the deposit. Without considering its effect, the propagation velocity, distance and duration of a flow-like landslide are likely to be overestimated, while the thickness of the final deposit tends to be underestimated.

- In comparison with the traditional one-layer models, the proposed two-layer model was shown to be more suitable for the simulation of the frontal plowing phenomenon in flow-like landslides, and could provide more reliable and accurate simulation results.

In Chapter 3 (Paper 2), we investigated the influence of slope gradient and gully channel on the run-out behavior of the Verghereto rockslide-debris flow. An improved depth-averaged model was adopted to study the run-out, entrainment, and deposition processes of this landslide. The digital elevation difference between the pre-failure topography and the post-failure topography was obtained through field and drone survey to illustrate the entrainment and deposition characteristics of this landslide and to validate the simulation results. The conclusions highlighted that:

- According to field investigation, we divided the run-out process of the Verghereto landslide into three stages. In the first stage, the landslide detached from the bed rock sliding on the relatively gentle surface in the source zone. Then in the second stage, the landslide descended quickly in the steep slope zone next to the source zone before slumping heavily on the low slope gradient zone, and in the meantime, the volume of the landslide increased by entraining the loose mass on the slope and the rock mass disintegrated quickly. In the final stage, the disintegrated rock mass converged into the gully and transformed into a debris flow, and then the flow propagated along the gully until it stopped at the outlet of the gully.
- Our simulation results suggested that the frictional strength change produced by the solid-fluid transformation process probably played an important role in determining the dynamic characteristics of this landslide. The run-out behavior and depositional characteristic of the landslide could be correctly simulated when this friction strength change of sliding mass is properly considered. The depth-averaged single-phase model adopted in this study performed well in the simulation of the Verghereto rockslide-debris flow.

- Topography had a dominant impact on the depositional characteristic of the Verghereto landslide. In the landslide area where the slope is relatively steep, the final digital elevation difference showed entrainment. By contrast, in low slope gradient zones, the deposit showed accumulation and deposition. However, bed entrainment occurred on both steep and gentle slopes.
- Additionally, the existence of a gully channel on the slope could enlarge the run-out distance of the landslide. In the potential rockslides similar to the Verghereto landslide, those with a gully on the slope may pose higher risk to the infrastructures in the outlet of the gully (at slope toe).

In Chapter 4 (Paper 3), we proposed an improved depth-averaged model which is capable of simulating bed entrainment and the impeding effect of check dams. In this model, the check dams were treated as rigid bodies, and the impeding effect was imposed by adding a velocity constraint to the upstream neighboring computational cells of the check dam cells (the computational cells occupied by check dams) when the thicknesses of flow in these upstream cells were smaller than the height of the dam. An improved computational scheme was adopted to speed up the simulation. The run-out process of the 2010 catastrophic Hongcuan gully debris flow was simulated by the new model, and the effects of check dams on the dynamic and bed entrainment processes of this debris flow were analyzed. We concluded that:

- The results indicated that bed entrainment played a dominant role in the formational and run-out processes of the Hongchun gully debris flow. Bed entrainment significantly altered the flow characters of this debris flow. Without bed entrainment, the peak value of flow quantity would decrease gradually from the upstream of the gully to the downstream, while the peak value would show an opposite tendency while bed entrainment was dominating. Therefore, bed entrainment should be considered in assessing the prevention effect of check dams to prevent inadequate design.

- Check dams could greatly change the dynamic and bed entrainment processes of this debris flow. They reduced the flow quantity and bed entrainment scale of the debris flow at the downstream side of the check dam, delaying the arrival time of the debris flow at downstream.
- Additionally, by effectively constraining the bed entrainment scale, the prevention effect of check dams tended to be better if they were constructed at the upper part of the gully.

In Chapter 5 (Paper 4), the improved model was further applied in assessing the efficiency of the real check dams in the Hongchun debris flow gully. We obtained the following conclusions:

- The results showed that these check dams could perform quite well in constraining the bed entrainment downstream of the gully.
- The average velocity, peak discharge, and final scale of a debris flow in the gully could be substantially reduced by constructed check dams.
- The impeding effect would be sufficient when the initial volume of the debris flow is less than 1.5 times that of the catastrophic debris flow event that occurred in this gully on 14 August 2010.

In summary, these improved depth-averaged models effectively enhanced the applicability of the traditional single-phase depth-averaged models in the simulation of rapid flow-like landslides and the related phenomena like frontal plowing, bed entrainment, and landslide-defense structure interaction. They can provide more reliable and accurate simulation results in comparison with the original depth-averaged models.

On the other hand, the present study has several limitations which need to be addressed in the future. For instance, although the two-layer model can depict the frontal plowing phenomenon to some extent, the current model cannot simulate the deformation in the landslide and the plowed material. In the field, we observed obvious compression

ridges in the terrace material. However, the two-layer model cannot reproduce this phenomenon. There are also many difficulties associated with the modeling of bed entrainment. The physically-based model adopted in the depth-averaged model can predict bed entrainment generally satisfactorily, but it is still very difficult to determine the distribution of erodible mass in the field. The physically-based model is a great simplification of the real bed entrainment process which is mechanically much more complex. Additionally, it is still an open question on how to simulate the rheological changes caused by bed entrainment and solid-fluid transformation. In terms of simulating the interaction process between defense structures and rapid flow-like landslides, the improved depth-averaged model proposed in this thesis can only be used to evaluate the impeding effect of the structures, while the complex interaction process like collision, runup and pill-up of the flow cannot be simulated by this model. To overcome the above limitations, more advanced models may be necessary, and further investigations on the mechanisms of these phenomena should be crucial.

Appendix A: Co-author declaration

This declaration states the independent research contribution of the PhD candidate for each paper compiled in the thesis.

List of Papers:

1. Shen W, Li T, Li P, Berti M, Shen Y and Guo J (2019a) A two-layer numerical model for simulating the frontal plowing phenomenon of flow-like landslides. Eng Geol 259: 105168.
2. Shen W, Berti M, Li T, Andrea B, and Qiao Z (2021)The influence of slope gradient and gully channel on the run-out behavior of rockslide-debris flow: an analysis on the Verghereto landslide in Italy. Landslides.
3. Shen W, Wang D, Qu H and Li T (2019) The effect of check dams on the dynamic and bed entrainment processes of debris flows. Landslides 16, 2201–2217.
4. Shen W, Wang D, He S, and Li T. (2020) Numerical assessment of the impeding effect of check dams in the Hongchun debris flow gully, Sichuan Province, China. Bull Eng Geol Environ 79, 2833–2845.

Paper No.	**Title and full bibliographic reference**	
Paper 1	Shen W, Li T, Li P, Berti M, Shen Y and Guo J (2019a) A two-layer numerical model for simulating the frontal plowing phenomenon of flow-like landslides. Eng Geol 259: 105168. https://doi.org/10.1016/j.enggeo.2019.105168	
Role of PhD candidate & overall contribution (%)	**Type of contribution**	**Contributions of Co-authors**
First author, 50-75%	Study design and writing, visualization etc.	Second author: Tonglu Li, Field investigation and editing Third author: Ping Li, editing and revision guide Fourth author: Matteo Berti, editing and discussion Fifth author: Yueqiang Shen, model development Sixth author: Jian Guo, model development

Paper No.	**Title and full bibliographic reference**
Paper 2	Shen W, Berti M, Li T, Andrea B, and Qiao Z (2021)The influence of slope gradient and gully channel on the run-out behavior of rockslide-debris flow: an analysis on the Verghereto landslide in Italy. Landslides.

	Submission to Landslides under revision	
Role of PhD candidate & overall contribution (%)	**Type of contribution**	**Contributions of Co-authors**
First author, 30-50%	Writing, visualization etc.	Second author: Matteo Berti, study desigh, writing the second section, field investigation, editing Third author: Tonglu Li, model development and editing Fourth author: Andrea Benini, field investigation Fifth author: Zhitian Qiao, editing

Paper No.	**Title and full bibliographic reference**	
Paper 3	Shen W, Wang D, Qu H and Li T (2019) The effect of check dams on the dynamic and bed entrainment processes of debris flows. Landslides 16, 2201–2217. https://doi.org/ 10.1007/s10346-019-01230-7	
Role of PhD candidate & overall contribution (%)	**Type of contribution**	**Contributions of Co-authors**
First author, 50-75%	Study design and writing, visualization etc.	Second author: Dongpo Wang, study design and field investigation Third author: Huanan Qu, field investigation Fourth author: Tonglu Li, model development and editing

Paper No.	**Title and full bibliographic reference**	
Paper 4	Shen W, Wang D, He S, and Li T. (2020) Numerical assessment of the impeding effect of check dams in the Hongchun debris flow gully, Sichuan Province, China. Bull Eng Geol Environ 79, 2833–2845. https://doi.org/10.1007/s10064-020-01755-5	
Role of PhD candidate & overall contribution (%)	**Type of contribution**	**Contributions of Co-authors**
First author, 50-75%	Study design and writing, visualization etc.	Second author: Dongpo Wang, study design and field investigation Third author: Siming He, editing Fourth author: Tonglu Li, model development and editing

Appendix B: Derivation of the depth-averaged model

In this section I introduce the basic derivation of the depth-averaged model proposed by us in Shen et al. (2018). The model is the foundation of the improved models in Paper 2, Paper 3 and Paper 4 presented in this thesis.

A global Cartesian coordinate system is adopted (as shown in Fig. A1a). The landslide is assumed to have a three-layer structure, consisting of a movable sliding mass, a thin erodible sliding zone and a fixed sliding surface (Fig. A1b). In nature, the erosion depth is limited, and the thickness of the erodible layer should be determined by field surveying.

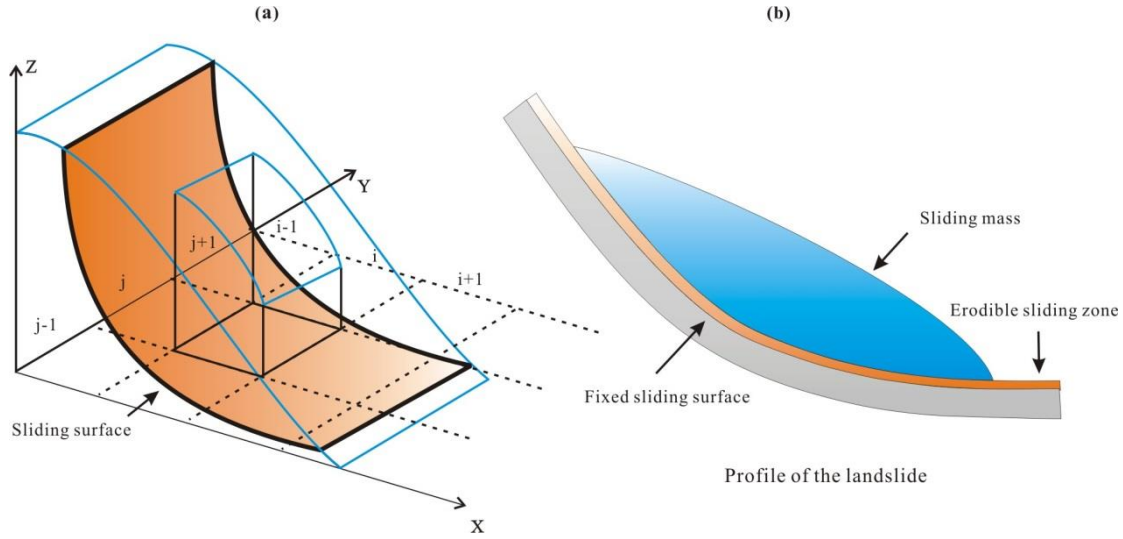

Fig. A1. (a) Coordinate setup in the landslide zone. **(b)** The assumed three-layer structure profile of the landslide.

Momentum equations

The governing equations can be deduced in a soil column. As shown in Fig. A2, the following assumptions are made regarding the forces acting on the column: (1) The bottom of the column is assumed to be a plane. The supporting force *N* is normal to the plane, and the resistance force *S* is parallel to the plane and opposite to the average velocity of the soil column. (2) The parallel resistance forces on the lateral surfaces are neglected. (3) The lateral pressure is assumed to increase linearly with soil depth. The second assumption is similar to the shallow water condition used in many depth-integrated models, and is reasonable because the width and length of the flow-like landslides are usually much larger than the depth.

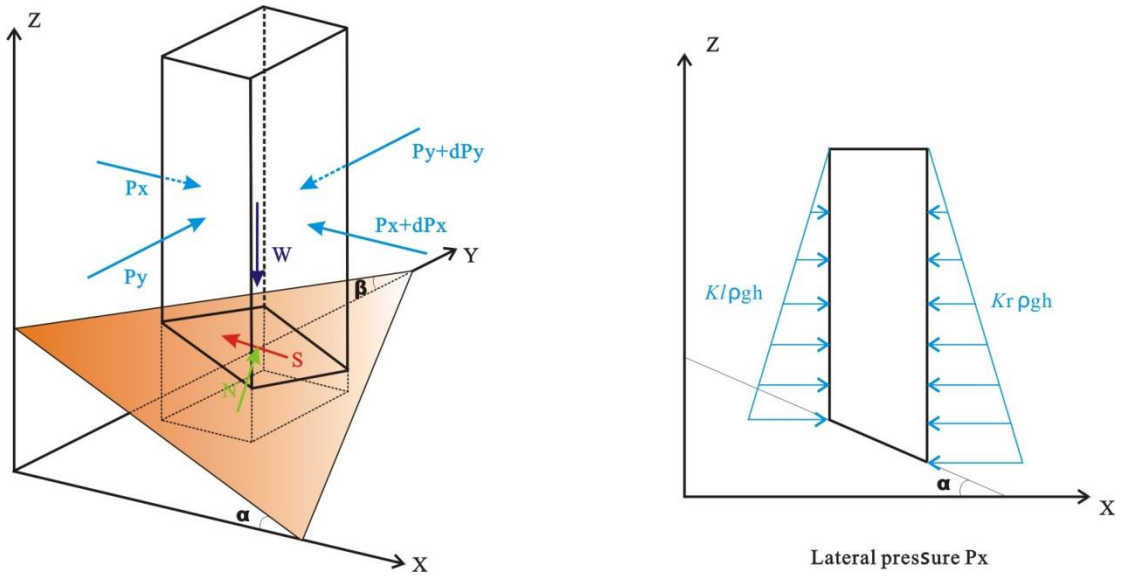

Fig. A2. Forces acting on the sliding mass column (*P* is the lateral pressure, *W* is the gravity, *N* is the supporting force, and *S* is the resistance force).

The momentum equations are deduced based on the momentum conservation of the soil column in the x and y directions. The following derivation takes the x direction as an example; this derivation is similar for the y direction. Based on the abovementioned assumptions, the equilibrium equation in the x direction is given by

$$a_x = \frac{-dP_x + N_x - S_x}{m} \tag{A.1}$$

where a_x is the acceleration in the x direction, dP_x describes the resultants of the lateral forces in the x direction, N_x is the projection of the supporting force N in the x direction, S_x is the projection of the resistance force S in the x direction, and m is the mass of the soil.

Supposing that the horizontal velocities along the column are identical, then a_x on the left side of Eq. (A.1) can be written as

$$a_x = \frac{\partial v_x}{\partial t} + v_x \frac{\partial v_x}{\partial x} + v_y \frac{\partial v_x}{\partial y} \tag{A.2}$$

where v_x and v_y are the average velocities in the x and y directions, respectively.

Pressure term

The first term on the right side of Eq. (A.1) can be written as

$$\frac{dP_x}{m} = kg \frac{\partial h}{\partial x} + g \frac{h}{2} \frac{\partial k}{\partial x} \tag{A.3}$$

where k is the lateral pressure coefficient, h is the thickness of the sliding mass, and g is the gravitational acceleration. In Eq. (A.3), k is the function of position and time, unlike the constant

applied in most other models. k is determined based on the state (i.e., active, static or passive state) of the sliding mass, as suggested by Savage and Hutter (1989):

$$\left.\begin{matrix} k_{pas} \\ k_{act} \end{matrix}\right\} = \frac{2}{\cos^2\varphi_i}\left(1 \pm \sqrt{1-\cos^2\varphi_i\left(1+\tan^2\varphi_a\right)}\right) - 1 \tag{A.4}$$

where φ_i is the internal friction angle, φ_a is the apparent basal friction angle, and k_{pas} and k_{act} are the passive and active lateral pressure coefficients, respectively.

Eq. (A.4) is used by Ouyang et al. (2013) based on the assumption that the sliding mass is either in a passive or active state, which is determined by the instantaneous strain rate of the soil. A strain-dependent k is widely used in Lagrangian methods (Hungr and McDougall 2009) but is not easily implemented in Eulerian methods. Therefore, k is taken as a discontinuous function of strain rate in some Eulerian methods, possibly resulting in a significant fluctuation of the numerical solution. To solve this problem, a modified approach is adopted here. k in the x direction is given by

$$k_x = \begin{cases} k_{pas}, & \frac{\partial v_x}{\partial x} \le -\varepsilon \\ \left(\frac{\partial v_x}{\partial x}/\varepsilon\right)\left(k_{pas}-k_0\right)+k_0, & -\varepsilon < \frac{\partial v_x}{\partial x} < 0 \\ k_0 - \left(\frac{\partial v_x}{\partial x}/-\varepsilon\right)\left(k_0-k_{act}\right), & 0 \le \frac{\partial v_x}{\partial x} < \varepsilon \\ k_{act}, & \frac{\partial v_x}{\partial x} \ge \varepsilon \end{cases} \tag{A.5}$$

where k_0 is the static soil pressure coefficient. Eq. (A.5) suggests that when the strain rate exceeds a threshold $|\varepsilon|$, the soil reaches either a passive state or an active state. When the strain rate is positive, the sliding mass shows a divergent tendency, so k would be lower than k_0. Otherwise, the sliding mass would show a convergent tendency. This approach is similar to that adopted by Ouyang et al. (2013). However, when the strain rate is lower than the threshold, instead of setting k equal to k_0, a linear interpolation method is used here. Therefore, k is a continuous function of the strain rate, creating continuous lateral pressure. The approach mentioned above is in agreement with the fact that the sliding mass is not always in a passive or active state but more often between these two states.

The sign of the strain rate reflects only the (convergent or divergent) tendency of the soil mass. $|\varepsilon|$ is used to estimate the magnitude of the strain rate that may cause the soil column to reach a passive or an active earth pressure state. However, it is difficult to determine the value of $|\varepsilon|$ in an Eulerian-based method because the strain in the soil column cannot be determined. Here, the following equation is proposed to estimate $|\varepsilon|$:

$$|\varepsilon| \approx \left|\frac{k_{pas}-k_0}{D\Delta t}\right| \tag{A.6}$$

where Δt is the time step and D is a dimensionless stiffness adopted in the strain-based method. In this paper, D=200 is adopted, as suggested by Mcdougall et al. (2004). Eq. (A.6) indicates that if the strain rate exceeded $|\varepsilon|$, k could change from k_0 to k_{pas} or k_{act} within one time step.

Supporting force term

The second term on the right side of Eq. (A.1) can be written as

$$\frac{N_x}{m} = \frac{N_{sx} + N_{cx}}{m} \tag{A.7}$$

where N_{sx} and N_{cx} are the projections of the static supporting force N_s and centrifugal supporting force N_c in the x direction, respectively. The centrifugal effect is taken into account by N_c.

If a sliding mass is moving on a flat surface, no additional force normal to the surface would be produced by the sliding mass. When the surface is curved, the forces must change. An additional force pointing in the direction normal to the surface must exist due to the basic centrifugal movement principle. The additional force caused by the curvature is the centrifugal force, which has not been properly considered by the former researchers.

The static supporting force N_s and centrifugal supporting force N_c are determined by

$$N_s - F_n = ma_{sn} = 0 \tag{A.8}$$

$$N_c = ma_{cn} = \mathrm{m}C\bar{v}^2 \tag{A.9}$$

where a_{sn} and a_{cn} are the static and centrifugal accelerations in the direction normal to the sliding surface, respectively, C is the curvature of the sliding surface, and $\bar{v}$ is the average velocity of the sliding mass. According to Eq. (A.8), N_s is equal to F_n, which is the projection of the resultant force of the other external forces in the direction normal to the sliding surface.

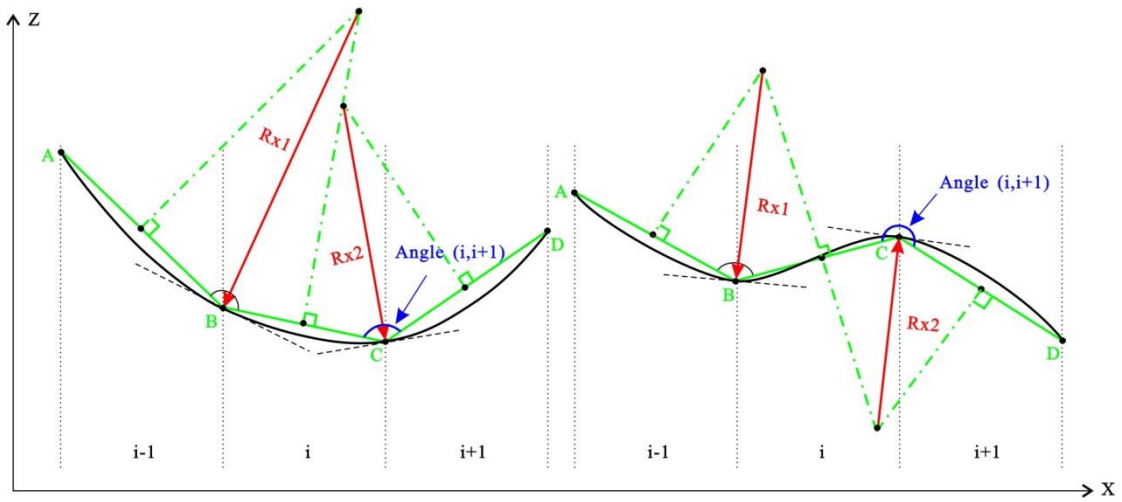

Fig. A3. Schematic diagram of the estimation of the curvature of the sliding surface in the x direction.

The curvature of the sliding surface in a specific column is interpolated by the curvature of the two nodes of the column, as shown in Fig. A3 for the x direction. In Fig. A3, the curvature of a column 'i' in the x direction is assumed to be the average value of the curvature in nodes B and C, and the value of N_c is assumed to be the sum of N_{cx} and N_{cy}. Then, Eq. (A.7) can be rewritten as

$$\frac{N_x}{m} = (Ag + B)\frac{\tan\alpha}{G} \tag{A.10}$$

where α and β are the parameters related to the dip angle of the sliding surface in the x and y directions, respectively (as shown in Fig. A2a), G is the geometric parameter, and A and B are parameters related to N_s and N_c, respectively. The expressions of G, A and B are given by Eqs. (A.11-A.15):

$$G = \tan^2\alpha + \tan^2\beta + 1 \tag{A.11}$$

$$A = 1 + \left(k\frac{\partial h}{\partial x} + \frac{h}{2}\frac{\partial k}{\partial x}\right)\tan\alpha + \left(k\frac{\partial h}{\partial y} + \frac{h}{2}\frac{\partial k}{\partial y}\right)\tan\beta \tag{A.12}$$

$$B = \frac{C_x}{\cos\alpha}\left(\frac{v_x}{\cos\alpha}\right)^2 + \frac{C_y}{\cos\beta}\left(\frac{v_y}{\cos\beta}\right)^2 \tag{A.13}$$

$$C_x = \frac{1}{2}\left(\frac{1}{R_{x1}} + \frac{1}{R_{x2}}\right) \tag{A.14}$$

$$C_y = \frac{1}{2}\left(\frac{1}{R_{y1}} + \frac{1}{R_{y2}}\right) \tag{A.15}$$

where R_{x1} and R_{x2} are the curvature radii of the nodes on either side of a column in the x direction, as shown in Fig. A3, and R_{y1} and R_{y2} are the corresponding radii in the y direction. The sign of the curvature radius is determined by the angle (i, i+1) as depicted in Fig. A3. If this angle is greater than 180 °, the corresponding radius of curvature R_{x2} is negative, and vice versa. The magnitude of the curvature radius of a node is determined by the two line segments nearby the node. For example, the perpendicular bisector of segment BC and that of segment CD intersects at a point, and the curvature radius at node C (R_{x2}) is obtained by connecting this point with node C.

Resistance force term

The third term on the right side of Eq. (A.1) can be written as

$$\frac{S_x}{m} = \frac{D_x S}{m} \tag{A.16}$$

where D_x is the parameter related to the direction of velocity and is given by

$$D_x = \frac{v_x}{\sqrt{v_x^2 + v_y^2 + v_z^2}} \tag{A.17}$$

where v_z ($v_z = v_x\tan\alpha + v_y\tan\beta$) is the average velocity in the z direction because the average velocity of the sliding mass is parallel to the sliding surface.

In Eq. (A.16), S can have different formulations based on the constitutive relations adopted. The commonly used constitutive relations in flow-like landslide simulation are the Mohr-Coulomb criteria and the Voellmy model. The Manning model is also widely used to simulate viscous shallow water problems.

The Mohr-Coulomb criteria is given by

$$S = N\tan\varphi_a + c\mathrm{dxdy}\sqrt{G} \tag{A.18}$$

where c is the cohesion of the sliding surface soil.

The Voellmy friction model is given by

$$S = N\tan\varphi_a + \frac{\rho g\left(v_x^{\,2} + v_y^{\,2}\right)}{C_z^2}\mathrm{dxdy}\sqrt{G} \tag{A.19}$$

where C_z is the Chézy coefficient. The second term on the right side of Eq. (19) reflects the influence of the air drag, turbulence and all other velocity-dependent resistances.

The Manning model is given by

$$S = \frac{\rho g n^2\left(v_x^{\,2} + v_y^{\,2}\right)}{h^{1/3}}\mathrm{dxdy}\sqrt{G} \tag{A.20}$$

where n is Manning's roughness.

Substituting Eqs. (A.2), (A.3), (A.10), and (A.16) into Eq. (A.1), the following momentum equation in the x direction is obtained:

$$\frac{\partial v_x}{\partial t} + v_x\frac{\partial v_x}{\partial x} + v_y\frac{\partial v_x}{\partial y} = -\left(kg\frac{\partial h}{\partial x} + g\frac{h}{2}\frac{\partial k}{\partial x}\right) + \left(Ag + B\right)\frac{\tan\alpha}{G} - \frac{D_x S}{m} \tag{A.21}$$

and similarly, that in the y direction can be written as:

$$\frac{\partial v_y}{\partial t} + v_x\frac{\partial v_y}{\partial x} + v_y\frac{\partial v_y}{\partial y} = -\left(kg\frac{\partial h}{\partial y} + g\frac{h}{2}\frac{\partial k}{\partial y}\right) + \left(Ag + B\right)\frac{\tan\beta}{G} - \frac{D_y S}{m} \tag{A.22}$$

Continuity equation

The continuity equation is deduced based on mass conservation within a column. The sliding mass is assumed to be incompressible, so mass conservation can be expressed by volume conservation, as shown in Fig. A4. Then, the continuity equation is given by

$$\frac{\partial h}{\partial t} + \frac{\partial Q_x}{\partial x} + \frac{\partial Q_y}{\partial y} - E = 0 \tag{A.23}$$

where $E=-\partial Z/\partial t$ is defined as the entrainment rate, the positive direction of E is the positive direction of the z axis; Z is the relative elevation of the sliding surface and varies due to entrainment; and $Q_x=v_x h$ and $Q_y=v_y h$ are flow quantities in the x and y directions, respectively.

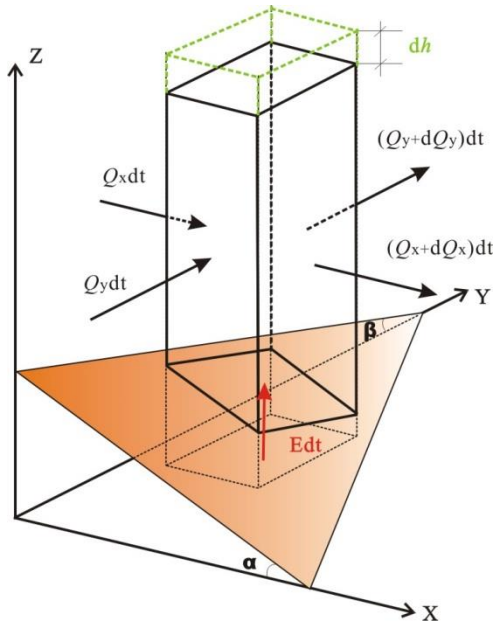

Fig. A4 Schematic diagram of a soil column for the derivation of the continuity equation.

Estimation of the entrainment rate E

Different methods were proposed to estimate the value of entrainment rate *E*. Iverson and Ouyang (2015) published a detailed review of landslide entrainment. According to their review, in existing models, the equations for entrainment rate *E* are formulated either by empirical methods or theoretical methods. The empirical equation proposed by McDougall and Hungr (2005) is simple and efficient and is widely used, but the equation lacks explicit dependence on boundary tractions (Iverson and Ouyang 2015). In contrast, a theoretical equation proposed by Fraccarollo and Capart (2002) accounts for the boundary traction and is thus more reasonable. According to Fraccarollo and Capart (2002), the equation for entrainment rate E is given by

$$E = -\frac{\partial Z}{\partial t} = \frac{\tau_b - \tau_r}{\rho V} \tag{A.24}$$

where V is the average velocity of the sliding mass, $V=(v_x^2+v_y^2)^{1/2}$ is adopted in this paper, τ_b is the shear stress exerted by the sliding mass on the erodible layer, and τ_r is the resistant shear stress of the erodible layer. Eq. (A.24) indicates that if τ_b is greater than τ_r, entrainment will occur. The value of E is also related to the velocity of the sliding mass V, reflecting the availability of momentum.

In summary, the governing equations are given by Eqs. (A.21-A.23).

Initial and boundary conditions

A flow-like landslide usually starts from a static state. It can move only if the gravity and pressure gradient overcome the basal resistance. Taking the x direction as an example, the starting condition can be written as

$$\left|-\left(kg\frac{\partial h}{\partial x}+g\frac{h}{2}\frac{\partial k}{\partial x}\right)+\left(Ag+B\right)\frac{\tan\alpha}{G}\right|\geq\left|\frac{DxS}{m}\right| \tag{A.25}$$

This initial condition should be applied in the region where the sliding mass is static.

The boundary conditions of this model can be classified into two categories, namely, the static boundary and moving boundary. The position of the boundary between the moving sliding mass and static sliding mass (or the dry bed) changes gradually due to the propagation of the flow-like landslide. This boundary is the moving boundary, and the velocity of the sliding mass along this boundary is set to zero (v_x=v_y=0). When a dry bed is present, the thickness should also be zero (h=0). A static boundary, such as the wall of a container, does not move during the calculation, and the velocity of the fluid in the direction normal to this boundary is set to zero (v_n=0). Another kind of static boundary is the zero-pressure boundary at which the lateral pressure is set to zero (i.e., h=0).

As in all depth-integrated models, the free surface boundary does not need to be determined by other techniques such as the volume of fluid (VOF) or level-set techniques because it is determined automatically from the calculated thickness across the sliding mass.

Reference

Fraccarollo L, Capart H (2002) Riemann wave description of erosional dam-break flows. J Fluid Mech 461: 183-228. doi: 10.1017/S0022112002008455

Hungr O, McDougall S (2009) Two numerical models for landslide dynamic analysis. Comput Geosci 35: 978–992. doi: 10.1016/j.cageo.2007.12.003

Iverson RM, Ouyang C (2015) Entrainment of bed material by earth-surface mass flows: review and reformulation of depth-integrated theory. Reviews of Geophysics 53: 27-58. doi: 10.1002/2013RG000447

McDougall S, Hungr O (2004) A model for the analysis of rapid landslide motion across three-dimensional terrain. Can Geotech J 41:1084–1097. doi: 10.1139/t04-052

McDougall S, Hungr O (2005) Dynamic modelling of entrainment in rapid landslides. Can Geotech J 42:1437–1448. doi: 10.1139/t05-064

Savage SB, Hutter K (1989) The motion of a finite mass of granular material down a rough incline. J Fluid Mech 199:177–215. doi: 10.1017/S0022112089000340

Shen W, Li T, Li P and Guo J (2018) A modified finite difference model for the modeling of flowslides. Landslides 15: 1577-1593. https://doi.org/10.1007/s10346-018-0980-6

Ouyang C, He S, Xu Q, Luo Y, Zhang W (2013) A MacCormack-TVD finite difference method to simulate the mass flow in mountainous terrain with variable computational domain. Comput Geosci 52:1–10. doi: 10.1016/j.cageo.2012.08.024